HAL
open science

Cell Mechanics : Mechanical Properties and Membrane Rupture Criteria

Lionel Guillou

▶ **To cite this version:**

Lionel Guillou. Cell Mechanics : Mechanical Properties and Membrane Rupture Criteria. Biomechanics [physics.med-ph]. Université Paris Saclay (COmUE), 2016. English. NNT : 2016SACLX041 . tel-01481900

HAL Id: tel-01481900

https://pastel.hal.science/tel-01481900v1

Submitted on 3 Mar 2017

HAL is a multi-disciplinary open access archive for the deposit and dissemination of scientific research documents, whether they are published or not. The documents may come from teaching and research institutions in France or abroad, or from public or private research centers.

L'archive ouverte pluridisciplinaire **HAL**, est destinée au dépôt et à la diffusion de documents scientifiques de niveau recherche, publiés ou non, émanant des établissements d'enseignement et de recherche français ou étrangers, des laboratoires publics ou privés.

NNT : 2016SACLX041

THESE DE DOCTORAT
DE
L'UNIVERSITE PARIS-SACLAY
PREPAREE A
L'ECOLE POLYTECHNIQUE

ECOLE DOCTORALE N° 573
Interfaces

Spécialité de doctorat: Physique

Par

Mr Lionel Guillou

Cell Mechanics:
Mechanical Properties and Criteria for Membrane Rupture

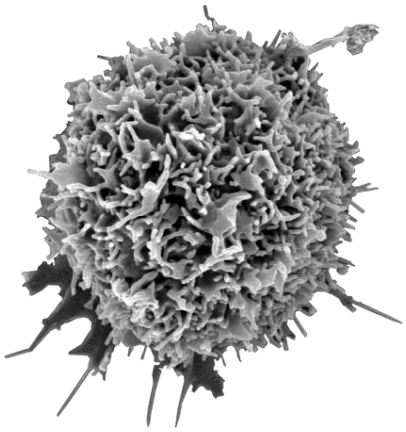

Thèse présentée et soutenue à l'Ecole Polytechnique, le 14 Septembre 2016

Composition du Jury :

Lenz, Martin	Université Paris-Sud	Rapporteur
Wagner, Christian	Universität des Saarlandes	Rapporteur
Asnacios, Atef	Université Paris-Diderot	Examinateur
Hivroz, Claire	Institut Curie	Présidente du jury
Husson, Julien	Ecole Polytechnique	Co-directeur de thèse
Barakat, Abdul I.	Ecole Polytechnique	Co-directeur de thèse

SYNTHESE

L'athérosclérose est une maladie artérielle chronique qui est une des causes majeures d'accidents vasculaires cérébraux et de crises cardiaques. Cette thèse a pour objectif de mieux comprendre certains facteurs spécifiques impliqués dans le dévelopement de cette maladie en abordant cette problématique sous l'angle de la mécanique.

L'athérosclérose se développe progressivement sur plusieurs décennies au cours desquelles l'artère se durcie progressivement. Son émergence est favorisée par la présence de cholestérol dans les artères, dont l'oxydation provoque une réaction inflammatoire des cellules endotheliales. Cette inflammation va attirer des leucocytes (globules blancs) qui vont s'attacher aux cellules endotheliales, puis transmigrer au travers d'elles. Les deux types de cellules qui jouent un rôle clef dans la genèse de l'athérosclérose sont donc les cellules endothéliales adhérentes et les leucocytes non-adhérents. Afin de savoir caractériser ces deux cellules actrices de l'athérosclérose, nous avons développé deux systèmes capables de mesurer leurs propriétés mécaniques.

Le premier, appelé "indentation de profil", utilise des micropipettes et des microindenteurs pour indenter une cellule. On accède à la force en mesurant la flexion d'un microindenteur de rigidité connue, tandis que la profondeur d'indentation est accessible optiquement. Ces deux mesures sont ensuite reliées par un modèle mécanique, qui permet d'accèder aux propriétés mécaniques des cellules. Les cellules étant des matériaux viscoélastiques, deux paramètres au minimum sont nécessaires pour les caractériser. L'avantage de notre système réside dans le fait qu'il peut être utilisé indifférement sur des cellules adhérentes et non-adhérentes, et qu'il permet le placement d'une micropipette qui permet de modifier l'environnement, notamment chimique, des cellules dont on mesure les propriétés mécaniques. Toutefois, son inconvénient principal est qu'il ne permet qu'un débit de ~10 cellules/heure.

Le second système permet de palier à cette limite pour les cellules non-adhérentes. Il consiste en un système microfluidique avec deux canaux perpendiculaires formant une croix. On fait entrer deux flux contenant des cellules de part et d'autre d'un canal, qui sont evacués dans les deux branches du canal orthogonal. Ainsi, on crée au centre de la croix une zone de flux extensionnel qui va déformer les cellules qui y passent. Les déformations de la cellule sont mésurées par une caméra positionnée sous la croix. Reliant là encore la force créée par le flux extensionel aux déformations

des cellules, nous accédons ainsi aux mêmes deux paramètres mécaniques qu'avec l'instrument précédent. L'avantage de cette technique est que le débit est maintenant beaucoup plus important, de l'ordre de ~10^6 cellules/heure.

De plus, nous nous sommes demandé, dans le contexte de l'athérosclérose, si la mécanique pouvait nous aider à comprendre quand les déformations des cellules, ou les contraintes exercées sur elles, pouvaient les endommager.

En effet, lorsque les plaques d'athérosclérose obstruent une partie trop grande du flux sanguin, le traitement le plus courant consiste à rouvrir le vaisseau avec un ballon et à le maintenir ouvert au moyen d'une endoprothèse artérielle, qui est un petit dispositif maillé et tubulaire. Cette procédure exerce des contraintes de compression considérables sur l'endothélium et l'endommage. Nous avons donc cherché à trouver un critère physique prédictif de la rupture de la membrane des cellules endothéliales en compression, puis avons comparé cela aux contraintes exercées sur l'endothélium durant la pose d'une endoprothèse artérielle. Nous trouvons que la contrainte de compression exercée durant la pose d'une endoprothèse artérielle, de l'ordre de ~100 kPa, est bien supérieure à la limite de rupture en compression d'une cellule endothéliale, de l'ordre de ~10 kPa. Des améliorations incrémentales de dispositifs d'endoprothèse artérielle existants ne seront donc pas suffisantes pour éviter d'endommager l'endothélium ; seules des innovations de rupture ou des changements de méthode pourraient résoudre cette limitation majeure de la prise en charge médicale actuelle.

Un autre scénario dans l'athérosclérose qui implique de larges déformations des cellules est la migration transendothéliale. Dans ce processus, les leucocytes créent un petit trou entre les cellules endothéliales dans lequel elles s'insèrent, puis ressortent, indemnes malgré cette extraordinaire déformation, de l'autre côté de l'endothélium. Nous avons donc cherché à comprendre quelles étaient les déformations maximales possibles des leucocytes sans qu'il y ait rupture. Nous avons distingué les cas, selon que ces déformations soient passives (comme lors du passage dans la microvasculature) ou actives (comme lors de la traversée de l'endothélium par les leucocytes). Dans le cas des déformations passives, nous trouvons que la membrane cellulaire casse quand l'extension de la surface membranaire dépasse les réserves exterieures de membranes cellulaires (soit typiquement ~40% de la surface initiale pour les lymphocytes T) contenues sous forme de plis et de petits picots appelés microvillosités. Les déformations actives peuvent en revanche être beaucoup plus importantes, avec des extensions de

membrane de l'ordre de ~100 à 200%. Cela suggère que des réserves intérieures de membrane sont utilisées lors des déformations actives des lymphocytes T.

REMERCIEMENTS

Septembre 2016.

Il y a dix ans, presque jour pour jour, je faisais mes premiers pas sur le plateau. Après plusieurs années d'abscence, le retour en septembre 2013 m'a fait tout drôle. Loin d'un retour en arrière, ce fut en fait le début d'une nouvelle aventure, guidée par Abdul Barakat et Julien Husson, mes deux directeurs de thèse. C'est eux tout d'abord que je veux remercier ici. Abdul pour sa qualité d'écoute et ses encouragements constants, ainsi que ses conseils toujours avisés et son ouverture d'esprit. Julien pour son aide déterminante à tous les moments clés, nos discussions quotidiennes, et plus généralement pour m'avoir ouvert les portes de la mécanique cellulaire et des sciences expérimentales. Je vous remercie tous deux sincèrement de votre soutien.

Je veux aussi saluer ici la Barakat-team pour avoir formé une équipe soudée qui s'entraide et permet à tout le monde de se sentir à l'aise. Outre Avin, Elizabeth, Brenna, Julie, Olga, Anna S., Carlo, ainsi que nos anciens (et pour certains futurs) membres, Gaëlle, David, Alexandra, Sidney, Valentin, Jowell, et Cécile (notamment pour m'avoir mis le pied à l'étrier avec FEBio), je veux temoigner de mon amitié à mes co-promotionnaire de doctorat, François et Johanne, avec qui j'ai partagé les hauts et les bas de la thèse, et surtout beaucoup de bons moments. J'associe à ces remerciements l'équipe d'Instent qui partage notre quotidien, et notamment ses membres de la première heure, Franz, Bruno, Myline et Pierluca, ainsi que Nathalie, avec qui nous partageons depuis longtemps une passion pour la biomécanique.

Merci aussi au LadHyX pour sa bonne ambiance, et à Christophe de m'y avoir accueilli. Un baroud d'honneur tout d'abord pour l'équipe de Charles avec qui nous partageons les locaux et les bocaux, ainsi que nos broc d'eau à midi. Je pense à Raphaël, Sébastien, Benoit, Gabriel, Cyprien, Micaela, Irma, Caro F. et ses anciens, Nicolas, Rémi et Magali D. notamment. Puis au soutien administratif et technique, en les personnes de Tonio, Dany, Toai, Delphine, Sandrine, Thérèse et Magali T., sans qui le labo ne serait que chaos. Merci à l'équipe FootHyX pour de grands moments de défoulade, et à ses membres Guillaume, Ambre, Caro C., Christophe, Manu, Olga, J-Phi, Marine, PB, sans oublier son membre honoraire Eline. Merci également à Cyprien d'avoir partagé l'écrasante responsabilité de représentant des non-permanents avec moi (ainsi que pas mal de sessions piscine) et à Camille avec qui nous co-gérions les séminaires. Sans oublier tous ceux rencontrés au détour d'un café, d'un séminaire ou d'un magnan, et avec qui la discussion fut toujours un plaisir: Pascal, Lutz, Timothée, Mathieu, Gaetan, Yifan, Eunok, Ana R. et bien d'autres. Je souhaite également remercier Emmanuel D. de ses conseils, notamment sur

l'indentation, et les membres du LMS avec qui nous partageons notre oxygène, en particulier Jean-Marc et Jean-Séb.

J'en profite pour remercier plus particulièrement tous mes autres co-bureaux (en plus de Jean-Séb) au cours de ma thèse, des premiers, Loïc et Anders, puis Sébastien un peu plus tard, qui m'ont montré les ficelles du métier et m'ont fait sentir tout de suite au chez moi, à Raphaël et Anna S., mes co-bureaux actuels, pour leur bonne humeur et leur simplicité. Enfin je remercie les responsables et ingénieurs du cours sur les hydroliennes que j'ai eu le plaisir d'enseigner, Alex, Ali, William, pour m'avoir fait confiance et m'avoir soutenu dans toutes mes propositions.

Une partie de ma thèse très stimulante fut effectuée au laboratoire de Sanjay Kumar à Berkeley, que je tiens à remercier avec toute son équipe pour leur sens de l'accueil. Je pense à George et Joanna surtout, pour leur chaleur et leur énergie, avec qui travailler est toujours un plaisir. Je remercie également mes autres collaborateurs durant ma thèse, et en particulier David, Claire et Stéphanie pour m'avoir beaucoup appris et toujours avec le sourire.

Je remercie enfin mon jury de thèse. Mes rapporteurs d'abord, Martin Lenz et Christian Wagner, pour leurs lectures attentives et leurs remarques éclairées. Les membres de mon jury ensuite, Claire Hivroz et Atef Ascnacios pour leur présence et les intéressants échanges scientifiques que nous avons eu le jour de la soutenance.

A tous, je souhaite bon vent, et espère que nous resterons en contact.

Pour finir, je remercie ma famille et mes amis, et au premier chef grand-parents, parents, frère et soeurs, cousins et cousines, d'avoir eu la patience de m'écouter expliquer à quoi mes travaux pouvaient servir et l'indulgence de ne pas répondre.

Merci à ma femme, Patricia, à qui je dédie ce manuscrit. Merci de me pousser, même quand je ne vais nulle part. Merci d'y croire quand je n'y crois plus.

To Patricia

TABLE OF CONTENTS

Introduction

Chapter 1. Mechanical properties of adherent and immobilized non-adherent cells

Chapter 2. Mechanical properties of non-adherent cells in suspension

Chapter 3. Membrane rupture criterion for adherent cells

Chapter 4. Membrane rupture criterion for non-adherent cells

Conclusions

Perspectives

Bibliography

Appendix

INTRODUCTION

"As the extension, so the force." It is by these words that Robert Hooke first explained the principles of linear elasticity, which he discovered in 1660. Only five years later, the same Hooke, from observations on cork (Figure I.1) using the newly invented optical microscope, would go on to discover the existence of cells (Hooke, 1665).

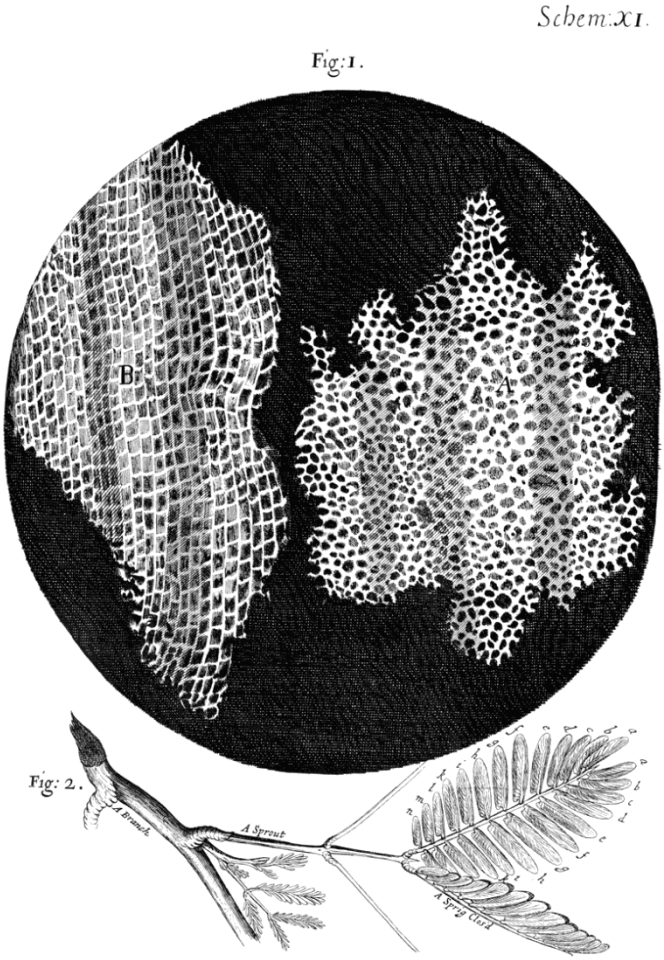

FIGURE I.1: Micrograph of cells in a cork, drawn by Robert Hooke in "Micrographia" (1665). (A) Transverse section. (B) Longitudinal section. (Public domain)

While those near-simultaneous discoveries would for centuries be thought of as very separate concepts, and form the basis of respectively mechanics and cell biology, they have recently been recognized as been tightly intertwined.

Indeed, many experimental observations over the past three decades have shown that mechanical inputs from the environment directly affect cellular behavior. For instance, shear stress due to blood flow affects endothelial cell shape and permeability (Malek and Izumo, 1996), and regions of disturbed arterial blood flow are prone to the development of atherosclerotic plaques (Ku *et al.*, 1985). If we now consider the substrate on which the cells adhere, the stiffness of the extracellular matrix has been shown to affect cell migration (Ulrich *et al.*, 2009), and perhaps even more crucially, to direct the lineage differentiation of stem cells (Engler *et al.*, 2006). These observations, and others, have led to the emergence of a new field of study whose purpose is to understand how cells convert mechanical signals into biological and chemical activity, a process termed mechanotransduction (Huang *et al.*, 2004).

In turn, the state of a cell is often reflected in its mechanical properties. This realization has been one of the key motivations for trying to measure those properties. Importantly, multiple diseases, from diabetes (McMillan *et al.*, 1978) and leukemia (Rosenbluth *et al.*, 2006) to breast cancer (Li *et al.*, 2008), have been shown to lead to significant changes in cellular mechanical properties. It is therefore natural that in recent years, the idea to use these mechanical properties as a label-free biomarker for disease state has emerged. Moreover, the concomitant advent of microfluidics and informatics has put the high-throughput and automated measurement of cellular mechanical properties within reach, rendering possible a new generation of diagnostic tools based on cell population mechanical "signature" (Gossett *et al.*, 2012; Mietke *et al.*, 2015; Otto *et al.*, 2015).

Our work focuses on cell mechanics in the context of atherosclerosis. Our main motivation in doing so is that atherosclerosis is the leading cause of mortality in the developed world, due to complications such as myocardial infarction and stroke (Beckman *et al.*, 2002). Atherosclerosis is a disease that develops in humans over decades and in which the arterial wall progressively thickens. It is promoted by the presence of excessively high levels of low-density lipoprotein (LDL) in the arterial wall, due to either genetic causes or lifestyle. The oxidation of the lipids contained in LDL marks the beginning of atherosclerosis (Berliner *et al.*, 1995). These oxidized lipids trigger an inflammatory response from endothelial cells, which attracts leukocytes (white blood cells) that are responsible for carrying out the immune response. In particular, monocytes, a type of leukocytes, are recruited from the bloodstream at the site of inflammation and migrate across the endothelial cell monolayer (a process termed transendothelial migration) (Woollard and Geissmann, 2010) to reach LDL (Østerud and Bjørklid, 2003). Monocytes then differentiate into macrophages, another type of leukocyte, to internalize LDL. In time, macrophages turn into foam cells and accumulate, forming an initial atherosclerotic plaque called "fatty streak". During that time, T lymphocytes are also recruited and become part of the plaque (Grivel *et al.*, 2011). Additionally, growth factors and cytokines (small proteins produced by cells) released by inflammed endothelial cells trigger the proliferation and migration of smooth muscle cells contained in the vessel wall,

which in turn triggers further thickening of the arterial wall (Rudijanto, 2007). In its final stages, the atherosclerotic plaque may cause vessel occlusion, either because it has become too thick or because the plaque ruptures and leads to the formation of a thrombus (blood clot) (Verstraete, 1990).

A rather unique feature of studying cell mechanics in the context of atherosclerosis is that both adherent (endothelial cells) and non-adherent (leukocytes) cells are involved. In Chapter 1, we present a novel technique, which we term "profile microindentation", that is able to measure the mechanical properties of both adherent and non-adherent cells (Figure I.2), provided that the latter are maintained in place using a micropipette (Guillou *et al.*, 2016).

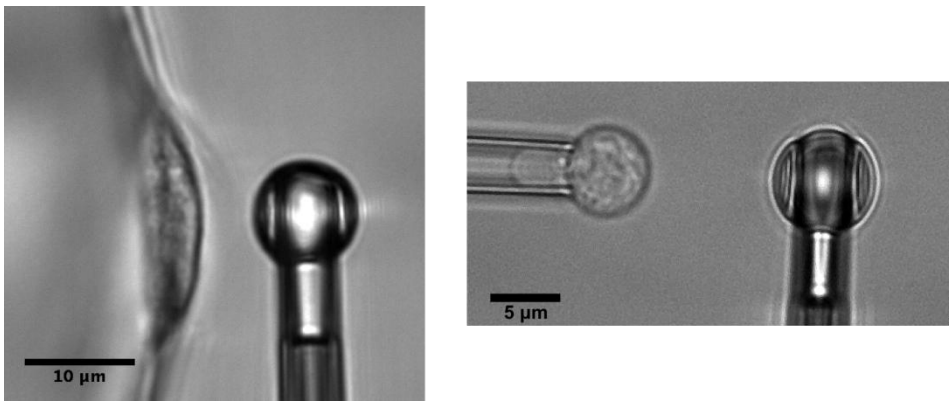

FIGURE I.2: "Profile microindentation" of an adherent (left) and non-adherent (right) cell. See Chapter 1 for explanation.

However, in the bloodstream, leukocytes are in suspension and not held in place. Therefore, being able to measure the mechanical properties of cells in suspension might provide a more accurate characterization of their mechanical properties. In Chapter 2, we present a microfluidic device that is able to achieve this (Figure I.3). Additionally, this device is able to detect subtle alterations in cell mechanical properties and thus opens the door to applications in the clinical setting where the mechanical "signature" of cell populations could potentially be used in the future to establish a medical diagnosis.

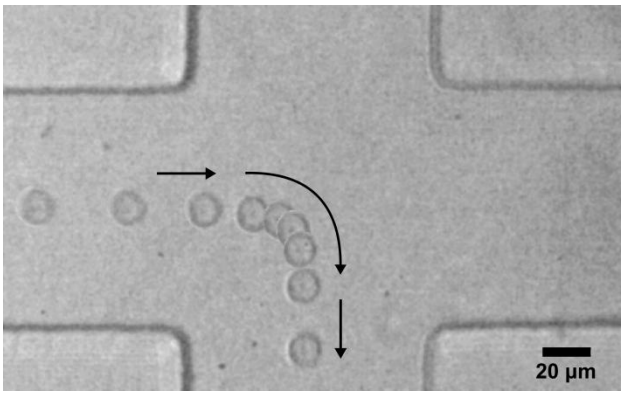

FIGURE I.3: Mechanical properties of cells in suspension are measured using a microfluidic device. See Chapter 2 for explanation.

Beyond using mechanical properties to characterize the state of a cell, we wondered if mechanics could also help us understand when deformations undergone by cells, or stresses exerted on them, could become harmful.

If we look at the late stages of atherosclerosis, this question can be posed in particular with regards to medical procedures. Indeed, at the point of advanced disease, the plaque becomes so large that it significantly reduces blood flow, and medical intervention becomes necessary to reopen the vessel. To this end, a catheter is introduced into the patient's radial or femoral artery and pushed through the vasculature to the site of the atherosclerotic plaque. There, a balloon is inflated to dilate the vessel walls. Often, a wired mesh called a stent is deployed at the same time to help maintain the vessel walls dilated (Cook *et al.*, 2007; Jennings *et al.*, 2014). While stent deployment is clearly beneficial to the patient, it has been shown to lead to substantial endothelial cell damage (Rogers *et al.*, 1999), which greatly increases the risks of thrombosis (Wu, M.D and Thiagarajan, M.D, 1996), a major cause of stroke and myocardial infarction. Because both the balloon catheter and the stent exert large forces on the endothelium, we hypothesized that these forces are responsible for the endothelial damage that is observed. In Chapter 3, we quantify the threshold of compressive force that leads to endothelial cell damage (Figure I.4) and compare it to the amount of force that is exerted during stent deployment. We also discuss the feasibility of avoiding endothelial cell damage in these procedures.

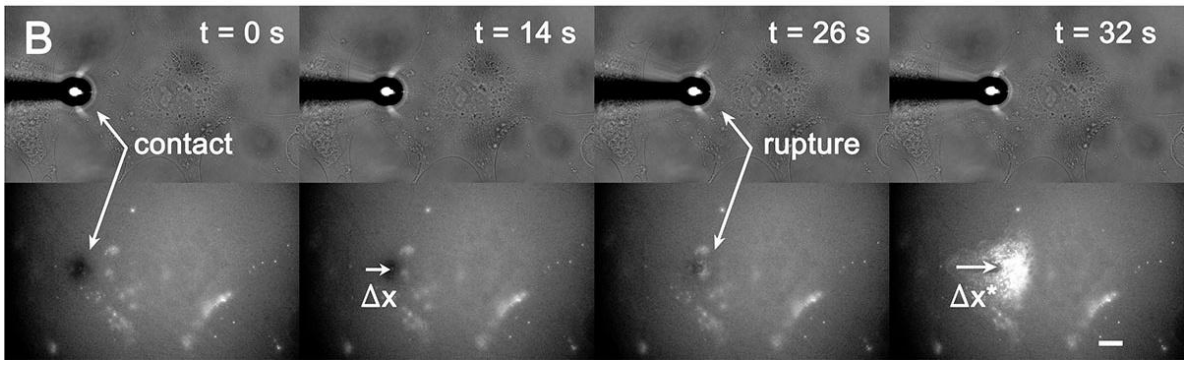

FIGURE I.4: Endothelial cell membrane ruptures at a critical compressive stress. The bar represents 10 μm. See Chapter 3 for explanation.

Turning to the early stages of atherosclerosis, we now focus on leukocytes. Indeed, we saw previously that during the development of the atherosclerotic plaque, T lymphocytes migrate across the endothelium due to the increased expression of adhesion molecules and inflammatory mediators by endothelial cells (Carman and Springer, 2004; Carman, 2009; Grivel *et al.*, 2011). This process requires leukocytes to deform dramatically to squeeze between endothelial cells (Figure I.5). Yet, despite the dramatic deformations and the membrane surface area increases required, there is no evidence, to our knowledge, of this process leading to membrane rupture *in vivo*. In Chapter 4, we therefore seek to understand how much leukocytes are able to deform before their membrane ruptures. Furthermore, we contrast situations of passive deformation, such as when cells pass through narrow vessels in the microvasculature, with situations of active deformation, such as during transendothelial migration.

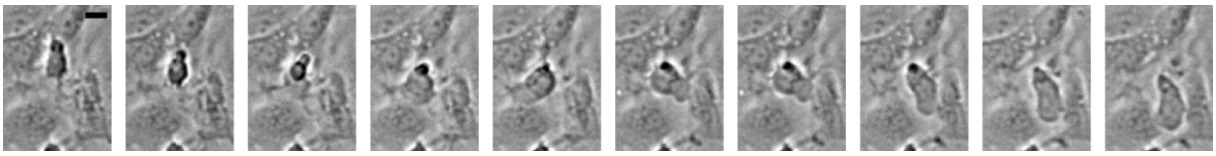

FIGURE I.5: Time-lapse of a lymphoblast (a type of leukocyte) migrating across an endothelium. The bar represents 10 μm. Images are taken every 15 seconds. See Chapter 4 for explanation.

CHAPTER 1

Mechanical properties of adherent and immobilized non-adherent cells

1.1 INTRODUCTION

In atherosclerosis, both adherent (endothelial cells) and non-adherent (leukocytes) cells are involved. In this chapter, we present a novel technique, which we term "profile microindentation", that is able to measure the mechanical properties of both types of cells.

This technique was described in an article (Guillou *et al.*, Scientific Reports 6, article number 21259, 2016, doi: 10.1038/srep21529), which we reproduce in section 1.2. In this work, we measure and discuss the mechanical properties of bovine aortic endothelial cells and show that we can track these properties over time as we modify the biochemical environment of the endothelial cell using another micropipette.

Further, in the supplementary material of this article, which we present in section 1.3, we show how this technique can be used to measure the mechanical properties of non-adherent cells maintained using a micropipette and present our results on CD4+ T lymphocytes.

The micropipette used to modify the biochemical environment can be used to place another cell in contact with the endothelial cell whose stiffness is measured. Hence, we use the "profile microindentation" setup to investigate the mechanics of transendothelial migration, a process central to the development of atherosclerosis. While this method does not allow us to obtain a sufficiently high throughput, we present our preliminary results in section 1.4.

Finally, in section 1.5, we present some of the "tips and tricks" gathered throughout this experimental work on the fabrication and the use of micropipettes and microindenters, in the hope that it will save time and pain to future experimentalists in our laboratory and elsewhere.

1.2 DYNAMIC MONITORING OF CELL MECHANICAL PROPERTIES USING PROFILE MICROINDENTATION

Lionel Guillou, Avin Babataheri, Pierre-Henri Puech, Abdul I. Barakat, Julien Husson

Abstract

We have developed a simple and relatively inexpensive system to visualize adherent cells in profile while measuring their mechanical properties using microindentation. The setup allows simultaneous control of cell microenvironment by introducing a micropipette for the delivery of soluble factors or other cell types. We validate this technique against atomic force microscopy measurements and, as a proof of concept, measure the viscoelastic properties of vascular endothelial cells in terms of an apparent stiffness and a dimensionless parameter that describes stress relaxation. Furthermore, we use this technique to monitor the time evolution of these mechanical properties as the cells' actin is depolymerized using cytochalasin-D.

Introduction

In cells, the cytoskeleton is a key determinant of mechanical properties. Therefore, biological processes that involve extensive cytoskeletal remodeling such as cell division, differentiation, and migration have been shown to be associated with changes in cell mechanical properties (Gossett *et al.*, 2012; Otto *et al.*, 2015). Cell responses to chemical and biophysical cues in their microenvironment also often lead to structural changes that impact mechanical properties (Wang and Doerschuk, 2000; Discher *et al.*, 2005; Trepat *et al.*, 2007; Mitrossilis *et al.*, 2009; Harris and Charras, 2011). For instance, during inflammation, leukocyte-endothelial cell interactions affect the mechanical properties of both cell types, which can in turn affect transmigration (Wang and Doerschuk, 2000; Wang *et al.*, 2001). There is, therefore, great interest in measuring the evolution of cell mechanical properties over time as a way of monitoring structural and functional changes that cells undergo during key biological processes. Furthermore, mechanical forces play a key role in the development of major diseases. For instance, the mechanical properties of tissues contribute in some cases to cancer progression and may also affect treatment outcome (Butcher *et al.*, 2009).

Several techniques have been developed to probe cell mechanical behavior. These include micropipette aspiration(Sato *et al.*, 1990; Hochmuth, 2000), atomic force microscopy (AFM) (Rotsch *et al.*, 1997; Sato *et al.*, 2000; Alcaraz *et al.*, 2003; Mahaffy *et al.*, 2004; Chaudhuri *et al.*, 2009; Raman *et al.*, 2011; Cartagena and Raman, 2014), micro-plates (Thoumine and Ott, 1997; Desprat *et al.*, 2005), optical tweezers (Laurent *et al.*, 2002; Yanai *et al.*, 2004), magnetic twisting cytometry (Fabry *et al.*, 2001; Laurent *et al.*, 2002), particle tracking (Yamada *et al.*, 2000; Tseng *et al.*, 2002), and microfluidic cell stretchers (Gossett *et al.*, 2012; Otto *et al.*, 2015). These various techniques have been used to probe either local (cortex, cytoplasm, etc.) or whole-cell mechanical properties at different spatial and time scales.

In this paper, we introduce profile microindentation (PM) as a simple and minimally disruptive method for assessing viscoelastic properties at a single-cell level. PM involves using a microindenter to indent a cell while using brightfield imaging from profile both to visualize the cell and to determine the deflection of the microindenter. The measurements can be made sufficiently rapidly (~10 s) to monitor the evolution of cell mechanical properties at biologically relevant time scales (few minutes to several hours). During the measurements, cell deformations are directly visible, offering a view of the cell that has seldom been reported (Chaudhuri *et al.*, 2009). Furthermore, we can readily add another micropipette to the setup to stimulate the cell locally in a highly controlled manner. This micropipette can, for instance, be used to "whiff" a drug or another chemical onto the cell, to bring another cell or micron-sized object such as an antibody-covered microbead in contact with the cell, or to directly stimulate the cell mechanically through aspiration or indentation. To demonstrate this capability, we "whiffed" cytochalasin-D onto

bovine aortic endothelial cells (BAECs) and measured the evolution of their mechanical properties over a period of more than 30 minutes. A limitation that this technique shares with many other systems that probe cell mechanical behavior is its relatively low throughput.

Methods

Endothelial cell culture

BAECs were kindly provided by A.-C. Vion and C. Boulanger and used between passages 4 and 12. The cells were cultured at 37 °C and 5% CO_2 in Dulbecco's Modified Eagle's medium (DMEM, Invitrogen, Carlsbad, CA, USA) supplemented with 10% fetal bovine serum (Invitrogen) and 1% penicillin/streptomycin (Invitrogen). The cells were passaged two to three times a week and re-suspended in fresh culture medium. One to two days before each experiment, the cells were trypsinized with trypLE (Invitrogen) and grown on Cytodex-3 dextran microcarrier beads (average bead size 175 μm, GE Healthcare Life Sciences, Velizy-Villacoublay, France). For the experiments, about 50 Cytodex-3 beads without cells were deposited onto the bottom of a thin-bottom petri dish (standard bottom μ-Dish 35 mm low, IBIDI, Martinsried, Germany or FluoroDish 35 mm, World Precision Instruments, Hitchin, UK) in phosphate buffered saline (PBS; Invitrogen). The PBS was then removed and ~10,000 trypsinized BAECs were introduced into the petri dish.

Human umbilical vein endothelial cells (HUVECs) for the profile microindentation experiments were kindly provided by A. Chipont, and originally purchased from PromoCell (PromoCell GmbH, Heidelberg, Germany). The cells were cultured at 37 °C and 5% CO_2 in endothelial cell growth medium (ECGM) procured from ZenBio (ZenBio, Research Triangle Park, North Carolina, USA). The protocol for depositing on Cytodex-3 beads differed from that used for BAECs in that after mixing cells and beads and letting them rest in the incubator for 30 min in a 2 mL eppendorf tube (Eppendorf France SAS, Montesson, France), the tube was placed for 3 hours on a rotating plate turning at 50 rpm and heated at 37°C to ensure optimal coverage of the beads. HUVECs used for the AFM experiments were obtained from PromoCell (ref. C-12203) and cultured according to the supplier's guidelines using ECGM-2 medium (ref. C-22011). Trypsin / EDTA was used for cell passaging.

While most experiments were performed at room temperature, we verified that our method could also be employed at physiological temperature (see supplementary discussion). In some experiments, cells were exposed to cytochalasin-D (Sigma-Aldrich, Taufkirchen, Germany) either by incubation or by "whiffing" the drug onto cells with a micropipette.

Microscope setup

In all microindentation experiments, the petri dish containing cells on Cytodex-3 beads was mounted on a TE300 inverted microscope (Nikon Instruments, Tokyo, Japan) placed on an air suspension table (CVI Melles Griot, Netherlands). The microscope was equipped with a 100x oil immersion, 1.3 NA objective (Nikon Instruments) for experiment monitoring and lower magnification objectives (40x, 20x, 10x, and 4x, Nikon) for micropipette positioning. Images were acquired using a Flash 4.0 CMOS camera (Hamamatsu Photonics, Hamamatsu City, Japan) controlled using the software LabVIEW (National Instruments, Austin, TX, USA). We will provide the LabVIEW codes upon request.The experiments were performed using either brightfield or fluorescence microscopy. Supplementary movie S1 online shows a demonstration video of profile microindentation.

Micropipette and microindenter fabrication

Borosilicate glass capillaries (1 mm OD, 0.78 mm ID, Harvard Apparatus, Holliston, MA, USA) were pulled on a P-97 micropipette puller (Sutter Instruments, Novato, CA, USA). To fabricate the micropipettes, an MF-900 microforge (Narishige, Tokyo, Japan) was used to cut the extremity of pulled capillaries to the desired diameter, ranging from ~4 to 50 μm. The diameter was assessed optically using calibrated graduations in the microscope's ocular. The micropipettes were then bent at a 45° angle (for the micropipette holding the Cytodex-3 bead) or a 60° angle (for the micropipette "whiffing" the drug) so that their extremities had the desired direction in the microscope's plane of view. To fabricate a microindenter, an MF-200 microforge (World Precision Instruments) was used to melt glass at the tip of the micropipette. During fabrication, using graduations in the microscope's ocular, we aimed for indenter tips that were 5 to 10 μm in diameter. The size was then precisely determined under the inverted microscope using the 100x objective. The microindenter's bending stiffness was evaluated against standard microindenters that had been previously calibrated. The standard microindenters were calibrated by measuring their deflection under the gravitational force exerted on their tip by a piece of paper of known mass. While microindenters made for these experiments were typically of rigidities ~5 to 10 nN/μm, their rigidity can be chosen as they are custom-made. Microindenters of rigidities as low as 0.1 nN/μm are routinely used in our laboratory for measurement of sub-nanonewton forces.

Micromanipulators and piezoelectric controller

The experimental setup was equipped with two motorized micromanipulators (MP285, Sutter Instruments) carrying two micropipette holders (IM-H1, Narishige) at

a 45° angle (different angle from the micropipette bending). One micropipette was used to hold Cytodex-3 beads, while the other one was used to "whiff" the drug onto the cell. A piezoelectric controller (TPZ001, Thorlabs, Newton, NJ, USA) along with a strain gauge reader (TSG001, Thorlabs) were used to control the microindenter. Because profile microindentation requires only a single-axis piezoelectric, a micromanipulator (or two if another micropipette is introduced), a camera able to acquire images at 30 Hz, and a high magnification objective, it is a technique that is relatively low-cost and simple to implement.

Actin visualization

To visualize intracellular actin filaments in living cells, BAECs were transfected with the live-cell actin marker LifeAct. A day before transfection, cells were plated on a 35 mm-diameter FluoroDish (World Precision Instruments) at densities that led to 50-80% confluence the following day. For transfection, cells were incubated at 37 °C in a mixture of 200 μL cell culture medium, 2 μg LifeAct DNA (pIRES-LifeAct-GFP-puro3, IBIDI), and 8 μL GeneCellin (DNA Transfection Reagent, BioCellChallenge, Signes, France) for a period of 24 h. The cells were then washed with new medium before imaging. For fluorescence excitation, an Intensilight (C-HGFIE, Nikon) lamp with GFP illumination was used.

Single-cell profile microindentation

Culturing cells on Cytodex-3 beads allowed us to image the cells in profile, which permitted visualization of cell deformation upon indentation. Cells were indented above the nucleus. During cell indentation, the Cytodex-3 bead was held in place using a micropipette with an aspiration pressure as shown in Figure 1.1. Using the piezoelectric controller, we applied a known displacement z to the base of the glass microindenter, with the piezoelectric controller moving at a constant speed v. We monitored the position d of the microindenter's spherical tip using an algorithm running in real-time in LabVIEW that cross-correlated the brightness profile of the current image with the brightness profile of the initial image before indentation, as already used by Husson et al. (Husson *et al.*, 2009) and Laan et al. (Laan *et al.*, 2008). This correlation was performed over a rectangular region of interest, and brightness was averaged over 4 pixels. Because we fit an entire region rather than a single pixel, our spatial resolution is smaller than the pixel size (60 nm/px at 100x magnification). Including the effect of ambient noise, we found that the standard deviation on the position of an indenter at rest was typically 30-40 nm. Contact between the microindenter and the cell was indicated by an increase in the indenter's deflection (d-z) compared to its initial value before any piezoelectric controller movement ($d_0 - z_0$). Because the indenter's deformation remained small during the indentation

(deformation ~deflection / length ~0.01), the applied force F was linearly related to the deflection through the indenter's stiffness $F = k_{ind}\ [(d - z) - (d_0 - z_0)]$. We continued the indentation until we reached a previously selected threshold force $F_{threshold}$.

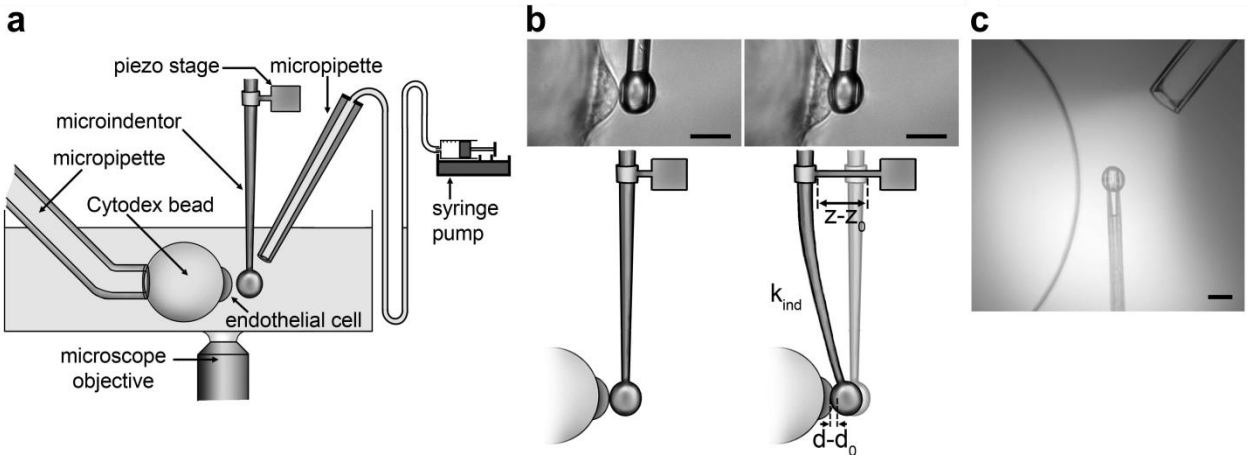

FIGURE 1.1: Experimental setup for profile microindentation. (a) Schematic (not drawn to scale) of the experimental setup used for profile microindentation. Microindenter is used to exert force on the endothelial cell adherent at the equator of the Cytodex-3 bead. (b) Microindenter before (left) and during (right) cell indentation. Scale bar is 10 μm. (c) Photograph of fluorescein "whiffed" by the micropipette on the Cytodex-3 bead in order to visualize the convection cone coming out of the micropipette. Scale bar is 10 μm.

We recorded the tip's position d_{max} (typically 1 to 2 μm indentation, which is approximately 20% of the cell thickness above the nucleus) at this point in time and then used a feedback loop to adjust in real-time the displacement z imposed by the piezoelectric controller to maintain that position constant as the cell relaxed. Thus, after the approach phase, the strain was maintained constant throughout the relaxation phase. We let the cell relax for at least 10 s before retracting the indenter. Data acquisition frequency was ~30 Hz. Thus, for data analysis, we had access to the force applied by the microindenter F, the tip's position d, the imposed piezoelectric controller movement z, and the time t of each measurement.

Atomic Force Microscopy

Adherent cells were cultured on 70% ethanol-cleaned glass slides in 6-wells culture plates, rinsed to remove unbound cells and fragments and mounted in a temperature-controlled chamber (Biocell, JPK Instruments, Berlin, Germany) set to

37°C. Cells were indented with a JPK Nanowizard 1 AFM (JPK Instruments), using the force mode with a closed loop 15 μm range piezo. The AFM sits on an Axiovert 200 microscope equipped with a Colibri 2 diode illumination system (Zeiss, Oberkochen, Germany) and a CoolSnap HQ2 camera (Photometrics, Tucson, AZ, USA). A glass sphere of diameter 10 μm was glued by micromanipulation (using a homemade micropipette/biomembrane force probe setup) to a gold-coated triangle-shaped MLCT cantilever (Bruker Instruments, Billerica, MA, USA), using UV polymerizable glue (Dymax OP-29) in order to measure cell mechanics on similar scales as in the microindentation experiments. The decorated AFM cantilever was calibrated in situ prior to the experiments using the thermal noise method implemented in the JPK SPM control software and found to be 11.5 nN/μm, compatible with the nominal data provided by the manufacturer (10 nN/μm). The approach and retract speeds of the indenter were 1 μm/s over a distance of 5 μm and the maximal applied force was set between 3 and 6 nN. The acquisition frequency was set at 1024 Hz.

Data and statistical analysis

Raw data acquired by LabVIEW were analyzed using a custom-written code in MATLAB (The MathWorks, Natick, MA, USA). We will provide the code upon request. AFM data were processed using JPK DP software (JPK Instruments) using built-in fitting procedures. Statistical comparisons between two groups were performed using the two-tailed Student t-test. Tests were unpaired unless otherwise noted. Statistical comparisons among three groups or more were performed using a one-way ANOVA test. Statistical comparisons between slopes were performed using an ANOCOVA test. Samples were deemed statistically significantly different for $p < 0.05$.

Results

Precision of displacement and force measurement in profile microindentation

The first step in the microindentation experiments is to calibrate the microindenters. We first determined precisely the density of a type of paper by measuring the mass of pieces of this paper whose surface area was then measured under the microscope (Figure 1.2). We then calibrated reference microindenters by measuring their deflection under known weights of pieces of paper. The results demonstrated that we remain in the linear elastic regime for the range of deformations tested. Microindenters used in the experiments were calibrated against the reference microindenters by measuring their deflections when pressed against each other

(Figure 1.2). The ratio of the deflections of the two microindenters directly provides the ratio of their rigidities.

To measure the position of the microindenters during profile microindentation, we acquire a profile of the light intensity on a line along the axis of indentation at a frequency of ~30 Hz. This intensity profile is compared using cross-correlation against a template profile for the image of the indenter. A parabolic fit over 10 pixels is then used to find the maximum of the cross-correlation curve (Figure 1.2), giving the position of the indenter.

At a magnification of 100x, the size of a pixel is ~60 nm. However, the parabolic fit used here allows sub-pixel resolution. Including the noise in the environment and at an acquisition frequency of ~30 Hz, we find on a typical day that we are able to determine the position of the indenter with a precision of half a pixel, or about ~30 nm (Figure 1.2). For a typical indenter of rigidity 5-10 nN/μm, this translates to a precision in force of 0.1-0.3 nN.

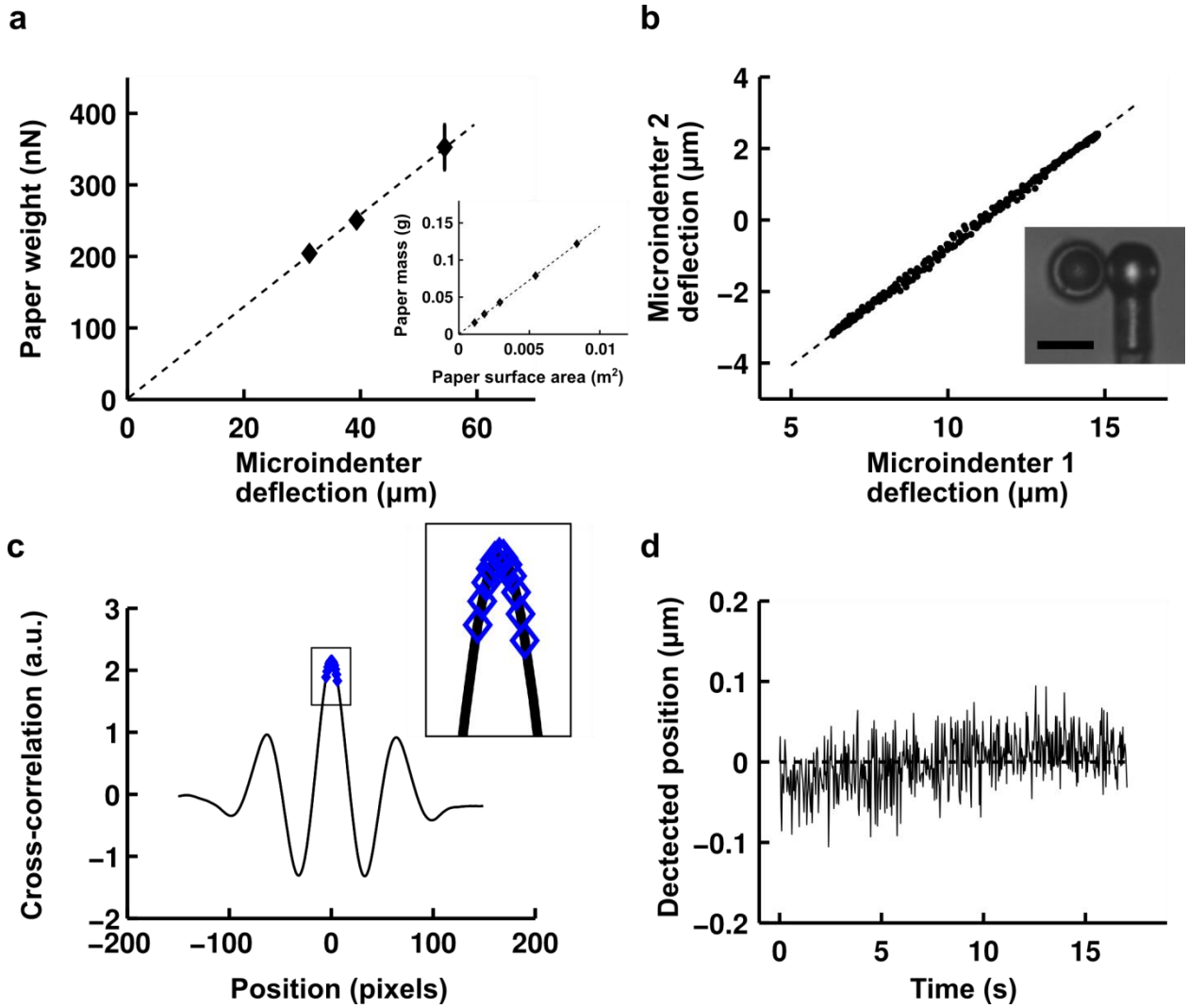

FIGURE 1.2: Profile microindentation calibration and noise level. (a) To calibrate a reference microindenter, its deflection under the weight of pieces of dry paper of known mass is measured. Data are mean ± s.e.m. Papers adhere to the tip by dipping the tip in oil. The inset shows how paper density was ascertained by measuring the masses of pieces of paper whose surface areas were then measured under the microscope. (b) Microindenters used in the experiments were calibrated against reference microindenters by measuring the ratio of their deflections when pushed against one another. Scale bar is 10 μm. (c) A profile of the light intensity was measured on a line along the axis of indentation, and a template profile for the image of the indenter on that line indenter shaft was taken. A parabolic fit over 10 pixels (blue diamonds, see inset) was used to find the maximum of the cross-correlation curve, giving the position with sub-pixel resolution (~30 nm, see panel d). (d) The position of the indenter was measured at rest over a period of ~15 s, comparable to the time of stress relaxation experiments performed, to evaluate the combined error stemming from noise in the environment and measurement error. At an acquisition frequency of ~30 Hz, the standard deviation of the position is 32 nm in the representative data shown.

Profile microindentation gives similar apparent stiffness values to Atomic Force Microscopy

We compared the apparent stiffness of HUVECs measured using profile microindentation to that obtained via AFM, as this latter method is widely used to measure cell mechanical properties (Rotsch *et al.*, 1997; Sato *et al.*, 2000; Alcaraz *et al.*, 2003; Mahaffy *et al.*, 2004; Chaudhuri *et al.*, 2009; Raman *et al.*, 2011; Cartagena and Raman, 2014). In both cases, we used an approach speed of 1 μm/s, a spherical indenter of radius 5 μm, indented on top of the nucleus and fit the entire force-deformation curve using a Hertzian model (assuming a Poisson's ratio of 0.5, see next paragraph for details). The threshold forces for indentation were in the same range, with 3-6 nN for AFM and 5 nN for profile microindentation, and so were the indenter rigidities, with respective values of 11.5 nN/μm and 5.0 nN/μm. The measurements were made at temperatures of ~37°C in both cases. The substrate was the main difference between the two setups. While HUVECs adhered to glass in the AFM experiment, they adhered to Cytodex-3 dextran beads in the profile microindentation experiment. However, with respective rigidities of ~70 GPa and ~50 kPa, both glass and dextran beads are much stiffer than cells, and previous investigators have shown that while substrate stiffness matters greatly when its rigidity is comparable to that of the cell, this is no longer the case when substrate stiffness is very high compared to the cell (Tee *et al.*, 2011). Indeed, the measured apparent stiffnesses were found to be similar using the two different methods (0.75±0.14 kPa for AFM vs. 0.95±0.21 kPa for profile microindentation; $p=0.55$) (Figure 1.3). Such a comparison validates the profile microindentation technique and positions it as a low-cost complementary approach to more conventional AFM colloidal indentation systems.

The repeatability of the measurements of apparent stiffness was also assessed under these experimental conditions by investigating how the apparent stiffness varied for a given cell during several consecutive measurements. The dispersion of the measurements was found to be about twice as high for profile microindentation compared to AFM, as the standard deviation for the normalized apparent stiffness was 0.1 for AFM and 0.2 for profile microindentation (Figure 1.3).

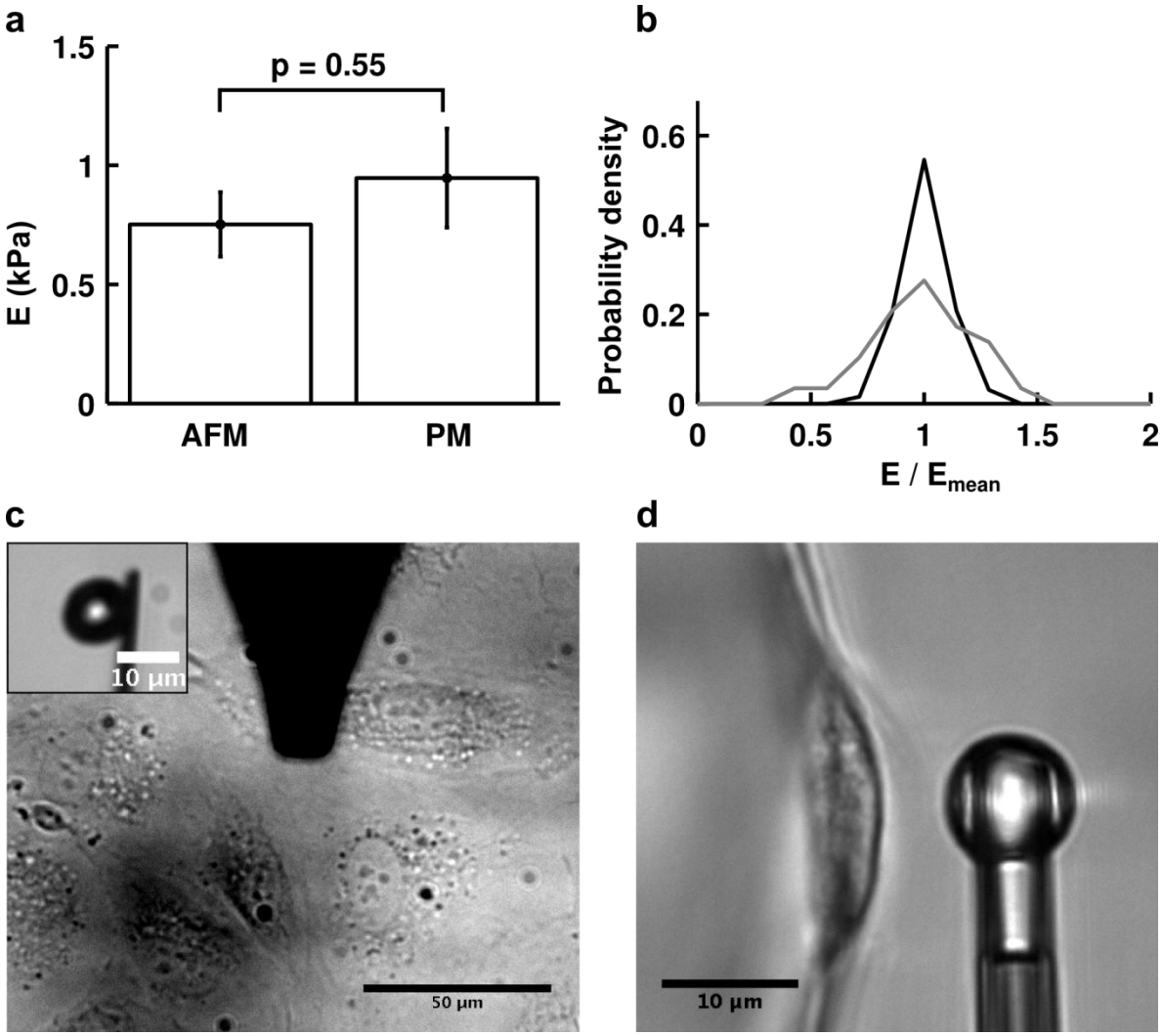

FIGURE 1.3: Comparison of apparent stiffness obtained by AFM and profile microindentation. (a) The difference between the two means is not statistically significant (p=0.55; two-tailed Student's t-test). Data are mean ± s.e.m. n = 5 cells for AFM and n = 10 cells for profile microindentation. (b) Probability density for the measure of the apparent stiffness of a given cell normalized by the mean apparent stiffness found for that cell. Black is for AFM and grey for profile microindentation. The same cells as in panel a are used. (c) Top view of AFM measurement of HUVEC rigidity. (Inset) Side view of the spherical probe glued to the tip used in the AFM measurement. (d) Side view of profile microindentation measurement of HUVEC rigidity.

In profile microindentation stress relaxation experiments, cell mechanical properties can be described by two independent parameters: an apparent stiffness E* and a dimensionless relaxation parameter α.

1. **The apparent stiffness E***

We first assess the cell rigidity by focusing on the approach phase of the indentation. The force-indentation curve of an adherent cell indented by a spherical indenter is well described by the classical Hertz equation (Johnson, 1985):

$$F = \frac{4}{3} E^* R^{1/2} \delta^{3/2} \qquad (1)$$

where F is the force, E* the apparent stiffness ($E^* = \frac{E}{1-\upsilon^2}$, with E the Young's modulus and υ the Poisson's ratio), R an effective radius which is a function of the indenter's radius R_{probe} and the cell apical surface radius of curvature R_{cell} ($R=1/(1/R_{probe}+1/R_{cell})$), and δ the indentation depth. In our case, the contact position d_c must be determined in order to assess indentation; therefore, we obtained E*, d_c and $F_0 = k_{ind}(d_0 - z_0)$ through a fit of the following equation:

$$k_{ind}(d - z) = F_0 + \mathrm{I}_{d-dc} \frac{4}{3} E^* R^{1/2} ((d - d_c))^{3/2} \qquad (2)$$

where $\mathrm{I}_{d-dc} = \begin{cases} 1 & if \quad d - d_c \geq 0 \\ 0 & if \quad d - d_c < 0 \end{cases}$

The characteristic function I_{d-dc} is used to take into account the pre-contact case in which no force is applied on the cell. An example of such a fit for a BAEC can be seen in Figure 1.4 and provides the first mechanical parameter: the apparent stiffness E* of the cell. We estimate the quality of the fit by evaluating the square root of the mean of the L2-norm of residuals between the fit and the experimental data. We obtain a value in the example given of 0.14 nN, which is of the same order of magnitude as our precision in force.

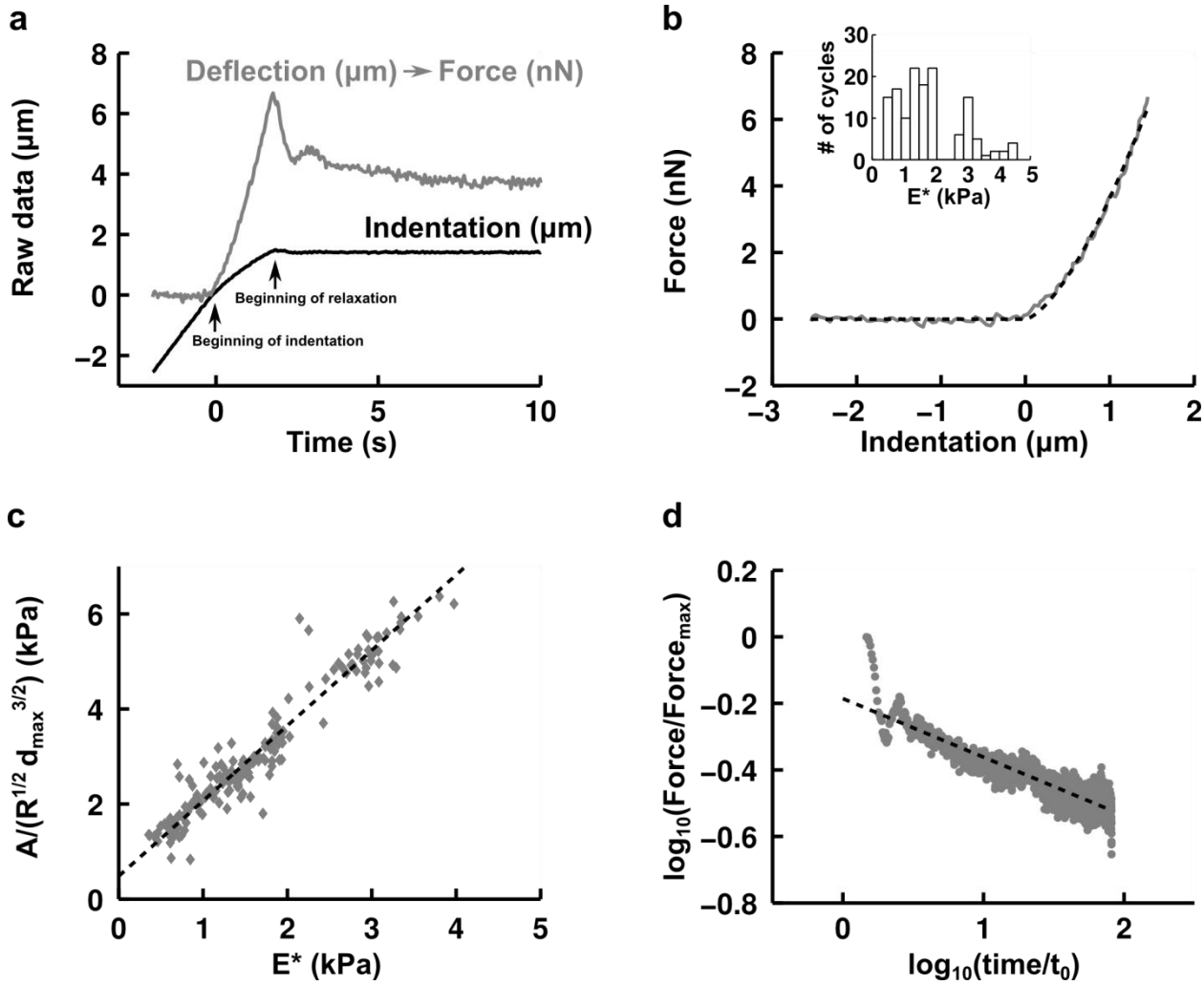

FIGURE 1.4: BAEC stress relaxation can be described using only two independent mechanical parameters: the apparent stiffness E* and the relaxation parameter α. (a) Example of raw data extracted from cross-correlation image analysis. We obtain the indentation $(d - d_c)$ (black curve) and the deflection $(d - z) - (d_0 - z_0)$ (grey curve). t = 0 s marks the beginning of the indentation (left arrow). By multiplying the deflection by the indenter's rigidity k_{ind} (nN/μm), we find the applied force F (nN). After the chosen force $F_{threshold}$ is attained (right arrow), we maintain the indentation constant, ensuring constant strain during force relaxation. (b) Example force-indentation curve fitted with a single parameter: the apparent stiffness E*. In this example, approach speed is 1.4 μm/s. Data acquisition frequency is approximately 30 Hz. The inset represents a histogram of the apparent stiffness E* of BAECs (n = 20 cells and N = 139 indentation curves) measured with a microindenter whose base is moving at 1.4 μm/s, fitting the first 1.0 μm of the force-indentation curve. (c) Scatter plot of $A/(R^{1/2}d_{max}^{3/2})$ as a function of E*, where A is the pre-factor in the force relaxation as given by equation (3), R is the effective radius given by $R = 1/(1/R_{probe}+1/R_{cell})$ with $R_{cell} \sim 20$ μm, d_{max} is the indentation maintained during relaxation, and E* is the apparent stiffness measured by fitting the first 1.0 μm of the force-indentation curve of BAECs (n = 51 cells and N = 191 indentation curves). The very good correlation

(correlation coefficient r = 0.95) shows that A and E* are inter-dependent variables, both measuring a cell's apparent stiffness. (d) Example force-time relaxation curve at fixed indentation. Cell relaxation is observed over 80 s. Time is normalized by t_0 = 1 s. Force is normalized by its maximum value attained at the first time point.

In our data analysis protocol, we perform the fitting of the force-indentation curve twice: a first time to get an approximate contact point d_{capp}, and a second time where we fit only the data where $d \in [d_{capp}-2\ \mu m;\ d_{capp}+1\ \mu m]$. For an indentation speed of 1.4 μm/s, we find E* = 1.8 ± 0.086 kPa (mean ± s.e.m.) (Figure 1.4), in line with values found in the literature (Satcher and Dewey, 1996; Hochmuth, 2000; Mathur *et al.*, 2001; Pesen and Hoh, 2005; Sato *et al.*, 2007). To obtain the Young's modulus, one can assume a Poisson's ratio of 0.5 (Sato *et al.*, 1990; Nijenhuis *et al.*, 2014), corresponding to an incompressible medium, which is best suited when modeling the cell as a homogeneous isotropic medium during moderate indentations. Here, "moderate indentations" denotes indentations in which the applied pressure P_{app} is small compared to the osmotic pressure P_{osm} of isotonic saline which acts to maintain cell volume constant (Hochmuth, 2000).

In support of this notion, during indentations with a P_{app} on the order of 1 kPa (close to our experimental values, see Figure 1.4 with P_{app} ~force / contact area ~7 nN/15 μm^2 ~0.5 kPa) observed with a confocal microscope, Harris and Charras reported no volume change (Harris and Charras, 2011) (see supplementary discussion for a more detailed discussion of appropriate values of Poisson's ratio depending on the experiment).

An advantage of the profile microindentation technique is the ability to readily determine the apparent stiffness of non-adherent cells. To do so, we hold the non-adherent cell with a micropipette. To showcase this capability, we measured the mechanical properties of human primary T lymphocyte CD4 cells (Supplementary Material, Figure 1.10).

2. The relaxation parameter α

Once the desired indentation d_{max} is attained, we observe force relaxation at fixed indentation (see Methods for details). We find that the force relaxes according to a weak power-law (Figure 1.4) following:

$$F(t) = A\left(\frac{t}{t_0}\right)^{\alpha} \qquad (3)$$

where F is the force, A is a fitting parameter, t is time, t_0 is an arbitrary time constant which we set at 1 s, and α is another fitting parameter. We observe that there are oscillations in the first ~30 points of our force relaxation curve in Figure 1.4

(corresponding to ~1 s since data acquisition frequency is ~30 Hz), which are due to our feedback loop that attempts to maintain the position constant.

We note that A is an extensive property. By analogy with the Hertz equation, we normalize A by $R^{1/2}d_{max}^{3/2}$ to make it an intensive property in order to compare it with the apparent stiffness E* found previously. We find that A and E* are nearly proportional to one another (Figure 1.4). This was observed to be true for ~200 indentations performed on ~50 cells at three different approach speeds (1.4 μm/s, 2.8 μm/s and 14 μm/s), using two different indenters, and with and without incubation in cytochalasin-D (a drug that depolymerizes actin filaments and renders cells softer). This indicates that A and E* are inter-dependent variables; henceforth, we choose to retain E*.

The apparent stiffness E* is indentation depth-dependent, while the relaxation parameter α is not.

In order to test the dependence of the apparent stiffness E* on the indentation length scale, we fitted identical force-indentation curves on intervals of increasing lengths, from $d \in [d_0–2\ \mu m;\ d_0+0.3\ \mu m]$ to $d \in [d_0–2\ \mu m;\ d_0+1.5\ \mu m]$, with the function described in equation (2). For each force-indentation curve, the values obtained for the apparent stiffness E* were normalized by those obtained when using the smallest interval $[d_0–2\ \mu m;\ d_0+0.3\ \mu m]$ (Figure 1.5). We find that the cell's apparent stiffness increases with the depth of indentation.

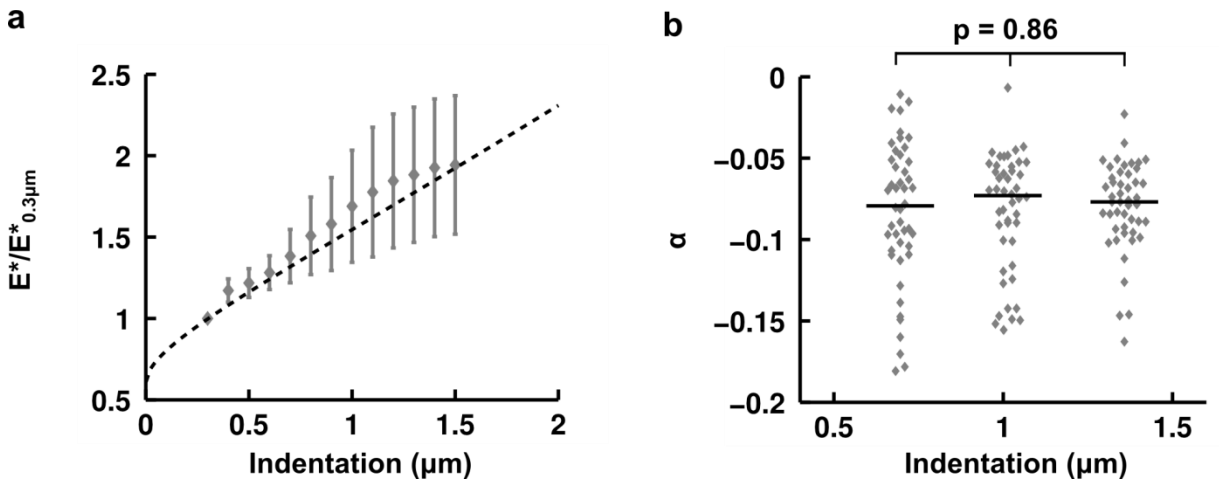

FIGURE 1.5: Effect of indentation depth on measured cell mechanical properties. (a) Apparent stiffness E* (mean: grey diamonds and S.E.M.: grey bars) of BAECs as a function of the indentation depth used for fitting the data (n = 20 cells). For each curve, E* was normalized by its value at an indentation depth of 0.3 µm. Also shown is the apparent stiffness E* obtained by fitting an analytical force-indentation curve taken from Dimitriadis' formula that accounts for cell depth (dotted black line) (Dimitriadis *et al.*, 2002). The unique fitting parameter, the apparent stiffness E*, was chosen to match experimental data at an indentation depth of 0.3 µm. Data are mean ± s.e.m. (b) Relaxation parameter α as a function of indentation depth. Each point (grey diamond) represents an indentation (n = 20 cells with 7 indentations each). Curves were separated into 3 groups sorted according to indentation depth. The x axis represents a group's mean indentation depth. Each group is represented as a violin boxplot (median: black line). A one-way ANOVA with the null hypothesis that all samples are drawn from the same population gives a p-value of 0.86.

To test the hypothesis that this increase is due to the effect of the substrate, as has been previously observed (Yu *et al.*, 1990; Saha and Nix, 2002), we fitted equation (2) for varying intervals to a theoretical force-indentation curve obtained using the following equation proposed by Dimitriadis et al. that accounts for substrate effects at small depths for an incompressible bonded substrate (Dimitriadis *et al.*, 2002):

$$F = \frac{4}{3} E^* R^{1/2} \delta^{3/2} (1 + 0.884\ \chi + 0.781\ \chi^2 + 0.386\ \chi^3 + 0.0048\ \chi^4) \qquad (4)$$

with $\chi = R^{1/2} \delta^{1/2} / h$, where we took for h the average of the cell heights measured in our experiments (h = 4.5 µm). Again, we normalized the values obtained for E* for various intervals by the value found for a maximum indentation of 0.3 µm, and we find good agreement with our data (Figure 1.5).

To further test if the relaxation parameter α was also indentation length scale-dependent, we investigated how it varied with indentation depth and found no significant difference at the depths tested (Figure 1.5). We conclude that this

parameter does not depend on length scale, as has been reported elsewhere using oscillating beads (Fabry *et al.*, 2001) or creep relaxation (Desprat *et al.*, 2005).

The apparent stiffness E* depends on indentation speed through the duration of the indentation

To test the dependence of our mechanical parameters E* and α on indentation speed, we compared the relaxation profiles at the two indenter speeds of 1.4 and 14 μm/s (Figure 1.6). Each force relaxation curve, obtained at a fixed indentation, was renormalized by its value after 10 s of relaxation. All the curves at a given speed were then averaged. When the reference time t = 0 s is taken to be the beginning of the indentation, we find rather good agreement between the two averaged relaxation curves, which collapse on a master curve. It thus follows, as can be seen in Figure 1.6, that the slower the indentation, the longer a cell will have to relax and hence the softer it will appear.

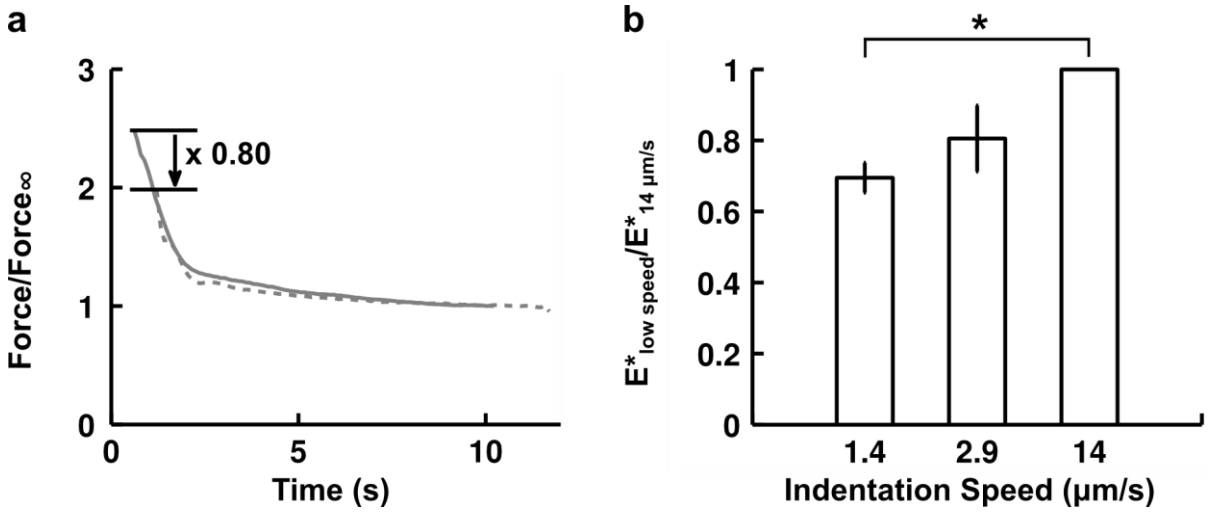

FIGURE 1.6: Effect of indentation speed on force relaxation and apparent stiffness. (a) Average force relaxation curve at fixed indentation for fast (n = 13 cells, grey line, indentation speed 14 μm/s) and slow (n = 20 cells, dotted grey line, indentation speed 1.4 μm/s) indentations. Force is normalized by its value after 10 s of relaxation for each cell. Time on the x axis starts at the beginning of indentation. (b) Comparison of cells' apparent stiffness as a function of indentation speed. For each cell, its apparent stiffness at low speed was normalized by its value at 14 μm/s. Data are mean ± s.e.m. n = 5 cells for 1.4 μm/s and n = 3 cells for 2.9 μm/s. The p-value from a paired two-tailed Student's t-test with the null hypothesis being that the ratio is equal to 1 is significant for 1.4 μm/s (p = 0.002) but not for 2.9 μm/s (p = 0.171). An indentation speed of 2.9 μm/s means that the full indentation will last approximately ~1 s.

Tracking the evolution of cell mechanical properties upon "whiffing" a drug onto a cell

Because we measure cell mechanical properties in ~10 s, we are able to repeat that measurement to determine how the mechanical properties of a particular cell evolve in response to an external stimulus applied locally to that cell. To demonstrate this capability, we used a micropipette to "whiff" cytochalasin-D onto a BAEC, as depicted in Figure 1.1. The mean "whiffing" fluid velocity is ~10 cm/s; thus, cytochalasin-D convection dominates diffusion (characteristic convection time $\tau_{convection}$ ~10^{-3} s << $\tau_{diffusion}$ ~10 s; see supplementary discussion for details). We performed measurements of mechanical properties every 30 s for a period of ~40 min. We compared our "whiffing" experiment to two other cases: a control case with no "whiffing" to verify that the mechanical measurements were not disruptive to the cell, and a case where the cells were continuously incubated in cytochalasin-D to see how effective "whiffing" a drug at a given concentration is compared to a more standard incubation protocol.

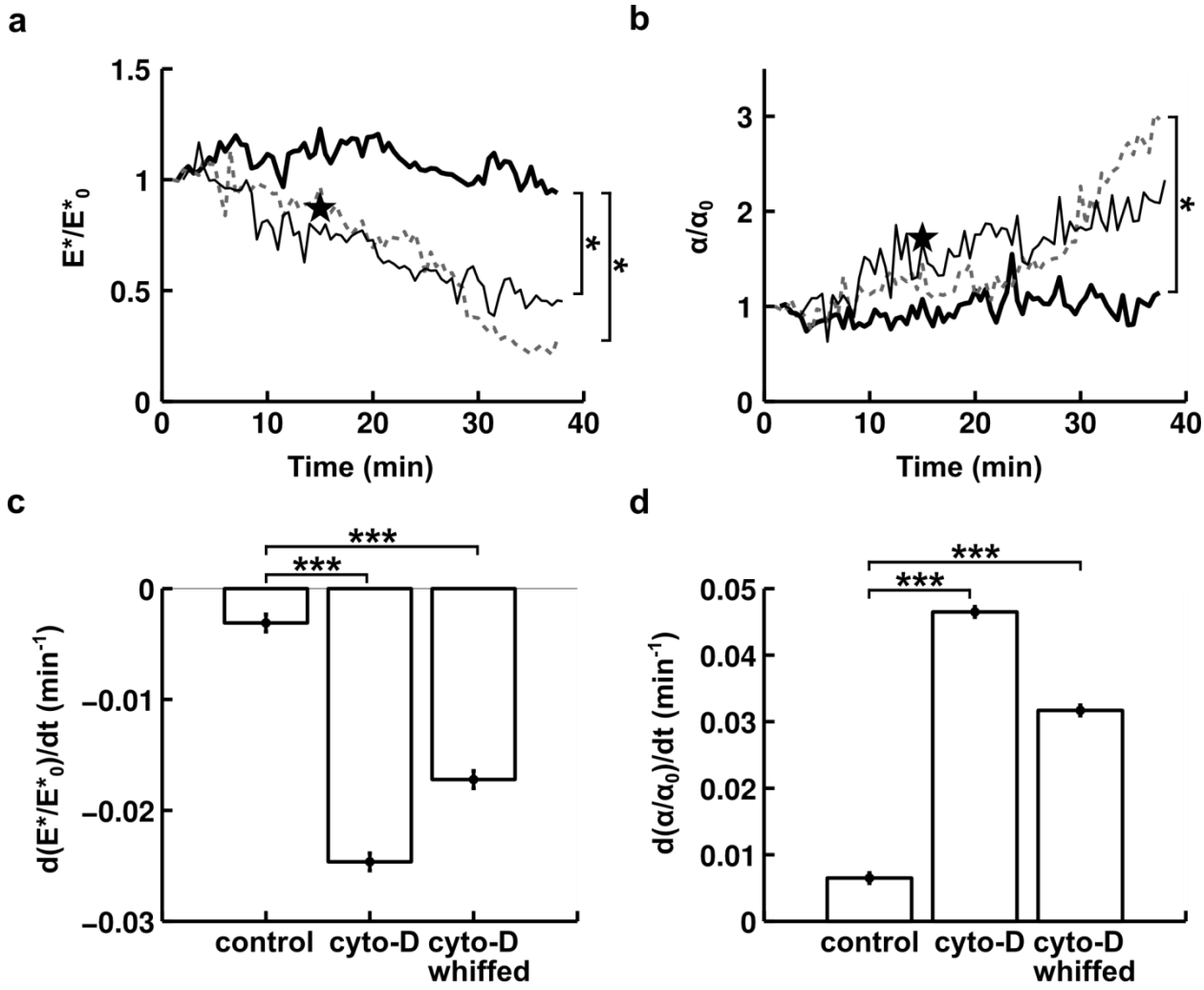

FIGURE 1.7: Impact of cytochalasin-D on BAEC mechanical properties. (a) Time evolution of BAEC apparent stiffness E*. E* is normalized by its value at t = 0 min E^*_0. The indentation speed is 1.4 μm/s. Thick black line is control (n = 7 cells), grey dotted line is for cells incubated in cytochalasin-D at 500 nM starting at t = 5 min (n = 9 cells), and thin black line is for cells that were "whiffed" with cytochalasin-D at 500 nM starting at t = 5 min (n = 5 cells). Large black pentagram positioned at t = 20 min represents a separate experiment where control cells' apparent stiffness, $E^*_{control}$ (n = 13 cells), was compared to that of cells incubated for 15 min in cytochalasin-D at 1000 nM, $E^*_{cyto\text{-}D}$ (n = 18 cells). The y-coordinate of the pentagram is $E^*_{cyto\text{-}D}/E^*_{control}$. (b) Time evolution of BAEC relaxation parameter α. The same notation as in panel a is used. (c) Time derivative of data in panel a: left column is control case, middle column represents cells incubated in cytochalasin-D, right column represents cells "whiffed" with cytochalasin-D. Data are mean ± s.e.m. Slopes in panel a were compared using the ANOCOVA test. *** indicates $p < 0.001$. (d) Time derivative of data in panel b. Data are mean ± s.e.m. The same notation as in panel c is used.

As can be seen in Figure 1.7, the cell's apparent stiffness E* decreases by ~50-70% over the duration of the experiment, in line with values found in the literature (Wu *et al.*, 1998). In addition to becoming softer upon initial indentation, the cell also relaxes faster, as indicated by a 2-3 fold increase in the relaxation parameter α over the duration of the experiment. Performing repeated indentations provides the advantage of directly observing the kinetics of a drug's activity on the cell. Here, we see that the rates of both the decrease in apparent stiffness and the increase in the relaxation parameter are relatively constant in time.

To compare cytochalasin-D action kinetics quantitatively, we compared the slopes of the time evolution of the mechanical properties using an ANOCOVA test. This allows greater statistical robustness ($p < 0.001$, see Figure 1.7) than comparing cases at selected time points, thus partially overcoming the drawback of this technique's low throughput. We find that, while the mechanical properties barely change in the control case, they evolve dramatically and qualitatively similarly in the two other cases. We note that with our choice of indentation duration (~1 s), the normalized apparent stiffness decreases nearly proportionally to the fluidization of the cell, as we have in all three cases $|d(\alpha/\alpha_0)/dt| \sim 2\,|d(E^*/E^*_0)/dt|$.

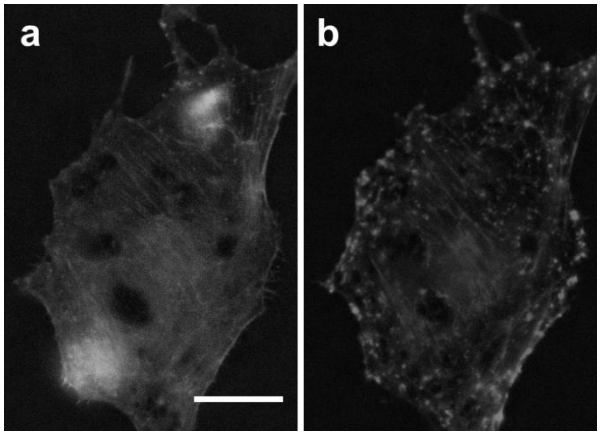

FIGURE 1.8: Effect of cytochalasin-D on BAEC actin filaments. (a) Control (untreated) BAEC. (b) Same cell as in panel a after incubation for 120 min in cytochalasin-D at 1000 nM. Note actin filament bundles being disrupted at various locations throughout the cell and actin aggregates forming at the cell periphery. Scale bar is 20 μm. See supplementary movies S2 and S3 online for time lapse of actin filament depolymerization over time under the effect of cytochalasin-D.

To confirm that cytochalasin-D had the intended effect of disrupting actin filaments, we used live-cell fluorescence imaging (LifeAct) to visualize actin filaments over time during incubation in cytochalasin-D (Figure 1.8). Most actin

filaments progressively depolymerize and form small bundles (bead-like structures in Figure 1.8).

Beyond simply "whiffing" a drug onto a cell, the second micropipette used for injecting cytochalasin-D above can also be used to bring in another cell and study cell-cell interactions and the effects of these interactions on mechanical properties. To demonstrate this capability, we used a micropipette to place human lymphoblast cells on human aortic endothelial cells (HAEC) and observed in profile view as the lymphoblast migrated on the endothelial cell surface (Supplementary Material Figure 1.11), all the while measuring the mechanical properties of the endothelial cell (data not shown).

Discussion

The scale-free power law found using profile microindentation is analogous to the one identified in creep relaxation and bead oscillation experiments. Indeed, the power-law behavior observed here has previously been reported, notably in creep relaxation (Desprat *et al.*, 2005) and in bead oscillation experiments where several orders of magnitude of frequencies were sampled (Fabry *et al.*, 2001). Following a calculation performed by Balland et al. (Balland *et al.*, 2006), we show in what follows that although our experiment is performed at constant strain rather than constant stress and in the time domain rather than the frequency domain, these approaches are equivalent.

By analogy with our stress relaxation function $F(t) = A(t/t_0)^{\alpha}$, we introduce the creep relaxation function $\varepsilon(t) = B(t/t_1)^{\beta}$ (strain evolution under constant stress) for an elastic body with identical mechanical properties. Following some mathematical derivations (see supplementary discussion for details), we find that $\alpha = -\beta$ and $A = \frac{1}{B\Gamma(1+\beta)(1-\beta)}$ ($\approx \frac{1}{B}$ for $0 < \alpha \ll 1$), where Γ is the Euler function. Thus, the power-law exponent we find for our constant strain experiment can be compared to previous work reported in the literature for creep relaxation and bead oscillations experiments simply by changing the sign.

The current results also show that the pre-factor A in the stress relaxation law $F(t) = A(t/t_0)^{\alpha}$ and the apparent stiffness E* measured during the cell indentation ramp-up are inter-dependent (Figure 1.4); therefore, E* and the relaxation parameter α are sufficient to describe cell indentation and subsequent relaxation.

In order to fit the force-indentation curve during the approach phase, we have used a non-adhesive contact model because the lack of measurable negative force indicates that the adhesive forces are small during this phase (see Figure 1.4). This is

not surprising because the ions present in the medium (DMEM) screen electrostatic interactions. The medium is further supplemented with 10% serum, and hence contains a large amount of bovine serum albumin (BSA), which has a well-known anti-adhesive effect. The non-adhesive contact assumption, however, is not expected to be valid after contact has been made during the retraction phase where, for example, an adhesive force $F_{ad} = 0.14\ F_{max}$ (F_{max} is the maximum force) is measured for the BAECs in the inset of Figure 1.4b. In this case, we can use the resulting adhesion energy per unit surface area defined as $\gamma = -F_{ad}/(3\pi R_{probe}) = 13\ \mu N/m$ to compute the dimensionless parameter λ proposed by Maugis (Maugis, 1992) $\lambda = \left(\frac{9 R_{probe}}{4\pi\gamma E^{*2}}\right)^{1/3}\left(\frac{16\gamma}{9\sqrt{3}h_0}\right) \sim 170$, where h_0 is the equilibrium separation between the surfaces, typically taken to be 0.4 nm for solids. Because $\lambda >> 5$, the Johnson-Kendall-Roberts (JKR) model would apply during the retraction phase (not treated here).

Further, we observe that cell relaxation curves are self-similar if we consider the beginning of indentation as the initial point. In our cell indentation experiments, cell relaxation appeared independent of indentation speed (from 1.4 to 14 μm/s) and exhibited a self-similar behavior when the beginning of indentation was taken as the initial time point, i.e. t = 0 s (Figure 1.6). This means that if one sets the origin of time for relaxation not at the beginning of relaxation per se but rather at the moment where mechanical energy is injected into the system, the force relaxation curves of two groups of cells (n = 20 cells and n = 13 cells) indented at very different speeds (1.4 μm/s and 14 μm/s respectively) collapse on a master curve. This finding suggests that cell relaxation is driven by the time at which an external energy input initializes the system. We therefore propose that this time point is more relevant to study cell relaxation than the beginning of cell relaxation, which corresponds to the end of the indentation phase.

Finally, by performing 10 second-long profile microindentations every 30 s for more than 30 min, we were able to monitor the viscoelastic properties of endothelial cells almost continuously for an extended period of time (Figure 1.7). In the control case, cell viscoelastic properties remained nearly constant over a period of time longer than 30 min (Figure 1.7), indicating that the measurement technique itself is minimally disruptive to the cell.

To demonstrate our ability to act on a single cell's local environment and to evaluate the impact of a local external stimulus on the cell's mechanical properties dynamically, we "whiffed" cytochalasin-D continuously onto a single BAEC (Figure 1.1) and monitored the evolution of cell mechanical properties over time using our profile microindentation technique. We chose cytochalasin-D because its effect on actin filaments is well documented and it has been reported to soften cells (Fabry *et al.*, 2001; Harris and Charras, 2011) and, perhaps less predictably, to render adherent cells more fluid-like (Fabry *et al.*, 2001) (interestingly, non-adherent cells, such as neutrophils, have been reported to soften but to become more solid-like (Roca-

Cusachs *et al.*, 2006)). Consistent with these previous studies, we find that adherent endothelial cells' apparent stiffness E* decreases over time (Figure 1.7), and that the absolute value of their relaxation parameter α (α has a negative sign) increases over time (Figure 1.7). Indeed, as discussed in (Fabry *et al.*, 2001), a value of the relaxation parameter α close to 0 indicates solid-like behavior, while a value closer to -1 (and therefore with an increased absolute value) indicates fluid-like behavior (to compare to the quantity termed x in the cited work, one needs to recognize that $\alpha = 1 - x$). Further, we observe that at a given concentration, cytochalasin-D affects a cell's mechanical properties in a near-continuous fashion. Finally, we note that at indentation speeds of ~1 s, the reduction in normalized apparent stiffness goes together with the fluidization of the cell, suggesting the same origin for both mechanical properties, presumably here the cytoskeleton as it is the primary component of the cell affected by cytochalasin-D (Figure 1.8).

These results demonstrate our ability to "whiff" a drug, in this case cytochalasin-D, at a well defined location and at selected time points and to simultaneously use profile microindentation to monitor the evolution of a cell's viscoelastic properties.

Conclusion

We demonstrate the ability of the profile microindentation technique to measure mechanical properties of both adherent and non-adherent cells. Using our profile microindentation technique, we show that an adherent cell's indentation and relaxation under constant strain can be characterized using only two mechanical parameters, the apparent stiffness E* and a relaxation parameter α. While the apparent stiffness E* depends on both indentation depth and speed, the relaxation parameter α is scale-free and is identical (with a minus sign) to the exponent in a weak power-law describing force relaxation found by other investigators using, for instance, bead oscillation (Fabry *et al.*, 2001) or creep relaxation (Desprat *et al.*, 2005) experiments. The apparent stiffness measured using profile microindentation matches that found using AFM, validating the approach.

Importantly, the profile microindentation technique offers the capability of easily adding a micropipette to the setup, which gives us the ability to test drugs by "whiffing" them onto a cell, at a controlled location and time, without introducing mechanical perturbation of the setup stability which is often challenging in AFM experiments. This makes this technique well suited to investigate the effect of a convective flux on a single-cell, to determine for instance if drug intake kinetics are impacted by fluid velocity when a drug is administered via convection-enhanced delivery, or if fluid shear stress in itself would impact a cell's physiology. In future investigations, the micropipette could be used to locally introduce an agonist or to

bring another cell in contact with the cell whose mechanical properties are being measured and thus explore the effect of cell-cell contact on cell mechanics.

Author contributions

A. I. B. and J. H. designed research; L. G. and J. H. performed profile microindentations; P.-H. P. performed atomic force microscopy experiments and analyzed AFM data; A. B. provided technical support; L. G. analyzed data; all authors wrote the paper.

Acknowledgments

The authors gratefully acknowledge Julie Lafaurie-Janvore for introducing them to the plasmid transfection technique for live actin imaging. The authors acknowledge Claire Hivroz and her team at the Curie Institute (Paris, France), in particular Michael Saitakis and Stephanie Dogniaux, for kindly providing the human lymphoblast cells and the human T lymphocyte CD4 cells. The authors acknowledge Delphine L'Huillier, Caroline Foubert, Caroline Frot, Daniel Guy, Antoine Garcia, and Do Chi Toai Vu for technical support. This work was supported by a permanent endowment in cardiovascular cellular engineering from the AXA Research Fund. Lionel Guillou is supported by a Gaspard Monge fellowship from the Ecole Polytechnique. P.-H. Puech is supported by Prise de Risques CNRS, ANR JCJC "DissecTion" (ANR-0909-JCJC-0091), PhysCancer "H+-cancer", Labex INFORM (ANR-11-LABX-0054) and the A*MIDEX project (ANR-11-IDEX-0001-02) funded by the "Investissements d'Avenir" French government program managed by the French National Research Agency (ANR) (to Inserm U1067 laboratory).

1.3 SUPPLEMENTARY MATERIAL

Equivalence between time and frequency domain and between creep and relaxation experiments

In the linear elastic regime, stress and strain are related as follows:

$$\sigma(t) = K(t)\varepsilon_0 + \int_0^t K(t-t')\dot{\varepsilon}(t')dt' \qquad (1)$$

where σ is the stress, t the time, K the stress relaxation function at fixed strain, ε_0 the strain at t=0, and $\dot{\varepsilon}$ the strain rate. This translates in the Laplace domain to

$$\tilde{\sigma}(s) = s\tilde{K}(s)\tilde{\varepsilon}(s) \qquad (2)$$

where the tilde denotes the Laplace transform. For a sinusoidal excitation $\varepsilon(t) = \varepsilon(w)e^{jwt}$ (with w the pulsation), we have $\sigma(t) = \sigma(w)e^{jwt}$ and the complex viscoelastic modulus G is defined by $G(w) = \sigma(w)/\varepsilon(w)$. In our experiment, $K(t) = A(t/t_0)^{\alpha}$, which translates in the Laplace domain to $\tilde{K}(s) = A\frac{\Gamma(1+\alpha)}{s(st_0)^{\alpha}}$, where Γ is the Euler function and $\Gamma(1+\alpha) = \int_0^{+\infty} exp(-x)x^{\alpha}dx$. Comparing to the result obtained for the creep function $J(t) = B(t/t_1)^{\beta}$ in Balland *et al.* (Balland *et al.*, 2006), we conclude that:

$$\alpha = -\beta \qquad (3)$$

and $A = \frac{1}{B\Gamma(1+\beta)(1-\beta)}$ $\left(\approx \frac{1}{B} \text{ for } 0 < \alpha << 1\right)$ (4)

Equation (3) implies that the power-law exponent for a constant strain experiment is the opposite of that of creep function experiments and oscillating bead trapping (Desprat *et al.*, 2005). We note that according to Fabry et al. (Fabry *et al.*, 2001), the exponent α provides access to the loss tangent η at low frequencies (η = $\alpha\pi/2$), which in turn provides access to the loss modulus, knowing the storage modulus (by definition, η = G''/G', where G'' is the loss modulus and G' the storage modulus).

Which value of a cell's Poisson's ratio for which experiment?

When the Poisson's ratio retains its original definition as one of two elastic moduli necessary to describe a homogeneous isotropic elastic medium, one should take a value of 0.5 for moderate cell compressions, indicating that cell volume is conserved. Indeed, Harris and Charras reported no volume change (Harris and Charras, 2011) when observing cell indentation with a confocal microscope for forces on the order of 10 nN corresponding to strains on the order of 10 to 40%. To the best of our knowledge, only in cases where large compressions are applied over long durations (deformations on the order of 100% over 300 s as in reference (Trickey *et al.*, 2006)) has overall cell volume change due to compression been reported. It is believed that the volume change then results from the efflux of fluid through the cell membrane, which means that a model of a cell as a continuous elastic medium is ill-defined in the first place, as a portion of the medium is "lost". Other values of Poisson's ratio that have been reported when modeling the cell as an elastic medium may have been the result of either indirect measurements (Ma *et al.*, 2012) or have resulted from approximating the cell as a two-dimensional medium (Maniotis *et al.*, 1997).

In some studies, investigators have sometimes used the term Poisson's ratio to refer to the Poisson's ratio in a biphasic or poroelastic model, which is a physical model distinct from the elastic medium. In the poroelastic model, what is sometimes referred to as the Poisson's ratio is strictly speaking the drained Poisson's ratio (Detournay and Cheng, 1993), also called the solid-phase Poisson's ratio, and refers to the compressibility of the solid-phase. For this solid-phase Poisson's ratio, typical values of 0.3-0.4 have been reported for the solid matrix in cells (Shin and Athanasiou, 1999; Trickey *et al.*, 2006; Moeendarbary *et al.*, 2013).

Convection dominates diffusion in "whiffing" experiment

In the present study, "whiffing" is accomplished by using a syringe to pressure an air reservoir that in turn pushes on the fluid containing the agent being "whiffed". For laminar flow (which we will verify at the end of the analysis) through a circular cross-section duct, Poiseuille's law (Poiseuille, 1844) relates the average flow velocity and the applied pressure difference as: $v = \frac{\Delta P R^2}{8 \eta L}$, where v is the mean fluid velocity, ΔP is the applied pressure difference, R is the radius of the cylindrical duct, η is the fluid dynamic viscosity, and L is the length of the duct. Because the hydraulic resistance R_h (defined as $R_h = \Delta P/Q$) in a Poiseuille flow scales as $1/R^4$, a good approximation of the overall micropipette resistance can be obtained by taking the resistance of the thin tip, where the radius is ~10^{-5} m, and neglecting the long shaft, where the radius is ~10^{-3} m.

Given an applied pressure difference ΔP ~1 kPa, a micropipette radius R ~10^{-5} m, a micropipette length L ~10^{-3} m, a dynamic viscosity η ~10^{-3} Pa.s (water at room temperature), we find an approximate mean velocity of 10^{-1} m/s. This leads to a Reynolds number close to the tip of the micropipette of $Re = \frac{\rho v R}{\eta}$ ~1 (ρ is the density of water), justifying our initial assumption of a laminar flow. The distance between the micropipette tip and the cell is L ~10^{-4} m, which leads to a characteristic time for convection of cytochalasin-D of $\tau_{convection}$ ~10^{-3} s. The diffusion time scales as L^2/D, where D is the diffusion coefficient. For spherical particles in a low-Reynolds number flow, D can be obtained from the Stokes-Einstein relation (Einstein, 1905) $D = \frac{k_B T}{6 \pi \eta R_{part}}$, where k_B is the Boltzmann's constant, T is the absolute temperature, and R_{part} is the radius of the particle. At room temperature, estimating that R_{part} ~10^{-9} m for cytochalasin-D (molar mass ~500 g/mol), we find a characteristic diffusion time constant of $\tau_{diffusion}$ ~10 s.

Comparison of profile microindentation at room temperature vs. physiological temperature

We built a custom-made Plexiglas chamber that allows passage for micropipettes while thermally insulating the Petri dish. Briefly, the chamber was heated with a resistance, where the electrical current was controlled by a PID system branched to a thermocouple device placed inside the chamber. We then calibrated our system to link the target temperature given to the PID to the medium temperature inside the Petri dish. Using this system, we were able to verify that cell indentations could be performed at physiological temperature without increasing the indenter vibrations too much. We find that cell stiffness increases by ~50% (Supplementary Material, Figure 1.9) when going from physiological temperature (37 °C) to room temperature (~20 °C), although this difference was not statistically significant. Surprisingly, past studies have shown both an increase (Petersen *et al.*, 1982) and a reduction (Sunyer *et al.*, 2009) in epithelial cell stiffness for this temperature variation.

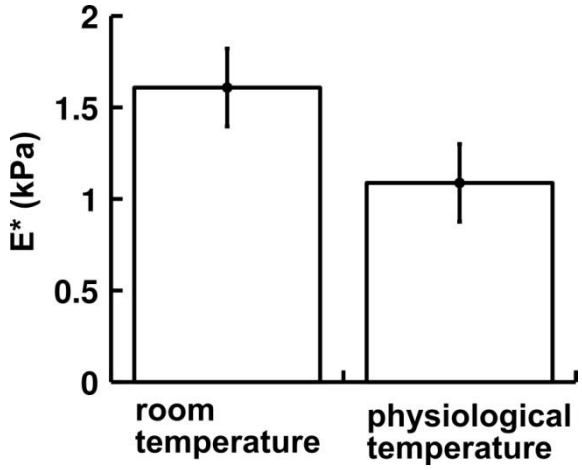

FIGURE 1.9: Effect of temperature on cell apparent stiffness. Indentation speed was 1.4 μm/s. Left column represents cells indented at room temperature, while right column represents cells indented at physiological temperature. Data is mean ± SEM. Difference is not statistically significant ($p = 0.08$).

Profile microindentation may also be used on non-adherent cells

To demonstrate the capability of using profile microindentation to determine the mechanical properties of non-adherent cells, we performed microindentations of human T lymphocyte CD4 cells that were held with a micropipette (Supplementary Material, Figure 1.10b). CD4 cells, kindly provided by C. Hivroz (Curie Institute, Paris, France), were maintained in RPMI medium with 10% SVF and 1% Hepes at 37°C and 5% CO_2 and were prepared according to the protocol in Larghi et al. (Larghi *et al.*, 2013). This study was conducted according to the Helsinki Declaration, with informed consent obtained from the blood donors, as requested by the Etablissement Francais du Sang. The indenter used had a rigidity of 1.2 nN/μm and a radius of 4 μm. The radius of each CD4 cell was measured to obtain the effective radius used in the Hertzian model.

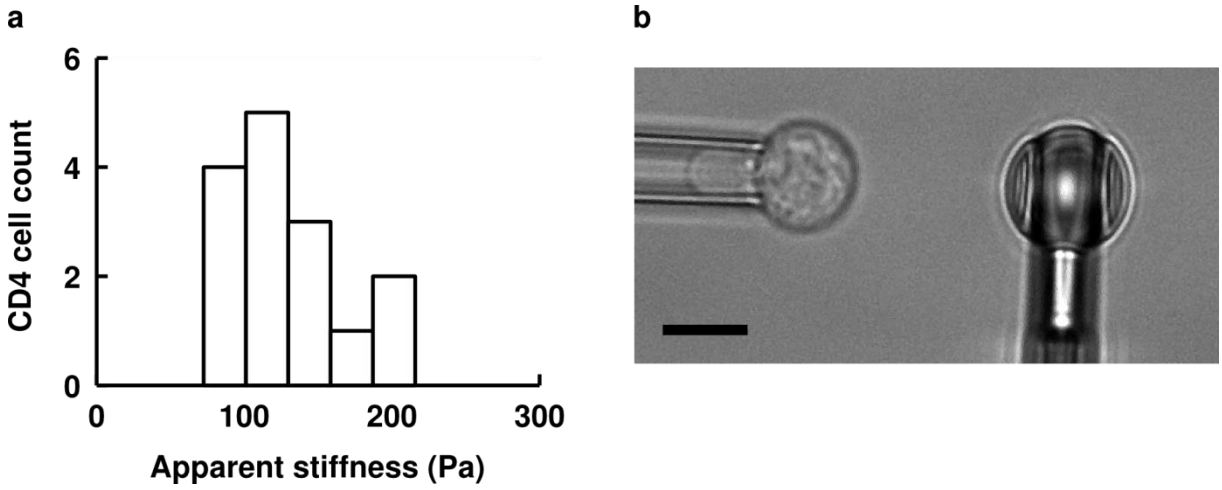

FIGURE 1.10: Profile microindentation of non-adherent human T lymphocyte CD4 cells. (a) Histogram of the apparent stiffness of CD4 cells indented at 0.8 μm/s. (d) Micrograph of a profile microindentation of a CD4 cell. Scale bar is 5 μm.

We found an apparent stiffness of 130 ± 11 Pa (mean ± s.e.m.) (Supplementary Material Figure 1.10a) using an indentation speed of 0.8 μm/s. Values reported in the literature for naïve CD4 cells range from 85 Pa after complete relaxation (Bufi *et al.*, 2015) to 250-300 Pa for indentation speeds between 0.1 and 1 μm/s (Chang, 2011). The setup and program used were the same as for microindentations of adherent cells, rendering comparisons easier then when different methods are used (typically micropipette aspiration for non-adherent cells and AFM for adherent cells).

Migration of a human lymphoblast cell on an endothelial cell in profile view

Profile microindentation may be combined with a second micropipette to observe, for instance, leukocytes migrating on endothelial cells. Supplementary Material Figure 1.11 illustrates that the micromanipulation of a human lymphoblast cell does not hinder its ability to migrate on a human aortic endothelial cell (HAEC). All the while, we may perform profile microindentation to monitor the evolution of the mechanical properties of the HAEC (data not shown).

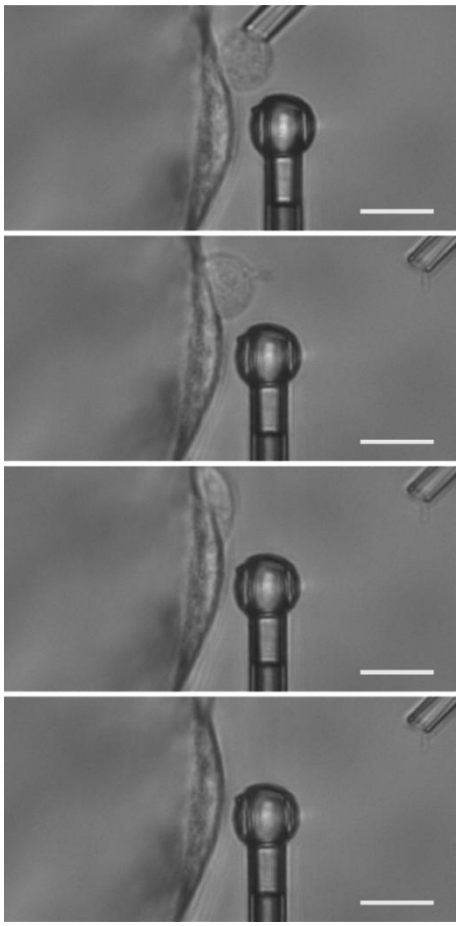

FIGURE 1.11: Profile view of the migration of a human lymphoblast cell on a HAEC. The mechanical properties of the HAEC may be monitored using a microindenter. Scale bar is 10 μm.

In these experiments, human lymphoblast cells were isolated from donor blood about 2 weeks before the experiment by S. Dogniaux and M. Saitakis (Curie Institute, Paris, France) according to the protocol described in Bufi et al. (Bufi *et al.*, 2015). The cells were maintained in RPMI 1640 medium, Glutamax Supplement GIBCO (Life Technologies # 61870-010) with 1% penicillin-streptomycin GIBCO (10,000 U/mL) (Life Technologies # 15140-122), 1% Hepes GIBCO 1M (Life Technologies # 15630-056), 0.1% 2-Mercaepthanol (50 mM) GIBCO (Life Technologies # 31350-010) and 10% FCS.

1.4 UNPUBLISHED DATA: STIFFNESS CHANGES OF ENDOTHELIAL CELLS DURING TRANSENDOTHELIAL MIGRATION

As discussed previously, transendothelial migration, the process by which leukocytes migrate across the endothelial barrier, is a key part of the early development of atherosclerosis (Woollard and Geissmann, 2010). While this may suggest transendothelial migration to be a process that is detrimental to our health, it is in fact also necessary to preserve it, as leukocytes must be able to exit the bloodstream and reach the surrounding tissue in order to carry out the immune response (von Andrian and Mempel, 2003; Valignat *et al.*, 2013; Crotty, 2015; DuPage and Bluestone, 2016). Given its central role in both atherosclerosis development and the immune response, it is not surprising that transendothelial migration has been the subject of intense scrutiny by researchers, in particular from the biochemical standpoint. This has enabled a better understanding of the various molecules involved in transendothelial migration and of their respective roles, from adhesion molecules and cytokines to acto-myosin in the cytoskeleton (Johnson-Léger *et al.*, 2000; Ley *et al.*, 2007; Muller, 2011). Much less, however, is known about the mechanics of this process.

Yet, recent results suggest that mechanics may indeed play an important role in transendothelial migration. For instance, recent experimental results show that the stiffness of the underlying substrate influences the extravasation rate of leukocytes: the stiffer the substrate, the higher the extravasation rate (Stroka and Aranda-Espinoza, 2011). Another interesting example was observed by Kang *et al.*, who reported that the stiffness of pulmonary microvascular endothelial cells decreases transiently for less than one minute upon adhesion of neutrophils (Kang *et al.*, 2010). Using atomic force microscopy, Kang *et al.* further reported an increase in stiffness of endothelial cells adjacent to the one to which a leukocyte adheres. An earlier study by the same Doerschuk laboratory reported an increase in endothelial cell stiffness within two minutes of neutrophil adhesion but only if the endothelial cells had been pretreated with TNF-α (Wang *et al.*, 2001). Interestingly, they also noted an increase in neutrophil stiffness during that period. Those earlier measurements were performed with magnetic twisting cytometry.

Given these observations, we wondered if our newly developed profile microindentation method would allow us to detect the mechanical "footprints" of transendothelial migration. Unlike most atomic force microscopes (with one notable exception, the JPK NanoWizard), profile microindentation allows the placement of a micropipette in the setup, which can be used to bring a leukocyte in contact with the endothelial cell (Figure 1.11). This micropipette can also be used to measure interesting physical quantities. Indeed, by aspirating the leukocyte, we are able to determine its stiffness (Hochmuth, 2000) and potentially track this parameter during

transendothelial migration. Moreover, by using various levels of aspiration pressure, we can potentially determine how much force is necessary to halt transendothelial migration and thus compute a "stall force". Finally, by increasing the aspiration pressure until detaching the leukocyte, we can theoretically determine the strength of the adhesive bond between a leukocyte and an endothelial cell.

These experiments proved much more tedious than initially anticipated for various reasons. First, while heating helps maintain cells healthy, it generates vibrations which render manipulation of cells with micropipettes, as well as the measurement of endothelial cell stiffness using profile microindentation, very difficult. Second, detaching activated leukocytes (in our case, T lymphocytes) from the bottom of the Petri dish without harming them proved difficult and very lengthy. Furthermore, during that time, the state of the cells degraded as they were in an environment that was not as well controlled as in the incubator. Finally, even if we successfully grab a leukocyte and place it on an endothelial cell, we then need that particular leukocyte to be active and to transmigrate almost immediately. We did not observe any transmigration in profile view and had only approximately 30% of leukocytes which migrated upon placement on an endothelial cell. Presumably, this is due both to some leukocytes being "damaged" during the freezing and thawing process and to their subsequent manipulation using a micropipette. Additionally, the leukocytes used here had not been activated, unlike the lymphoblasts we obtained later in the thesis from the Curie Institute. Even for the leukocytes that did migrate, we did not detect any clear trend in the evolution of the endothelial cell stiffness during that migration (Figure 1.12). Altogether, it is very difficult to obtain the type of sample size that is needed to draw any conclusions using this method. Indeed, it is estimated that a sample size of at least n=10 would be necessary for each physical parameter considered given the large standard deviation in endothelial cell stiffness measurements (see for instance Figures 1.3 and 1.6), which needs to be multiplied by the number of cases tested, for instance to look at drugs such as cytochalasin-D that affect molecules involved in transendothelial migration. For comparison, the 7 curves shown in Figure 1.12, out of which only 3 showed migrating leukocytes (with 0 transmigration observed), took three full days of experiment, performed over two weeks to prepare the cells.

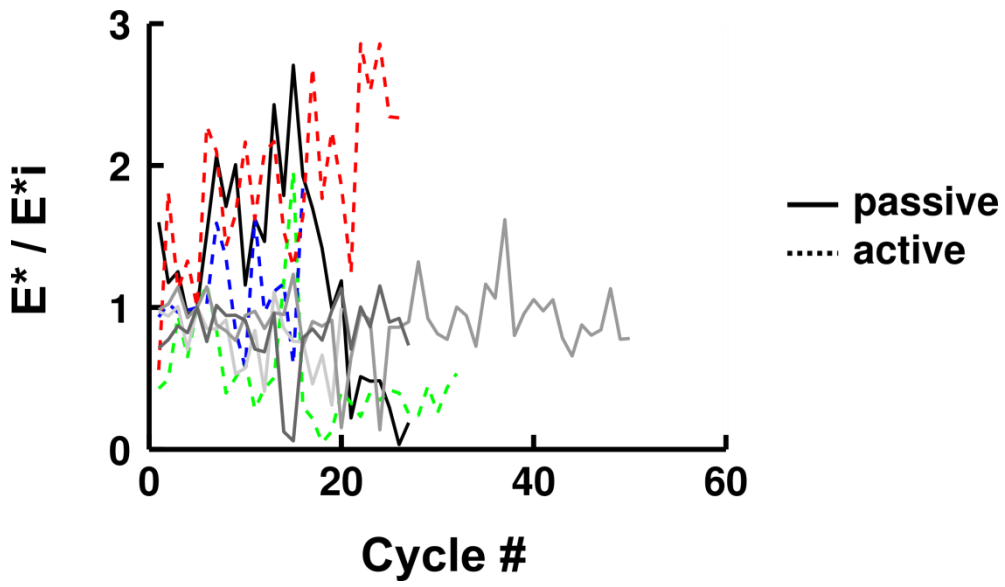

FIGURE 1.12: Evolution of human aortic endothelial cell (HAEC) stiffness following the placement of a leukocyte (in our experiments, a CD4+ T lymphocyte) using a micropipette. On the y axis, we plot of the Young's modulus E* normalized by its value E*i during the first indentation cycle. On the x axis, we plot the indentation cycle, with one cycle corresponding to 30 seconds. Each curve represents one endothelial cell. Leukocytes were categorized as "active" (continuous lines in shades of grey) if we observe some migration upon placement on the endothelial cell. Leukocytes were categorized as "passive and adherent" (dotted line in bright colors) if they remained on the endothelial cell upon removal of the micropipette, but did not visibly migrate. Leukocytes that did not adhere or that we could not categorized with certainty were ignored.

However, we had one preliminary result which points to the idea that while profile microindentation combined with a second micropipette might not be the most appropriate or efficient method to investigate the mechanical "footprint" of transendothelial migration, it may yet be sufficiently sensitive to detect it. To simplify our previous protocol which was proving too difficult, we turned to a method where we co-incubated endothelial cells with leukocytes and compared the stiffness of endothelial cells with and without a visibly adherent leukocyte. To do so, we inflamed human aortic endothelial cells (HAEC) cultivated on Cytodex-3 beads using TNF-α at 50 ng/mL for a period of 12 to 48 hours. Prior to the indentation experiment, we co-incubated HAEC with human resting CD4+ T cells for at least 30 min. We then performed profile microindentation experiments on HAEC with and without adhered T lymphocytes (Figure 1.13). We found that HAEC on which T lymphocytes had visibly adhered were significantly softer than the ones without. However, the relaxation parameter α was nearly identical between the two groups.

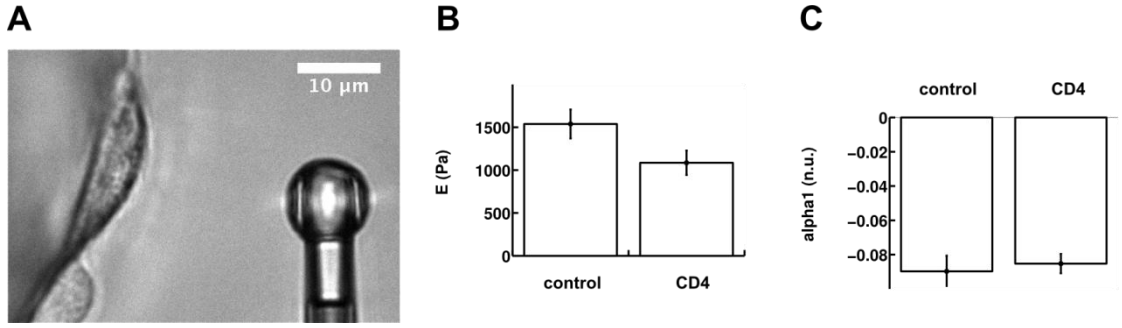

FIGURE 1.13: Change in mechanical properties of endothelial cells due to adhesion of CD4+ T cells. (A) Image of the profile microindentation experiment. Scale bar is 10 µm. Above, left, an endothelial cell seen in profile. Below, left, a CD4+ T cell is in contact with the endothelial cell. (B) Young's modulus of endothelial cells were no CD4+ T cell was in contact (left, n = 25) and where a CD4+ T cell was seen (right, n = 21). p = 0.05 between the two groups. (C) Relaxation parameter α of endothelial cells were no CD4+ T cell was in contact (left, n = 25) and where a CD4+ T cell was seen (right, n = 21). p = 0.70 between the two groups.

1.5 METHOD BOX: FABRICATING, FILLING AND USING A MICROPIPETTE AND A MICROINDENTER: TIPS AND TRICKS

Successfully employing micropipettes and microindenters in experiments is something of an art form in and of itself. Therefore, we believe it may be useful for both experimentalists in other laboratories, and future users of micropipettes in our own laboratory, to report some of the tips and tricks accumulated during our work that allow successful fabrication, manipulation and use of micropipettes. These descriptions complement the methods sections in our papers and should be viewed more as a set of tips than formal protocols.

Fabricating straight microcapillaries (microindenters or micropipettes)

To make a microcapillary whose stiffness is on the order of ~10 nN/μm, or equivalently a micropipette of typical diameter ~3-5 μm, use a borosilicate glass capillary of outer diameter 1.0 mm and inner diameter 0.78 mm (Harvard Instruments). Center the capillary in the micropipette puller (P-97, Sutter) to obtain two capillaries of equal lengths, and gently tighten the screws on both sides of the capillaries to lock its position. Select the pre-programmed program 5 (Heat = 488, P = 400, Pull = 50, Vel = 140, Time = 89), press "Enter", then "Pull". To retrieve a capillary, loosen the screw while holding the capillary with the other hand. Note that, to make shorter and stiffer microcapillaries, you may select the pre-programmed program 10 (Heat = 472, P = 500, Pull = 100, Vel = 140, Time = 100).

Adding a spherical tip to make microindenters

To add a spherical tip, place the capillary obtained on the microforge (MF-200, World Precision Instruments). Use the low magnification objective to center it roughly, then go to high (5x) magnification (Figure 1.14).

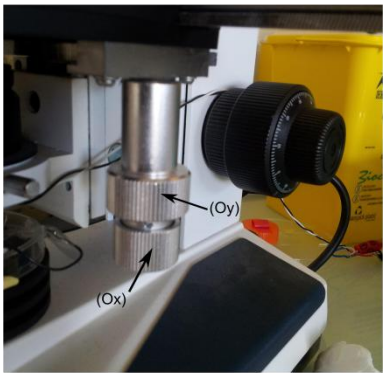

FIGURE 1.14: Microforge axis to center capillary

After heating the glass sphere (press "Polish"), make contact using the capillary, and play with the retraction speed and the depth of entry into the glass sphere to make a small or large spherical tip. Usually, fast retraction leads to larger spheres. Conversely, if you retract the capillary too slowly, the glass will enter the microindenter without forming a tip at all. If the ball of glass at the end of the capillary is too ellipsoidal, you can approach it to the heated glass sphere to slightly melt it, which will make it rounder. Also, it sometimes helps to pre-cut the capillary to the desired diameter using the other microforge (MF-900, Narishige).

Bending microcapillaries (microindenters or micropipettes)

To bend a capillary, use the microforge MF-900. Position the capillary so that the part that you want bent is directly above the edge of the hot wire. Position yourself about one to two capillary diameter above the hot wire. Select a temperature of 35-50 (no unit, this uses the graduation system of the MF-900) to avoid bending the capillary too rapidly. 35 will be slow and appropriate for diameters of ~10 µm or under. To bend faster, or bend capillaries of diameters ~50-100 µm, prefer temperatures of ~50. Use the angular graduations in the ocular to have a precise bending angle. A typical use case is a bending angle of 45° to end up with a horizontal micropipette tip. We suggest bending instead to 40°, as this will avoid contact of the tip with the bottom of the Petri dish and will avoid positioning issues during the experiment. The focus for image acquisition remains sufficiently good for all intended purposes. For more complex designs that involve several bending angles, we suggest using screws linked with Patafix to visualize the end result and ascertain that all the bending angles are correct. Also note that once the capillary is bent, a tip cannot be added. Therefore, to make a bent microindenter, first add the tip, then bend it.

Calibrating microindenters

Julien Husson developed a Matlab code that allows extremely precise and semi-automated calibration of microindenters against another microindenter of known stiffness. The starting point is to calibrate "first-generation" microindenters. This can be done in one of two ways. One method is to calibrate these standard microindenters by measuring their deflection under the gravitational force exerted on their tip by a piece of ultrathin paper of known mass (Basu *et al.*, 2016). A second method consists of using a commercial force probe (model 406A with a force range of 0-500 nN, AURORA SCIENTIFIC INC., Aurora, ON, Canada). Both methods are much longer than Julien's Matlab code which will allow a calibration in ~15 min. Therefore, always prefer this last method, provided that you have "first-generation" microindenters whose stiffness roughly matches the one you expect for your newly fabricated microindenter.

Filling micropipettes

This is a very important step and can cause much delay in the experiments if not done carefully. The problems may arise because of breaking micropipettes, or more commonly getting an air bubble stuck that will render the micropipette unusable. If the micropipette has a diameter larger than ~10 μm, you can directly fill it by pushing the desired medium (usually water or cell culture medium) through it. To do so, use a bendable tube that will channel the filling medium from a syringe to your microcapillary (Figure 1.15).

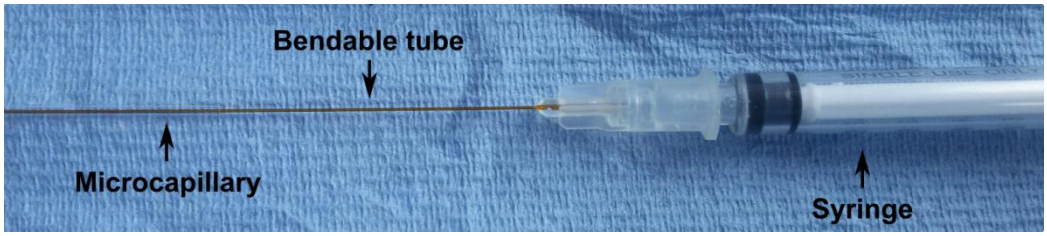

FIGURE 1.15: Filling by pushing

If the micropipette diameter is smaller than ~10 μm, you should first aspirate medium through the narrow tip. To do so, place the capillary inside a silicone tube to make an impermeable seal with a syringe (Figure 1.16).

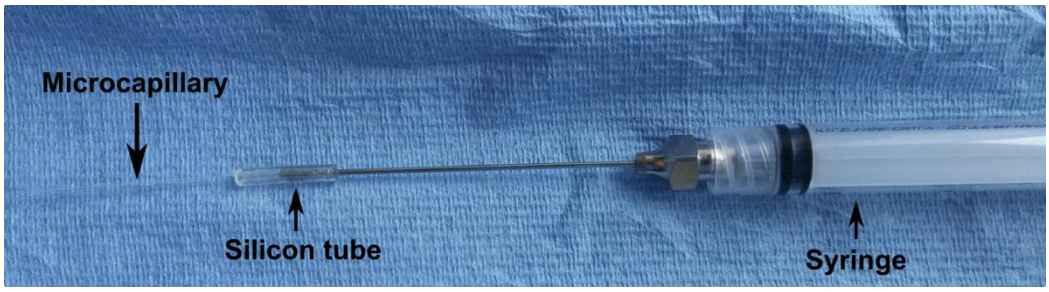

FIGURE 1.16: Filling by aspiration

Use small syringes, from 1.5 to 5 mL, as small diameter syringes lead to less force being necessary to sustain a given aspiration pressure. That way, your arms will be less tired and you reduce the risk of trembling. If the microcapillary has an angle of ~45°, which will very often be the case, you can press the bent angle against the wall of a 1.5 mL Eppendorf tube that contains your filling medium, orienting it so that the tip is in the middle of the Eppendorf tube (Figure 1.17). That will minimize the chances of breaking the tip while requiring minimal filling medium (less than 1.5 mL). Also, you can face the window and hold the tube in front of you to see the microcapillary being filled (Figure 1.17). That way, you can make sure it is working and know when to stop. Usually, you can stop at or slightly before the point when the microcapillary diameter reaches 500-800 μm.

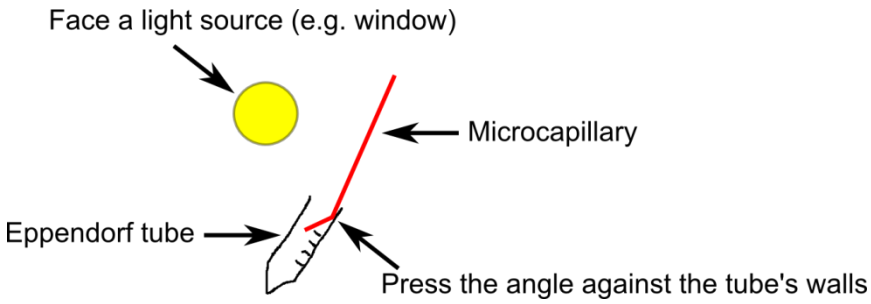

FIGURE 1.17: Filling a bent micropipette of diameter of less than 10 μm by aspiration

If the microcapillary is straight, you may be better off using a large dish (e.g. a 50 mL Falcon tube or a Petri dish) to contain the filling medium. That way, you will minimize the chances of hitting the dish's walls and breaking the microcapillary tip.

If you see that a micropipette is not aspirating, you can try using a syringe to push through it, which might unblock it. If after two attempts it is not unblocked, start making a new micropipette and do not try to perform experiments with a semi-functional or non-functional micropipette; you will end up wasting much more time than if you just start anew.

Making microcapillaries non-adhesive

Some manufacturers, such as Sigma with their Sigmacote product, sell chemical agents to help make microcapillaries non-adhesive. In experiments that involve cells, we find that those are, to a large extent useless. Indeed, if you are using complete cell culture medium, it will have a significant amount of albumin. If you let the microindenter or microcapillary sit in this medium for over 5 min, it will get coated with albumin and become non-adherent. Be careful of not approaching any cells before this period, as they will get stuck to your microcapillary and you will not be able to get rid of them afterwards. If you wish to try getting rid of things that got stuck, however, we suggest flicking with your finger at the microcapillary holder. Before doing so, raise the microcapillary so that it does not risk breaking against the bottom of the dish.

Repairing a broken microindenter

If the tip of a microindenter is broken (for example because you hit the bottom of the Petri dish), there is nothing you can do. However, if the shaft is broken (for example while you were holding it), you can take a new rod and glue it to the part of the microindenter that contains the tip using glue polymerized with UV light. It is fast and robust.

1.6 PROFILE MICROINDENTATION VS AFM: COMPARISON OF COST AND TIME REQUIRED TO SET IT UP

Building the profile microindentation setup from scratch could take about 4-6 weeks for an experienced scientist. In addition to this, developing the software could take an additional 4 weeks (based on the time it took Julien Husson to develop the code). Moreover, knowing how to make cantilevers, minimize noise, fabricate and fill micropipettes, could take a 2-3 months ramp-up (based on incoming interns and PhD students). For the AFM, we lack the direct experience. Potentially the setup is less lengthy to the scientist as some elements are pre-built (the software in particular), but we expect additional time to be lost in discussions with the vendor, and again some more lead time to wait for a technician to deliver and install the AFM. We also expect based on discussions with other laboratories that use an AFM, that there is a similar ramp-up time of 2-3 months to know how to properly use the apparatus.

In terms of cost, if setting up profile microindentation *de novo* (no pre-existing equipment whatsoever), we expect an initial investment of ~50-55 kEUR, and annual costs of ~100 EUR (not including maintenance cost if some material, such as the micromanipulators, are broken). However, if there is pre-existing material, that investment can be greatly diminished. For instance, if the laboratory already owns a microscope, that investment is reduced to ~30 kEUR, and if the laboratory is already performing micropipette experiments (e.g. for micropipette aspiration or electrophysiology), the investment could be lower than ~3 kEUR (essentially the costs associated with the piezoelectric device).

Although the price of an AFM varies widely, from ~50 to 300 kEUR (and even higher for some), we estimate an initial setup cost to be around ~175 kEUR for a typical life science AFM mounted on an inverted optical microscope. The annual cost (outside maintenance) associated with operating this AFM will be at least ~2 kEUR (each cantilever costs ~10 EUR vs 0.10 EUR for capillaries from which we make).

Profile Microindentation			
Item	**Brand**	**Fixed cost (EUR)**	**Variable cost (EUR/year)**
Inverted microscope TE300	Nikon	8500	
Air suspension table	CVI Melles Griot	2000	
Motorized micromanipulator MP-285	Sutter Instruments	8500	
Micropipette holder IM-H1 (2x)	Narishige	400	
Piezoelectric controller TPZ001	Thorlabs	550	
Strain gauge reader TSG001	Thorlabs	500	
3-axis platform RB-13M (manual)	Thorlabs	1250	
100x objective	Nikon	1800	
20x objective	Nikon	500	
4x objective	Nikon	200	
Camera Flash 4.0 CMOS	Hamamatsu	12000	
Borosilicate glass capillaries	Harvard Apparatus		100
Micropipette puller P-97	Sutter Instruments	7500	
Microforge MF-900	Narishige	6500	
Microforge MF-200	World Precision Instruments	3300	
TOTAL		**53500**	**100**

Atomic Force Microscopy			
Item	**Brand**	**Fixed cost (EUR)**	**Variable cost (EUR/year)**
Inverted microscope TE300	Nikon	8500	
Air suspension table	CVI Melles Griot	2000	
Nanowizard	JPK	150000	
100x objective	Nikon	1800	
20x objective	Nikon	500	
4x objective	Nikon	200	
Camera Flash 4.0 CMOS	Hamamatsu	12000	
Cantilever	JPK		2000
TOTAL		**175000**	**2000**

CHAPTER 2

Mechanical properties of non-adherent cells in suspension

2.1 INTRODUCTION

In the previous chapter, we presented a method that was able to measure the mechanical properties of non-adherent cells, provided that they are maintained in place using a micropipette. However, in the bloodstream, leukocytes are in suspension and not held in place. Therefore, being able to measure the mechanical properties of cells in suspension might provide a more accurate characterization of their mechanical properties.

To this end, we employed a microfluidic device with a cross-slot shape and flowed cells in suspension through it. When cells pass the center of this cross-slot, they are subjected to an extensional stress, which can be quantified analytically. By measuring cell deformation, we are then able to deduce the cell mechanical properties. We described the fabrication, analytical modeling and validation of that device in an article (submitted), which we reproduce in section 2.2. Some further details on the calibration of this device and the measurement of cell mechanical properties are presented in the supplementary material of this article, which we reproduce in section 2.3.

Because calibration was a fundamental aspect of this work, and certainly to validate the analytical model, we looked for a body of known stiffness that could serve as a test case. Dextran beads, which are commercial, soft and small, seemed to be a good candidate. However, their stiffness had not been directly measured previously (albeit indirect measurements existed that gave an order of magnitude, see section 2.2). Therefore, in section 2.4, we present the results of microindentation and micropipette aspiration experiments on two different types of dextran beads and show that the polymers we studied appear stiffer in extension than in compression, a property that other types of polymers appear to exhibit.

2.2 MEASURING CELL VISCOELASTIC PROPERTIES USING A MICROFLUIDIC EXTENSIONAL FLOW DEVICE

Lionel Guillou*, Joanna B. Dahl*, Jung-Ming G. Lin*, Abdul I. Barakat, Julien Husson, Susan J. Muller, Sanjay Kumar

* equal contribution

Abstract

The quantification of cellular mechanical properties is of tremendous interest in biology and medicine. Recent microfluidic technologies that infer cellular mechanical properties based on analysis of cellular deformations during microchannel traversal have dramatically improved throughput over traditional single-cell rheological tools, yet the extraction of material parameters from these measurements remains quite complex due to challenges such as confinement by channel walls and the domination of complex inertial forces. Here we describe a simple microfluidic platform that uses hydrodynamic forces at low Reynolds number and low confinement to elongate single cells near the stagnation point of a planar extensional flow. In tandem, we present a novel analytical framework that enables determination of cellular viscoelastic properties (stiffness and fluidity) from these measurements. We validated our system and analysis by measuring the stiffness of cross-linked dextran microparticles, which yielded reasonable agreement with previously reported values and our micropipette aspiration measurements. We then measured viscoelastic properties of 3T3 fibroblasts and glioblastoma tumor initiating cells (GBM TICs). Our system captures the expected changes in elastic modulus induced in 3T3s and TICs in response to agents that soften (cytochalasin D) or stiffen (paraformaldehyde) the cytoskeleton. The simplicity of the device coupled with our analytical model allows straightforward measurement of the viscoelastic properties of cells and soft, spherical objects.

Introduction

While it has been long understood that soluble factors from the cellular microenvironment can strongly influence cellular behavior, it is becoming increasingly clear that physical and especially mechanical inputs can also affect cell behaviors such as migration, proliferation and differentiation (Engler *et al.*, 2006; Ulrich *et al.*, 2009; Hung *et al.*, 2013; Rubashkin *et al.*, 2014). Cells frequently respond to mechanical stimuli by adaptively tuning their intrinsic mechanical properties, and significant evidence suggests that this "mechanoadaptation" is key to transducing these inputs into biochemical signals that mediate cell behavior. Moreover, because disease states are often accompanied by changes in cell and tissue mechanics, there has been growing interest in using cell mechanical properties as a label-free biomarker (Bissell *et al.*, 2002; Paszek *et al.*, 2005; Levental *et al.*, 2009; Egeblad *et al.*, 2010; Ulrich *et al.*, 2010). As a result, there is much interest in developing platforms to quickly and accurately quantify cellular mechanical properties. These new platforms would not only facilitate advances in understanding how cells stabilize their shape and process mechanical cues but also give rise to novel clinical diagnostic tools.

Traditional techniques to study the mechanical properties of single cells include micropipette aspiration (MPA), atomic force microscopy (AFM), optical stretching, and magnetic bead cytometry (Huang *et al.*, 2004; Lee and Lim, 2007; Rodriguez *et al.*, 2013). While these methodologies have been instrumental in elucidating the molecular basis of cellular mechanics, they require highly skilled operators and sophisticated equipment and, most importantly, suffer from low experimental throughput. For example, AFM and optical stretching techniques have sampling rates on the order of 1 cell per minute (if not slower), which severely reduces statistical power and complicates if not precludes the identification of rare cellular subpopulations. Additionally, many of these techniques require either direct contact between a probe and cell, adhesion to two-dimensional culture substrates, or both, which may invite measurement artifacts.

To address these issues, microfluidic tools have recently been explored as a strategy to measure cellular structural and mechanical properties with a rapidity that may be better suited to drug discovery and clinical application (Gossett *et al.*, 2012; Dudani *et al.*, 2013; Khan and Vanapalli, 2013; Tse *et al.*, 2013; Lange *et al.*, 2015; Mietke *et al.*, 2015; Otto *et al.*, 2015). While these approaches have indeed massively improved measurement throughput and reduced operator skill/bias issues relative to traditional measurements, the extraction of cell mechanical properties (e.g. elastic modulus) remains challenging primarily due to complex viscous forces that severely complicate analysis of deformations.

Recently, Guck and colleagues performed rapid cell deformability measurements with a device that squeezed cells into a bullet shape as the cells passed through square constriction channels (Mietke *et al.*, 2015; Otto *et al.*, 2015). By

using a viscous medium (viscosity μ ~ 15 mPa·s, versus 1 mPa·s for water at room temperature), the device could be operated at low Reynolds number (Re ~ 0.1), thereby enabling the development of an analytical model from which elastic moduli of cells could be determined from the resulting deformations (Mietke *et al.*, 2015). While this method has proven quite powerful, it is both analytically demanding and requires accurate edge detection of a complicated shape to extract elastic properties.

In an attempt to achieve high-throughput mechanical measurements within a simpler geometry, Di Carlo and colleagues developed higher-Reynolds number (Re > 40) microfluidic systems that measure cell deformability with throughput ranging from 1000 cells/second (Tse *et al.*, 2013) to 65,000 cells/second (Dudani *et al.*, 2013). By elongating cells at the stagnation point of extensional flow or pinching cells with two sheathing flows, they successfully developed population "signatures" based on distributions of cell deformability vs. size. These population signatures responded in expected ways to cytoskeletal drugs in the pinched-flow sheathing device for which strain rates and imposed cell strains were not too large (Dudani *et al.*, 2013) (the expected effects of cytoskeletal depolymerization drugs were not detected in the high strain rate, high strain extensional flow device (Gossett *et al.*, 2012)) and enabled prediction of disease state from clinical samples (Gossett *et al.*, 2012; Tse *et al.*, 2013). Nonetheless, this work did not present an analytical route to extract cell constitutive model parameters, instead requiring numerical solutions due to the high inertial component of the flow. Thus, there remains a significant need for microfluidic strategies to measure cellular viscoelastic properties in a simple geometry subject to well-defined deformation forces.

In this study we present a novel cross-slot microfluidic system that addresses these limitations. By strategically choosing our device geometry and suspending fluid, we are able to greatly simplify both the experimental workflow and mechanical analysis and thereby arrive at a single analytical equation that relates deformation, channel geometry, and cellular viscoelastic parameters. The expected elliptical deformed shape is more easily analyzed and less sensitive to noise in image processing compared to a more complicated shape with rapid changes in curvature. We validate the approach by measuring the elastic properties of cross-linked dextran hydrogel particles, using independent micropipette aspiration measurements and previously published values for stiffness as comparisons. We then apply this system to measure the apparent shear modulus and fluidity (viscosity parameter) of 3T3 fibroblasts and primary glioblastoma tumor initiating cells (GBM TICs) and show that we can capture expected changes in cell stiffness in the presence of specific pharmacologic agents.

Materials and Methods

Microfluidic Device Fabrication

Microfluidic cross-slots were fabricated using standard soft lithography. This geometry, consisting of two channels that intersect at 90 degrees, is a convenient platform for generating a planar extensional flow. Masters for the cross-slots used for the cell experiments were made from SU-8 patterned on silicon wafers following standard soft lithography approaches (Xia and Whitesides, 1998). Briefly, silicon wafers were pre-cleaned with piranha solution (3:1 sulfuric acid to hydrogen peroxide), washed with DI water, and baked at 120°C for 20 minutes to remove any moisture. After spin-coating a 30-μm layer of SU-8 2025 photoresist (Microchem, Boston, MA) onto the wafer, the wafer was exposed to 365-nm UV light at ~40 mW/cm^2 for 12 s under a mylar mask printed with the cross-slot pattern (Artnet Pro, San Jose, CA). After development, wafers were pretreated with trichloro (1H,1H,2H,2H-perfluoroocytl)silane to prevent adhesion of the polydimethylsiloxane (PDMS) to the silicon wafer. PDMS and curing agent (Sylgard 184, Dow Corning, Midland, MI) were mixed in a 10:1 ratio, degassed, and poured over the silicon master. The PDMS was cured overnight at 80°C before the PDMS patterns were removed. Inlet and outlet holes were punched with an 18-gauge blunt needle (McMaster Carr, Elmhurst, IL). The PDMS devices were bonded to glass microscope slides after oxygen plasma treatment, and bonding was finalized by curing the PDMS/glass device in an oven at 80°C overnight. The cross-slot channel geometries for the cell experiments had widths of 70 or 100 μm, a depth of 30 μm, and channel lengths to the cross-slot region of 1 or 2 mm.

For the dextran particle experiments, which required very deep devices, masters were made from dry-film photoresist on stainless steel wafers. Prior to lamination, the steel wafers were rinsed with acetone and water. Two layers of 100 μm-thick dry-film photoresist (Riston GoldMaster GM100 photoresist, DuPont, Research Triangle Park, NC) were laminated onto the steel wafer with the rollers heated to 120°C (Akiles Prolam Ultra, Mira Loma, CA). The dry-film photoresist was exposed to 365-nm UV light at ~40 mW/cm^2 for 10 s under a mylar mask printed with the cross-slot pattern (Artnet Pro, San Jose, CA). The laminate was developed with 10% K_2CO_3 solution and then dried. The PDMS cross-slot devices were prepared from the dry-film photoresist masters in the same manner as from the SU-8 masters. These large devices with 200 μm depth, 400 μm width, and channel lengths of 2 mm, accommodated the large (40-100 μm diameter) dextran hydrogel particles.

Cell Culture

NIH 3T3 mouse fibroblasts (ATCC, Manassas, VA) were cultured on tissue culture plastic in complete medium consisting of Dulbecco's Modified Eage's Medium (DMEM) (Gibco, Carlsbad, CA) with 10% calf serum (JR SCIENTIFIC, Woodland, CA) and 1% penicillin/streptomycin (Gibco). Primary GBM TICs were collected in a

previous study after informed consent from male patients who underwent surgical treatment and Institutional Review Board approval (Deleyrolle *et al.*, 2011). The TIC neurospheres were propagated in neurosphere assay growth conditions (Deleyrolle and Reynolds, 2009) with serum-free medium (Neurocult NS-A Proliferation kit, Stem Cell Technologies, Vancouver, Canada) supplemented with epidermal growth factor (EGF) (20 ng/ml, R&D Systems, Minneapolis, Minnesota), basic fibroglast growth factor (bFGF) (R&D Systems) and 2 μg/ml heparin (Sigma, St. Louis MO, USA) The gliomaspheres were serially passaged every 5 to 7 days, when the spheres reached a diameter of ~150 μm. Gliomaspheres were dissociated with trypsin/ethylenediaminetetraacetic acid (0.05%) for 2 minutes and then replated in fresh media with the addition of EGF, bFGF, and heparin. Both cell cultures were grown in a humidity-controlled 5% CO_2 incubator at 37°C.

Pharmacologic studies

For studies with cytochalasin D (CytoD), cells were incubated with 10 μM CytoD (Sigma-Aldrich, St. Louis, MO) for 30 minutes prior to the experiment. CytoD was then also added to the suspending solution at 10 μM to ensure exposure to a constant CytoD concentration during cross-slot deformation. For paraformaldehyde (PFA) studies, cells were fixed with 4% PFA (Alfa-Aesar Haverhill, MA) in phosphate-buffered saline (PBS) for 10 minutes in culture and then washed 3 times with PBS to remove any residual PFA prior to resuspension. Because PFA irreversibly cross-links cellular proteins upon transient treatment, it was not necessary to include PFA in the medium during measurement.

Cross-slot Deformation Experiments

Cells and dextran hydrogel particles were suspended in 20% (cells), 30% or 40% (dextran particles) w/v 20000 Da polyethylene glycol (PEG20000)/PBS solution in order to operate in the low Reynolds number regime and to reliably focus the majority of cells/particles during cross-slot deformation. The PEG had a viscosifying effect so that a given fluid stress could be applied at lower fluid velocities to make image capture and analysis of cell and dextran particle deformation easier. The viscosity of the PEG20000/PBS solution was measured at 25°C using an Anton Paar Physica MCR 301 rheometer with a 50 mm parallel plate geometry. The measured viscosities were nearly constant across the tested strain rates (1-2000 s^{-1}): 35 to 50 mPa·s for 20% w/v solutions, ~100 mPa·s for 30% w/v solutions and ~200 mPa·s for 40% w/v solutions (Supplementary Material Figure 2.6). The high concentration of PEG also increased the density of the suspending solution to 1.03-1.05 g/mL so that cells and dextran particles were approximately neutrally buoyant. Thus, during observation of deformation at the mid-channel height (i.e. 15 μm above the glass

bottom surface for cells in the 30 μm deep device), most cells and particles were in focus and candidates for measurement. 3T3 and GBM TIC cells were trypsinized into a single cell suspension and then resuspended in the PEG20000/PBS solution. For cells treated with CytoD, drug at the same concentration as for incubation was included in the solution to prevent recovery of the cytoskeleton from the depolymerization. Typical cell densities were 8-10 million cells/mL as measured by a hemocytometer. The cross-linked dextran beads were Sephadex G200 beads in powder form (GE Healthcare, Little Chalfont, United Kingdom) and were simply added to the PEG20000/PBS solution.

The cell and dextran particle suspensions were loaded into 1 mL syringes (BD Falcon, San Jose, CA). Cell and particle suspensions were infused into the cross-slot device using a syringe pump (Cole-Parmer 74900 series dual syringe pump) at constant flow rates ranging from 50–1400 μL/hr for the cells and 2.5–40 mL/hr for the dextran hydrogel particles. To account for the compliance in the microfluidic device and tubing, the system was allowed at least 2 minutes to equilibrate before data capture after each new flow rate adjustment.

Cells or dextran particles flowing in both cross-slots were elongated at constant strain rate in extensional flow and observed passing through the stagnation point region. Deformation was imaged in phase contrast mode using a Nikon TE2000-E2 microscope with a 40x objective (~2 px/μm), and the plane of focus was the device centerplane. Images were captured by using a high-speed Phantom Miro M310 camera at 2000 frames per second with 20 μs exposure in order to obtain several images per cell or particle, thereby capturing the evolution of the deformation, and to minimize blurring due to cell or particle movement. All movies were captured within 30 minutes of the trypsinization process.

Cell and dextran particle deformation images were analyzed with custom software written for ImageJ (NIH) and Matlab (2013v, Mathworks). Cell strain was defined as $\varepsilon = (a-b)/(a+b)$, where a and b are the long and short axes, respectively, of an ellipse fitted manually to the outer edge of the cell membrane (Figure 2.1A and Supplementary Material Figure 2.8). The cell strain measurement was taken at the time point in which the cell was closest to the stagnation point. This definition of ε is the magnitude of engineering strain along the x- and y-axes: $\varepsilon = |(R-R_0)|/R_0 = |\Delta R|/R_0$ where the change in sphere radius at the surface is $\Delta R > 0$ along the y-axis (outlet flow axis) and $-\Delta R$ along the x-axis (inlet flow axis). Note that the sphere strain along the z-axis is zero for planar extensional flow due to zero velocity in the z-coordinate direction and therefore no contribution to the velocity gradient that determines the viscous fluid stresses acting on the sphere surface.

Cells were excluded from analysis if one of the following criteria was met:

- The cell was not spherical before entry into the cross-slot, as the analytical model becomes invalid since the assumed initial state for deformation computation is incorrect.
- The cell was not sufficiently centered in the channel width direction (closer than 25% of the channel width to the walls) or was adherent to another object (e.g., another cell), as the analytical model becomes invalid since the object does not experience the assumed strain rate.
- The cell membrane appeared damaged.
- The cell was either very large or very small compared to other cells (for a distribution of the cell size of the analyzed population of cells, see in the Supplementary Material Figure 2.9), as these cells may be apoptotic, multinucleated, or otherwise abnormal and empirically demonstrated very large or very small deformations far outside the population average.

The same exclusion criteria applied to dextran hydrogel particles, though the criterion related to the assumed strain rate was the only one that applied in practice because the particles were all initially spherical and intact.

The mechanical properties of cells and dextran particles were determined from the analysis of the deformation due to the known viscous forces. At a given flow rate, cell type, and drug treatment, the reported deformation under those experimental conditions was computed as the average deformation of $10 \leq n \leq 30$ cells with an uncertainty defined as the standard error of the mean. Mechanical property parameters were obtained through linear regression with a least-squares fit of the observed strain ε to cross-slot extensional strain rate $\xi U/D$ (for cells, log-log plot) or viscous stress $\mu\xi U/D$ (for dextran particles, linear plot) based on the theory described in the Results Section where ξ, U, and D are defined. The uncertainties in the linear fits and the significance of the differences in measured material properties between the cell pharmacologic studies are evaluated using analysis of covariance (ANOCOVA).

Micropipette Aspiration Experiments

Micropipettes were fabricated from glass capillaries as described in Guillou et al. (Guillou *et al.*, 2016) and mounted on motorized micromanipulators. The aspiration pressure was applied using an air-filled syringe and determined using a home-made pressure sensor as described in Hogan et al. (Hogan *et al.*, 2015). Aspiration pressure was increased from 0 to 10 kPa by incremental steps of 2 kPa. After each pressure step, an image of the aspirated Sephadex bead was acquired using a 40x objective.

Results

Theoretical analysis of the deformation of an elastic body in a cross-slot device

We begin by calculating the viscous stresses experienced by spherical bodies flowing through the stagnation point region of a cross-slot device and apply these findings to the simple case of an isotropic, linearly elastic spherical particle. Our result is valid in the limit of low Reynolds number flow and small deformations of the particle. Indeed, these two modeling assumptions were met in the upcoming results as we observed cell strains of $0.01 < \varepsilon < 0.18$ under operating conditions in which the flow Reynolds number was small, specifically $0.006 < Re < 0.2$ (range of all experimental parameters given in Table 2.1 in the Supplementary Material). Therefore the effects of fluid inertia can be assumed to be negligible compared to viscous fluid forces and omitted from our model. In contrast, the Reynolds number in the cross-slot devices of Di Carlo and colleagues (Gossett *et al.*, 2012; Dudani *et al.*, 2013) were finite at operating conditions ($Re > 40$) and therefore fluid inertia would need to be included in the modeling of cell deformation in their system.

Our system parameters are the channel half-width D, the channel height h, the medium dynamic viscosity μ, the fluid density ϱ and the mean flow velocity U (see Figure 2.1). We define the flow Reynolds number as $Re = \varrho UD/\mu$ and consider only the case where $Re \ll 1$. Hence, viscous forces dominate inertial forces and we assume Stokes flow. The cross-slot generates approximately planar extension flow, in which the velocity field is $\mathbf{v} = \Omega(-x\mathbf{i} + y\mathbf{j})$ and Ω is the uniform extensional strain rate. Therefore, in the stagnation point region under these laminar flow conditions, the velocity gradient is nearly constant. In particular, along the inlet center streamline (x-axis), the velocity gradient is approximately $\Omega = U_{in}/D$, indicating the velocity decreases linearly from U_{in}, the velocity at the entry of the cross-slot region ($|x| = D$), to zero at the stagnation point. Other investigators previously confirmed this velocity behavior along the center streamline using micro-PIV measurements (Haward *et al.*, 2012). We introduce the normalized entrance velocity $\xi = U_{in}/U$, and the stagnation point region velocity gradient is $\Omega = U_{in}/D = \xi U/D$. Because U and D are set by the experimental conditions, ξ is the only remaining factor that must be derived to obtain the velocity gradient in the stagnation point region.

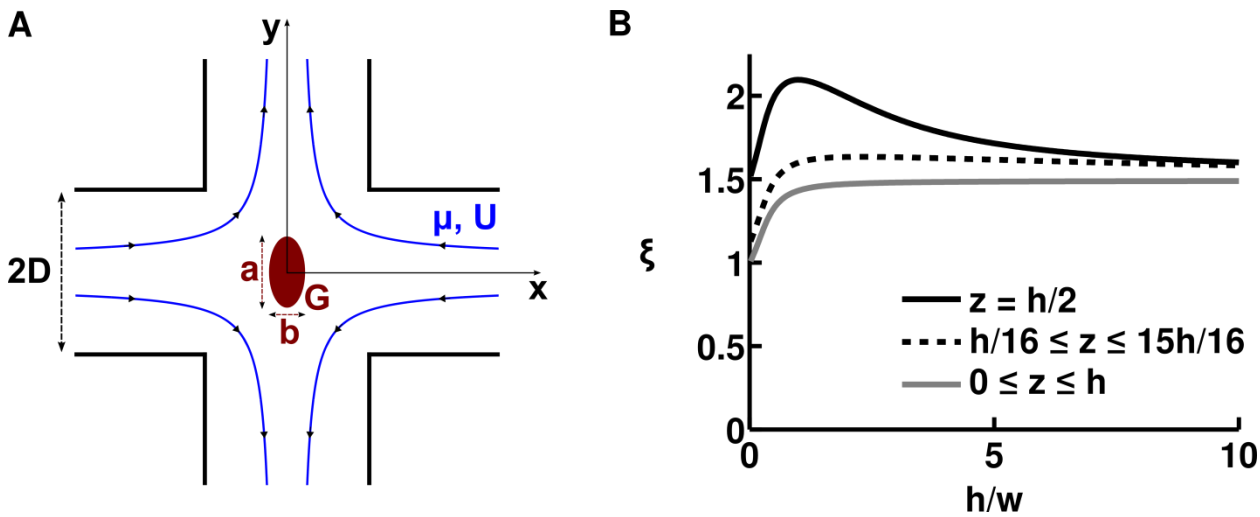

FIGURE 2.1: Cross-slot flow field. (A) Cross-slot device containing a body (red) that is initially spherical but then elliptically deforms under elongational viscous fluid stresses (flow streamlines in blue). D is the channel's half-width. a and b, respectively, denote the long and short axes of the ellipse. G is the shear modulus of the body. μ is the fluid dynamic viscosity and U is the mean flow velocity. (B) Normalized entrance velocity $\xi = U_{in}/U$ at the entrance to the cross-slot stagnation point region ($|\mathbf{x}| = \mathrm{sqrt}(x^2 + y^2) \leq D$), as a function of the channel's aspect ratio, A = h/w, where h and w (w = 2D) are the channel height and width, respectively. Values for normalized entrance velocity are computed using our derived analytical expression for ξ_{max} and ξ_{min}. z denotes the position of the vertical axis, with the channel occupying $0 \leq z \leq h$. ξ_{max} is plotted as a black line and corresponds to an object at the vertical center of the channel, where the velocity is maximal. ξ_{min} is plotted as a grey line and corresponds to objects that are in the middle of the channel's width but distributed equally along the height of the channel. The dotted black line indicates an example of the normalized entrance velocity ξ for objects that are in the middle of the channel's width and distributed equally along the height of the channel with the exclusion of the very bottom and the very top of the channel (in this example, we excluded 1/8 of the total channel height). This final value (dotted black line) is the one that best matches experimental observations.

In a first step, we restrict our analysis to the position of maximal in-plane (x-y) velocity gradient, corresponding to an object that is at the channel's vertical center (z = h/2) and in the middle of the channel's width (y = 0) where $U_{in} = U_{max}$. In such a case, $\xi = \xi_{max} = U_{max}/U$. Using the known velocity profile for laminar flow through a rectangular channel (Lee *et al.*, 2007), we are able to derive an analytical expression for ξ_{max} in terms of a Fourier series in the channel aspect ratio A = h/(2D) = h/w:

$$\xi_{\max} = \frac{3/2 - 6\sum_{n=0}^{\infty} \frac{(-1)^n}{\lambda_n \cosh(\lambda_n / A)}}{1 - 6A\sum_{n=0}^{\infty} \frac{\tanh(\lambda_n / A)}{\lambda_n^5}} \qquad \text{where } \lambda_n = \frac{(2n+1)\pi}{2} \qquad \text{(Equation 1)}$$

We note that for A < 1, both infinite series in Eq. 1 can be approximated by their first term with an error for ξ_{max} of less than 1%. For 1 < A < 3, one must add the second series term to maintain an error of less than 1%. Further, we verified that in the quasi-2D limit where A goes to 0 (corresponding to a very flat channel), ξ_{max} converges to 3/2, the well-known maximum-to-mean velocity ratio in a 2D parabolic flow. We also note that because inverting the width and height does not affect the maximum nor the mean velocity, $\xi_{max}(A) = \xi_{max}(1/A)$.

In a second step, we relax the constraint that the body must be located at the channel mid-height because it is difficult to perfectly focus all cells in experiments. Still assuming that the body is at the center of the channel width direction, the body may now be located anywhere on the vertical axis so that $U_{in} = U_{w/2}$. We use the same approach as above, and derive the normalized velocity $\xi_{min} = U_{w/2}/U$ in terms of a Fourier series:

$$\xi_{\min} = \frac{1 - 6A\sum_{n=0}^{\infty} \frac{1}{\lambda_n^4 \cosh(\lambda_n / A)}}{1 - 6A\sum_{n=0}^{\infty} \frac{\tanh(\lambda_n / A)}{\lambda_n^5}} \qquad \text{where } \lambda_n = \frac{(2n+1)\pi}{2} \qquad \text{(Equation 2)}$$

ξ_{min} is plotted for aspect ratios between 0 and 10 in Figure 2.1B (solid grey line). We note that for A < 1, both infinite series in Eq. 2 can be approximated to their first term with an error for ξ_{min} of less than 1%. For 1 < A < 3, one must add the second series term to maintain an error of less than 1%.

In experiments, objects were predominantly near the mid-plane of the channel, so ξ assumed values that lie between ξ_{min} and ξ_{max}. To further refine the expression for the experimental value of ξ, we adjust Eq. 2 to take into account the radius of the object being deformed, in which case we find that the normalized velocity is almost always close to 1.5 (see Figure 2.1B and Supplementary Material for more details), except for high aspect ratio channels that are seldom used in microfluidics, in part because objects will often be out of focus as a consequence. For simplicity, we retain this value of 1.5 in our subsequent experimental analysis. Thus, the velocity gradient in our device is $\Omega = \xi U/D$, where ξ is expressed analytically as a function of the aspect ratio A = h/w of the device. In the experiments reported here, $\xi \sim 1.5$.

By scaling arguments and analysis of the cross-slot flow field, we can therefore reasonably assume that objects sufficiently close the stagnation point are

deformed by our derived strain rate $\xi U/D$. The results for ξ are derived in the absence of cells or particles. We verified that the size of cells was sufficiently small to avoid perturbations to the flow as evidenced by the small value of the Stokes number Stk ~ $10^{-6} \ll 1$ (see details in Supplementary Results). Our Hele-Shaw simulation results of the cross-slot flow field and reported particle image velocimetry measurements ((Kantsler *et al.*, 2008) Figure S2) indicate that the strain rate is constant in the stagnation point region. According to our Hele-Shaw simulations, for distances smaller than 25% of the channel width away from the stagnation point, the local strain rate is within 95% of the maximum value at the stagnation point (Supplementary Material Figure 2.7).

Having characterized the velocity gradient in the device, we consider the simple case of an isotropic, linearly elastic material deforming in a pure and infinite planar extensional flow. Murata (Murata, 1981) analyzed the general problem of an incompressible elastic sphere deforming in an arbitrary, low Reynolds number flow field in the limit of small deformations ($\varepsilon \ll 1$). From Murata's example solution for the surface of a sphere deforming in planar extensional flow, we obtain the following relation for the strain in this flow field: $\varepsilon = (5\Omega\mu)/(2G)$, where G is the shear modulus and the strain is defined as $\varepsilon = (a-b)/(a+b)$ (Figure 2.1A). Plugging in our expression for the velocity gradient Ω, we find an expression for the strain of an elastic sphere deforming in our cross-slot device:

$$\varepsilon = \frac{a-b}{a+b} = \frac{5}{2}\xi\frac{U}{D}\frac{\mu}{G} \quad \text{(Equation 3)}$$

Extension of the theory to the deformation of a viscoelastic body in a cross-slot device

We next extend the relation to the deformation of a viscoelastic body in planar extensional flow. Because the fluid velocity gradient is uniform in a cross-slot and because the fluid forces exerted on a cell are largely dominated by viscous forces that are proportional to this homogenous velocity gradient, a body moving through the cross-slot's central region ($|\mathbf{x}| \leq D$) will be submitted to viscous stresses proportional to $\tau \sim \mu\xi U/D$, assuming the disturbance to the velocity field due to the presence of the cell is small (see details in Supplementary Results). While for an elastic body, the uniform viscous stresses means an instantaneous and constant deformation, the deformation of viscoelastic bodies such as suspended cells changes with time under loading by a constant stress and depends not only on the force magnitude but also the rate at which the force is applied. One choice of model to capture viscoelastic behavior is the simple two-parameter power law for a time-dependent cell stiffness. This phenomenologic law has been shown to describe cell mechanical behavior for several cell types over a wide range of time scales as measured by several techniques

including optical magnetic twisting cytometry (Fabry *et al.*, 2001; Trepat *et al.*, 2007), atomic force microscopy indentation (Alcaraz *et al.*, 2003), and microfluidic constriction channel traversal (Lange *et al.*, 2015). The power law can be expressed mathematically as follows (Fabry *et al.*, 2001):

$$G(t) = G_0 \left(\frac{t}{t_0} \right)^{-\alpha} \quad \text{(Equation 4)}$$

where t_0 is an arbitrary reference time, G_0 is the value of the shear modulus at time t_0, and the fluidity parameter α describes the dependence of the shear modulus on time. The case of a purely elastic body is recovered by choosing $\alpha = 0$, and a Newtonian fluid corresponds to $\alpha = 1$. For a viscoelastic material with $0 < \alpha < 1$, the power-law model predicts that as the deforming force is applied more quickly (smaller t), the material appears stiffer (larger G(t)). A rigorous implementation of this relaxation modulus G(t)—the viscoelastic, time-dependent analog of the shear modulus G for an elastic material—requires a more complicated stress-strain relationship involving an integral in time. This constitutive law would need to be incorporated into the time-dependent version of the governing equations for the solid undergoing infinitesimal deformations, which are more complicated than the steady-state versions used to derive Eq. 3. In a simplistic approach, we will not explicitly consider the time-dependent modulus G(t) in the governing equations, but rather consider the cell to be an elastic sphere with an 'effective' shear elastic modulus $G(t_{cs})$, where $G(t_{cs})$ is G(t) evaluated at the time-scale t_{cs} of cross-slot deformation. Thus we have taken a phenomenological approach as opposed to a rigorous mechanics derivation by replacing G in Eq. 3 by $G(t_{cs})$. We show below that, despite these simplifications, this power-law adequately describes our own measurements of suspended cells.

We observed the deformation of single cells at the time point nearest to the stagnation point and thus extract the time-dependent shear modulus at a certain time after the start of deformation. By varying the flow rate, we sample a range of deformation times and strain rates. Using our knowledge of the well-defined extensional flow field, we calculate the average time of deformation at a given flow rate experienced by the cells as they travel from the end of the channel towards the stagnation point. This time of deformation is expected to scale with D/U. By symmetry, we considered the upper quadrant of the cross-slot defined by $x > 0$ and $y > 0$. When entering the cross-slot, the body travels at a velocity of the extensional flow field $\mathbf{v} = u\mathbf{i} + v\mathbf{j}$ where $u(x) = -\Omega x$ and $v(y) = \Omega y$. Therefore, choosing $t = 0$ to be the point in time where the body enters the cross-slot region at $|x| = D$ and starts being exposed to the extensional stresses, integration along the streamline yields the x coordinate of cell position to be $x = D \exp(-\Omega t)$. This is equivalent to a time of extensional deformation $t = -1/\Omega \ln(|x/D|)$ for an object that started at $x = D$ at $t = 0$ and is now located at a new $x < D$ after flowing entrained in the extensional flow field. We restrict the analysis to bodies whose centers are located in the region where

x ϵ [0;D/2] and y ϵ [0;D/2], equivalent to our experimental criteria that bodies are imaged close to the stagnation point. The average time of deformation for cells observed in the region x,y ϵ [0, D/2] is therefore:

$$t_{cs} = \frac{-1}{D/2}\int_0^{D/2}\frac{1}{\Omega}\ln\left(\frac{x}{D}\right)dx = (1+\ln(2))/\Omega \qquad \text{(Equation 5)}$$

This equation yields the expected scaling with D/U, apparent when rewritten as t_{cs} = (1+ln(2))D/(ξU). Notwithstanding this result, we note that any other choice of zone is possible; both derivation methods for the normalized velocity ξ and the time spent in the cross-slot t_{cs} would have remained valid and would have just led to different final equations. For instance, choosing the entire cross-slot would have led to t_{cs} = 1/Ω.

This derivation of t_{cs} assumes that the cell travels at the fluid velocity. We performed several particle-tracking measurements and found that, within experimental error, cells traveled close to the expected maximum fluid velocity. Our results are supported by theoretical and simulation results from from Guck and colleagues showing that objects travel at >90% of the maximal fluid velocity when the degree of confinement is r_{cell}/R_{eq} < 0.4 where r_{cell} is the cell diameter and R_{eq} is the equivalent channel radius ((Mietke *et al.*, 2015) Figure 2A). Defining R_{eq} based on hydraulic mean radius of our rectangular channels (R_h = 23 μm), these results predict that cells with diameter r_{cell} < 9.2 μm travel at >90% of the maximal fluid velocity. Thus r_{cell} < 9.2 μm is an upper bound on cell size for the range of applicability of our model. The histograms of cell size presented in Figure 2.7 in the Supplementary Material show that cells measured are below this upper bound with an average cell radius around 7 μm.

Combining Eqs. 3, 4 and 5, we present the following analytical relation that relates the observed body deformations with the cross-slot dimensions, the suspending fluid viscosity, and the applied flow rate via two fitting parameters, α and G_0, that describe the body's viscoelastic behavior:

$$\varepsilon = \frac{5}{2}\frac{\mu}{G_0}\left(\frac{1+\ln(2)}{t_0}\right)^{\alpha}\left(\frac{\xi U}{D}\right)^{1-\alpha} \qquad \text{(Equation 6)}$$

G_0 corresponds to the apparent stiffness for a given time t_0. In our analysis of cell deformation, we will choose t_0 = 5 ms, the average t_{cs} across all cell experiments, as a time scale that is naturally suited for the apparent stiffness.

Experimental validation of the deformation of an elastic body in a cross-slot device

In order to experimentally assess the validity and accuracy of the model, we performed studies on a model elastic body whose mechanical properties had been

previously determined using other systems. Our theory required that this body be initially spherical and that it deforms at low Reynolds number. We chose Sephadex G200 cross-linked dextran beads with diameters ranging from 40 to 100 μm, which are the most deformable of all commercially available Sephadex beads due to their large porosity. These particles are spherical in a stress-free state and deformed in cross-slot experiments operated at low Reynolds number ($0.001 < Re < 0.1$). Our experimental system required that the average flow velocity U be less than ~0.18 m/s, as velocities above this value precluded accurate tracking of deformations.

We introduced Sephadex G200 beads into our cross-slot device and observed deformations in the vicinity of the stagnation point (Figure 2.2A). Since with the employed magnification, a Sephadex bead is typically 50 to 100 pixels in diameter, the lowest strains (engineering strains) detectable for an individual Sephadex is of the order of 1% (the fitting of an ellipse rounds up or down to the nearest pixel). By employing solutions of varying viscosities (105, 179, and 201 mPa·s) and flow rates (2.5–40 mL/hr), we sampled a wide range of strain rates ($\xi U/D \sim 65–1300\ s^{-1}$). As predicted by Eq. 3, the mean particle deformation was linearly related to the applied stress, with a shear modulus (slope) of $G = 8.6 \pm 0.5$ kPa (Figure 2.2B).

We then validated these stiffness measurements by performing micropipette aspiration experiments on the same Sephadex G200 beads in the same suspending PEG/PBS medium (Figure 2.2C). Application of linear elasticity theory (Theret *et al.*, 1988) to relate the entry length of the dextran beads inside the micropipette with the aspiration pressure yielded shear moduli of $G_{asp} = 6.4 \pm 0.2$ kPa. This is in reasonable agreement with our cross-slot measurement and in order-of-magnitude agreement with previous measurements by osmotic deswelling (Edmond *et al.*, 1968) and suspension rheology (Evans and Lips, 1990) (Figure 2.2D). Microscale mechanical measurements are expected to be more sensitive than bulk measurements to microscopic structural inhomogeneities, such as defects or variations in cross-linking density (Shin *et al.*, 2004). This means that measured values are quite sensitive to the method of force application. For instance, localized application of force (aspirate one region of particle in MPA) could be expected to give different results than more homogenous applied forces (elongation in a uniform velocity gradient in cross-slot microfluidic device) that may present a more averaged response that masks microparticle structural inhomogeneity. Furthermore, each method makes simplifying assumptions in order to extract material properties from primary measurements such as deformation, thereby introducing systematic error that is not included in reported measurement uncertainty, typically a population standard deviation or standard error of the mean.

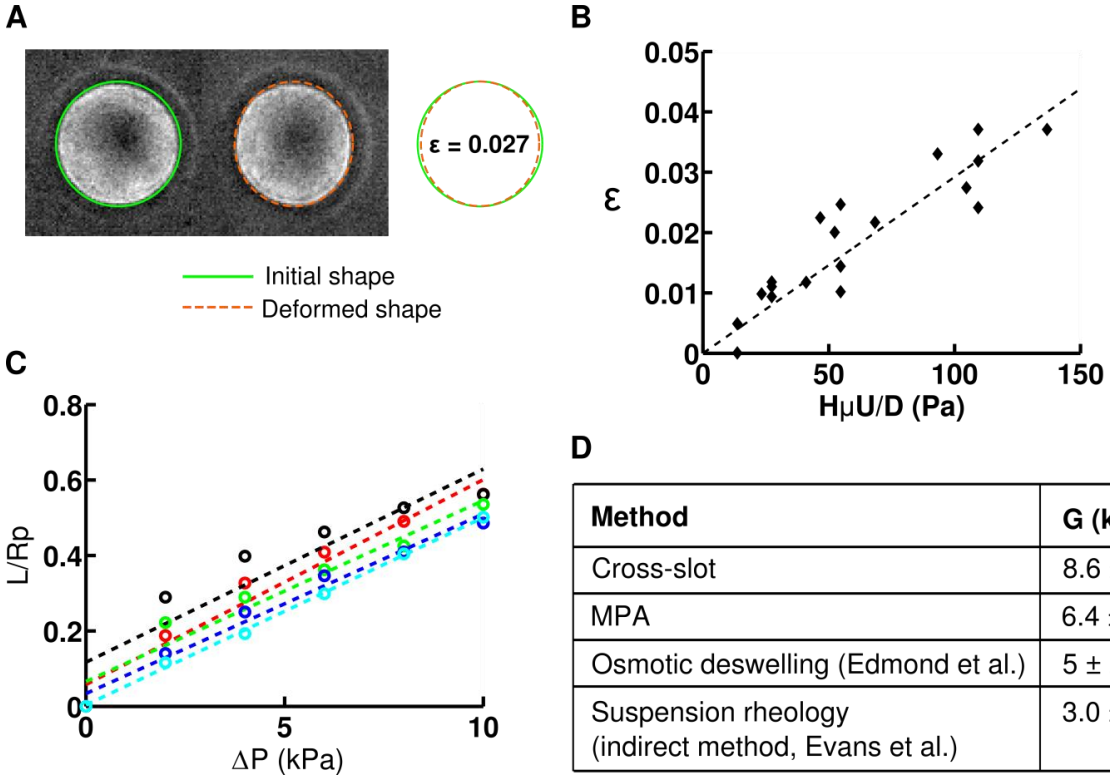

Method	G (kPa)
Cross-slot	8.6 ± 0.5
MPA	6.4 ± 0.2
Osmotic deswelling (Edmond et al.)	5 ± 2
Suspension rheology (indirect method, Evans et al.)	3.0 ± 0.4

FIGURE 2.2: Validation of cross-slot mechanical measurements with cross-linked dextran hydrogel particles. (A) Time-lapse of a Sephadex G200 cross-linked dextran particle stretching in extensional flow as it passes through the stagnation point region. The shear modulus is extracted from the observed deformation. Cross-slot dimensions are 400 μm wide and 200 μm deep. The strain rate is $\xi U/D \sim 520\ s^{-1}$ at 20 mL/hr flow rate. Right: Overlay of the ellipses manually fitted to images of the dextran particle at the entrance of the cross-slot region and at the location closest to the stagnation point. The deformation was chosen to be an average case of all observed deformations.(B) Deformation of Sephadex G200 beads as a function of the applied stress. Suspending fluids with three viscosities were used, μ = 105 mPa·s, 179 mPa·s and 201 mPa·s. A linear regression of $\varepsilon = 5\xi\mu U/(2GD)$ provides the shear modulus of G = 8.6 ± 0.5 kPa. Reported uncertainties of our measurements are the standard errors of the mean values of the population of dextran beads. (C) Micropipette aspiration of Sephadex G200 beads. The entry length L is normalized by the micropipette radius R_P and plotted as a function of the applied pressure ΔP. Each color represents a different bead (n = 5 beads), and the shear modulus is inversely proportional to the slope. (D) Comparison of shear modulus values obtained with our cross-slot measurements, our micropipette aspiration (MPA) measurements, and previously published values based on osmotic deswelling (Edmond *et al.*, 1968) and suspension rheology (Evans and Lips, 1990).

Measuring the viscoelastic properties of 3T3 and GBM TICs

Having validated our analysis and experimental platform, we progressed to measuring mechanical properties of living cells. For proof-of-principle studies, we focused on NIH 3T3 fibroblasts, which have been mechanically characterized by AFM (Rotsch *et al.*, 1999; Solon *et al.*, 2007), optical stretching (Wottawah *et al.*, 2005; Chan *et al.*, 2015), and MPA (Zhou *et al.*, 2010). To explore the potential of our cross-slot device for novel discovery, we also characterized GBM TICs, a stem-like subpopulation of GBM tumors thought to drive tumor initiation, recurrence and therapeutic resistance (Galli *et al.*, 2004; Bao *et al.*, 2006; Deleyrolle *et al.*, 2011). Importantly, manipulation of mechanics and mechanotransductive signaling in GBM TICs was recently shown to significantly reduce tissue invasion and extend survival (Wong *et al.*, 2015).

Our model's assumption that the deforming body is initially spherical is a reasonable approximation for cells in suspension in general (Guck *et al.*, 2005), and for circulating white blood cells in particular (Schmid-Schönbein *et al.*, 1980; Ronald *et al.*, 2001). For a subset of cells, we measured a deformation (mean ± standard error of the mean) of $\varepsilon = 0.0004 \pm 0.004$ (n = 21) and $\varepsilon = 0.007 \pm 0.003$ (n = 28) for 3T3 and GBM TICs, respectively, before entry into the central region of the cross-slot (each sample set taken from two separate experiments on two different days). As another measure of cell sphericity, we also evaluated cell circularity index, defined as $c = 4\pi A/(P^2)$ where A the cell area and P the cell perimeter. (A value of c = 1 indicates a perfect circle while a value of c = 0 indicates a line.) From the ellipses manually fitted to the same subset of cells, we found $c = 0.998 \pm 0.001$ and $c = 0.998 \pm 0.001$ for 3T3 and GBM TICs, respectively, showing that cells are spherical before entering the cross-slot central region.

In separate experiments, we infused both cell types through the device at various flow rates (50–1400 μL/hr) that produce a wide range of strain rates ($\xi U/D \sim 280–6800\ s^{-1}$) and imaged cellular deformations at the stagnation point as with the Sephadex particles (Figure 2.3A). We found that the deformation agreed well with the power-law model in Eq. 6, as demonstrated by the linearity of the log-log plots of cell strain ε vs. cross-slot velocity gradient $\xi U/D$ (Figure 2.4B and 2.4C). This relationship continued to hold when we independently varied cross-slot width (w = 2D), fluid viscosity (μ), and flow rate (determines average flow velocity U = Q/A), which are the three tunable parameters in the power-law model (Figure 2.3B).

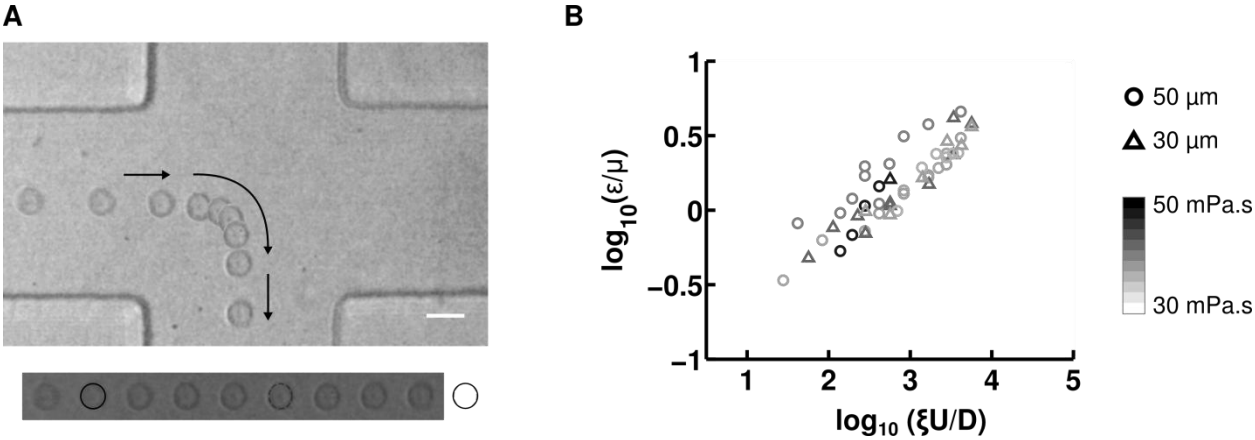

FIGURE 2.3: Measurement of cellular viscoelastic properties. (A) Time-lapse images of a 3T3 fibroblast stretching in extensional flow as it passes through the stagnation point region. Arrows denote the direction of movement. Viscoelastic power-law constitutive model parameters are extracted from the observed deformation. Cross-slot dimensions are 100 μm wide, 30 μm deep and the strain rate is $\xi U/D \sim 1690\ s^{-1}$ at 500 μL/hr flow rate. The time between images 0.5 ms, and the scale bar is 20 μm. We can observe that cell deformation increases as cells pass through the central region of the cross-slot, as is further detailed in Figure 2.10 in the Supplementary Material. (B) Control TIC cross-slot deformation at various flow rates in devices of varying dimensions and for different suspending fluid viscosities. Each data point represents a separate experimental condition, with $10 \leq n \leq 30$ fitted for the reported average deformation. Marker color indicates fluid viscosity μ using a grey scale (from white: 30 mPa·s to black: 50 mPa·s) while pattern indicates cross-slot half-width D (triangle: 35 μm, circle: 50 μm). Flow rates varied between 10 μL/hr and 1000 μL/hr. Height was kept constant at 30 μm.

The power law relationship in Eq. 6 predicts that a log-log plot of viscosity-normalized strain (ε/μ) vs strain rate (ξU/D) would be linear and may be fitted to extract the cellular shear modulus (G) and fluidity parameter (α). Accordingly, for 3T3 cells, we obtained a shear modulus of $G_0(t_0) = 0.59 \pm 0.05$ kPa (Figure 2.5) for $t_0 = 5$ ms. Previous measurements on suspended 3T3 cells using optical stretchers yielded shear moduli of ~70-80 Pa ((Chan *et al.*, 2015) Figures 2A and 3B) and 100 ± 10 Pa ((Wottawah *et al.*, 2005) Figure 2) for a deformation time scale of t = 200 ms. In turn, if we set our time scale t_0 to 200 ms in our cross-slot experiment, we find that G_0(200 ms) = 101 ± 8 Pa, which is very consistent with the values found using an optical stretcher. For GBM TICs, we measured a stiffness of $G_0(t_0) = 0.44 \pm 0.03$ kPa. Again, this value is in close proximity to previous AFM measurements on this same cell line that found values of 0.8-0.9 kPa (43). The measured cell fluidity parameter was similar for both cell types: $\alpha = 0.48 \pm 0.04$ for 3T3 cells and 0.50 ± 0.04 for TICs.

We next explored the sensitivity of the measurement to perturbations of cytoskeletal assembly and mechanics. For our softening studies, we used CytoD (10 μM), which has been previously shown to disrupt the 3T3 actin cytoskeleton (Ribeiro *et al.*, 1997; Ailenberg and Silverman, 2003). As expected, inhibition of actin polymerization by treatment with CytoD increased cellular deformation at all strain rates and reduced shear modulus (0.40 ± 0.05 kPa for 3T3 cells and 0.22 ± 0.04 for TICs). Those values are statistically significantly different from the control case, with $p \leq 0.01$ between all groups (see Table 2.2 in the Supplementary Material for individual p-values). Conversely, covalent crosslinking of cells with PFA increased the shear modulus (0.93 ± 0.08 kPa for 3T3 cells and 0.73 ± 0.05 for TICs). Here also, the values were statistically different from the control case, with $p \leq 0.01$ between all groups. Despite these changes in stiffness, neither CytoD nor PFA produced statistically significant changes in fluidity for either cell type.

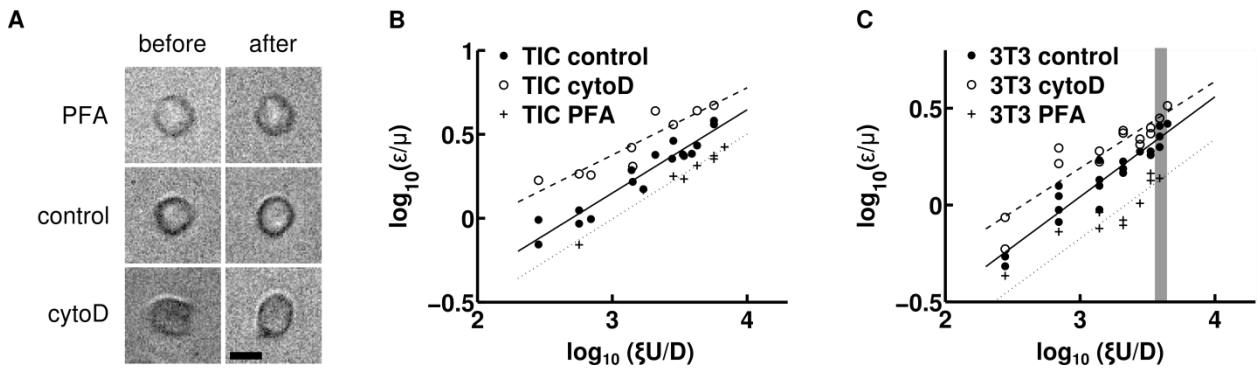

FIGURE 2.4: Softening and stiffening effects of drugs that affect the cytoskeleton on TIC and 3T3 deformations measured in the cross-slot. (A) Images of 3T3 fibroblasts before (left) and after (right) deformation by the extensional flow in the cross-slot. We took a cell from all three cases: incubation in PFA (top), control (middle) and incubation in cytochalasin D (bottom). In all three cases, $\xi U/D \sim 4100\ s^{-1}$. Cells were chosen to be representative of the average deformation at this strain rate. The scale bar is 10 μm (B, C). Linear regression of the log-log plots based on $\varepsilon = 5\xi\mu U/2GD$ (— solid lines control, -- dashed cytoD, … dotted PFA) yield the cell power-law material properties under control and drug conditions: the fluidity parameter α is obtained from the slope and the shear modulus G_0 at a specified time scale $t_0 = 5$ ms is obtained from the intercept. The cross-slot deformation of both GBM TICs (B) and 3T3 fibroblast cells (C) are consistent with the power-law model as indicated by the linearity of the log-log plots. Each data point represents a separate experimental condition (i.e. $\xi U/D$ strain rate and drug condition), with $10 \leq n \leq 30$ cells fitted for the reported average deformation. In panel (C), the grey zone corresponds to the strain rate chosen for the cells in panel (A). For clarity, error bars reflecting the uncertainty in strain measurements (standard error of the mean) is omitted. See in Supplementary Material Figure 2.11 for versions of (B,C) with vertical error bars and

Tables 2.3 and 2.4 in the Supplementary Material for the cross-slot extensional strain rate (ξU/D), strain (ε) and strain uncertainty for each point plotted in (B, C).

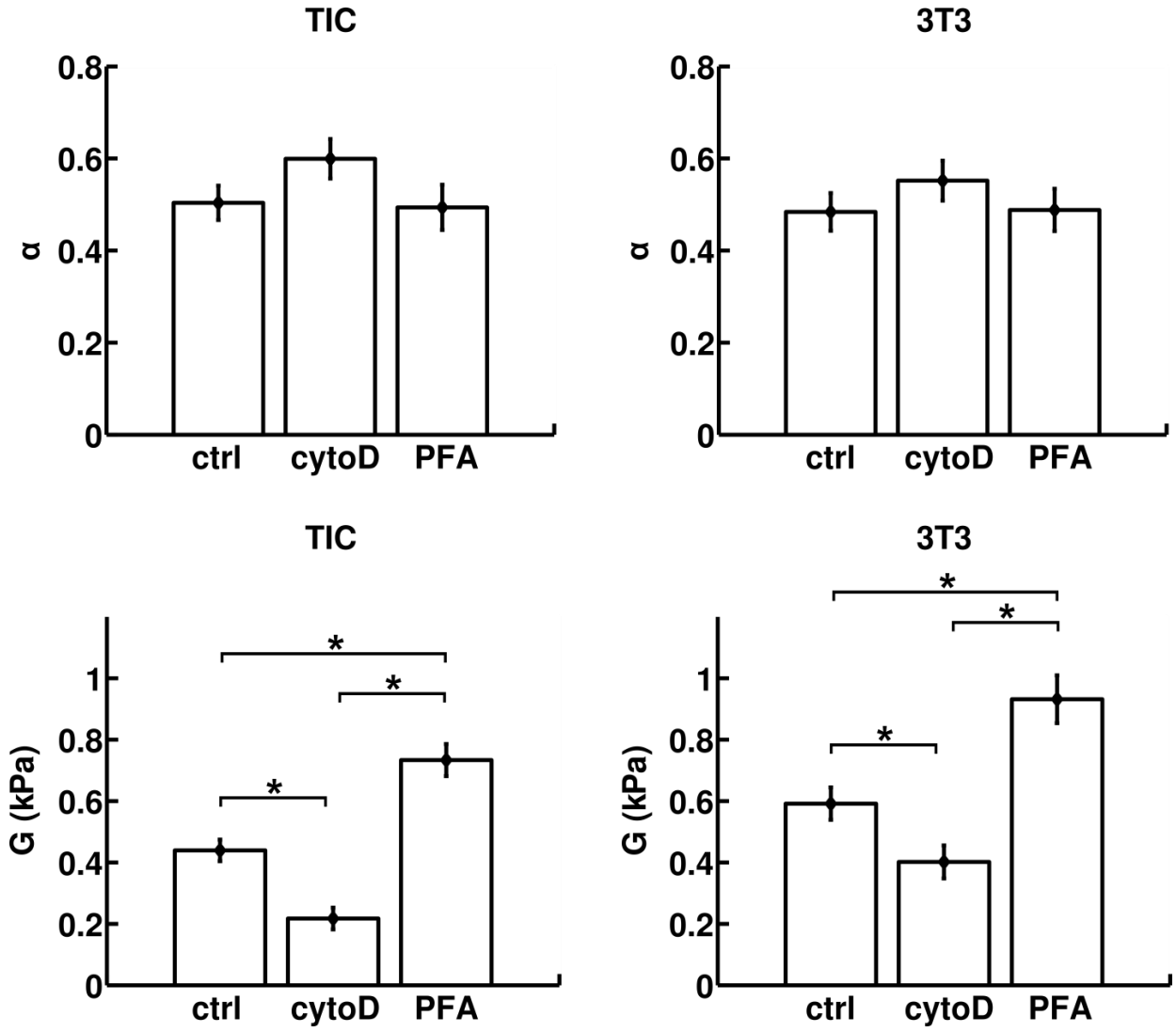

FIGURE 2.5: Power-law material parameters, the fluidity parameter α and the shear modulus $G = G_0(t_0)$, evaluated at the average time scale of cell cross-slot deformation t_0 = 5 ms for GBM TICs and 3T3 fibroblasts under different pharmacological interventions. The values of α and G are determined by linear regression and the error bars are derived from analysis of covariance (ANOCOVA). While the fluidity of the cells does not change appreciably, CytoD significantly softens and PFA significantly stiffens both cell types (*$p \leq 0.01$).

Discussion

Cellular mechanical properties serve as a powerful and promising label-free marker for gaining insight into molecular changes within the cell or characterizing different cellular states for potential diagnostic information. Recent advances in microfluidic technology have allowed the high-throughput measurement of cellular mechanical properties with single cell resolution. Such platforms are strongly positioned to detect potential differences in rare subpopulations of cells that may drive disease progression, which would otherwise be masked in bulk- or population-based mechanical measurements. In order to improve on previous studies, we have developed an analytical equation for a simple PDMS-based microfluidic platform to measure and quantify cellular mechanical properties. The strength of our model lies in its simplicity, with a single equation that uses easily obtainable parameters, as well as its adaptability, as it can be readily extended to account for other viscoelastic material laws.

It is interesting to note that while at least one previous study (Gossett *et al.*, 2012) has successfully captured changes in stiffness and correlated these differences to phenotype, it did not report changes in stiffness when cells were treated with cytoskeletal depolymerization drugs. The authors hypothesized that this may be because the high strain rates in their system ($\xi U/D \sim 2 \cdot 10^5\ s^{-1}$) effectively fluidize the cytoskeleton and are instead dominated by the viscous properties of the cytosol and chromatin. Consistent with this explanation, the lower strain rates employed in our device ($300 \leq \xi U/D \leq 7000\ s^{-1}$) and many other single cell platforms (e.g. optical tweezers) would facilitate measurement of cytoskeletal mechanics. Key to achieving this regime is our use of high-viscosity fluid medium ($\mu \sim 40$ mPa·s), which enabled us to achieve similar stresses and cellular deformations at much lower strain rates similar to Guck and colleagues who used a viscosified suspending solution of $\mu = 15$ mPa·s (Mietke *et al.*, 2015). Another factor that may contribute to the ability to detect the effects of cytoskeletal depolymerization drugs is the magnitude of cell strain. A different high-throughput device from Di Carlo and colleagues (Dudani *et al.*, 2013) extended cells asymmetrically with pinching sheathing flows so that the leading edge of the cell experienced higher shearing stresses than the trailing edge operated at similar strain rates ($\xi U/D \sim 1 \cdot 10^5\ s^{-1}$, though a less accurate estimate because the flow is not pure extensional flow) as their cross-slot device in (Gossett *et al.*, 2012) but deformed the cells less. The high-strain-rate cross-slot device in (Gossett *et al.*, 2012) deformed cells to strains of $\varepsilon \sim 0.32$ for control and depolymerization drug treated cells while the pinched-flow stretching device in (Dudani *et al.*, 2013) deformed control cells to $\varepsilon \sim 0.15$ and treated cells to $\varepsilon \sim 0.2 - 0.3$. Our high-viscosity cross-slot system only deformed cells up to a maximum $\varepsilon = 0.18$, a relatively small strain. Consequently, we were able to detect the effect of both softening (CytoD) and stiffening (PFA) interventions in two different cell lines. Moreover, these interventions did *not* significantly change cell fluidity, further consistent with the notion that the strain rates we imposed were insufficient to fluidize the cytoskeleton.

Although our stiffness measurements of both the Sephadex beads and 3T3 cells are of the same order of magnitude as previously published results, there is still a slight variation among all the values, as well as among previously published results. These variations may be due to differences in measurement modalities across these reports. While the cross-slot platform measures the deformation on a 1-10 ms time scale, the other methods employed (AFM, MPA, osmotic de-swelling and suspension rheology) are performed on a 1-10 second time scale. Additionally, previous measurements have shown that Sephadex bead stiffness increases by ~30% when decreasing the deformation time scale from 10^4 to 10 seconds (Evans and Lips, 1990). Hence, we speculate that when decreasing the time scale further from 1 second to 1-10 ms, one would expect some moderate stiffening to occur.

Similarly, for 3T3 cells, reduced time scales unsurprisingly seem to lead to higher apparent stiffnesses. Indeed, in another study, a millisecond-time scale platform measured higher cellular stiffness values than did AFM, which typically involves measurements on the time scale of seconds (Moeendarbary *et al.*, 2013). In the future, it would be valuable to measure bead or cellular mechanical properties across various time scales within the same device. These studies would clarify the exact relationship between the time scale of measurement and the resulting values. Modulation of the viscosity of the suspension medium within our device, as well as the flow rate and the device dimensions, may offer the opportunity to systematically explore these time scales.

Conclusion

We have developed an experimental and analytical strategy to measure cellular mechanical properties based on deformations within a microfluidic cross-slot device. By creating measurement conditions that reduce strain rates and developing an analytical model, we successfully detected perturbations to cytoskeletal assembly and mechanics, which is a significant innovation for cross-slot-based systems and enables comparison with more traditional single-cell mechanics measurements. We envision that this technology will prove valuable for the rapid mechanical characterization of living cells in suspension, thereby accelerating fundamental studies of cellular mechanics and establishing a platform for future diagnostic technologies.

Author contributions

S.J.M., S.K., L.G., J.B.D. and J.G.L. designed research; L.G., J.B.D. and J.G.L. performed research; A.I.B., J.H., S.J.M. and S.K. supervised research; L.G., J.B.D. and J.G.L. analyzed data; all authors wrote the manuscript.

More specifically, L.G. participated in about half of the cell deformation experiments in cross-slot, performed the micropipette aspiration of Sephadex beads, helped analyze the cell deformation data (one of the two users compared in the supplementary material), and led the theoretical modeling effort.

Acknowledgements

The authors declare no conflict of interest. Lionel Guillou is supported by a Gaspard Monge fellowship from the Ecole Polytechnique. This material is based upon work supported by the National Science Foundation Postdoctoral Research Fellowship in Biology under Grant No. 1308051 to J.B.D. The work was also supported by grants from the National Science Foundation (105539 to S.K., 1066334 to S.J.M.), the National Institutes of Health (1R01NS074831, 1R21CA174573, 1R21EB016359 to S.K., T32GM098218 training grant support to J.G.L.), the W.M. Keck Foundation (Science and Engineering Grant to S.K.), the Cancer Research Coordinating Committee (fellowship to J.G.L), and a permanent endowment in cardiovascular cellular engineering from the AXA Research Fund.

2.3 SUPPLEMENTARY MATERIAL

Derivation of the normalized entrance velocity ξ that best matches experimental measurements

Experimental values for ξ will lie between ξ_{min} and ξ_{max}, provided that we restrict our analysis to objects that are near the center of the channel. In such instances, the objects will be spread in the vertical axis between the heights r and h-r, where r is the radius of the spherical object. Indeed, it is not possible for a spherical object's center to get closer to the channel walls than r. We show an example in Figure 2.1B (dotted black line) where r = h/16, corresponding to an experimental case in which the channel height is 200 μm and the object's radius is at least 25 μm. To obtain those ξ values, we take the mean velocity along the heights considered using the velocity profile provided in (Lee *et al.*, 2007). We find using these formulas that for our devices and objects (both dextran beads and cells), the analytical values for ξ are close to 1.5 (between 1.48 and 1.62). We also experimentally measure object velocities in the cross-slot, and find that they are about 1.5 times the mean velocity in the channel. Therefore, for simplicity, we use the value ξ = 1.5 in our experimental analysis.

Cells do not perturb the flow sufficiently to modify the strain rate in the device

For the calculations of strain rate in the cross-slot, it is assumed that the flow field is unaffected by suspended cells. To determine if the presence of cells in the fluid flow affects the fluid velocity and gradients, we inspect the Stokes number of the suspended cells, which is the ratio of particle momentum relaxation time (i.e. exponential decay of particle velocity due to drag) to the characteristic time scale of the continuum fluid phase. For neutrally buoyant particles with a small particle Reynolds number ($Re_p = Re(d_p^2/D^2) = \varrho U d_p^2/(\mu D) < 0.013$), the momentum relaxation time scale is independent of density and can be expressed as $\tau_{mom} = d_p^2/(18\nu_c)$ where $\nu_c = \mu_c/\varrho_c$ is the kinematic viscosity of the continuum fluid phase and d_p the diameter of the dispersed particles. Cells with a typical diameter of 10 μm and suspended in 20% w/v PEG20000/PBS (ϱ_c ~ 1040 kg/m^3, μ_c ~ 0.04 Pa·s) thus have a momentum relaxation time of $\tau_{mom} = 1.4\cdot10^{-7}$ seconds. The characteristic flow time scale is taken to be the inverse of the velocity gradient in the cross-slot region, Ω. The smallest strain rate in our cell cross-slot experiments is Ω = 34 s^{-1}, leading to a maximum characteristic flow field time scale of $\tau_{flow} = 2.9\cdot10^{-2}$ seconds. Thus, the Stokes number for our cell cross-slot experiments $Stk = \tau_{mom}/\tau_{flow} = 5\cdot10^{-6} << 1$. Thus, the suspended cells follow the flow field streamlines instantaneously, and the strain rate in a cross-slot device Ω is undisturbed by the presence of the cells.

Uncertainty in cell strain measurements: User bias and small strains

We verified that the manual strain measurement was accurate within 2% strain by having different individuals analyze the same set of cells and set of cross-slot experiments (Supplementary Material Figure 2.8). Observed cell strains were small at the lower strain rates, so that the difference in length of the major and minor axes was close to 1 pixel. We mitigated the limitation of resolving small deformations by measuring several cells per data point ($10 \leq n \leq 30$), which resulted in a clear trend of increasing strain with increasing strain rate for both cell types and all pharmacological conditions.

Viscous forces acting on a virtual spherical or ellipsoidal surface in planar extensional flow

The suspending fluid that is considered to be a Newtonian fluid has a Cauchy stress tensor of the form $\mathbf{T} = -\text{grad}(p) + \mu(\text{grad}(\mathbf{v}) + \text{grad}(\mathbf{v})^T)$ where p is the fluid pressure, μ the dynamic viscosity, and $\mathbf{v}$ the fluid velocity. Assume that the perturbations to the fluid velocity field due the presence of the cell are small, which is reasonable for our system as argued above. Due to the uniform velocity gradient in planar extensional flow $\text{grad}(\mathbf{v}) = [-\Omega\ 0\ 0;\ 0\ \Omega\ 0;\ 0\ 0\ 0]$ where Ω is the extensional strain rate, the viscous contribution to the fluid stress tensor is independent of location in the extensional flow field. Therefore, the force from the fluid (traction vector $\mathbf{t} = \mathbf{Tn}$) acting on the cell surface only depends on the local outward unit normal vector $\mathbf{n}$ of the cell surface. The viscous force vectors on the equator of a sphere and ellipsoid located anywhere in planar extensional flow, not just the stagnation point, are shown in Supplementary Material Figure 2.12. The magnitude of each fluid force vector is proportional to $\mu\Omega$ and the z-component of the normal vector.

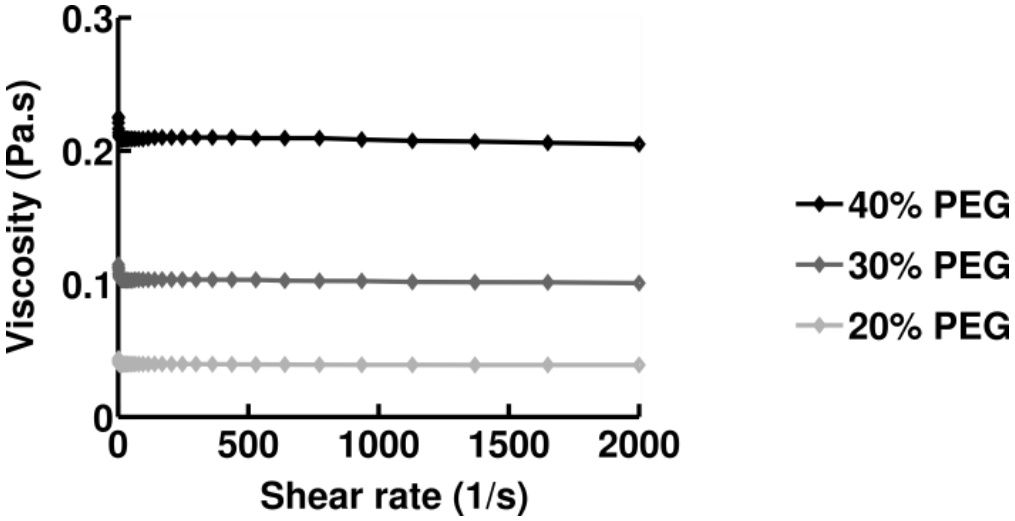

FIGURE 2.6: Macroscale rheologic measurements of PEG20000/PBS solutions used in cell cross-slot deformation experiments. Black line indicates 40% w/v PEG20000 in PBS, dark grey line indicates 30% w/v and light grey line 20% w/v. After initial transients at the experiment start-up, the viscosity is constant for strain rates of 1–2000 s^{-1} indicating the fluid is Newtonian. The reported viscosities for each batch are the average of 2 independent rheometry measurements.

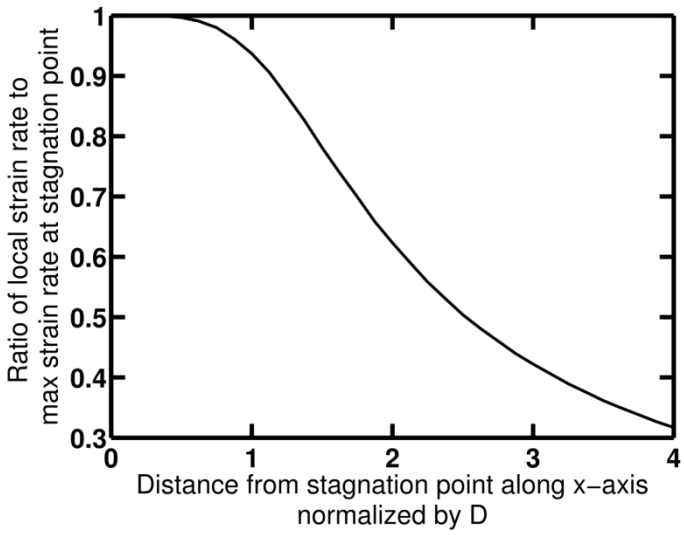

FIGURE 2.7: Ratio of local strain rate $\dot{\varepsilon}$ = du/dx to maximum strain rate at the cross-slot stagnation point as a function of the distance along the central inlet streamline as predicted in Hele-Shaw simulations. This streamline corresponds to the x-axis (cf. Figure 2.1A). The strain rate is approximately constant within a distance D (the channel half width) of the stagnation point, an indication that the flow field is indeed hyperbolic extensional flow. Thus, objects in the stagnation point region experience a constant strain rate.

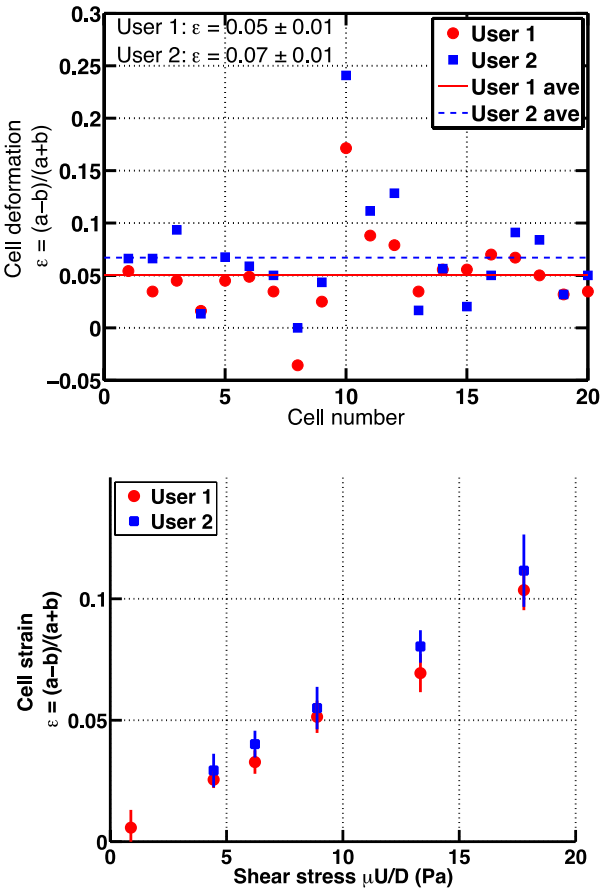

FIGURE 2.8: Impact of user bias on cell strain measurements is negligible. Left: Independent strain measurements performed by two users of a set of individual cells from a single cross-slot experiment (TIC control case, flow rate 300 μL/hr). Right: Independent cell strain measurements for several flow rates for control TICs by two users. Each marker is the average strain of n ≥ 10 cells and the error bars indicate ± standard error of the mean. Users independently selected qualifying cells to analyze and manually fitted ellipses in order to measure cell strain. User 2 systematically measures larger cell strain but agrees closely with User 1. For the results reported in the manuscript, User 1 performed most of the measurements.

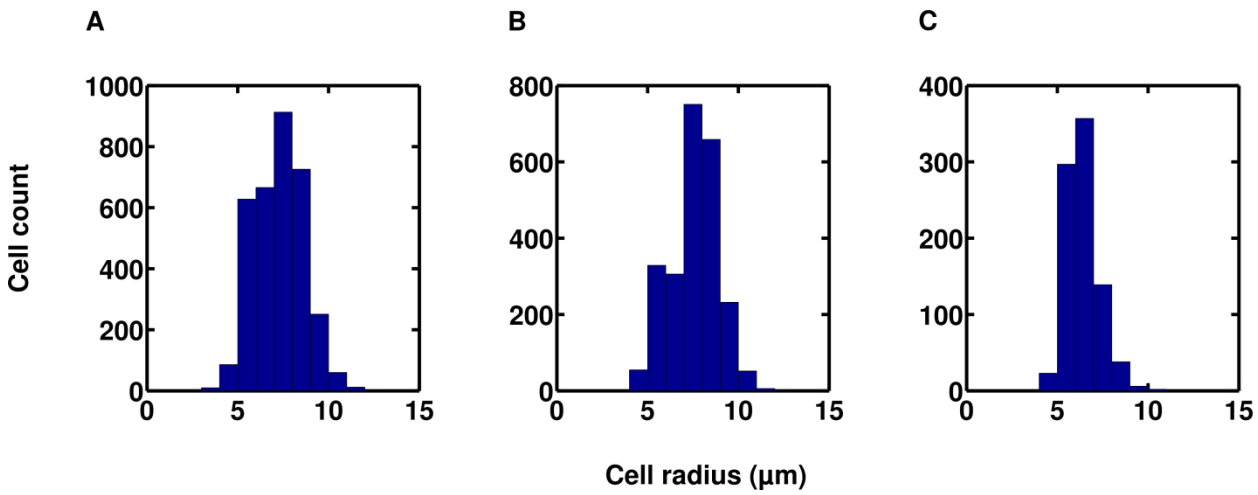

FIGURE 2.9: Histogram of cell radii. All analyzed cells are included. (A) Both TIC and 3T3 cells, in both control and drug conditions, are included (n = 3,357 cells). (B) Only TICs in control case are included (n = 1,288 cells). (C) Only 3T3 cells in control case are included (n = 321 cells).

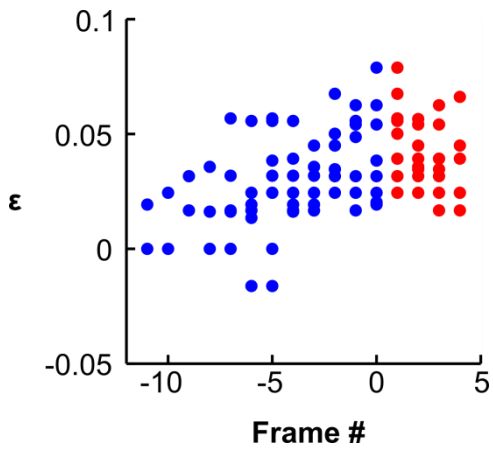

FIGURE 2.10: Cell deformation increases as they enter the cross-slot's central region $|\mathbf{x}| \leq D$ (blue dots), up until the point where they leave the central region and the deformation starts decreasing (red dots). Frame 0 marks the entry of the central region of the cross-slot. Cell deformation was tracked from the moment they entered the central region. Frame rate is approximately 40 fps. The cells in this example are 3T3 cells in control case at a flow rate of 250 μl/hr, with n = 8 cells tracked in this example.

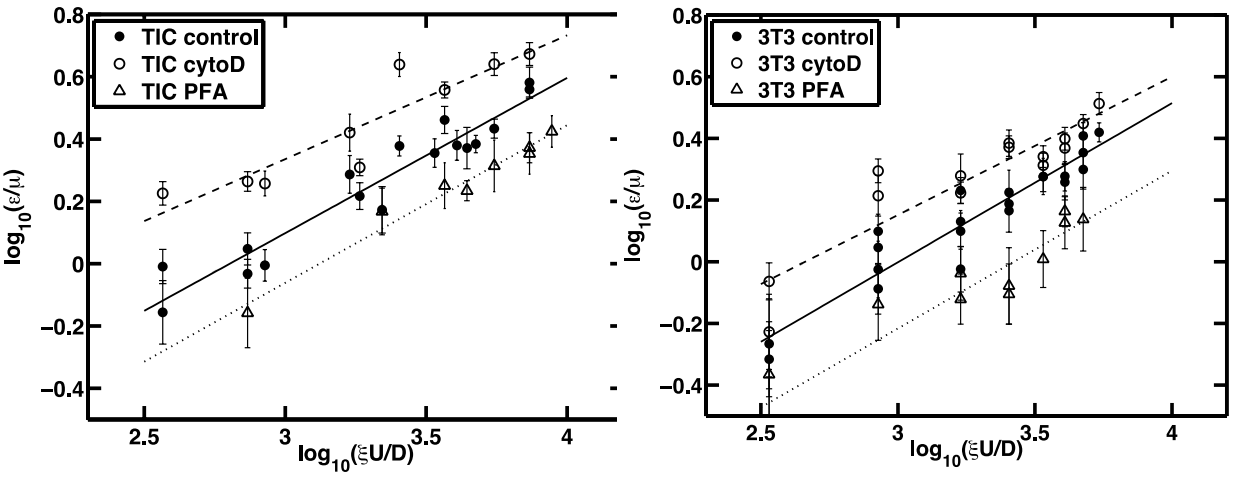

FIGURE 2.11: Cell cross-slot measurements including error bars reflecting the uncertainty in strain measurements (standard error of the mean). Error propagation (Bevington and Robinson, 2003) was used to plot these uncertainties for the quantity $\log(\varepsilon/\mu)$: $\sigma_{\log(\varepsilon/\mu)} = [d(\log(\varepsilon/\mu))/d\varepsilon]^2 \cdot (\sigma_\varepsilon)^2 = \sigma_\varepsilon/\varepsilon$.

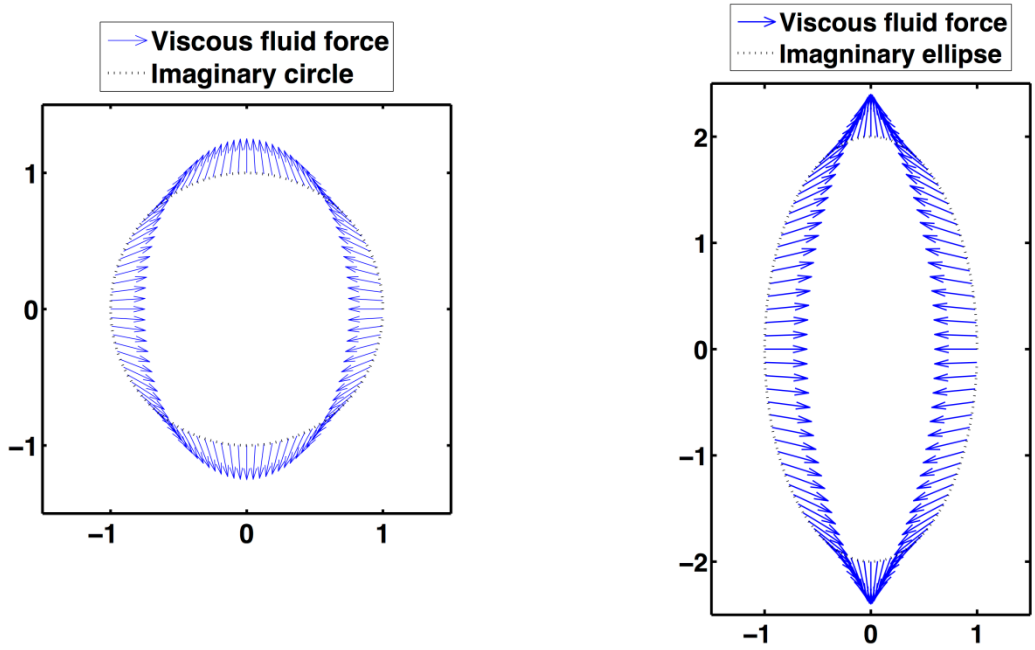

FIGURE 2.12: Viscous fluid forces acting on the surface of a sphere (left) and ellipsoid (right) in planar extensional flow that is unperturbed by the presence of the object. The force vectors in the x-y plane at the equator have a uniform magnitude equal to $2\mu\Omega$ (μ fluid viscosity, Ω extensional strain rate) and different directions.

Cell Type	μ	W	U	Re = ϱUD/μ	ξU/D	n	ε = (a-b)/(a+b)
	[mPa·s]	[μm]	[mm/s]		s^{-1}		
TIC	36 ≤ μ ≤ 42	w = 70, 100	7 ≤ U ≤ 159	0.0057 ≤ Re ≤ 0.19	283 ≤ ξU/D ≤ 6800	10 ≤ n ≤ 27	0.029 ≤ ε ≤ 0.18
3T3	37.5 ≤ μ ≤ 38.3	w = 100	9 ≤ U ≤ 148	0.013 ≤ Re ≤ 0.20	278 ≤ ξU/D ≤ 4440	10 ≤ n ≤ 30	0.009 ≤ ε ≤ 0.12

TABLE 2.1: Range for various experimental parameters over all experimental conditions tested for the glioblastoma tumor initiating cells (TIC) and 3T3 fibroblast cells. U = Q/(h·w) is the average flow velocity in the channels based on the specified flow rate Q and channel cross-sectional dimensions (width w = 2·D, height h = 30 μm). The suspending fluid viscosity μ was measured before each set of experiments (sample measurements Supplementary Material Figure 2.6). The flow Reynolds number Re is based on microchannel dimensions, fluid properties, and flow rate. n is the number of cells used to determine the average strain ε that makes up each data point in Figure 2.4(B,C).

Comparison Groups	3T3 p-value	TIC p-value
Control vs. CytoD	0.012	0.0002
Control vs. PFA	0.0094	0.0015
CytoD vs. PFA	0.0004	$8.5 \cdot 10^{-6}$

TABLE 2.2: Statistical significance (p-values) of multiple regression analysis of covariance.

TIC	Fluid viscosity μ	Channel wideth w = 2·D	Mean flow velocity U	Flow Reynolds number Re = ρUD/μ	Extensional strain rate ξU/D	Number of cells n	Average strain ε = (a-b)/(a+b)	Strain uncertainty σ_ε
	mPa·s	μm	mm/s		s^{-1}			std error of mean
TIC CONTROL								
Day 1	42	70	6.61	0.0057	283	14	0.029	0.007
			13.23	0.0115	567	15	0.047	0.006
			39.68	0.0344	1701	12	0.06	0.01
			79.37	0.0688	3401	16	0.10	0.02
			132.28	0.1146	5669	15	0.16	0.02
Day 2	36	100	23.15	0.0334	694	11	0.036	0.004
			46.30	0.0669	1389	15	0.07	0.01
			69.44	0.1003	2083	15	0.086	0.006
			92.59	0.1337	2778	15	0.082	0.009
			111.11	0.1605	3333	14	0.09	0.01
			129.63	0.1872	3889	11	0.087	0.006
Day 3	37.6	70	6.61	0.0064	283	12	0.037	0.005
			13.23	0.0128	567	18	0.035	0.004
			33.07	0.0320	1417	20	0.062	0.006
			66.14	0.0640	2834	20	0.11	0.01
			99.21	0.0960	4252	27	0.102	0.007
			132.28	0.1281	5669	22	0.136	0.008
TIC CYTOCHALASIN D								
Day 2	36	100	23.15	0.0334	694	18	0.065	0.006
			46.30	0.0669	1389	20	0.09	0.01
			69.44	0.1003	2083	15	0.16	0.01
Day 3	37.6	70	6.61	0.0064	283	14	0.063	0.005
			13.23	0.0128	567	16	0.069	0.005
			33.07	0.0320	1417	20	0.077	0.005
			66.14	0.0640	2834	20	0.136	0.008
			99.21	0.0960	4252	20	0.16	0.01
			132.28	0.1281	5669	20	0.18	0.02
TIC PFA								
Day 1	42	70	13.23	0.0115	567	20	0.029	0.007
			39.68	0.0344	1701	19	0.06	0.01
			79.37	0.0688	3401	18	0.072	0.005
			132.28	0.1146	5669	10	0.10	0.01
Day 3	37.6	70	66.14	0.0640	2834	20	0.07	0.01
			99.21	0.0960	4252	20	0.08	0.01
			132.28	0.1281	5669	20	0.08	0.01
			158.73	0.1537	6803	20	0.10	0.01

TABLE 2.3: Raw data for glioblastoma tumor initiating cells (TIC) mechanical measurements. The uncertainty (σ_ε) in the average strain measurement (ε) at each experimental condition is the standard error of the mean.

3T3	Fluid viscosity μ	Channel wideth w = 2·D	Mean flow velocity U	Flow Reynolds number Re = ρUD/μ	Extensional strain rate ξU/D	Number of cells n	Average strain ε = (a-b)/(a+b)	Strain uncertainty σ_ε
	mPa·s	μm	mm/s		s^{-1}			std error of mean
3T3 CONTROL								
Day 1	37.75	100	23.15	0.0319	694	16	0.047	0.006
			46.30	0.0638	1389	11	0.047	0.006
			69.44	0.0957	2083	22	0.058	0.003
			111.11	0.1531	3333	15	0.071	0.008
			129.63	0.1786	3889	25	0.10	0.01
			148.15	0.2041	4444	27	0.099	0.007
Day 2	38.3	100	23.15	0.0314	694	10	0.043	0.005
			46.30	0.0629	1389	10	0.065	0.006
			69.44	0.0943	2083	11	0.056	0.009
			92.59	0.1257	2778	10	0.072	0.008
			111.11	0.1509	3333	10	0.069	0.009
			129.63	0.1760	3889	19	0.09	0.01
Day 3	37.5	100	23.15	0.0321	694	10	0.035	0.007
			46.30	0.0642	1389	10	0.051	0.004
			69.44	0.0963	2083	14	0.06	0.01
			92.59	0.1284	2778	13	0.07	0.01
Day 4	37.5	100	9.26	0.0128	278	10	0.020	0.007
			23.15	0.0321	694	18	0.031	0.006
			46.30	0.0642	1389	10	0.035	0.006
			129.63	0.1798	3889	12	0.07	0.01
3T3 CYTO D								
Day 1	37.75	100	9.26	0.0128	278	21	0.033	0.005
			23.15	0.0319	694	15	0.074	0.007
			46.30	0.0638	1389	30	0.063	0.005
			69.44	0.0957	2083	12	0.089	0.008
			92.59	0.1275	2778	10	0.083	0.007
			111.11	0.1531	3333	27	0.095	0.008
			129.63	0.1786	3889	10	0.106	0.007
			148.15	0.2041	4444	20	0.12	0.01
Day 2	38.3	100	9.26	0.0126	278	17	0.023	0.006
			23.15	0.0314	694	16	0.06	0.01
			46.30	0.0629	1389	12	0.07	0.01
			69.44	0.0943	2083	20	0.093	0.009
			92.59	0.1257	2778	21	0.079	0.007
			111.11	0.1509	3333	26	0.09	0.01
3T3 PFA								
Day 3	37.5	100	9.26	0.0128	278	15	0.016	0.005
			46.30	0.0642	1389	15	0.028	0.005
			69.44	0.0963	2083	15	0.031	0.009
			111.11	0.1541	3333	15	0.055	0.006
Day 4	37.5	100	9.26	0.0128	278	11	0.009	0.005
			23.15	0.0321	694	15	0.027	0.007
			46.30	0.0642	1389	15	0.034	0.007
			69.44	0.0963	2083	15	0.029	0.007
			92.59	0.1284	2778	14	0.038	0.008
			111.11	0.1541	3333	15	0.05	0.01
			129.63	0.1798	3889	15	0.05	0.01

TABLE 2.4: Raw data for 3T3 fibroblast cell mechanical measurements. The uncertainty (σ_ε) in the average strain measurement (ε) at each experimental condition is the standard error of the mean.

2.4 UNPUBLISHED DATA: DIFFERENCE IN MECHANICAL PROPERTIES OF POLYMERS BETWEEN ASPIRATION AND INDENTATION: DEXTRAN AND SILICONE

When calibrating our microfluidic system for cell mechanics, we used Sephadex G200 beads as a model system. However, the mechanical properties of those beads had not been previously characterized, so we needed to do so ourselves. We chose for the paper to compare the stiffness found using our cross-slot device (combined with our analytical model) with the one found using micropipette aspiration. In the process of choosing the best method, we tested microindentation and microaspiration for Sephadex (GE Healthcare, Little Chalfont, United Kingdom) and Cytodex-3 (GE Healthcare Life Sciences, Velizy-Villacoublay, France), two types of dextran beads. We further compared both of these methods to macroscopic stretching using a silicone polymer employed by dentists called the Elite Double 8 (Zhermack, Badia Polesine, Italy) which can be made in larger quantities (Figure 2.13). While this work was beyond the scope of the paper, we report these results here.

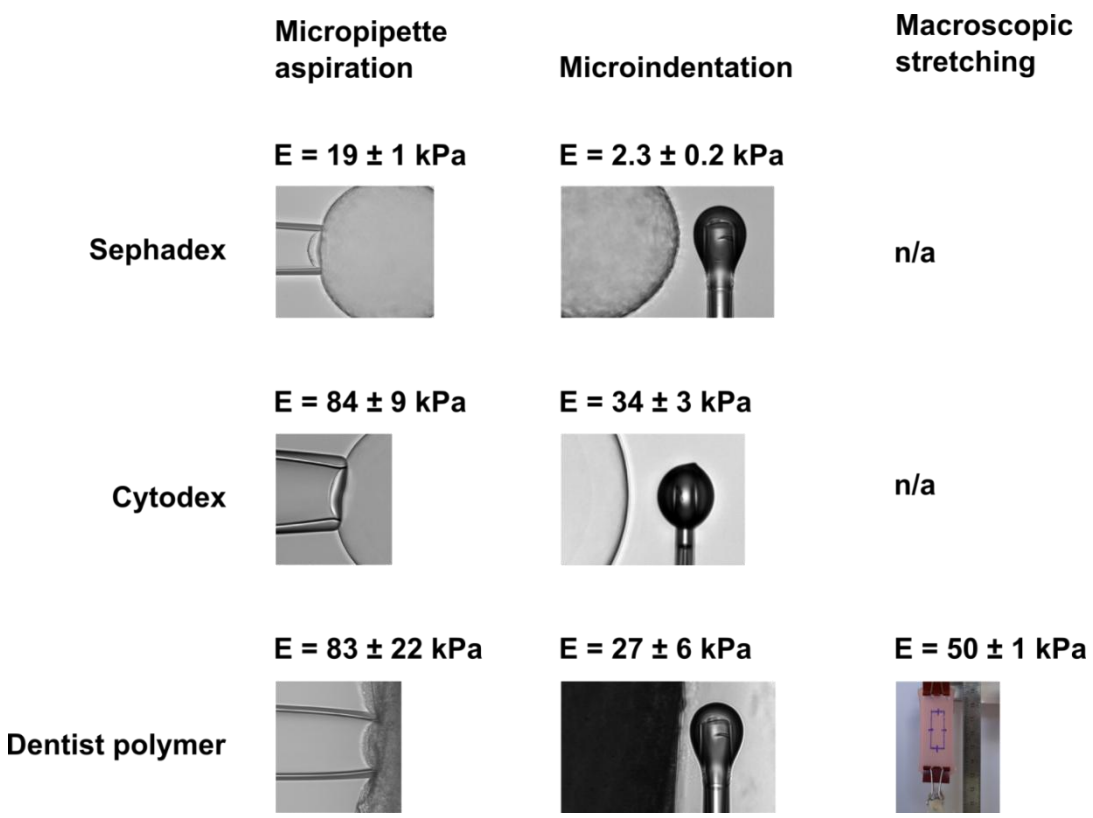

FIGURE 2.13: Comparison of stiffness measurements of polymers

We find that for the three polymers we tested, the stiffness was 3 to 10 fold higher in aspiration experiments compared to indentation experiments. Uniaxial tension was in between those two values. Upon comparing results from micropipette aspiration, nanoindentation, bulk uniaxial extension and compression, Buffinton *et al.* (Buffinton *et al.*, 2015) reported that for silicone, the testing method did not matter much, while for hydrogels, micropipette aspiration yielded higher stiffness values than indentation. Our results match the ones they obtained for hydrogels, but unlike their silicone (they tested Ecoflex, Dragon Skin (Smooth-On, Easton, PA, US) and PDMS Sylgard 184 (Dow Corning, Midland, MI, US)), our type of silicone also seems to share that behavior of higher resistance to stretching than to indentation. In conclusion, it is important to keep in mind that when both extension and compression of polymers are involved in a mechanical measurement (such as in cross-slot experiments), the stiffness from extension will dominate the overall mechanical behavior.

CHAPTER 3

Membrane rupture criterion for adherent cells

3.1 INTRODUCTION

Beyond the characterization of cell mechanical properties, we wondered if mechanics could also help us understand when deformations undergone by cells, or stresses exerted on them, could become harmful.

In particular, when atherosclerotic plaques significantly reduce arterial blood flow, interventional radiologists or cardiologists seek to reopen the vessel through angioplasty (balloon inflation), often combined with stenting (placement of a wired mesh that helps maintain the vessel open). This procedure exerts considerable compressive stresses on the endothelium. We therefore sought to understand the amount of compressive force that is necessary to injure an endothelial cell and compared this stress to the stress generated by stenting. We presented those results in an article (submitted) and reproduce them in section 3.2.

The method of "tilted microindentation" employed to test endothelial cell membrane rupture also allows the measurement of cell mechanical properties, with only a single micromanipulator required. We present the analytical model that describes this, along with other results, in the supplementary material of the article and reproduce it in section 3.3.

In the article, we argue that compressive forces exerted on endothelial cells also generate a large amount of radial strain. This assertion is supported by both numerical simulations of large cell indentations and direct experimental visualization of radial strain during "tilted microindentation". To visualize this radial strain, we tracked mitochondria using a fluorescent marker and used particle image velocimetry (PIV) software to compute subcellular displacements within the endothelial cell. Because we believe this method holds much promise for future applications, as it allows easy computation of 2D deformations at the subcellular level of adherent cells, we present some further details on this method in section 3.4.

3.2 MECHANICAL CRITERION FOR THE RUPTURE OF A CELL MEMBRANE UNDER COMPRESSION

David Gonzalez-Rodriguez*, Lionel Guillou*, Francois Cornat, Julie Lafaurie-Janvore, Avin Babataheri, Emmanuel de Langre, Abdul I. Barakat, and Julien Husson

* equal contribution

Abstract

We investigate the mechanical conditions leading to the rupture of the plasma membrane of an endothelial cell subjected to a local, compressive force. Membrane rupture is induced by tilted microindentation, a technique to perform mechanical measurements on adherent cells. In this technique, the applied force can be deduced from the measured horizontal displacement of a microindenter's tip, as imaged with an inverted microscope and without the need for optical sensors to measure the microindenter's deflection. We show that plasma membrane rupture of endothelial cells occurs at a well-defined value of the applied compressive stress. We use numerical simulations to estimate the magnitude of the compressive stresses exerted on endothelial cells during the deployment of a stent.

Introduction

It has become increasingly clear over the past two decades that cells feel and respond to physical cues in their environment (Discher *et al.*, 2005). Endothelial cells in particular have been shown to be highly sensitive to the mechanical forces to which they are subjected (Malek and Izumo, 1996). Beyond mechanical forces that are naturally found in the body, human intervention may also trigger new and different mechanical forces on the endothelium. For instance, minimally invasive surgical procedures often require the use of catheters, which push strongly against the endothelium. Angioplasty and stenting procedures, which have become routine interventions for about eight million patients each year worldwide (Cook *et al.*, 2007; Jennings *et al.*, 2014; Weiss and Elixhauser, 2014), also apply great compressive stresses on the endothelium and have been shown to lead to substantial endothelial damage (Rogers *et al.*, 1999). Endothelial damage, in turn, may lead to thrombosis (Wu, M.D and Thiagarajan, M.D, 1996), a major cause of stroke and myocardial infarction. It is therefore of great interest to understand the mechanism by which mechanical forces, and in particular compressive forces, can damage endothelial cells.

The goal of this article is to characterize the mechanics of endothelial cell rupture under compressive stress. Endothelial cells line the arterial walls and are continuously subjected to mechanical forces, which often cause membrane wounding. Using mouse models, it has been estimated that, under normal physiological conditions and at any given time, between 1% and 18% of aortic endothelial cells exhibit wounded membranes (Yu and McNeil, 1992). The plasma membrane has the ability to recover from disruption, so that endothelial cells can remain viable in spite of wounding (McNeil and Steinhardt, 1997). However, under high stresses, such as those arising during the deployment of a stent, endothelial cells can be wounded beyond repair (Edelman and Rogers, 1998). Plasma membrane rupture under compressive stress has previously been studied in red blood cells using Atomic Force Microscopy (AFM) (Hategan *et al.*, 2003; Sen *et al.*, 2005) and in mouse myoblasts using a whole-cell compression apparatus (Peeters *et al.*, 2005). However, in both instances, the shape and size of the compressive apparatus was maintained constant, yielding a single critical force value. Here we introduce the technique of tilted microindentation, a versatile tool to study cell mechanics, and we apply this technique to characterize the rupture of endothelial cell membranes under compression applied on contact areas ranging from 1 to almost 100 μm^2.

Atomic Force Microscopy is the technique of reference to study adherent cell mechanics. In AFM, forces are applied onto a cell through a cantilever ending at a sharp tip, with a typical radius at its extremity of about 10 nm. Such a sharp tip induces high local strains that can exceed the linear regime, thus introducing artifacts in the determination of the cell's mechanical properties (Dimitriadis *et al.*, 2002; Carl and Schillers, 2008). To avoid such artifacts, an alternative technique is often used

where a micrometric bead is attached to the tip of the AFM cantilever (Ducker *et al.*, 1991; Mahaffy *et al.*, 2000; Darling *et al.*, 2008). In AFM, the applied force is deduced from the deformation of the cantilever, whose measurement requires the use of an optical sensor, most commonly a system of photodiodes collecting a laser beam reflected by the cantilever. While precise and versatile, AFM requires expensive equipment; moreover, the AFM head is bulky and restrains access to the sample. In this article we introduce tilted microindentation, an inexpensive and unobstructive technique to exert controlled compressive nanonewton forces and to characterize cellular mechanics over the scale of the μm^2. Using a micropipette puller and a microforge, we fabricate a glass microindenter consisting of a cantilever beam of adjustable stiffness (0.5 to 200 nN/μm) and a tip of adjustable shape (spherical or flat) and size (tip diameter of 2-10 μm), which allows discrimination of the effects of force versus stress. This device is similar to the *cell poker* developed by McConnaughey et al. (McConnaughey and Petersen, 1980; Daily *et al.*, 1984). However, the cell poker requires an optical sensor in order to deduce the cantilever deflection and the corresponding applied force. In the technique we propose, the microindenter is tilted so that the applied force can be deduced from measuring the horizontal displacement of the microindenter's tip over the sample. The applied force is hence deduced from the sample image acquired with an inverted microscope, thus eliminating the need for optical sensors and allowing simultaneous fluorescence imaging. The uncertainty of the force measurement is smaller than 1 nN when the most flexible microindenter is used.

By using tilted microindenters of different rigidities and tip geometries, and by varying the microindenter's angle of attack, in this article we show that microindentation-induced membrane rupture occurs at a constant normal stress of 12.4±0.6 kPa. Because our stress criterion is scale-independent over the range of contact areas studied here, we speculate that our criterion is relevant to stent deployment, where the typical strut size is on the order of 100 μm (Murphy *et al.*, 2003). We also present numerical simulations to interpret the mechanics of cell indentation and to estimate the compressive stresses exerted on endothelial cell membranes during stent deployment.

Materials and Methods

Endothelial cells

Bovine aortic endothelial cells (BAECs) were kindly provided by A.-C. Vion and C. Boulanger and used between passages 4 and 12. BAECs were cultured at 37 °C and 5% CO_2 in Dulbecco's Modified Eagle's medium (DMEM, low glucose, INVITROGEN, Carlsbad, CA, USA) supplemented with 10% fetal bovine serum (INVITROGEN) and 1% penicillin/streptomycin (INVITROGEN). One to two days

before an experiment, cells were cultured in thin-bottom Petri dishes (FLUORODISH 35 mm, WORLD PRECISION INSTRUMENTS, Hitchin, UK). For experiments in which the cells were exposed to cytochalasin D, we used the same protocol as in Hogan et al. (Hogan *et al.*, 2015): the cells were incubated for 30 min in a solution containing 1 mg/mL cytochalasin D from Zygosporium masonii (SIGMA-ALDRICH, Taufkirchen, Germany). The Petri dish was then rinsed and experiments were performed in fresh medium.

Microscope and Micromanipulator

Experiments were performed on a TE300 inverted microscope (NIKON INSTRUMENTS, Tokyo, Japan) placed on an air suspension table (CVI MELLES GRIOT, Netherlands). The microscope was equipped with a 100x oil immersion, 1.3 NA objective (NIKON INSTRUMENTS) for experiment monitoring and lower magnification objectives (40x, 20x, 10x, 4x, and 2x, Nikon) for micropipette positioning. Images were acquired using a Flash 4.0 CMOS camera (HAMAMATSU PHOTONICS, Hamamatsu City, Japan). The experimental setup was equipped with a motorized micromanipulator (MP285, SUTTER INSTRUMENTS, Novato, CA, USA) carrying a micropipette holder (IM-H1, NARISHIGE, Tokyo, Japan) at a controlled angle α and holding a microindenter. The microscope was equipped with a heating stage set to 37 °C, guaranteeing a constant temperature slightly lower than 37 °C but higher than room temperature. Before each experiment, a Petri dish was taken out of the incubator and medium was exchanged with pre-heated culture medium supplemented with 160 μg/mL propidium iodide (SIGMA-ALDRICH). The dish was placed on the stage with oil immersion and the 100X objective was focused in the cell-substrate plane under brightfield illumination. The microindenter was positioned in the dish in the center of the field of view and ~50 μm above the cell level. The microindenter was left at least ten minutes in buffer before contacting any cell, in order to let the serum proteins in the medium adsorb onto the tip and avoid its adhesion to cells. The illumination source was an Intensilight lamp (NIKON INSTRUMENTS), exposure time was set to 80 ms and a neutral density filter 4 or 8 was used. Fluorescence aperture diaphragm was adjusted to limit exposure in the field of view. A region of interest was defined using the Micromanager software (Edelstein *et al.*, 2014).

Microindenter fabrication and calibration

Microindenters were prepared as described in Guillou et al. (Guillou *et al.*, 2016). Briefly, borosilicate glass capillaries (1 mm OD, 0.78 mm ID, HARVARD APPARATUS, Holliston, MA, USA) were pulled on a P-97 micropipette puller (Sutter Instruments, Novato, CA, USA). An MF-200 microforge (WORLD

PRECISION INSTRUMENTS, Hitchin, UK) was used to melt glass at the tip of the micropipette. The microindenter's bending stiffness was evaluated against standard microindenters that had been previously calibrated. One method to calibrate these standard microindenters was to measure their deflection under the gravitational force exerted on their tip by piece of ultrathin paper of known mass. (Basu *et al.*, 2016) We confirmed this initial method by using a commercial force probe (model 406A with a force range of 0-500 nN, AURORA SCIENTIFIC INC., Aurora, ON, Canada).

Measuring cell membrane rupture

For measurements on the cytoplasm, endothelial cells with flat lamellipodia were chosen. The microindenter was lowered using the finest setting of the micromanipulator. Contact was made as indicated by the onset of bead sliding over the surface of the cell, which was defined as the reference position. The illumination was then switched to fluorescence excitation at 580 nm and the indentation process was recorded. The microindenter's base was lowered by manual control in order to maintain a mean vertical translation speed of typically 1 μm/s. Our initial protocol involved switching between brightfield and fluorescence illumination to detect the position of the bead at contact. We later identified that under fluorescence illumination, bead contact was detected by the sensitive CMOS camera as a dark spot in the background fluorescence due to the cell's autofluorescence. As soon as an increase in fluorescence was detected (which was initiated in close vicinity of the microindenter's tip), the translation was stopped, and both the horizontal distance from the reference position, Δx, and the vertical displacement of the microindenter's base δ (as indicated by the micromanipulator controller) were measured. The microindenter was then retracted by bringing its tip to a rest position at 10 μm above contact with the cell. For experiments with an angle of attack β different from 0, the approach angle was set using a virtual axis option available in the micromanipulator controller.

Characterization of the moderate indentation regime

In order to study the moderate indentation regime and deduce cell mechanical properties, brightfield illumination was used. Once the chosen cell had been centered in the field of view, the microscope was focused on the cell's basal plane, and a region of interest was selected to limit computer memory usage. The contact with the cell was visualized by the deformation of the cell surface. The probe was raised 5 μm above contact before starting the indentation experiment. Indentation induces changes in cell height; thus, if the microscope was focused at the initial bead position, the bead would move out of focus, which would increasingly interfere with the

detection of the bead's edge at increasing indentation. To avoid this bias, we kept a defocused image of the bead by focusing the microscope 3.5 μm below the basal plane of the cell. The acquisition was then started at 100 frames per seconds and 5 ms exposure time, and a linear translation of the base of the probe was started at 2 μm/s. We used the software ImageJ (Schneider *et al.*, 2012) to measure the position of the edge of the bead as a function of time: we normalized and smoothed the brightfield images, and then defined a line coinciding with the straight trajectory of the bead sliding on the surface of the cell. We used this line to obtain a so-called kymogram, i.e. a graph where the intensity level along this line was reported at each frame. The kymogram was then thresholded in order to select the dark rim of the bead. The image was binarized according to this threshold to obtain (position, frame number) coordinates of the edge of the binary image (see Supplementary Material Figure 3.6). These coordinates were converted to proper distances and times using the GRAPHPAD Prism software (GRAPHPAD SOFTWARE, CA, USA). In Prism, a least squares method was applied to fit the curve of bead horizontal displacement over time. From the fit of each curve, two experimental parameters were extracted, D_{lin} and Δx_{lin} (see Supplementary Material Figure 3.5B for parameter definitions).

Simulations of cell indentation

In our simulations of cell indentation, the endothelial cell is modeled as a nearly-incompressible (Dimitriadis *et al.*, 2002; Harris and Charras, 2011) hyperelastic neo-hookean (Peeters *et al.*, 2005; Or-Tzadikario and Gefen, 2011; Vargas-Pinto *et al.*, 2013) material, with a Poisson's ratio of 0.49 and a Young's modulus of 1 kPa. The microindenter's spherical tip is considered infinitely rigid compared to the cell. The deformation of the microindenter's cantilever is not modeled; rather, the cell indentation is instead taken as the input. The endothelial cell is fixed on an infinitely rigid substrate, to represent the focal adhesions that are observed experimentally on a glass substrate (Hogan *et al.*, 2015). The contact between the microindenter and the cell is implemented using the augmented Lagrangian method with a penalty factor of 10^5, sufficient to prevent interpenetration. Simulations were performed in FEBio version 1.5.2 (Maas *et al.*, 2012) with the Pardiso solver (Kuzmin *et al.*, 2013). The mesh was generated using Gmsh version 2.8.3 (Lee *et al.*, 2011). The spherical indenter's tip was meshed using linear 4-node tetrahedral elements, with a coarse mesh at the center of the sphere and a fine mesh at the surface which makes contact with the cell. A structured mesh consisting of linear 8-node hexahedral elements was defined throughout the entire cell. We performed a mesh convergence study: the error in the computed forces between the mesh of choice and a very fine mesh having 100 times more elements is 2%. We verified that our numerical results were insensitive to further refinements of the microindenter's mesh as well as to an increase in the size of the domain that represents the cell.

Simulations of stent deployment. For the 2D stent implantation simulations, the artery is represented by a 300 μm thick single layer, modeled as an elastic material with a Poisson's ratio of 0.45 and a Young's modulus of 1 MPa (Walke *et al.*, 2005). The strut of the stent has a 100 μm x 100 μm square cross section, which is modeled as an elasto-plastic material with a Young's modulus of 270 GPa, a Poisson's ratio of 0.27, a yield strength of 300 MPa and a tensile strength of 650 MPa, corresponding to 316L stainless steel (Hibbeler). The stent indentation is an input variable which ranges from 0 to 50% of the stent strut size (Karalis *et al.*, 2012). The external boundary of the arterial wall is subjected to a spring foundation displacement condition, with a spring constant of 300 Pa, chosen to represent the radial elasticity of an artery (Wei *et al.*, 2012). The contact between the stent strut and the arterial wall is implemented using the augmented Lagrangian method (Guo *et al.*, 2012). Simulations were performed in the multi-physics finite element commercial software COMSOL version 5.0 (COMSOL AB, Stockholm, Sweden). The mesh was generated with COMSOL mesh generator using linear 4-node triangular elements for both the arterial wall and the stent strut, with a refined mesh for both solids in the neighborhood of the contact region. We performed a mesh convergence study: the error in the computed pressures between the mesh of choice for the artery and a very fine mesh having 100 times more elements is 2%.

Results

Tilted microindentation allows applying a controlled force on adherent cells. A microindenter made of a flexible glass microfiber of bending stiffness k_m with a glass bead of radius R at its tip is held by a micromanipulator placed on an inverted microscope (Figure 3.1).

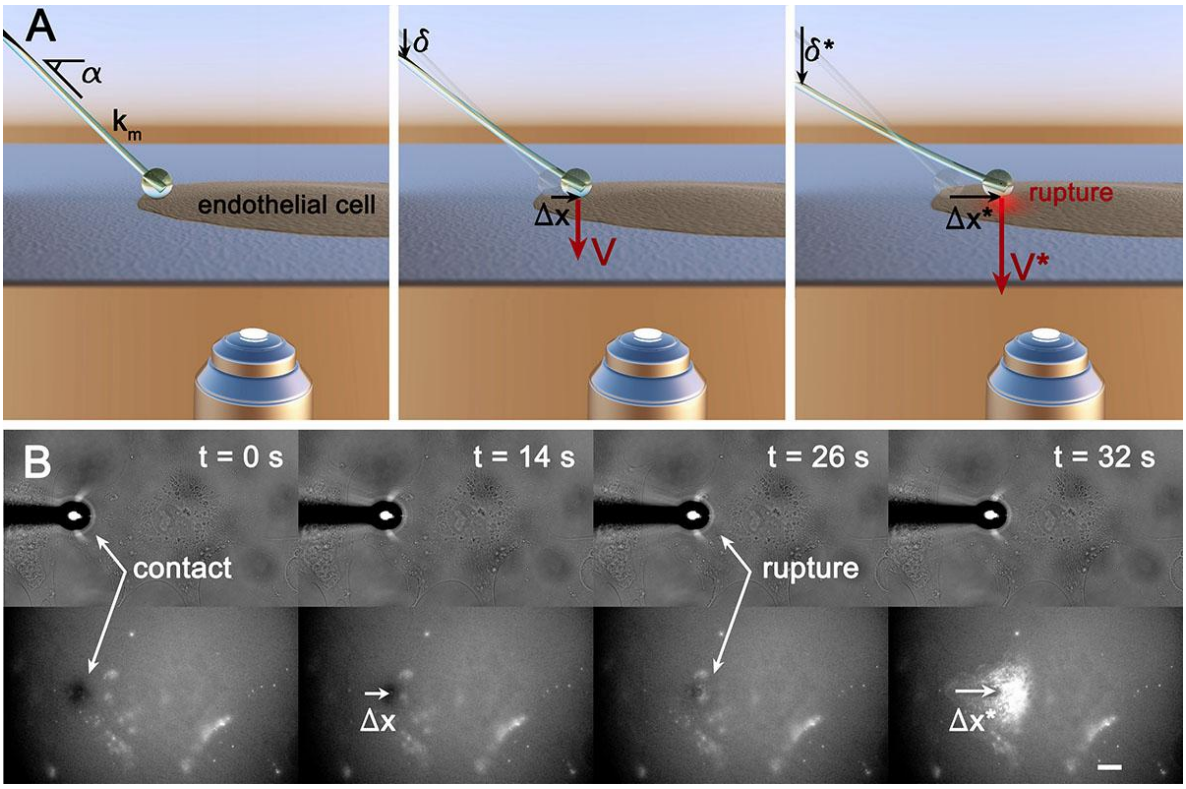

FIGURE 3.1: Description of tilted microindentation. (A) Schematic view of the tilted microindentation setup. The applied normal force, V, can be deduced from the measured horizontal displacement of the microindenter's tip, Δx. Membrane rupture occurring at displacement Δx^* is visualized by the fluorescent propidium iodide signal. (B) Application of tilted microindentation to measure the normal force required to induce the rupture of an endothelial cell membrane. Membrane rupture is visualized by the fluorescent propidium iodide signal. The bar represents 10 μm.

The microindenter is held at a controlled angle α with the horizontal plane of the sample, and its tip is placed on top of an endothelial cell cultured on the bottom of a Petri dish on the microscope's stage. We impose a displacement to the upper end of the microindenter and record the resulting horizontal displacement of the microindenter's tip, Δx (Figure 3.1). From this measurement, and based on an analytical model of the cell response to force, we can deduce the force applied by the microindenter. The analytical model is explained in detail in the supplementary information. Briefly, we assume the cell to behave as a non-adhesive homogeneous isotropic linear elastic solid up to a maximum indentation, $\Delta z = \Delta z_{max}$, at which point the cell becomes infinitely rigid when compared to the microindenter. Indeed, the cell will appear progressively stiffer as the indentation increases relative to the sample thickness (Dimitriadis *et al.*, 2002), saturating at indentations of ~80% of the cell height, where the cell becomes nearly infinitely rigid (Peeters *et al.*, 2005; Krause *et al.*, 2013). At weak indentation, the cell's reaction to deformation is thus

$V = k_{cell}(\Delta z)^{3/2}$, where according to Hertz's model $k_{cell} = \frac{4}{3}E^*\sqrt{R}$ and $E^* = \frac{E}{1-\nu^2}$, with E and ν being the Young's modulus and Poisson's ratio of the cell (Johnson, 1985). Tilted microindentation allows us to analyze moderate indentations to estimate the local apparent Young's modulus of the cell (see Supplementary Material Figure 3.7 and supplementary information).

Beyond the maximum indentation $\Delta z = \Delta z_{max}$, we consider that the cell behaves as a rigid body with Coulomb friction, i.e., we assume $\Delta z = \Delta z_{max} =$ constant and a constant dynamic friction coefficient μ between the microindenter and the cell membrane. As discussed below, we have shown that in our experiments μ is negligibly small. As detailed in the supplementary information, the resulting relationship between Δx and V at large indentation is

$$V = 2k_m \Delta x / \sin(2\alpha) . \quad (1)$$

To maximize the precision of the measured force, one should maximize the measured value of Δx to minimize its relative uncertainty. This is attained at an optimal tilt angle of $\alpha = 45°$, which we have selected for all of our experiments. Thus, from measuring the horizontal displacement at membrane rupture, Δx^*, Eq. (1) yields the normal force V^* needed to rupture the membrane of an endothelial cell. We use propidium iodide as a reporter of this rupture. Propidium iodide is initially present in the extracellular medium. Upon membrane rupture, this intercalating agent enters the cell cytoplasm and becomes rapidly fluorescent. Other fluorescent probes can also be used, such as the calcium probe Fluo-4.

The indentation force at membrane rupture is independent of the microindenter's bending stiffness

Figure 3.2A shows the horizontal displacement of the microindenter's tip at membrane rupture, Δx^*, as a function of the inverse of the microindenter's bending stiffness, $1/k_m$, for several microindenters with spherically shaped tips of radius 6.1±0.6 μm. The microindenters are tilted at $\alpha = 45°$. The figure shows that the applied normal force at rupture, $V^* = 2k_m \Delta x^* =$ 229±24 nN, is independent of the microindenter's stiffness. Different stiffnesses yield significantly different tip displacements at rupture, indicating that membrane rupture is induced by the applied force and not by an imposed horizontal stretching associated with the horizontal displacement of the microindenter's tip.

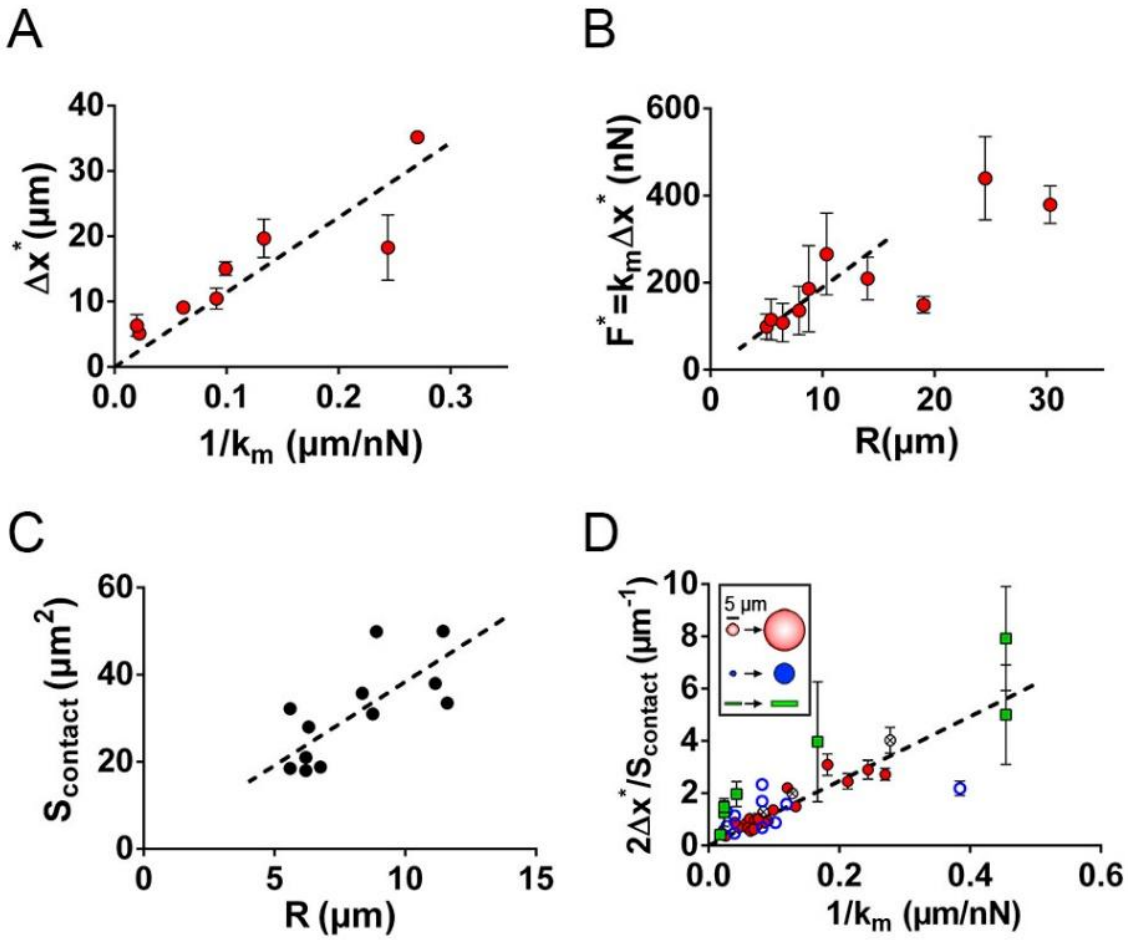

FIGURE 3.2: Characterization of membrane rupture with tilted microindentation. (A) Horizontal displacement of the microindenter's tip at cell membrane rupture, Δx^*, as a function of the microindenter's stiffness, k_m, for microindenters with a spherical tip of diameter 12.2±1.2 μm. Microindenters are tilted at α = 45°. The dashed line is a linear regression through the experimental data. (B) Compressive force at cell membrane rupture, F^*, as a function of the microindenter tip's radius, R, for a fixed indenter stiffness, k_m = 14.9±1.6 nN/μm for 10 indenters and 6 to 13 cells for each indenter. (C) Contact surface area between the microindenter's spherical tip and the cell, $S_{contact}$, as a function of the microindenter's tip radius, R. The straight line is a linear regression through the experimental data, $S_{contact}$ (μm^2) = 3.84 R (μm). (D) Normalized horizontal displacement of the microindenter's tip at membrane rupture, Δx^*, as a function of the microindenter's stiffness, k_m, for different geometries of the microindenter's tip (recapitulated in the inset): spherical tip (full circles, N = 133 cells), rectangular flat tip (empty squares, N = 41 cells), circular flat tip (empty circles, N = 134 cells). The encircled crosses correspond to spherical-tip microindentation measurements upon cytochalasin-D treatment. Error bars represent standard error of the mean. For all cases, α = 45°. The straight line is a fit of Eq. (4) with σ^* = 12.4 kPa. Inset: representation of the range of sizes and geometries used for the microindenter's tip (from top to bottom: spherical, circular flat, and rectangular flat tips, relative sizes are respected).

The membrane ruptures at a constant normal microindentation stress

We investigated whether the relevant criterion for indentation-induced membrane rupture should be based on the total force, on an equivalent surface tension (with units of force per unit length), or on the applied stress (force per unit surface area). To distinguish between force and tension/stress, we first varied the tip size. Figure 3.2B shows the rupture force, F^*, obtained for spherical tips of different radii and constant stiffness (k_m = 14.9±1.6 nN/μm, for 10 indenters and 6 to 13 cells for each indenter). The rupture force increases linearly with the indenter's radius, R, up to R~15 μm. We note here that a critical force increasing linearly with the tip radius is compatible with both a critical tension and a critical stress, as we further discuss below. Beyond R~15 μm, the measured force no longer systematically increases with R. Indeed, for such large radii, the indenter tip size becomes comparable to the whole cell, so that confining the indented region to the cytoplasm, without also probing thicker regions above the nucleus, is no longer systematically possible. Altogether, measurements in Figure 3.2B show that the rupture force is not constant but depends on tip size.

To distinguish between a rupture criterion based on a critical tension and one based on a critical stress, we next varied the indenter's shape, while at the same time exploring a range of indenter stiffness. We fabricated microindenters with tips of different sizes and shapes: spherical tips from 4.6 to 23.2 μm in diameter, flat tips of circular cross-section (from 1.8 to 8.6 μm in diameter), and flat tips of rectangular cross-section (from 1.4 to 3.0 μm in thickness, 8.9 to 16.8 μm in width, and a relatively constant width-to-thickness aspect ratio r = 5.4±0.8). All microindenters are tilted at α = 45°, so that, according to Eq. (1), the stress exerted by the microindenter tip onto the cell at rupture is $2k_m\Delta x^*/S_{contact}$, where $S_{contact}$ is the contact area between the tip and the cell. For flat tips, $S_{contact}$ is the tip's area. For spherical tips, the contact area can be determined experimentally from the shaded region induced by the contact. At low indentation force, the contact area increases with the indentation force, but once the microindenter starts to significantly slide horizontally over the cell, the measured contact area remains constant. Figure 3.2C shows the measured final contact area for spherical-tip microindenters of different radii. The measurements are well fitted by the linear relationship

$$S_{contact}\,(\mu m^2) = 3.84\,R\,(\mu m). \qquad (2)$$

We also investigated the contact area through numerical simulations (Supplementary Material Figure 3.7). The simulations, which account for large deformations and for finite thickness effects, yield a contact area that is well represented by a modified version of Hertz's theory,

$$S_{contact} = \lambda\pi R\Delta z, \qquad (3)$$

where λ = 2 is a correction to Hertz's theory taking into account the finite cell thickness. The value λ = 2 corresponds to the membrane perfectly conforming to the spherical shape of the indenter up to the indentation depth Δz, as was also assumed by Hategan et al. (14). The agreement between numerical experiments and Eq. (3) is good in the range $1 < R/h < 10$, corresponding to our experimental conditions. Comparing Eqs. (2) and (3), we deduce the maximum depth of indentation of the cell, Δz_{max} = 0.6 μm.

Figure 3.2D shows the normalized horizontal displacement at membrane rupture for various sizes and shapes of the microindenter tip as a function of microindenter stiffness. The measurements are globally well described by a critical rupture stress σ^*, i.e.,

$$2\Delta x^*/S_{contact} = \sigma^*/k_m, \quad (4)$$

which is obtained by dividing Eq. (1) by the contact area. The best fit to the spherical-tip microindenter measurements is obtained with σ^* = 12.4 kPa, which is also a good global fit for all measurements (Supplementary Material Figure 3.9A). In contrast, a rupture criterion based on a critical tension, γ^*, would lead to a rupture force scaling with the perimeter of the contact surface, $P_{contact}$. One would thus obtain the relationship $2\Delta x^*/P_{contact} = \gamma^*/k_m$. Fitting our measurements based on this critical tension criterion is less convincing, as shown in Supplementary Material Figure 3.9B. In conclusion, membrane rupture occurs at a critical compressive stress of 12.4±0.6 kPa regardless of the size, shape, and stiffness of the microindenter.

The stress required to rupture the membrane is insensitive to the integrity of the actin cytoskeleton

Figure 3.2D includes experimental data of cell microindentation performed on endothelial cells treated with cytochalasin-D, an inhibitor of actin polymerization. The results in the presence of cytochalasin-D (encircled crosses) are indistinguishable from control conditions (full circles), indicating that the critical stress for microindenter-induced membrane rupture is uncorrelated with the integrity of the cell's cytoskeleton.

Changing the microindenter's angle of attack provides quantification of microindenter-membrane friction, which is negligible

To characterize the friction between the microindenter's tip and the cell membrane, we performed microindentation experiments at fixed angle α = 45° and with different values of the microindenter's angle of attack. In these experiments, the position of the upper end is lowered at a constant speed, along a straight trajectory that forms an angle of attack β with the vertical direction (note that β = 0 for all cases presented

above). For an arbitrary angle of attack, and by assuming that the vertical cell deformation at rupture is small compared to the vertical deformation of the microindenter, an analytical model of cell microindentation (see supplementary information) predicts a horizontal displacement at rupture given by

$$\Delta x^* = \delta^* (\tan\alpha - \tan\beta) = \frac{V^*}{k_m}(\tan\alpha - \tan\beta)(\cos^2\alpha + sign(\beta - \alpha)\mu \sin\alpha \cos\alpha), \quad (5)$$

where δ^* is the vertical displacement at rupture of the upper end of the cantilever upon rupture. Figure 3.3A shows the experimentally observed horizontal displacement at rupture, Δx^*, as a function of δ^* (1 - tan β). The measured slope is very close to 1, in agreement with Eq. (5). To estimate the friction coefficient μ, we plot $k_m \Delta x^*/(S_{contact}\sigma^*)$ versus β in Figure 3.3B.We fit the curve with two free parameters, σ^* and μ, for each indenter. This leads to σ^* = 14±8 kPa, and μ = 0.12. In the data analysis leading to the estimate of σ^* = 12.4±0.6 kPa presented above, we had assumed μ = 0. If we reanalyze the previous data (Figure 3.2D) accounting for Coulomb friction with μ = 0.12, we obtain a critical stress of σ^* = 16 kPa, indicating an uncertainty of at most 30% in the reported value of σ^* due to a potential friction effect. Since this uncertainty is comparable to other sources of experimental uncertainty, such as cell-to-cell variability, frictional effects can reasonably be neglected when studying membrane rupture. Figure 3.3B shows indeed that Eq. (5) with μ = 0 also provides a very good fit to the experimental results, validating our original assumption that friction force can be neglected with respect to the normal force. This assumption is further supported by our experimental observation that if the vertical motion of the upper end of the microindenter is switched from downwards to upwards, the microindenter's tip immediately changes gliding direction without detectable stick-slip behavior. It is noted that by changing the angle of attack, we induce membrane rupture for very different values of the horizontal displacement Δx^*, which is even nearly zero for β = 45°. This result supports the conclusion stated above that microindenter-induced membrane rupture occurs at a given value of the normal stress applied onto the cell and is not due to an applied horizontal shear.

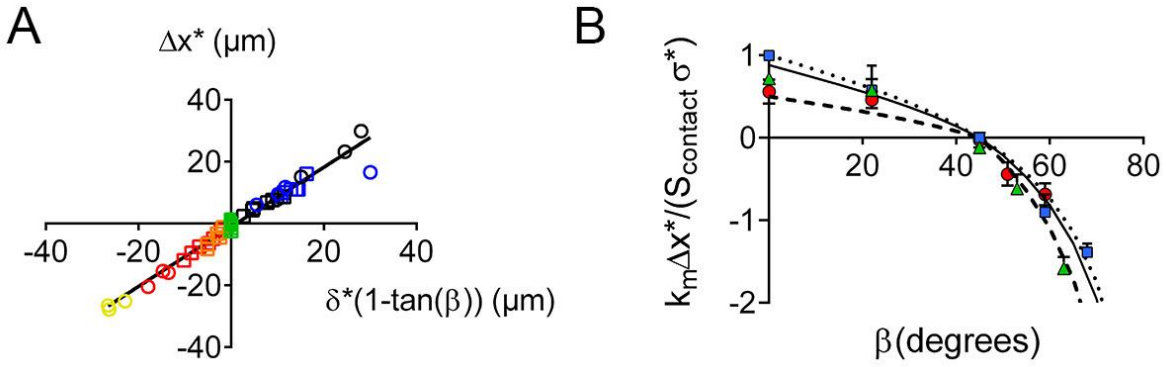

FIGURE 3.3: Horizontal displacement of the microindenter's tip at membrane rupture, Δx^*, obtained for different microindenter's angle of attack, β. Microindenters are tilted at α = 45° and their tips are spherical. (A) Δx^* equals δ^* (1 - tan β) (fitted slope of 0.96 ± 0.02). The symbols are experimental measurements obtained with two different indenters for β varying from 0 to 68 degrees (black: 0, blue: 22, green: 45, orange: 51, red: 59, and yellow: 68 degrees). (B) Normalized displacement, $k_m\Delta x^*/(S_{contact}\sigma^*)$, versus β. The symbols are experimental measurements obtained with three different indenters. The error bars indicate the standard error of the mean. The curves represent the predictions of Eq. (9) after normalization and given that α = 45°, $2k_m\Delta x^*/(S_{contact}\sigma^*) = (1 - \tan\beta)(1 + \mathrm{sign}(\beta - \alpha)\,\mu)$, with μ = 0 (dotted line), μ = 0.12 (solid line), or μ = 0.5 (dashed line).

The applied compressive force can be measured by measuring the vertical displacement of the upper end of the microindenter, δ, at an arbitrarily chosen angle of attack

The results shown in Figure 3.3A indicate that measuring Δx^* by microscopy is equivalent to measuring the length δ^* (1 - tan β). From a practical standpoint, the latter method is straightforward if using a motorized micromanipulator that displays the displacement of the upper end of the microindenter, as is the case here. Moreover, this latter method allows studying indentations at α = 45° and β = 45°, for which the horizontal tip displacement Δx vanishes (Supplementary Material Figure 3.10). In this way, tilted microindentation allows applying a controlled compressive force to a fixed location on the cell, simply by measuring the displacement δ indicated by the micromanipulator controller. This alternative method prevents the tilted microindenter from probing different cell spots, as is the case for an angle of attack β = 0° and also allows us to compare the rupture force obtained on the thin cytoplasmic regions versus that on top of the cell nucleus (Supplementary Material Figure 3.11). Interestingly, the obtained displacements δ^* (hence compressive force) are comparable, even if slightly larger on top of the nucleus (Supplementary Material Figure 3.11A). This indicates that the rupture criterion is essentially the same on the thin and thicker parts of the cell. We note that the reported displacements at rupture

δ^* were independent of the radius of the indenter's tip (Supplementary Material Figure 3.11B). This precludes artifacts due to differences in local curvature on top of the nucleus and on top of the cytoplasm, as well as a finite thickness effect that would make the indenter essentially probe the rigid substrate. Both such artifacts would yield values of δ^* that depend on the ratio of the indenter's tip radius to the cell thickness, which varies from about 1 μm on top of the cytoplasm to 3.8±0.4 μm (mean ± SD, N = 6 cells) on top of the nucleus.

The cell is radially strained in the vicinity of the microindenter

We performed numerical simulations to investigate the mechanism by which a normal stress can induce membrane rupture. Figure 3.4A shows the maximum radial strain induced in a hyperelastic medium by the microindenter's compression. At large indentation, a small increase of the indentation depth will result in a large increase in the radial strain in the region surrounding the microindenter's tip. For a typical indentation of $\Delta z_{max} \approx 0.6$ μm and assuming a typical endothelial cell thickness $h \approx 1$ μm, Figure 3.4A yields a maximum radial deformation $\varepsilon_{rr} \approx 1$ (or 100%), occurring at the periphery of the microindenter and underneath the cell membrane (see inset of Figure 3.4A).

To confirm the presence of the radial strain predicted by our numerical computations, we have visualized the displacement field in the cell induced by indentation by tracking fluorescently labeled mitochondria using a Particle Image Velocimetry software. We observed displacements that are orthogonal to the sliding direction of the microindenter, which are therefore indicative of radial strain. We note that those radial displacements increased with the sliding Δx, which is related by Eq. (1) to the applied compressive stress.

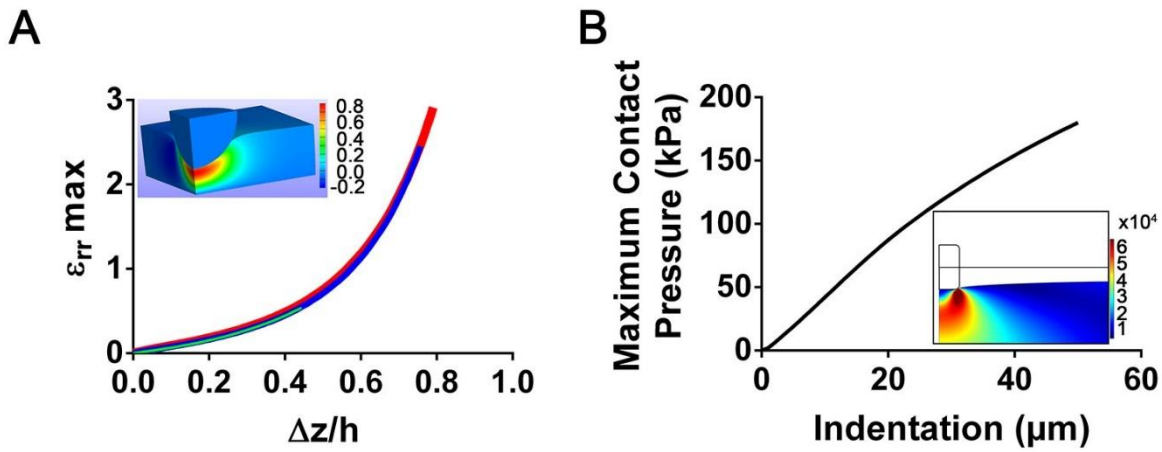

FIGURE 3.4: Simulations of cell microindentation and strut deployment. (A) Maximum radial cell deformation as a function of the normalized indentation as predicted by numerical simulations. The three curves, which are practically superposed, correspond to R/h = 1 (thick red line), R/h = 2 (intermediate blue line), and R/h = 10 (thin light green line). The inset shows a colormap of the radial deformation under the microindenter for the case R/h = 1 and $\Delta z/h$ = 0.49. (B) Maximum contact pressure evaluated along the contact line between the stent strut and the arterial wall as obtained from 2D numerical simulations of stent deployment. The inset shows a colormap of the von Mises stress in the arterial wall for a value of stent indentation equal to one half the strut thickness.

Pressures exerted during the deployment of stents induce rupture of endothelial cell membranes

We compared the critical stress for rupture determined here with typical conditions arising during surgical interventions. To investigate the typical pressures exerted during stent deployment, we have performed two-dimensional numerical simulations of the deployment of a stent onto an arterial wall. In our simulations, the arterial wall is modeled as a uniform elastic material of equivalent elastic modulus of 1 MPa (Walke *et al.*, 2005). Figure 3.4B shows the pressures exerted on the arterial wall, and thus on the monolayer of endothelial cells, during stent apposition. The inset in Figure 3.4B shows the von Mises stress induced in the arterial wall at maximum indentation. We predict a maximum compressive stress on the order of 180 kPa, which is consistent with values reported for three-dimensional simulations (Holzapfel, 2005).

Discussion

The critical stress established by tilted microindentation is consistent with previous measurements of cell membrane rupture

We showed that, independently of the size, shape, and stiffness of the microindenter, endothelial cell membrane rupture occurs at a normal microindentation stress of 12.4±0.6 kPa. We further showed that this value is approximately constant over different regions of the cell (cytoplasm vs. nucleus). The value of the reported critical stress is consistent with typical forces for compression-induced membrane rupture reported in the literature. Using an AFM, Hategan et al. reported an indentation force for rupture of the red blood cell membrane at slow loading of about 14 nN, and a corresponding indentation depth of 1.23 μm. They estimated the corresponding contact area between their AFM tip and the membrane to be ~3 μm^2 (Hategan *et al.*, 2003), which yields a normal stress of ~11 kPa. Using a flat circular indenter acting over the whole cell surface, which they estimated to be ~570 μm^2, Peeters et al. measured a membrane rupture force for mouse myoblasts of 8.7 μN (Peeters *et al.*, 2005), which corresponds to a normal stress of 15 kPa. Using a parallel-plate compression setup, Weiss et al. investigated the conditions leading to loss of membrane integrity of Ehrlich ascites tumor cells. Their results corresponded to a typical compressive stress for membrane rupture on the order of 3 to 6 kPa, again in reasonable agreement with the order of magnitude of the critical stress reported here (Weiss *et al.*, 1991). Rupturing lipid bilayers by compressing them with an atomic force microscope, Loi et al. measured forces ranging from 2 to 12 nN for tip radii ranging between 26 and 86 nm (Butt and Franz, 2002; Loi *et al.*, 2002). As their force curves imply a penetration of the AFM tip of a few nanometers, one can postulate that Eq. (2) is applicable to estimate the contact area, which leads to a compressive stress ranging from 17 to 43 kPa. This also is in reasonable agreement with our results, especially taking into account that incorporating peptides in lipid bilayers (hence getting a model somewhat closer to a cell membrane) makes them easier to break following micropipette aspiration (Evans *et al.*, 2003) and AFM indentation (Butt and Franz, 2002) measurements. Kagiwada et al. (Kagiwada *et al.*, 2010) reported that a typical force of 3 nN is required to insert a nanoneedle of 200 nm in diameter into a cell. Here the contact area is critical when estimating a compressive force: although using Eq. (2) to estimate $S_{contact}$ leads to a critical stress of about 8 kPa, it is probably more accurate to estimate the contact area as that of a spherical cap, $S_{contact} \sim 2\pi R^2$, leading to a larger stress of about 50 kPa. In another study using nanoneedle geometries, Xie et al. (Xie *et al.*, 2013, 2015) investigated the penetration of nanowires fixed to a substrate into cells that adhere onto this substrate. They used a cell membrane rupture criterion based on activation energy theory and leading to a critical membrane tension to be reached before rupture (Butt and Franz, 2002; Evans *et al.*, 2003). In this study tensile forces of about 1 nN are applied to the tip of nanowires of radius R = 50 nm. By again considering a contact area equal to half a spherical cap, $S_{contact} \sim 2\pi R^2$, one deduces an alternative rupture criterion based on a

critical stress of about 60 kPa, which is again comparable to our results, albeit somewhat larger.

Cell membrane rupture forces have not only been studied in compression: Tan et al. (Tan *et al.*, 2011) used micropipette aspiration to break the plasma membranes of fibroblasts. They deduced an average transmembrane protein–lipid cleavage strength γ^* of about 3 mN/m. We convert this value to a typical tensile stress by dividing the force $F^* = 2\pi\gamma^* R$ (with $R \sim 1$ μm being the radius of the micropipette) by the pipette cross-sectional area, πR^2. This yields a critical rupture stress of $2\gamma^*/R \sim 6$ kPa, again comparable to our measurements.

To summarize this overview of existing literature, both compressive and pulling stresses deduced from existing measurements are consistent with the critical stress of 12 kPa reported here. We note, however, that the values reported in studies using nanoscale tips are somewhat larger, which suggests differences between the rupture mechanisms induced by nanometric and by micrometric tips.

The mechanical rupture criterion based on a critical compressive stress is consistent with a microscopic energetic criterion to nucleate a hole through the membrane

We have concluded that microindentation induces membrane rupture through the normal stress exerted on the cell. The question remains of how this constant compressive stress translates into a mechanism of membrane rupture. Indeed, following the work of Evans et al., who used micropipette aspiration to rupture lipid vesicles, membrane rupture is commonly characterized by a critical tension rather than a critical stress. In the case of micropipette aspiration experiments, this critical tension induces sufficient stretching of the membrane to rupture it (Evans *et al.*, 2003). However, unlike the aforementioned study, in our work the membrane is confined between the indenter and the substrate. Our setup thus resembles the configuration investigated by Butt et al., who investigated both experimentally and theoretically the rupture of a supported lipid bilayer compressed by an AFM tip (Butt and Franz, 2002; Loi *et al.*, 2002). Following a reasoning similar to that of Butt et al., rupture occurs when release of the elastic energy stored in the indenter suffices to dislodge a sufficiently large number of membrane lipid molecules to nucleate a hole. The elastic energy released by the indenter at membrane rupture is equal to $k_m\delta^* dz(\tan\alpha - \tan\beta)$, where dz corresponds to the additional vertical displacement of the indenter allowed by membrane rupture. The energy required to dislodge n lipid molecules is of the order of nk_BT. If we estimate that $n \sim S_{contact}/S_{lipid}$, with $S_{lipid} \sim 1$ nm^2 being the membrane surface area occupied by a lipid molecule, by equating the two energies we obtain a membrane rupture criterion of the form:

$$\sigma^* = \frac{V^*}{S_{contact}} = \frac{k_B T}{dz S_{lipid}} . \quad (6)$$

The value of the vertical displacement of the microindenter at rupture, dz, will lie between the thickness of the lipid bilayer (of the order of 10 nm) and the remaining thickness of the compressed cell (of the order of 1 μm), yielding a value of σ^* between 10 and 400 kPa. However, we note two reasons why this range is probably overestimated. First, we probably overestimate the number of molecules that must be dislodged to rupture the membrane, which we have taken as the number of lipids in the contact area, since, as pointed out by Butt et al., only a subset of molecules need to be dislodged for the process of rupture to start. Second, as discussed in the Results section, microindentation induces a radial deformation of the cell, thus introducing a membrane stretching energy that will facilitate rupture. Therefore, we presume that a realistic value of σ^* afforded by the energetic argument should be towards the lower end of the estimated range above, which is consistent with our measured experimental value.

Membrane rupture may occur during cell-cell interactions

Carman et al. (Carman *et al.*, 2007; Carman, 2009) described how T lymphocytes use "invadosome-like protrusions" to probe endothelial cells and to select the location to undergo transcellular diapedesis. This echoes the findings of Shulman et al. (Shulman *et al.*, 2011) that T lymphocytes can be guided during transendothelial migration by intraendothelial chemokine stocks. T lymphocytes reach these stocks by projecting filopodia that invade endothelial cells. Furthermore, Ueda et al. had previously shown that during the formation of the immune synapse, T-cells emit pseudopodia that penetrate deeply into the antigen-presenting cell (Ueda *et al.*, 2011). The pushing forces generated by these filipodia/protrusions were not measured in these studies. However, by using the micropipette force probe that we recently developed (Basu *et al.*, 2016), we measured that, when brought in contact with activating microbeads, T cells can generate pushing forces in the range of ~500 pN via a single thin protrusion, whose tip can be roughly estimated to have a 50 to 500-nm radius (unpublished). This leads to a compressive stress of ~0.5 to 75 kPa. Together with the results presented here, this suggests that T protrusions generated by T cells should be able to rupture the membrane of cells with which they interact.

Rupture of endothelial cell membranes during stent deployment

The present experimental and numerical results indicate that given the stress levels during stent deployment, generalized rupture of endothelial cell membranes and hence massive endothelial damage cannot be avoided. This conclusion is consistent with medical observations reporting that stent deployment, even if only lasting a few

seconds, completely destroys the endothelium along the strut region (Rogers *et al.*, 1999). Consistent with the literature (Lally *et al.*, 2005), we predict stresses and strains that are highly concentrated at the edge of the stent strut (Figure 3.4B); it is thus in this region that we expect the arterial wall damage to be most acute.

Comparison of the critical compressive stress with variations in blood pressure

The variation of aortic pressure between diastole and systole in a healthy adult is on the order of 50 mmHg, or 6.7 kPa. This is approximately one half of the critical compressive stress we measured here, above which there is a risk of membrane rupture of endothelial cells. This implies that under normal physiological conditions, pressure variations in the bloodstream are unlikely to cause the membrane damage that is observed in vivo (Yu and McNeil, 1992). Besides, it is possible that a more spatially uniform pressure as is found in the bloodstream causes less damage than the non-uniform compressive stress applied in our experiments. Hence, we speculate that the critical pressure required for membrane rupture in vivo could be even higher than 12 kPa (90 mmHg). We conclude that material resistance properties of endothelial cells are finely tuned to withstand physiological pressure variations, unlike the case of human interventions such as stenting procedures or angioplasties.

Conclusions and perspectives

In summary, we have introduced tilted microindentation, a simple and cost-effective technique to exert controlled compression forces on adherent cells. We have applied this technique to characterize the mechanics of endothelial cells under compression. In our experiments, the friction between the glass microindenter and the cell membrane is negligible; thus, the microindenter applies only a normal force on the cell. At low force (indentation smaller than 0.5 μm), cell indentation mechanics can be interpreted using Hertz's model, from which we deduce an apparent Young's modulus of endothelial cells of about 2 kPa (Supplementary Material Figure 3.7). For a maximum indentation estimated at 0.6 μm, the remaining cell debris behave as nearly incompressible, although the compression stress continues to increase with increased indentation. Endothelial cell membrane rupture occurs at a constant compressive stress of 12.4±0.6 kPa, which at the molecular level appears to correspond to the energy required to nucleate a hole through a lipid membrane. This value of critical stress is in agreement with published results for indentation-induced membrane rupture in other cell types measured using other techniques, thus suggesting some degree of generality of this result. Our numerical simulations of stent deployment show that the stresses induced during this surgical procedure are significantly higher than those required to rupture the endothelial cell membrane.

Thus, generalized and inevitable damage of endothelial cell membrane occurs during the currently used protocols for stent deployment.

In perspective, tilted microindentation can be used to investigate endothelial cell fate upon membrane damage as well as the mechanisms of membrane repair following rupture. We have previously used micropipettes to rupture the plasma membrane of endothelial cells in order to study ensuing mitochondrial fission (Gonzalez-Rodriguez *et al.*, 2015). In this previous study we did not control the force exerted by the microindenter. The present work establishes a technique to predict and control the force necessary to break the membrane. Importantly, the technique presented here allows us to control the extent of the damage done to the cell membrane. In addition to improving our understanding of endothelial cell responses to membrane rupture, such as mitochondrial fission, tilted microindentation provides a highly versatile be a tool for studying membrane repair. Indeed, membrane repair processes are expected to differ depending on the size of the wound created in the membrane (Andrews *et al.*, 2014), which can be tuned by applying a controlled force with an indenter of controlled size.

Acknowledgments

The authors acknowledge Caroline Frot, Antoine Garcia, Daniel Guy, Delphine L'Huillier, Magali Tutou, and Do Chi Toai Vu for technical support. This work has benefited from the financial support of the LabeX LaSIPS (ANR-10-LABX-0040-LaSIPS) managed by the French National Research Agency under the "Investissements d'avenir" program (n°ANR-11-IDEX-0003-02). This work was also supported by an endowment in cardiovascular cellular engineering from the AXA Research Fund. Lionel Guillou was supported by a Gaspard Monge doctoral fellowship from Ecole Polytechnique. Francois Cornat was supported by a doctoral fellowship from Ecole Normale Superieure. Julie Lafaurie-Janvore was funded by postdoctoral fellowships from the Fondation Lefoulon-Delalande and the AXA Research Fund.

Author contributions: D.G.-R, E.L., A.I.B. and J.H. designed research; D.G.-R., L.G., F.C., and J.H. performed research; J.L.-J., and A.B. contributed new reagents/analytic tools; D.G.-R., L.G., F.C., and J.H. analyzed data; and D.G.-R., L.G., F.C., A.I.B., and J.H. wrote the paper.

More specifically, Lionel Guillou (L.G.) performed the numerical simulations modeling a cell indentation using FEBio (the ones of a stent deploying in an artery, which were performed using Comsol, were done by F.C.), estimated numerically the radial strain during indentation, performed the experiment looking at 2D

deformations in a cell during indentation using a fluorescent tracker of mitochondria to substantiate this numerical finding through experimental evidence, performed a few tilted microindentation experiments (the vast majority were performed by J.H.) and contributed to discussions interpreting our data, in particular with respects to the estimation of the surface area of contact during indentation and the comparison of our results to *in vivo* situations.

3.3 SUPPLEMENTARY MATERIAL

Analytical model relating the displacement of the microindenter's tip to the vertical force it exerts on the cell

We model the microindenter as an inextensible, linear elastic cantilever beam of length l and bending modulus $E_m I$ (Supplementary Material Figure 3.5A). The tip of the cantilever is attached to a spherical bead of radius R (alternatively, in some of the experiments, the tip is cut and forms a flat punch parallel to the cell surface). The upper end of the cantilever is clamped so as to control its position and prevent rotation. The microindenter is held tilted, initially forming an angle α with the horizontal plane of the sample. During indentation, the position of the upper end is lowered at constant speed, along a straight trajectory that forms an angle of attack β with the vertical direction. We denote the vertical and horizontal displacements imposed to the upper end as δ and λ, respectively. The motion of the upper end induces a vertical indentation of the cell, Δz; moreover, the microindenter's tip glides horizontally by a distance Δx. The cell exerts reaction forces on the bead in the horizontal and vertical directions, denoted H and V. After indentation, the beam adopts a deformed shape described by $\theta(s)$, where θ is the local angle of the beam axis with the horizontal direction and s is the curvilinear coordinate (Supplementary Material Figure 3.5A). The function $\theta(s)$ can be obtained by imposing equilibrium of torques acting on the cantilever's bead:

$$-Hz - Vx = B\frac{d\theta}{ds}. \tag{1}$$

Hereafter we make use of nondimensional variables, denoted by a hat (^). The unit length and force for nondimensionalization are defined based on the microindenter's length, l, and stiffness, $k_m \equiv E_m I / l^2$. By expressing (x,z) in terms of (s,θ), Eq. (1) yields an integral equation for $\theta(s)$:

$$\pm\frac{1}{\sqrt{2\hat{F}}}\int_{\theta_0}^{\theta}\frac{d\theta}{\sqrt{\cos(\theta_F-\theta)-\cos(\theta_F-\theta_0)}} = s, \tag{2}$$

where $F = \sqrt{H^2+V^2}$ is the magnitude of the reaction force and $\theta_F = \mathrm{atan}(V/H)$ is the angle of the reaction force with the vertical. In Eq. (2), we will keep the positive sign in front of the integral, which corresponds to a deformed shape where $d\theta/ds > 0$, consistent with the experimental curvature of the microindenter. Assuming small deformations, i.e., assuming $\hat{F} = F/(k_m l) \ll 1$, from Eq. (2) we can obtain an asymptotic expansion for θ near $s = 0$ in powers of $\hat{F}$:

$$\theta = \theta_1 + \frac{\hat{F}\sin(\theta_F-\theta_1)}{2}\hat{s}^2 - \frac{\hat{F}^2\sin(2\theta_F-2\theta_1)}{48}\hat{s}^4 + O(\hat{F}^3). \tag{3}$$

The three unknowns in Eq. (3), $\hat{F}$, θ_F, and θ_1, are determined by the following three boundary conditions, reflecting the proscribed upper end rotation and the beam's inextensibility:

$$\theta(\hat{s}=1)=\alpha\ , \tag{4}$$

$$\int_0^1 \cos\theta\, d\hat{s} = \cos\alpha + \hat{\lambda} + \Delta\hat{x}\ , \tag{5}$$

$$\int_0^1 \sin\theta\, d\hat{s} = \sin\alpha - \hat{\delta} + \Delta\hat{z}\ . \tag{6}$$

We propose a simple material characterization of the cell where it behaves as a non-adhesive homogeneous isotropic linear elastic solid up to a maximum indentation, $\Delta z = \Delta z_{max}$, at which point the cell becomes infinitely rigid when compared to the microindenter. Indeed, the cell will appear progressively stiffer as the indentation becomes larger compared to the sample thickness (Dimitriadis *et al.*, 2002), saturating at indentations of ~80% of the cell height, where the cell becomes nearly infinitely rigid (Peeters *et al.*, 2005). At weak indentation, the cell's reaction to deformation is thus $V = k_{cell}(\Delta z)^{3/2}$, where according to Hertz's model $k_{cell} = \frac{4}{3}E^*\sqrt{R}$ and $E^* = \frac{E}{1-\nu^2}$, with E and ν being the Young's modulus and Poisson's ratio of the cell (Johnson, 1985). Neglecting horizontal friction (i.e., $H = 0$ and $\theta_F = \pi/2$), Eqs. (3-6) yield to leading order

$$\Delta x_{eff} = \Delta x + \lambda = \frac{2\sin(2\alpha)}{9}\frac{E^*\sqrt{R}}{k_m}\delta^{3/2}\ . \tag{7}$$

Beyond the maximum indentation, $\Delta z = \Delta z_{max}$, we reach the second regime where we treat the cell as infinitely rigid and write, to leading order,

$$\Delta x_{eff} = \Delta x + \lambda = \tan\alpha(\delta - D_{lin})\ , \tag{8}$$

where D_{lin} is a constant (Supplementary Material Figure 3.5B). We consider that the cell behaves as a rigid body with Coulomb friction, i.e., we assume $\Delta z = \Delta z_{max}$ = constant and $|H/V| = \mu$, the dynamic friction coefficient between the microindenter and the cell membrane. With these assumptions, Eqs. (3-6) yield, to leading order:

$$\Delta x = \delta(\tan\alpha - \tan\beta) = \frac{V}{k_m}(\tan\alpha - \tan\beta)(\cos^2\alpha + sign(\beta-\alpha)\mu\sin\alpha\cos\alpha)\ . \tag{9}$$

Eq. (9) can be applied to membrane rupture conditions, denoted by an asterisk (*): $\Delta x = \Delta x^*$, $V = V^* = \sigma^* S_{contact}$. By measuring Δx^* for different values of the angle of attack, β, Eq. (9) enables the calculation of the friction coefficient μ. If we consider the case where the imposed displacement of the upper end is vertical ($\beta = 0$) and assuming negligible friction between the microindenter and the cell ($\mu \approx 0$, see discussion in the main text), Eq. (9) simply reduces to

$$V = 2k_m\Delta x/\sin(2\alpha)\ . \tag{10}$$

Moderate indentations provide an estimate of the cell's apparent Young's modulus

The normal force applied by the microindenter onto the cell can be deduced from the measurement of the horizontal displacement of the microindenter's tip. By assuming that the contact between the microindenter and the cell is described by Hertz's model (Edelstein *et al.*, 2014), we can use tilted microindentation to estimate the local apparent Young's modulus of the cell. To this end, we record the horizontal displacement of the microindenter's tip, Δx, as a function of the imposed vertical displacement of its upper end, δ. We obtain an indentation curve of the form represented in Supplementary Material Figure 3.5B. We can fit a straight line to the large deformation regime of the resulting curve, and thus deduce D_{lin} and the corresponding tip displacement, Δx_{lin} (Supplementary Material Figure 3.5B). Supplementary Material Figure 7 shows the measured relationship between D_{lin} and Δx_{lin} for indentations performed on the cell's perinuclear region (Supplementary Material Figure 7A) and on the cytoplasmic region (Supplementary Material Figure 7B). By normalizing Δx_{lin} according to Eq. (7), the measurements collapse onto a straight line whose slope equals the apparent, local Young's modulus, E^*. From the measurements in Supplementary Material Figure 7 we deduce an apparent Young's modulus of 1.9±0.2 kPa at the thicker perinuclear region and of 2.5±0.3 kPa at the thinner cytoplasmic region. We note that the variability among different experimental repetitions appears comparable to the variability between different cell regions, so we cannot satisfactorily resolve the intracellular variability of the Young's modulus with our current experimental setup. Nevertheless, disregarding intracellular variability, we measure Young's moduli that are consistently of the order of the kPa, in agreement with typical values previously reported for endothelial cells (ref 44 in main text).

Supplementary Figures

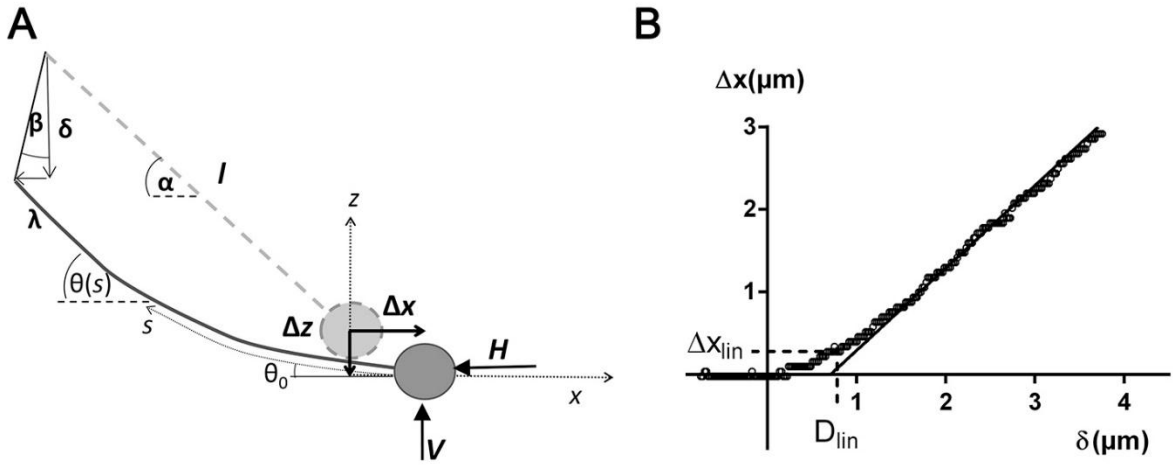

FIGURE 3.5: Relationship between imposed vertical displacement and horizontal displacement of the microindenter's tip. (A) Geometric parameters defining the deformation of the microindenter. (B) Example of the measured horizontal displacement of the microindenter's tip, Δx, as a function of the imposed vertical displacement of the upper end of the microindenter, δ.

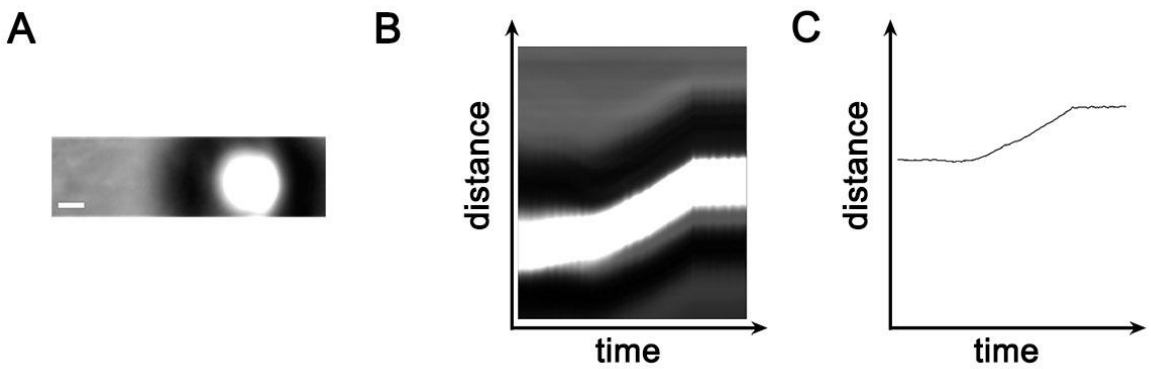

FIGURE 3.6: Analysis of tilted microindentation used to characterize the moderate indentation regime. (A) Image extracted from movie taken during experiment. (B) Kymogram obtained after importing movie in ImageJ, normalizing and smoothing the images, and then defining a line along the horizontal bead trajectory when sliding on the surface of the cell. The kymogram represents this line at each frame, forming a distance – time graph coded in intensity. (C) The kymogram is then thresholded in order to select the dark rim of the bead. The image is binarized according to this threshold, resulting in the distance-time graph shown. The resulting (position, frame number) coordinates of the edge of the binary are then stored in a text file.

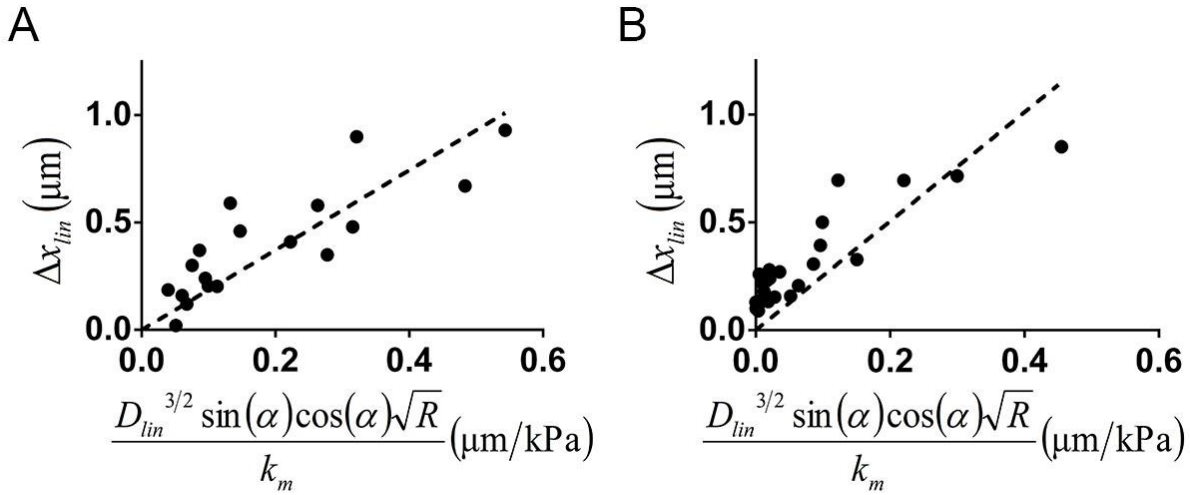

FIGURE 3.7: Measured horizontal displacement of the microindenter's tip, Δx_{lin}, corresponding to an imposed vertical displacement of the upper end of the microindenter $\delta = D_{lin}$. The horizontal axes are normalized as suggested by Eq. (7). (A) Measurements of microindentation on the cell's perinuclear region. The slope of the linear regression yields an estimate of the Young's modulus of the perinuclear region, $E^* = 1.9 \pm 0.2$ kPa. (B) Measurements of microindentation on the cytoplasmic region. The slope of the linear regression yields the estimate $E^* = 2.5 \pm 0.3$ kPa.

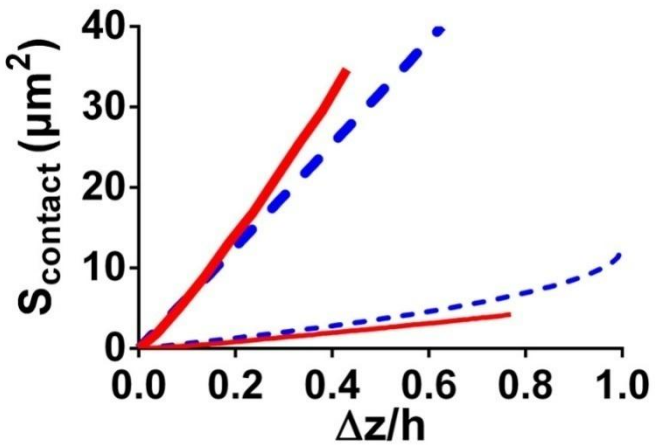

FIGURE 3.8: Numerical simulations (solid lines) of the relationship between the contact area, $S_{contact}$, and the indentation normalized by the cell thickness, $\Delta z/h$. The cell is modeled as a hyperelastic medium of finite thickness, h. The dashed lines correspond to the modified Hertz model, $S_{contact} = 2\pi R \Delta z$. The thin lines correspond to $R/h = 1$ and the thick lines to $R/h = 10$.

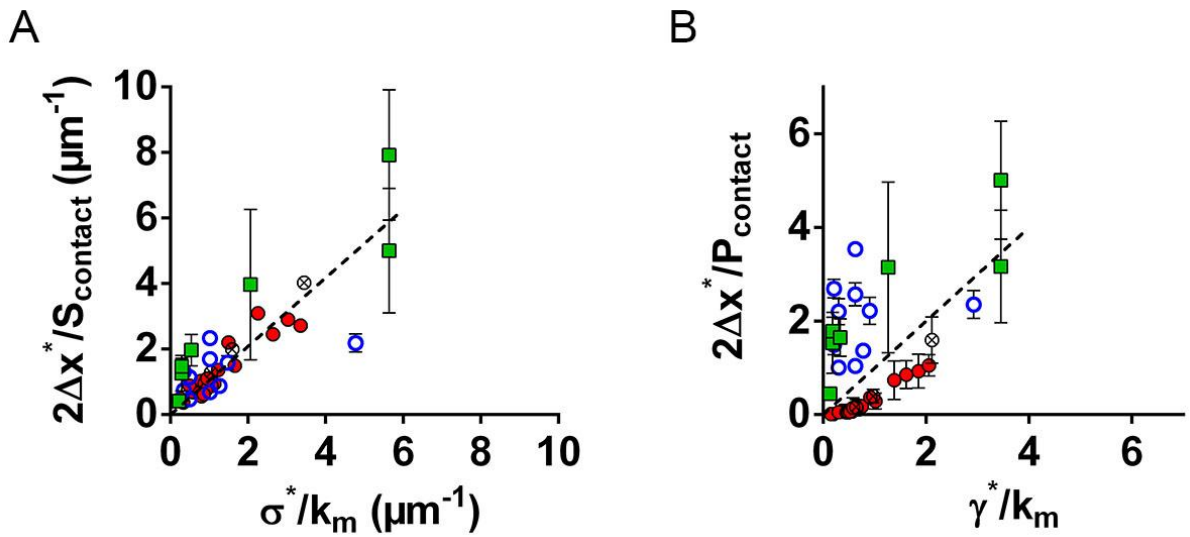

FIGURE 3.9: Comparison between the goodness of fit of two rupture criteria, based on either a critical stress (in plot A) or a critical tension (in plot B). Data from Figure 2D in the main text are used. The displacement of the microindenter's tip at membrane rupture, Δx^*, is normalized by either the area, $S_{contact}$, (in plot A) or by the perimeter, $P_{contact}$, (in plot B) of the contact surface between the microindenter's tip and the cell. This normalized displacement is represented as a function of the inverse of the stiffness, k_m, normalized by either a best-fit critical stress, $\sigma^* = 12.4$ kPa, (in plot A) or by a best-fit critical tension, $\gamma^* = 7.6$ nN/μm, (in plot B). Different geometries of the microindenter's tip are used: spherical tip (full circles, N = 133 cells), rectangular flat tip (empty squares, N = 41 cells), circular flat tip (empty circles, N = 134 cells). The encircled crosses correspond to spherical-tip microindentation measurements upon cytochalasin-D treatment. Error bars represent standard error of the mean. For all cases, $\alpha = 45°$. The dashed line is a linear fit of all data. A dashed line of slope 1 and coefficient of determination of 1 would indicate that the proposed normalization yields a perfect collapse of all data. (A) The best linear fit obtained with a critical stress criterion, with $\sigma^* = 12.4$ kPa, has a slope of 1.04±0.06 and a coefficient of determination $R^2 = 0.7$. (B) The best linear fit obtained with a critical tension criterion, $\gamma^* = 7.6$ nN/μm, has a slope of 1.0±0.1 but a markedly lower value of $R^2 = 0.25$.

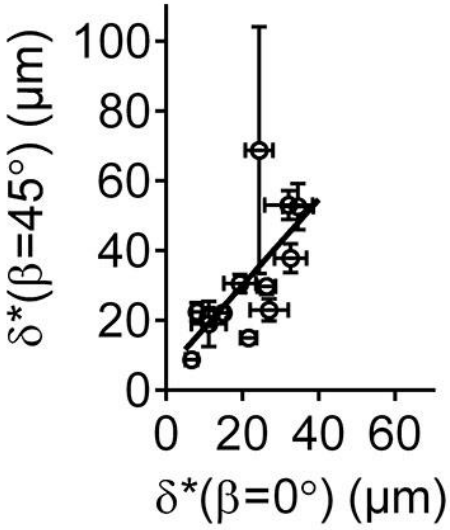

FIGURE 3.10: Cell membrane rupture is obtained for the same vertical displacement of the upper end of the microindenter, δ^*, for angles of attack $\beta = 0$ degrees and $\beta = 45$ degrees. Each circle represents between 4 and 7 cells with 13 different microindenters of spherical tips. Error bars are standard error of the mean. The straight line is a linear fit of the data: $\delta^*(\beta = 45°) = (1.2\pm0.4)\ \delta^*(\beta = 0°) + (6\pm9)$ μm.

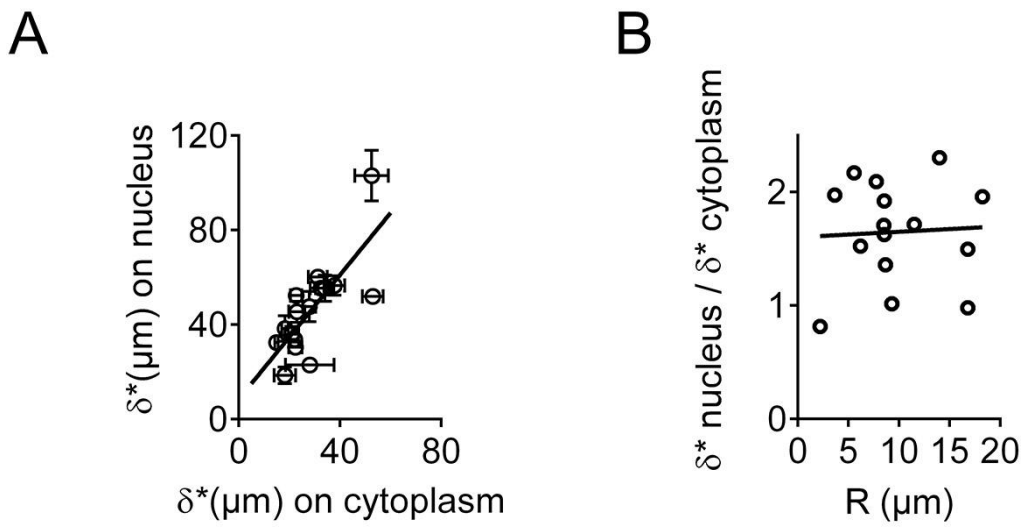

FIGURE 3.11: (A) Cell membrane rupture occurs at a comparable but slightly larger displacement δ^* when compressing a cell on top of the nucleus than when compressing it on top of the thin parts of its cytoplasm. The microindentation is performed at an angle of attack $\beta = 45$ degrees with 11 microindenters with spherical

tips of varying radius R. Each circle represents between 4 and 9 cells, error bars are standard error of the mean. The straight line is a linear fit of the data: $\delta^*_{nucleus}$ = (1.3±0.3) $\delta^*_{cytoplasm}$ + (9±9) μm. (B) The ratio $\delta^*_{nucleus}/\delta^*_{cytoplasm}$ is independent of the radius of the microindenter, R. The data are the same as in (A) but plotted against R. The straight line is a linear fit to the data, $\delta^*_{nucleus}/\delta^*_{cytoplasm}$ = (1.6±0.3) + (0.005±0.025)R.

3.4 METHOD BOX: USING MITROTRACKER AND PIV TO FOLLOW 2D DEFORMATION OF AN ADHERENT CELL

To investigate the membrane rupture mechanisms during tilted microindentation, we wanted to visualize the deformations in the horizontal plane of bovine aortic endothelial cells during indentation. To this end, we developed a method that combines fluorescence microscopy with PIV analysis. In our opinion, this method holds much promise for future applications, and we therefore present its functioning and potential for further development here.

The first step is to incubate cells in Mitotracker M7510 for 30 min, as detailed by Gonzalez-Rodriguez *et al.* (Gonzalez-Rodriguez *et al.*, 2015), in order to make the mitochondria visible under fluorescence microscopy. As a test case, we perform tilted microindentation on a bovine aortic endothelial cell with fluorescently labeled mitochondria and acquire 10 frames per second during this indentation using fluorescence microscopy. We then use the CRToolbox developed and made freely available online by Julien Diener at https://sites.google.com/site/crtoolbox/home to track the displacements of the mitochondria (Diener *et al.*, 2012). From there, we use a custom-made Matlab code to visualize the 2D displacements (Figure 3.12).

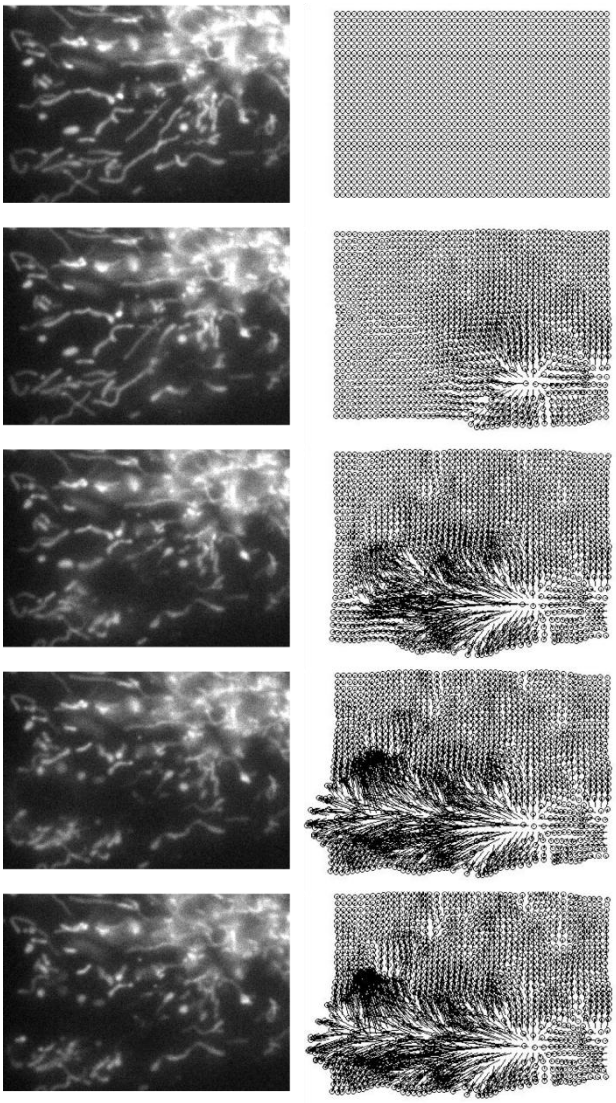

FIGURE 3.12: Fluorescently labeled mitochondria are used to track 2D horizontal displacements at the subcellular level. On the left side, the fluorescent images are obtained using a 100x microscope. On the right side, lines indicate the displacement of virtual particles (shown as circles) compared to the frame of reference (first frame).

In further iterations of this method, it would be possible to use the Matlab interface with Micromanager to import the fluorescent images live at a frequency of 10-100 Hz, depending on the size of the region of interest (ROI). Then, if the PIV tool were to run in parallel, using the first image as a reference image, we could imagine seeing cell displacements and deformations live. This is in essence similar to the profile microindentation tool developed by Julien Husson, which uses cross-correlation of the image of the microindenter's tip to determine its position. The main difference is that the cross-correlation needed here provides information in 2D,

compared to 1D for the microindentation, and therefore requires considerably more computing resources. Because of the time required to run the PIV tool and to render its output visually useful (for instance, to create a horizontal deformation map), the frequency of refreshing of this 2D information would be considerably lower than 10-100 Hz, possibly ~0.1 Hz, although that remains to be tested (and optimized).

In summary, we believe this method holds promise as a tool to study the mechanics and physics of adherent cells. For instance, one could imagine employing such a tool to further study membrane rupture of endothelial cells in a more quantitative manner.

CHAPTER 4

Membrane rupture criterion for non-adherent cells

4.1 INTRODUCTION

Having studied membrane rupture of endothelial cells, we then turned our attention to leukocytes and sought to identify a physical criterion predictive of membrane rupture for this second cell type involved in atherosclerosis.

To trigger membrane rupture, we employed micropipette aspiration. We then compared the increase in membrane surface area at rupture with measurements of "true" (total) membrane surface area using scanning electron microscopy. We presented those results in an article (submitted) and reproduce them in section 4.2, along with the corresponding supplementary material, which we reproduce in section 4.3. We further investigated in this work how membrane surface area evolves during active deformations and in particular during transendothelial migration, a process central to atherosclerosis.

To reproduce conditions that mimic transendothelial migration *in vivo*, it is necessary to control the temperature throughout the experiment. To this end, we built a custom-made temperature control chamber. We present how an experimentalist can make his/her own chamber with a limited budget in section 4.4.

During *in vitro* experiments of active cells in a Petri dish, such as transendothelial migration experiments, it is often of interest to track the migration of cells. During the time spent at the Kumar laboratory at UC Berkeley, we encountered many researchers who would spend hours tracking cells manually. Therefore, we built a tool that uses ImageJ and Matlab to perform automated cell tracking and present this tool in section 4.5.

During micropipette aspiration, such as performed to investigate the membrane rupture of leukocytes, cells undergo large deformations. We developed a code using Matlab, Gmsh and FEBio (all open source except for Matlab) to compute these deformations for a cell modeled as an elastic solid. This modeling of a non-adherent cell as an elastic solid, while unusual (such a cell would typically be modeled as a viscous liquid contained in a cortical cell with a surface tension), is motivated by our results that show that T lymphocytes behave as would an elastic solid during profile microindentation (see for instance Figures 4.2 and 4.10). While the outcome of these simulations was not directly useful in interpreting our own

results, we hope they can be of further use and therefore present them in section 4.6 We also provide the full simulation code in the Appendix section of this manuscript.

Finally, we observed during this work on membrane rupture of leukocytes that cell tension in T lymphocytes increased with apparent membrane surface area. Hence, we wondered if this would also correlate with the efficiency of pore-forming molecules. This question was motivated by recent work by Basu *et al.* (Basu *et al.*, 2016) which showed such an effect for perforin. We present our results for saponine and Jurkat cells in section 4.7.

4.2 T LYMPHOCYTE PASSIVE DEFORMATION IS CONTROLLED BY UNFOLDING OF MEMBRANE SURFACE RESERVOIRS

Lionel Guillou, Avin Babataheri, Michael Saitakis, Armelle Bohineust, Stéphanie Dogniaux, Claire Hivroz, Abdul I. Barakat, and Julien Husson

Abstract

T lymphocytes in the human body routinely undergo large deformations, both passively when going through narrow capillaries and actively when transmigrating across endothelial cells or squeezing through tissue. We investigate physical factors that enable and limit such deformations and explore how passive and active deformations may differ. Employing micropipette aspiration to mimic squeezing through narrow capillaries, we find that T lymphocytes maintain a constant volume while increasing their apparent membrane surface area upon aspiration. Human resting T lymphocytes, T lymphoblasts and the leukemic Jurkat T cells all exhibit membrane rupture above a critical membrane area expansion that is independent of either micropipette size or aspiration pressure. The unfolded membrane matches the excess membrane contained in microvilli and membrane folds, as determined using scanning electron microscopy. In contrast, during transendothelial migration, a form of active deformation, we find that the membrane surface exceeds by a factor of two the amount of membrane stored in microvilli and folds. These results suggest that internal membrane reservoirs need to be recruited, possibly through exocytosis, for large active deformations to occur.

Introduction

The ability of T lymphocytes to both patrol the vasculature and to extravasate into surrounding tissue is a central feature of the human adaptive immune response (von Andrian and Mempel, 2003; Valignat *et al.*, 2013; Crotty, 2015; DuPage and Bluestone, 2016). Accomplishing these tasks requires T lymphocytes to undergo large deformations, both passively as they move through narrow capillaries during their patrols (Fung, 2013), and actively upon extravasation at a site of inflammation or injury (Carman and Springer, 2004; Carman, 2009; Carman and Martinelli, 2015). In certain cell types, for instance neural cells during brain trauma, excessive strain can cause membrane damage both *in vitro* (Geddes *et al.*, 2003) and *in vivo* (Pettus *et al.*, 1994; Pettus and Povlishock, 1996). To our knowledge, however, there have been no reports of T lymphocyte membrane damage *in vivo* despite the large deformations that these cells undergo. In the present study, we wanted to understand how T lymphocytes respond to large passive deformations. We asked specifically if there was a physical criterion for these deformations to trigger membrane rupture and whether or not this criterion changed during the life of a T lymphocyte (when the resting T lymphocyte becomes a lymphoblast). Finally, we investigated whether such a criterion would also apply to large active deformations as occurs during cell spreading and extravasation.

Results

A T lymphocyte increases its surface area at constant volume when entering in a narrow capillary

To mimic the partial or complete passage of T lymphocytes through a narrow capillary *in vivo*, we aspirate T lymphocytes into glass micropipettes of a few microns in diameter. After grabbing T lymphocytes using a small aspiration pressure (10 to 20 Pa), we apply a constant aspiration pressure ΔP (Figure 4.1A) and observe the entry of the aspirated cell for 5 minutes. Measuring the cell dimensions before and after this aspiration period, we show that cell volume is constant regardless of the T lymphocyte activation state, the aspiration pressure or the capillary size (Figure 4.1B and Supplementary Material Figure 4.8). We note that the volumes seen here for T lymphocytes are consistent with what we find using fluorescent staining and confocal microscopy (Supplementary Material Figure 4.9). The preservation of the volume during aspiration is consistent with the fact that applied aspiration pressures, on the order of ~10-1000 Pa, are much lower than the cellular osmotic pressure of ~10^6 Pa maintaining the cell volume constant. In order to accommodate the constant volume constraint during aspiration, cells depart from their initial relatively spherical shape, which is the geometric shape that minimizes surface area for a given volume. As a result, their surface area increases, so that the membrane of a T lymphocyte is stretched when it passes through a capillary.

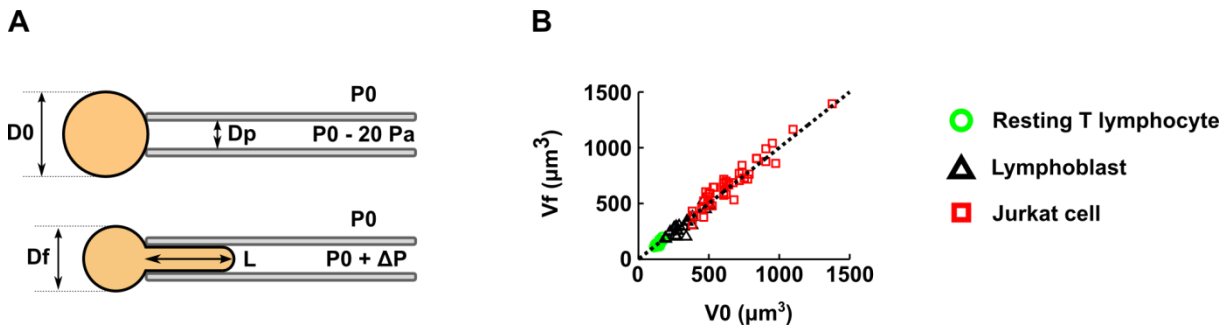

FIGURE 4.1: T lymphocyte volume is conserved during micropipette aspiration. (A) Diagram of a micropipette aspiration experiment. We impose an aspiration pressure P0+ΔP (ΔP assumes only negative values) and measure the initial cell diameter D0, the final cell diameter Df, the micropipette diameter Dp and the final entry length L. (B) Plot of the final cell volume Vf (see Supplementary Material Figure 4.8 for details on volume measurement), as a function of the initial cell volume V0. Data points fall on the dotted line of slope one (Vf = V0), showing that cell volume is conserved.

Surface area expansion of T lymphocytes is accompanied by an increase in cell stiffness

In order to determine if resting T lymphocytes respond mechanically to passive deformations undergone during their aspiration into a micropipette, we measure the evolution of their effective stiffness as determined by microindentation. Microindentation consists of applying a known compressive force to a T lymphocyte while measuring the resulting indentation (Figure 4.2). Using a model linking the applied force to the measured deformation allows the extraction of the mechanical parameters of the cell, such as its elastic properties (Guillou *et al.*, 2016).

First, we find that resting T lymphocyte behavior upon indentation is consistent with an elastic solid model. Indeed, the force-indentation curves we obtain are well described by the classical Hertz model, which is a standard model used to describe the indentation of an elastic solid (Johnson, 1985) often employed to analyze atomic force microscopy experiments (Dimitriadis *et al.*, 2002; Krause *et al.*, 2013). In this model, the indentation force, F, applied to an incompressible elastic substrate is related to the resulting indentation of this medium, δ, through the relationship $F = 16/9\ E\ \delta^{3/2}$. Thus, the force is directly proportional to the Young's modulus of the material E, which measures the elasticity of the medium (expressed in Pascals), and to the indentation raised to the power 3/2. As other types of elastic behavior exist, which are described by an exponent of the indentation other than 3/2 (Lomakina *et al.*, 2004), we fit our data using a more general relationship $F = \alpha\ \delta^{\beta}$, where α and β are adjustable fitting parameters. We find that β = 1.55 ± 0.14 (mean ± SD) for a set of 201 cell indentations (Figure 4.2C), in excellent agreement with the prediction of the Hertz model of β = 3/2 (see example curve in Supplementary Material Figure 4.10).

From the fitted value of α = 16/9 E we deduce that E = 77 ± 8 Pa (mean ± standard error of the mean) when the cell membrane is not stretched.

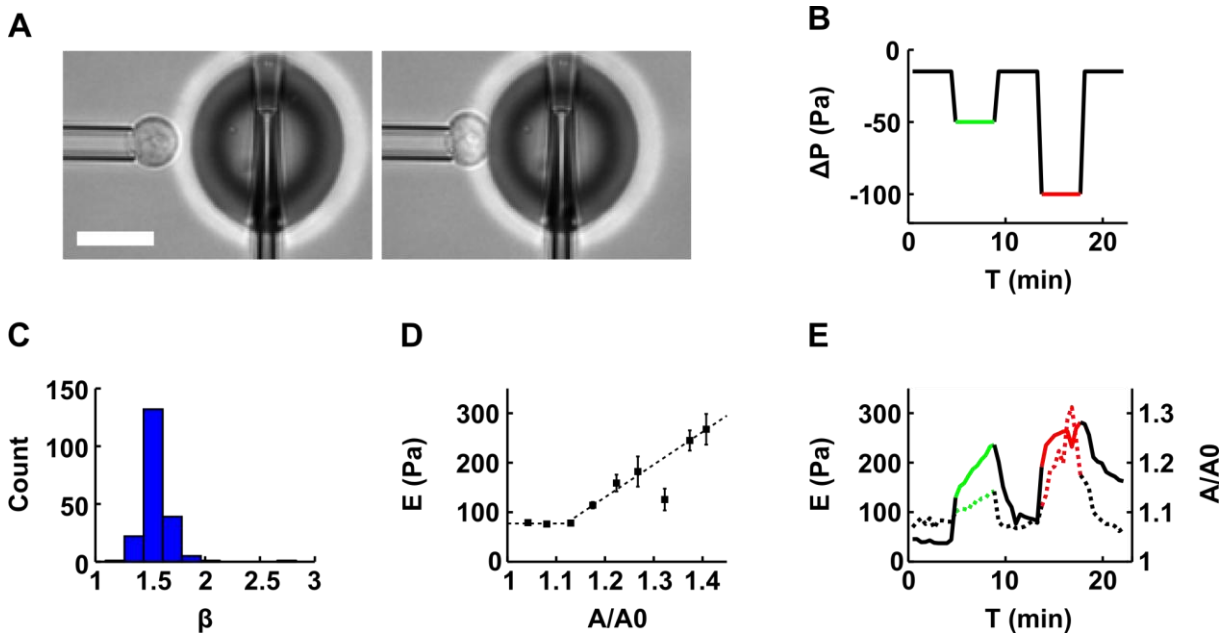

FIGURE 4.2: Resting T lymphocyte's apparent stiffness increases with apparent membrane surface area. (A) Example of a resting T lymphocyte being aspirated into a micropipette while its apparent stiffness is measured using profile microindentation. Scale bar is 10 μm. (B) Plot of the aspiration pressure ΔP used to hold the resting T lymphocytes during profile microindentation as a function of time. Each resting T lymphocyte is indented approximately 50 times, once every 30 seconds. In black, aspiration pressure is -15 Pa, green is -50 Pa and red is -100 Pa. (C) Histogram of the indentation scaling exponent β found during the profile microindentations. We fit the force-indentation curve using the relation $F = \alpha\ \delta^{\beta}$, with F the force, δ the indentation, and α and β two fitting parameters. (D) Plot of the apparent stiffness E as a function of the normalized apparent membrane surface area A/A0, where A0 is the initial membrane surface area and A the membrane surface area at the time where the apparent stiffness E is measured. Bars represent the standard deviation. We have N = 5 cells and n = 201 microindentations. The number of cells decreases for large values of A/A0. The 3 last points to the right correspond to only 5, 7 and 2 microindentations respectively, compared to more than 30 on average for the 6 points to the left. Dotted line represents the best fit using the phenomenological relation E = E0 for A/A0<(1+ε) and E = E0 + k (A/A0-(1+ε)) for A/A0>(1+ε). (E) Plot of the apparent stiffness E (left axis, dotted line) and the normalized apparent membrane surface area A/A0 (right axis, continuous line) averaged over n = 5 cells, as a function of time.

Second, we find that the effective cell stiffness increases with the apparent membrane surface area (Figure 4.2D). The increase in apparent membrane surface area is evaluated by tracking the ratio A/A0, where A is the apparent membrane surface area at the time of indentation, and A0 is the initial apparent membrane surface area. To test if this increase in cell stiffness depends on the applied aspiration pressure, we submit cells to a constant pressure while monitoring both the effective stiffness and the ratio A/A0. We find that both increase continuously under a constant aspiration pressure (Figure 4.2E). When different aspiration pressures are applied, the relationship between the effective stiffness and the apparent membrane surface area remains the same, i.e. the data points lie on the same $E = f(A/A0)$ curve. Furthermore, the relationship is reversible, in the sense that when aspiration pressure is reset to a low level (typically 10-20 Pa), both effective stiffness and apparent membrane surface decrease, following the same conserved relationship. We find that – similar to the approaches of Herant *et al.* and Lam *et al.* (Herant *et al.*, 2005; Lam *et al.*, 2009) – this relationship is well described by the phenomenological law $E = E0$ for $A/A0<(1+\varepsilon)$ and $E = E0 + k\,(A/A0-(1+\varepsilon))$ for $A/A0>(1+\varepsilon)$ (fit in Figure 4.2D), where E0 is the initial effective stiffness, k is an elastic expansion modulus and ε is a measure of membrane slack, corresponding to the fraction of initial apparent membrane surface area that can be taken before it is necessary to unfurl folds or microvilli. Fitting our data with this relation, we find $E0 = 77 \pm 8$ Pa, $k = 660 \pm 80$ Pa and $\varepsilon = 12 \pm 2\%$ (mean ± standard error of the mean). This finding is consistent with a previous estimate of human primary CD4+ T lymphocytes' stiffness of 85 ± 5 Pa using a parallel plates technique (Bufi *et al.*, 2015). Also, we find that T lymphocytes have about twice as much membrane slack as neutrophils, for which $\varepsilon = 6\%$ (Herant *et al.*, 2005).

Previous micropipette aspiration experiments have shown that membrane expansion is directly associated with an increase in cell tension γ for both neutrophils (Herant *et al.*, 2005) and macrophages (Lam *et al.*, 2009). In fact, the dependence of cell tension on membrane expansion takes the same form as we found for effective stiffness, i.e. $\gamma = \gamma 0$ for $A/A0<1+\varepsilon$ and $\gamma = \gamma 0 + k\,(A/A0-(1+\varepsilon))$ for $A/A0>1+\varepsilon$ (Lam *et al.*, 2009). Hence, the increase in effective stiffness we measure here is a direct indication that cell tension also increases. The connection between these two mechanical properties is further supported by recent experiments that show that the effective stiffness of a non-adherent cell, as measured by microindentation, is directly related to its cortical tension via the relation $E = \gamma^2\,(\pi D0)/(4hF)$ (Cartagena-Rivera *et al.*, 2016). In this relation, E is the apparent stiffness of the cell, γ its cortical tension, D0 the cell diameter, h the cell's cortical thickness, and F the indentation force. Taken together, these results show that apparent membrane surface area is a good predictor of cell mechanical properties.

T lymphocyte membrane ruptures at a well-defined entry length for a given capillary size

Beyond measuring how effective stiffness is reversibly linked to an increase of cell apparent area, we seek to understand if it is possible to induce permanent damage to a T lymphocyte by forcing it through a narrow capillary. To do so, we again employ micropipette aspiration as a proxy for passage into capillaries and use propidium iodide as a reporter of membrane rupture (Figure 4.3 A-C).

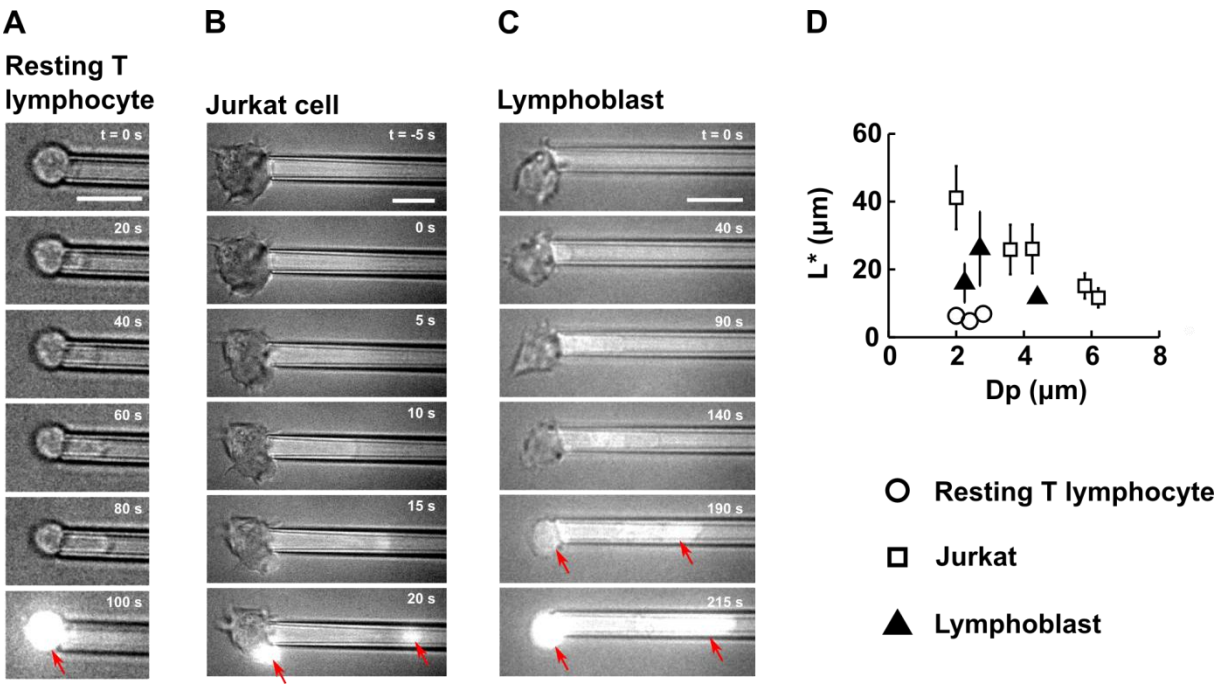

FIGURE 4.3: T lymphocyte membrane ruptures at a well-defined entry length L* during micropipette aspiration. (A-C) Example of membrane rupture triggered using micropipette aspiration for (A) a resting T lymphocyte, (B) a Jurkat cell and (C) a lymphoblast. Scale bar is 10 µm. The time is indicated in the top right hand corner, with t = 0 s chosen as the time at which the aspiration pressure goes from - 20 Pa to ΔP. A background of brightfield light is kept to visualize the cell throughout the experiment. Upon membrane rupture, propidium iodide enters the cell and binds to DNA, emitting a bright fluorescent signal (red arrows). (D) Plot of the entry length at rupture L* versus the micropipette diameter Dp for three cell types: resting T lymphocytes, Jurkat cells and lymphoblasts. Bars represent the standard deviation.

We observe that the membrane of resting T lymphocytes ruptures at a well-defined entry length L* = 6.3 ± 1.1 µm (mean ± SD) for micropipette diameters Dp varying between 2.0 and 2.8 µm (Figure 4.3D). For larger micropipette diameters, the membrane of resting T lymphocytes does not rupture, as cells are entirely aspirated

into the pipette, provided that a sufficient aspiration pressure is applied. Because of the experimental difficulties associated with performing micropipette aspiration with micropipettes below 2.0 μm in diameter, the range of micropipette diameters explored for resting T lymphocytes is *de facto* limited to values between 2.0 and 3.0 μm. To further explore the effect of micropipette diameter on membrane rupture, we perform micropipette aspirations on Jurkat cells, a leukemic T cell line commonly used as a model for T lymphocytes. Jurkat cells are larger than resting T lymphocytes, with an average diameter D0 = 10.6 ± 1.0 μm (mean ± SD) compared to D0 = 6.7 ± 0.4 μm (mean ± SD) for resting T lymphocytes, and therefore allow a wider range of micropipette diameters. We find that while the entry length at rupture L* is still a well-defined quantity for a given micropipette diameter Dp, L* decreases as Dp increases (Figure 4.3D). Also, we note that for a given micropipette diameter, the entry length at rupture is much greater for Jurkat cells than for resting T lymphocytes.

Activated T lymphocytes, also referred to as lymphoblasts, are much more effective at extravasating than resting T lymphocytes (Springer, 1994). This is due to the increased expression of receptors to certain chemokines and adhesion molecules. Yet mechanical and morphological properties of these activated T lymphocytes might also contribute to these functions. Thus, to understand how activating T lymphocytes affects their ability to deform, we perform micropipette aspirations on lymphoblasts. We find that lymphoblasts are slightly larger than resting T lymphocytes with an initial diameter D0 of 8.1 ± 0.7 μm (mean ± SD) and that their entry length at rupture L* = 19.0 ± 9.2 μm (mean ± SD) is 3 times as large as that of resting T lymphocytes (Figure 4.3D). Activation therefore considerably increases a T lymphocyte's ability to deform its membrane.

Maximum deformation of T lymphocyte at rupture does not depend on aspiration pressure

In order to test if the value of aspiration pressure affects the maximal entry length at rupture, L*, we vary aspiration pressure while holding the micropipette diameter constant. We find that, for a given micropipette diameter Dp, L* does not depend on the aspiration pressure for both resting T lymphocytes and Jurkat cells (Figure 4.4A). Nonetheless, higher aspiration pressures lead to shorter rupture times, as the cell entry into the micropipette occurs faster (Figure 4.4B). This shows that neither the level of aspiration pressure nor the duration of aspiration are intrinsic parameters to describe membrane rupture of T lymphocytes.

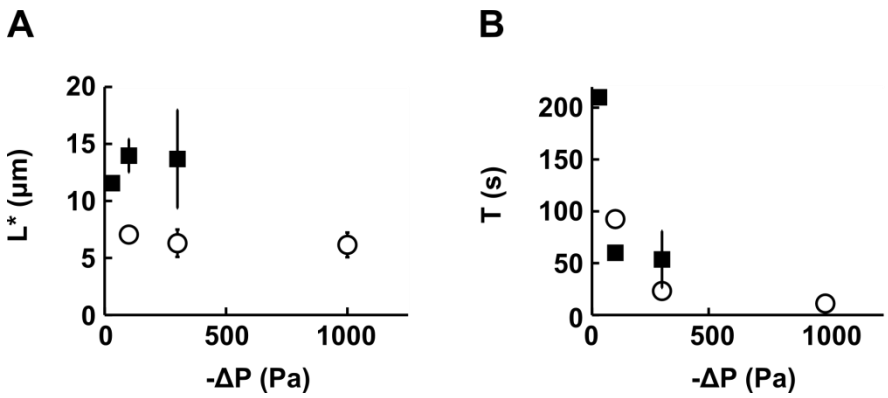

FIGURE 4.4: Effect of the aspiration pressure on T lymphocyte membrane rupture. (A) Plot of the entry length at rupture L* as a function of the absolute value of the aspiration pressure ΔP for resting T lymphocytes (white circles) and Jurkat cells (black squares). (B) Plot of the duration of micropipette aspiration T to rupture as a function of the absolute value of aspiration pressure ΔP for resting T lymphocytes (white circles) and Jurkat cells (black squares). Bars indicate standard deviation. For resting T lymphocytes, micropipette diameters between 2.0 and 2.8 µm were included (n = 14 ruptured cells). For Jurkat cells, micropipette diameters between 5.8 and 6.2 µm were included (n = 10 ruptured cells).

T lymphocyte membrane rupture occurs at a critical apparent membrane expansion

To elucidate the factor limiting passive deformations of T lymphocytes, we seek to obtain a criterion that is predictive of T lymphocyte membrane rupture. As noted above, cell volume is conserved during micropipette aspiration, so that the apparent membrane surface area increases as soon as the cell departs from a spherical shape that minimizes its surface area. Membrane expansion is again defined as the ratio between the apparent membrane surface area A divided by the initial apparent membrane surface area A0. Computing this membrane expansion across all the capillary sizes tested, we find that a critical membrane expansion defining a threshold beyond which membrane rupture is a criterion that predicts our data for both resting T lymphocytes and Jurkat cells fairly accurately (Figure 4.5). We find a critical membrane expansion A*/A0 = 1.22 ± 0.09 and A*/A0 = 1.48 ± 0.15 (mean ± SD) for resting T lymphocytes and Jurkat cells, respectively, where A* is the apparent membrane surface area at rupture. Lymphoblasts, on the other hand, show more variability, with A*/A0 = 1.36 ± 0.27 (mean ± SD). In the case of Jurkat cells, we also observe that for larger micropipette diameters, the critical membrane expansion decreases slightly, a possible bias being that large micropipette diameters are associated with lower aspiration pressures and shorter rupture times (Supplementary Material Figure 4.11). It is therefore possible that, in Jurkat cells, membrane expansion is favored by a longer squeezing time.

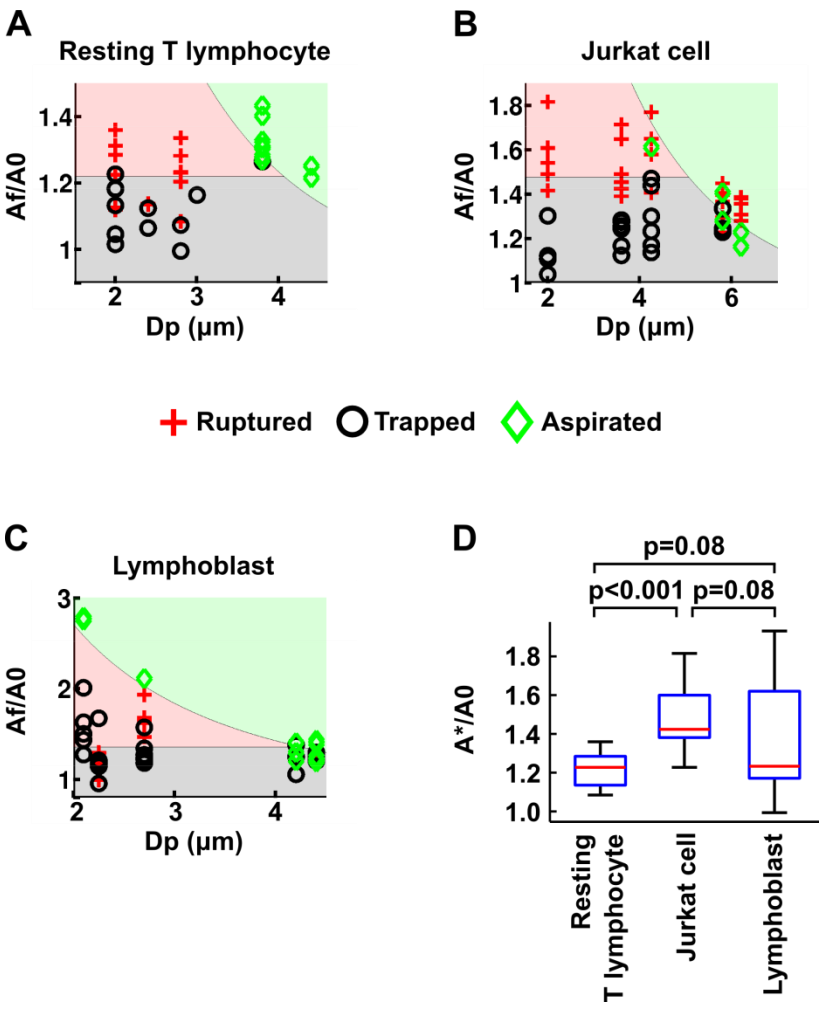

FIGURE 4.5: T lymphocyte membrane rupture occurs at a critical increase in apparent membrane surface area A*/A0. (A-C) "Phase diagram" of cell state after micropipette aspiration, depending on the micropipette diameter Dp and the membrane expansion, defined as the final apparent membrane surface area Af divided by the initial apparent membrane surface area A0. The phase diagrams are given for various cell types and conditions: (A) resting T lymphocytes, (B) Jurkat cells and (C) lymphoblasts. As shown in the legend, a red cross indicates a cell whose membrane ruptured, a black circle a cell that stayed trapped after 5 minutes of aspiration, and a green diamond a cell that was entirely aspirated inside the micropipette. The red filling indicates that in this zone, cell membranes are expected to rupture. The grey filling indicates that in this zone, a cell is expected to stay trapped inside the micropipette without rupturing or being entirely aspirated. The cutoff on the vertical axis between the red and the grey zone is chosen as the mean increase in apparent membrane surface area. The green filling indicates that in this zone, cells are expected to be entirely aspirated based on geometrical considerations and volume conservation. (D) Boxplot of the normalized apparent membrane surface area at rupture A*/A0 for the cell types and conditions reported in (A-C).

While our rupture criterion relates to membrane expansion, it is still consistent with a criterion based on a threshold in cell tension as used by others to describe the rupture of the membrane of fibroblasts (Tan *et al.*, 2011) or lipid vesicles (Evans *et al.*, 2003). In fact, as mentioned before, previous investigators have found that cell tension and membrane expansion are directly related in neutrophils (Herant *et al.*, 2005) and macrophages (Lam *et al.*, 2009). In our experiments, Laplace's law, while imprecise outside equilibrium, allows us to roughly estimate the cell tension at rupture γ^*. We find that $\gamma^* = 0.5 \pm 0.4$ mN/m (mean ± SD) for resting T lymphocytes, 1.2 ± 0.9 mN/m for lymphoblasts and 1.3 ± 0.8 mN/m for Jurkat cells. Interestingly, those values are close for all cell types, suggesting that this critical tension is an intrinsic mechanical parameter shared by the membrane of different cell types. However, this critical value might be different for adherent cells, as Tan *et al.* who used micropipette aspiration to rupture the membranes of fibroblasts, found a higher – although consistent – value of γ^*~3 mN/m at rupture (Tan *et al.*, 2011).

The amount of membrane deployed by T lymphocytes before rupture matches the stock of membrane contained in microvilli and membrane folds

While T lymphocytes may appear smooth (with some ruffles in the case of lymphoblasts and Jurkat cells) under optical microscopy, observations at the submicron scale under scanning electron microscopy reveals that the surface of T lymphocytes is covered with microvilli and membrane folds (Figure 4.6). For resting T lymphocytes and lymphoblasts, we mainly see microvilli, while for Jurkat cells, most of the excess membrane is found in the form of membrane folds.

The excess membrane contained in the microvilli of resting T lymphocytes has been previously estimated using scanning electron microscopy (Majstoravich *et al.*, 2004). To do so, Majstoravich *et al.* assumed a cylindrical shape for microvilli and measured the microvilli density (4.1 per μm^2), average length (380 nm) and average diameter (100 nm). This led them to estimate a relative excess membrane of ~49% for resting T lymphocytes. We note that earlier work in the 1980s that used a combination of transmission electron microscopy and stereology found values ranging from 21% (Boesen and Hokland, 1982) to ~130% (Schmid-Schönbein *et al.*, 1980).

We follow the same approach as Majstoravich *et al.* using scanning electron microscopy. For lymphoblasts, we find a microvilli density of 6.9 per μm^2, a length of 284 ± 140 nm (mean ± SD) and a diameter of 62 ± 13 nm (mean ± SD) (Figure 4.6D,E). This translates to a relative excess membrane of ~40% for lymphoblasts.

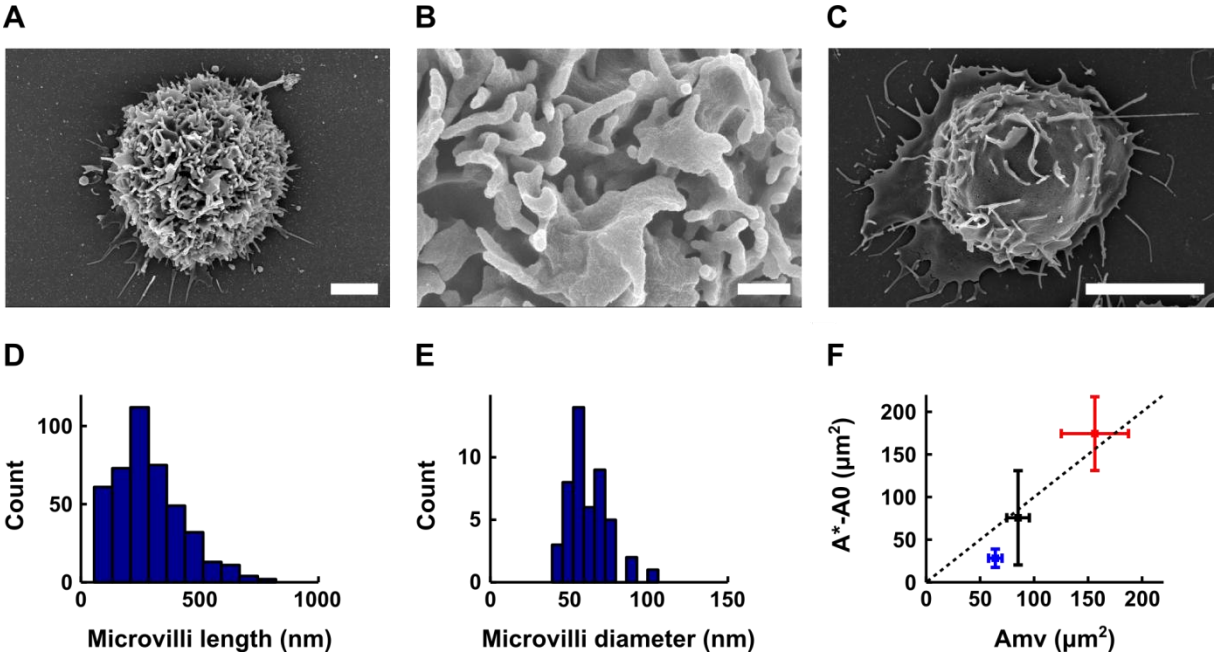

FIGURE 4.6: Maximum membrane surface area increase during micropipette aspiration is of the same order of magnitude as the excess membrane contained in microvilli and membrane folds. (A-C) Scanning electron microscopy images of a lymphoblast (A, B) and a Jurkat cell (C). Scale bars are 2 μm (A), 400 nm (B) and 5 μm (C). (D) Histogram of lymphoblasts' microvilli lengths (n = 432 measurements, N = 10 cells). We find the length is 284 ± 140 nm (mean ± SD). (E) Histogram of lymphoblasts' microvilli diameters (n = 48 measurements, N = 1 cell, as we observed that the diameter was well conserved across cells). We find the diameter is 62 ± 13 nm (mean ± SD). (F) Plot of the maximum increase in apparent membrane surface area during micropipette aspiration experiments (defined as the apparent membrane surface area at rupture A* minus the initial apparent membrane surface area A0) as a function of the estimated excess membrane contained in microvilli and membrane folds, Amv, for resting T lymphocytes (blue), Jurkat cells (red) and lymphoblasts (black). Squares represent the mean, bars represent the standard deviation. Dotted line represents the A*-A0 = Amv (slope equal to 1) line.

For Jurkat cells, we take a slightly different approach. Indeed, we do not see as many microvilli on the surface of Jurkat cells, but we see many more membrane folds (Figure 4.6 A,C). Therefore, instead of assuming that the excess membrane is contained in cylindrical microvilli, we assume that most of the excess membrane is in the form of infinitesimally fine membrane folds whose height can be estimated for a given cell using the folds seen in profile. Using this approach, we find a relative excess membrane of ~41% for Jurkat cells. Consistently with this estimate, an earlier study that used capacitance, as measured by patch clamping, as an indirect method to estimate surface area, found that Jurkat cell had an external membrane reservoir of ~40-70% of their apparent membrane surface area (Ross *et al.*, 1994).

To assess if the membrane stored in ruffles and microvilli is sufficient to explain the deformation of T lymphocytes in micropipettes, we compare the maximum membrane surface area deployed using micropipette aspiration (defined as the apparent membrane surface area at rupture A* minus the initial apparent membrane surface area A0) with the excess membrane surface area contained in microvilli and folds and find that they are in good qualitative agreement for resting T lymphocytes, lymphoblasts and Jurkat cells (Figure 4.6F). Consistently with this picture, others showed that, upon osmotic swelling, Jurkat cell membrane ruptures if the surface area increases beyond what is contained in their external membrane reservoir (Ross *et al.*, 1994).

T lymphocyte membrane expansion during active deformation can greatly exceed the limit observed in passive deformation

In order to determine how our criterion of maximum membrane expansion for passive deformations applies to active deformations, we reproduce in vitro two situations in which the T lymphocyte is activated: one in which a T lymphoblast migrates across an endothelial monolayer (Figure 4.7), and one in which it spreads on an activating surface (Figure 4.7). Both were chosen because we expect the apparent membrane surface area to increase substantially and because they occur on time scales comparable to the micropipette aspiration experiments (~3 min for transendothelial migration and ~20 min for cell spreading).

We find that in both cases, the apparent membrane surface area reaches values that are much larger than the limit found in passive deformations, with an area of 526 ± 98 μm^2 (mean ± SD) after transendothelial migration and 489 ± 103 μm^2 (mean ± SD) after cell spreading. These values are similar to each other and both statistically significantly higher than the initial apparent membrane surface area of lymphoblasts, 213 ± 26 μm^2 (mean ± SD), and their apparent membrane surface area at rupture upon micropipette aspiration, 288 ± 64 μm^2 (mean ± SD).

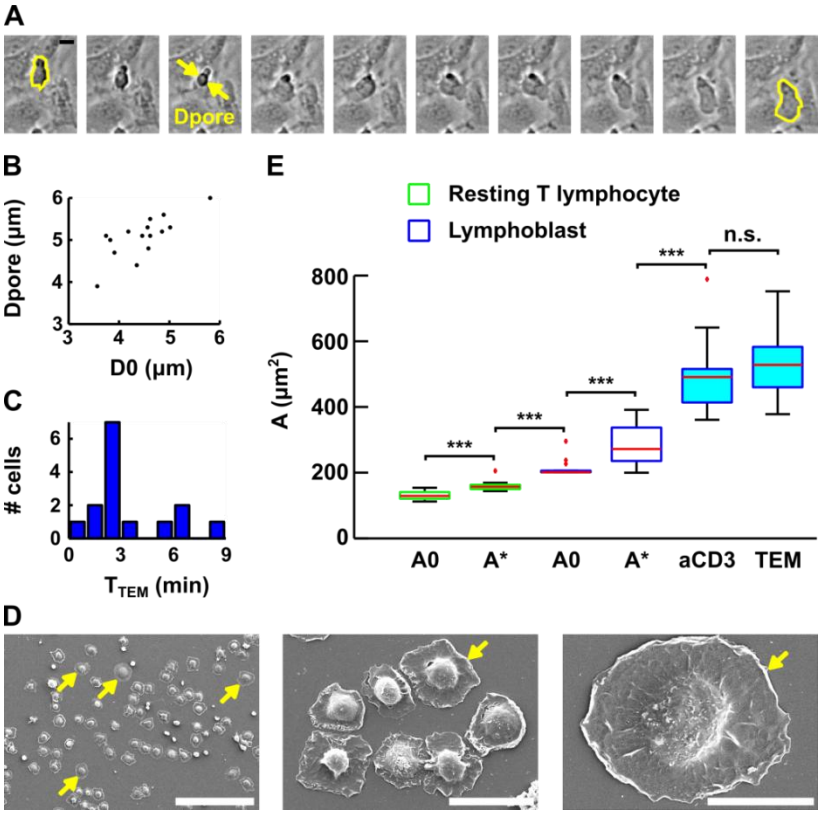

FIGURE 4.7: Evolution of lymphoblasts' membrane surface area during transendothelial migration and cell spreading. (A) Time lapse of a lymphoblast transmigrating between human aortic endothelial cells. Scale bar is 10 µm. Images are taken every 15 seconds. The projected surface area Sproj is represented in yellow before (left-most image) and after (right-most image) transendothelial migration. The pore diameter Dpore is estimated by taking the image in which the lymphoblast width is identical both above and below the pore (yellow arrows). (B) Pore diameter Dpore during transendothelial migration as a function of the lymphoblast's projected diameter before transendothelial migration (computed using D0 = Sproj / 2π, where Sproj is the projected surface area and D0 an equivalent diameter for a sphere whose projected area is Sproj). (C) Histogram of the duration of transmigration. The mean duration is 3 ± 2 min (mean ± SD). (D) Scanning electron microscopy images of lymphoblasts spreading on a substrate coated with anti-CD3+anti-CD28 activating antibodies. Scale bars from left to right are 100 µm, 20 µm and 10 µm. Yellow arrows indicate spread cells. (E) Boxplots of the apparent membrane surface area of T lymphocytes under both passive (white-filled box) and active (blue-filled box) deformations. The bottom and top of the box indicate the 25th and the 75th percentile, respectively. Red '+' symbols indicate outliers. From left to right, we have: resting T lymphocytes initially (column 1, A0, n = 14) and at rupture (column 2, A*, n = 14) aspirated using a micropipette, lymphoblasts at rest (column 3, A0, n = 14) and at rupture (column 4, A*, n = 14) aspirated using a micropipette, lymphoblasts spread on anti-CD3+anti-CD28 mAbs (column 5, aCD3, n = 17), and lymphoblasts after transendothelial migration (column 6, TEM, n = 15). *** indicates $p<0.001$. n.s. indicates $p>0.05$.

Discussion

The amount of membrane surface reservoirs is predictive of T lymphocyte membrane rupture

We showed that the amount of membrane area expansion is predictive of membrane rupture of T lymphocytes passing through narrow capillaries and that the limiting factor is the amount of excess membrane contained in microvilli and membrane folds. This result holds regardless of whether the T lymphocyte is activated or not (resting T lymphocyte and T lymphoblast) and regardless of whether it is a primary cell or a leukemic cell (primary T lymphocytes and Jurkat T cell). We therefore speculate that there could be a degree of generality to these results and that they may also be valid for other types of leukocytes. This is supported by the observation made by Evans *et al.* that the excess membrane area of granulocytes is what enables them to pass through capillaries as small as 2.6 μm in diameter (Evans and Kukan, 1984).

Membrane surface reservoirs allow T lymphocytes to pass unharmed through the microvasculature

We have shown that T lymphocytes, when aspirated into a micropipette, retain a constant volume and that beyond a critical membrane expansion of ~20% to ~50% (depending on the cell type), T lymphocyte membrane ruptures. T lymphocytes passing through a capillary assume a sausage-like shape, similar to what has been reported for chondrocytes and neutrophils (Hochmuth, 2000). This means that the smaller the capillary, the higher the T lymphocyte membrane expansion needs to be to pass through it. This further means that for each type of T lymphocyte, there exists a critical capillary size under which the T lymphocyte will either be trapped or rupture depending on the pressure exerted on it. This critical diameter is given by the intersection of the two lines in the "phase diagrams" (by analogy with physical phase diagrams) on Figure 4.5. We deduce a minimum capillary size of 4.1 μm for resting T lymphocytes, 4.2 μm for lymphoblasts and 5.1 μm for Jurkat cells.

Human capillaries are in the range of 5-10 μm (Fung, 2013), which is in some cases smaller than the typical size of a T lymphocyte but always sufficiently large for the T lymphocyte to pass through without risking membrane rupture or getting trapped, according to our results. Therefore, we suggest that the excess membrane contained in the microvilli and membrane folds of T lymphocytes is tightly regulated to enable them to pass unharmed through the microcirculation.

Pore size during extravasation is determined by T lymphocyte, not endothelial cell

Our in vitro transmigration assay allows for the quantification of the endothelial pore size during T lymphocyte transmigration. We find a diameter of 5.1 ± 0.5 μm. Consistent with this value, images from previous studies indicate pore sizes from transmigrating T lymphocytes of 5.3 μm (Carman and Springer, 2004) and 5.4 μm (Shulman *et al.*, 2011). Importantly, we observe that the pore size increases with cell size (Figure 4.7B), which suggests leukocytes and not endothelial cells determine the size of this pore. Furthermore, the pore size is comparable to the size of the smallest capillaries that a T lymphocyte may find itself going through without rupture. Hence, the pore size might be an optimum that minimizes the mechanical effort needed to create it, while also minimizing the risk of leukocyte membrane damage during transmigration.

Active deformations of T lymphocytes require more membrane than is available in surface reservoirs

We have shown that the membrane surface area of lymphoblasts during cell spreading and transendothelial migration is ~200-250 μm^2 higher than the external membrane surface area of lymphoblasts, even when accounting for microvilli and membrane folds. This means that additional membrane must be recruited during active deformations. We propose that this is enabled by internal membrane reservoirs, possibly through exocytosis.

Indeed, there are numerous examples where cells have been shown to recruit additional membrane through exocytosis to enable large active deformations. For cell spreading, there is direct evidence in fibroblasts that the increase in membrane surface area is enabled by exocytosis (Gauthier *et al.*, 2011). Similarly, during phagocytosis, the dramatic increase in macrophage membrane surface area is enabled by exocytosis (Hackam *et al.*, 1998; Bajno *et al.*, 2000; Niedergang *et al.*, 2003; Braun *et al.*, 2004). Drosophila cellularization provides yet another example. Indeed, exocytosis has been shown to add membrane to the cell surface to enable the furrow ingression needed for cellularization (Figard *et al.*, 2013). Finally, multiple cell types (AS49, 16HBE 140-, CHO and NIH 3T3 cells) have been observed to use exocytosis to enable expanding volumes during hyposmotic swelling (Groulx *et al.*, 2006). Interestingly, Groulx *et al.* remarked that the membrane surface area can increase 3.6 fold under normal conditions but only 1.7 fold when exocytosis is blocked. This difference in membrane surface area is consistent with the difference we observed between passive and active deformations. Indeed, during passive deformations, we saw a 1.2-1.5 fold increase in membrane surface area, whereas during active deformations, we saw a ~2.5 fold increase in membrane surface area for lymphoblasts. The difference between the two cases would presumably be made up by exocytosis, as in hyposmotic swelling. Hence, we believe that numerous active cell processes involving large deformations, including cell spreading and

transendothelial migration, but also phagocytosis and even embryonic development for some species, are critically dependent on exocytosis. Failing that, their membrane surface area would not be able to increase sufficiently for these large deformations to occur.

Materials and Methods

Cell purification and culture

All cells used in this study were human cells. This study was conducted according to the Helsinki Declaration, with informed consent obtained from the blood donors, as requested by the Etablissement Francais du Sang.

Human primary CD4+ T lymphocytes were negatively selected from PBMCs isolated from blood of healthy donors with the CD4 T cell isolation kit (#130-096-533, Miltenyi Biotec) as described previously (Chemin *et al.*, 2012).

To obtain CD4+ T lymphoblasts, 6-well plastic plates were coated with anti-CD3 (OKT3 clone, # 16-0037-85 from eBioscience 2.5 µg/ml in 1.3 ml final) overnight at 4°C. Wells were washed and 5.4×10^6 purified primary human CD4+ T cells were plated per well in the presence of soluble anti-CD28 (LEAF Purified anti-human CD28 # BLE302923 – Biolegend ,2.5 µg/ml) and recombinant IL-2 (20 U/ml). Fresh medium containing IL-2 (20 U/ml) was added every 3 days and lymphoblasts were used from day 6.

Jurkat cells (clone 20; obtained from Dr. A. Alcover, Pasteur Institute, Paris, France) were grown in Glutamax-containing RPMI 1640 (Invitrogen Life Technologies, Carlsbad, CA) supplemented with 10% fœtal calf serum as described previously (Blanchard *et al.*, 2002).

Primary human aortic endothelial cells (HAEC) were purchased from ThermoFisher Scientific and cultured in medium 200 (M200500, ThermoFisher Scientific) supplemented with low serum growth supplement (S00310, ThermoFisher Scientific). They were passaged three times a week using trypsin followed by resuspension in fresh medium.

Optical microscopy

In all micropipette aspiration, profile microindentation and transendothelial migration experiments, the petri dish containing cells was mounted on a TE300 inverted microscope (Nikon Instruments, Tokyo, Japan) placed on an air suspension table (CVI Melles Griot, Netherlands). The microscope was equipped with a 100x oil immersion, 1.3 NA objective (Nikon Instruments) for experiment monitoring and

lower magnification objectives (40x, 20x, 10x, and 4x, Nikon) for micropipette positioning. Images were acquired using a Flash 4.0 CMOS camera (Hamamatsu Photonics, Hamamatsu City, Japan).

Micropipette aspiration

Micropipette aspiration experiments were performed using a micropipette connected to a water reservoir, as described previously (Guillou *et al.*, 2016). We left the micropipettes in complete medium for at least 5 minutes before starting experiments to avoid cell adhesion to the micropipette wall. Propidium iodide (Sigma-Aldrich) at a concentration of 40 μg/mL was used as a reporter of membrane rupture. For membrane rupture experiments, we left a background of brightfield light to visualize the cell before rupture. The fluorescent signal from the propidium iodide was sufficiently intense to be visible despite this light. Image sequences were acquired using Micro-Manager (Vale Lab, UCSF) (Edelstein *et al.*, 2010).

Profile microindentation

To perform microindentations, cells were held using a micropipette and indented using a thin glass capillary, as described previously (Guillou *et al.*, 2016). Briefly, we impose a displacement to the base of the glass capillary using a piezoelectric controller (TPZ001, Thorlabs), and monitor the position of the capillary tip by using optical microscopy combined with cross-correlation image analysis. We used a microindenter of stiffness 0.54 nN/μm and radius 11 μm whose base we displaced at a speed of 0.5 μm/s.

Transendothelial migration

For transendothelial migration experiments, HAEC were grown to confluence in thin-bottom Petri dishes (FluoroDish 35 mm, World Precision Instruments), and inflamed overnight in TNF-α (CYT-252-5μg, Biovalley) at a concentration of 50 ng/mL. The next morning, the TNF-α was washed twice with HAEC medium. The Petri dish was then placed in a custom-made Plexiglas chamber to maintain the temperature at 37 °C. The chamber was heated by heating pads (Radiospare) connected to an electrical generator (ALR3002M, ELC) via a PID controller. The target temperature of the PID was set to 40 °C, with the input temperature to the PID given by a thermocouple placed inside the chamber at a fixed location. The chamber was also sealed at the top to minimize air flow and temperature gradients. Further, the objective was heated at a target temperature of 40 °C using an objective heater (Okolab). Both target temperatures were chosen after control experiments revealed

that the actual temperature of the medium inside the Petri dish was 37 °C (as measured by a thermocouple inside the medium) when the target temperatures were both set to 40 °C. After waiting 20 min for the temperature to equilibrate inside the HAEC medium, 500 mL of lymphoblasts at a concentration of ~10^6 cells/mL were injected using a 1 mL pipette. Brightfield images were then acquired every 15 seconds for a period of 60 min, under 10x magnification.

Data analysis

Images were analyzed using ImageJ (US NIH), and data were analyzed using a custom written Matlab (Mathworks) code. Data are reported as mean ± standard deviation, both in the text and in plots, unless specified otherwise. Samples were deemed statistically significantly different (*) for $p < 0.05$ using Student's unpaired t-test. (***) indicates $p < 0.001$.

Scanning electron microscopy

Scanning electron microscopy was performed on T lymphocytes (1.50×10^5) incubated for 20 min at room temperature on slides pre-coated with 0.02% poly-L-lysine alone (or followed by incubation with anti-CD3 (OKT3 clone, # 16-0037-85 from eBioscience) and anti-CD28 (LEAF Purified anti-human CD28 # BLE302923 – Biolegend) at 10μg/ml, overnight at 4°C). The cells were then washed in phosphate buffer pH 7.4 (PB), fixed overnight at 4°C in PB + 2% glutaraldehyde, and finally washed in PB. Samples were then dehydrated by passing through a graded series of ethanol solutions, then dried by the CO_2 critical-point method (CPD75 Quorum Technologies) and coated by sputtering with a 20-40 nm gold thin layer using a Scancoat Six (Edwards). Acquisitions were performed using a GeminiSEM 500 (Zeiss), except for the cell spreading experiments for which acquisitions were performed using a Cambridge Stereoscan 260.

Fluorescent staining and confocal microscopy for cell volume measurement

Cells were fluorescently stained and their volume measured using a confocal microscope as detailed previously (Bufi *et al.*, 2015). Briefly, cells were plated on fibronectin (10 μg/mL, Sigma-Aldrich)-coated glass coverslips, fixed, permeabilized and stained for DAPI (Life Technologies) and phalloidin-Alexa-546 (Life Technologies). The samples were observed on an inverted spinning-disk confocal microscope Nikon TiE (Nikon, Tokyo, Japan) equipped with a piezo-stage NanoScanZ mounted on a Marzhauser XYZ motorized scanning stage. Three-dimensional stacks of images were acquired with a step of 0.2 mm using a 100x

immersion oil objective and an EM-CCD iXon 897 Andor camera (Andor, Belfast, UK). Images were analyzed using the ImageJ software.

Acknowledgements

The authors acknowledge Caroline Frot, Antoine Garcia, Daniel Guy, Delphine L'Huillier, Magali Tutou, and Do Chi Toai Vu at LadHyX for technical support. The authors also acknowledge Virginie Bazin from the Electron Microscopy platform at Université Pierre et Marie Curie. This work has benefited from the financial support of the LabeX LaSIPS (ANR-10-LABX-0040-LaSIPS) managed by the French National Research Agency under the "Investissements d'avenir" program (n°ANR-11-IDEX-0003-02). This work was also supported by an endowment in cardiovascular cellular engineering from the AXA Research Fund. Lionel Guillou was supported by a Gaspard Monge doctoral fellowship from Ecole Polytechnique. This research has received funding from the National Institute of Health and Medical Research (INSERM), from ANR (ANR-12-BSV5-0007-01, ImmunoMeca) and Fondation pour la Recherche Médicale (FRM, FRM DEQ20140329513). MS was financed by FRM and AB was financed by la Ligue contre le Cancer and l'Association de Recherche contre le Cancer (ARC).

4.3 SUPPLEMENTARY MATERIAL

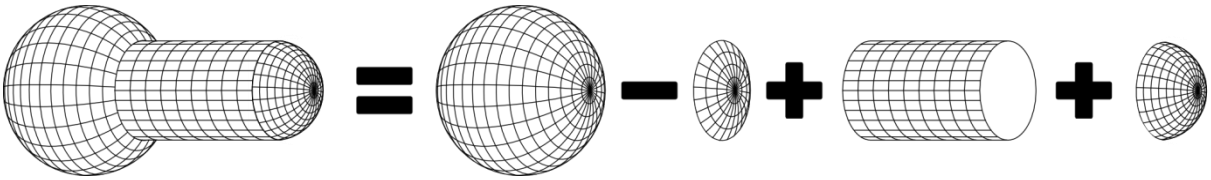

FIGURE 4.8: Equations for computing the area and volume of a cell aspirated into a micropipette.

We assume that micropipette aspiration of a cell constitutes an axisymmetric system around the axis of the micropipette.

The initial cell volume before aspiration is:

$$V0 = \frac{4}{3}\pi\left(\frac{D0}{2}\right)^3$$

During aspiration, the height and volume of the small dome that needs to be subtracted are:

$$hdome = \frac{Df}{2} - \left(\left(\frac{Df}{2}\right)^2 - \left(\frac{Dp}{2}\right)^2\right)^{1/2}$$

$$Vdome = \frac{hdome}{6}\pi\left(3\left(\frac{Dp}{2}\right)^2 + hdome^2\right)$$

The final volume during aspiration is:

$$Vf = \frac{4}{3}\pi\left(\frac{Df}{2}\right)^3 - Vdome + \pi\left(\frac{Dp}{2}\right)^2 L + \frac{2}{3}\pi\left(\frac{Dp}{2}\right)^3$$

The initial cell area before aspiration is:

$$A0 = \pi(D0)^2$$

During aspiration, the area of the small dome that needs to be subtracted is:

$$Adome = 2\pi\left(\frac{Df}{2}\right)hdome$$

The final cell area during aspiration is:

$$Af = \pi(Df)^2 - Adome + \pi(Dp)L + 2\pi\left(\frac{Dp}{2}\right)^2$$

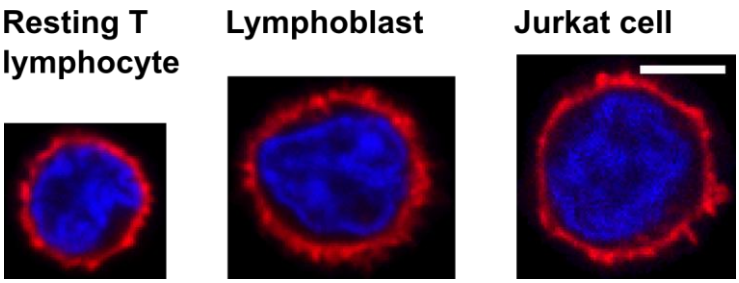

FIGURE 4.9: Fluorescent staining of T lymphocytes used to estimate cell volume. F-actin is in red and nucleus is in blue. Scale bar is 5 μm. We find V0 = 274 ± 75 μm^3 (n = 298), 473 ± 136 μm^3 (n = 143) and 797 ± 250 μm^3 (n = 68) (mean ± SD) for resting T lymphocytes, lymphoblasts and Jurkat cells respectively. This is slightly higher than the apparent volume we estimated using optical microscopy of cells in suspension, but still in good agreement.

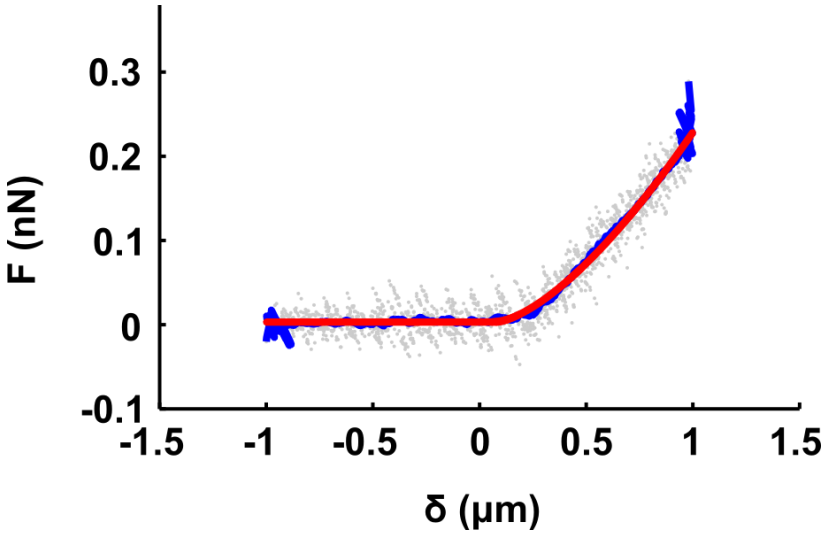

FIGURE 4.10: Compressive force F exerted on a cell during microindentation, as a function of the indentation δ. The raw data, in grey, are acquired at a frequency of ~350 Hz. In blue we plot a moving average of the raw data over 50 points. In red, we overlay the best fit found using the Hertz model.

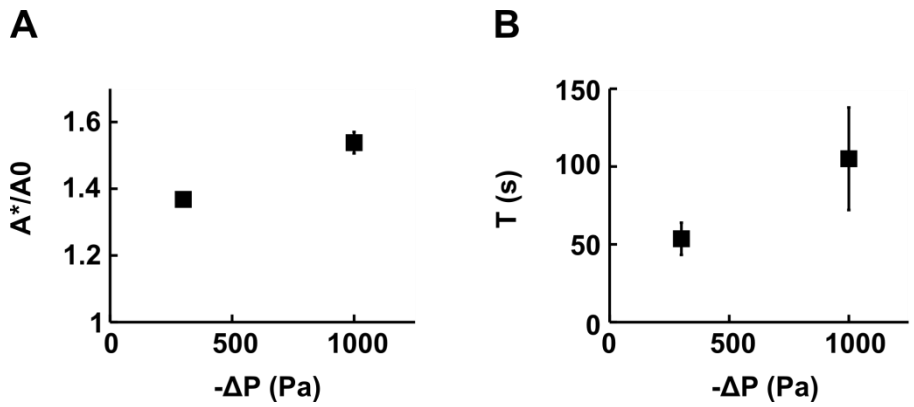

FIGURE 4.11: Effect of aspiration pressure on Jurkat cell membrane rupture. (A) Plot of the membrane expansion at rupture A*/A0, as a function of the absolute value of the aspiration pressure ΔP for Jurkat cells (n = 22 ruptured cells). (B) Plot of the duration T of micropipette aspiration before rupture, as a function of the absolute value of the aspiration pressure ΔP for Jurkat cells (n = 22 ruptured cells). The two aspiration pressures with the most ruptured cells (ΔP = -300 and -1000 Pa), which account for over 80% of the total number of Jurkat cell ruptures, were selected for this plot.

4.4 METHOD BOX: DEVELOPMENT OF A TEMPERATURE CONTROL CHAMBER

The protocol to perform transendothelial migration experiments *in vitro* was detailed in the methods sub-section of section 4.2. However, that description does not detail how we built a custom-made temperature control chamber, which can be employed for many uses other than transendothelial migration. We describe this custom-built chamber here to help future users in our laboratory as well as to provide guidance to other laboratories that may be interested in such chambers while wanting to save on the associated cost.

The chamber is built using plexiglas. A hole is made at the center to allow easy access and passage of pipettes, micropipettes and microindenters. When none of these are used, we recommend using a Petri dish as a lid to limit temperature gradients inside the chamber (Figure 4.12).

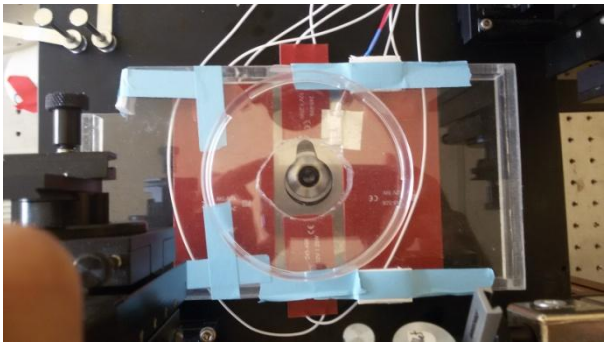

FIGURE 4.12: Layout of the experiment system with the lid and a thermocouple inside.

The chamber is heated by heating pads (Radiospare) connected to an electrical generator (ALR3002M, ELC). For this generator, the optimal voltage is set to 16.2 V (Figure 4.13).

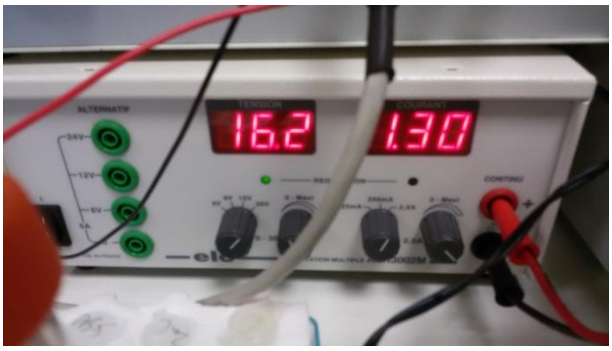

FIGURE 4.13: Electrical generator voltage is set to 16.2 V.

The generator is controlled by a PID controller. The target temperature of the PID is set to 39/40°C (Figure 4.14), and its input temperature is determined by a thermocouple that is positioned at a fixed location inside the chamber.

FIGURE 4.14: Heating system target temperature.

We recommend using aluminum tape to maintain the thermocouple in position (Figure 4.15). Indeed, tape allows easy removal if necessary, but office tape is affected by the temperature and will lose its stickiness over time.

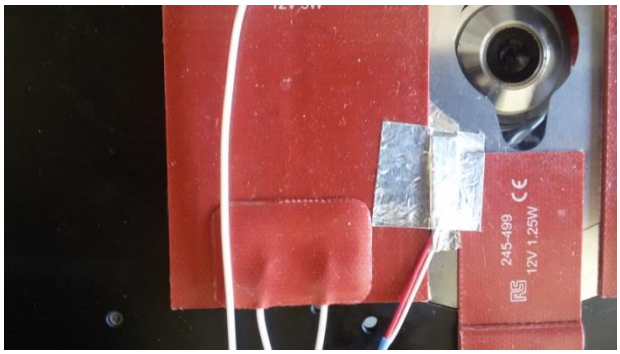

FIGURE 4.15: Aluminum tape is used to maintain the thermocouple in place. This thermocouple serves as an input to the PID controller.

Once the PID controller and the electrical generator are turned on and the lid is in place, it takes 20 to 30 min for the temperature to equilibrate around 37°C inside the chamber and the medium (Figure 4.16). Especially at high magnification (e.g. 100x), it is essential to wait, otherwise the focus will keep shifting until the temperature settles due to thermal expansion.

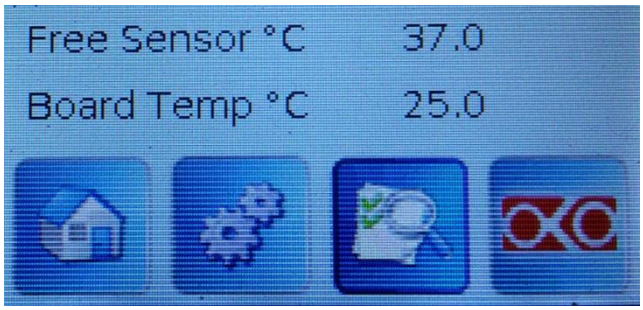

FIGURE 4.16: Measurement of temperature inside the fluorodish using a thermocouple.

If using the 100x oil objective, it is necessary to heat the objective in order to avoid cooling through the oil (we observed adherent endothelial cell retraction because of temperature shocks otherwise). We use an objective heater (Okolab) to do so, and set its temperature to 40°C. Both target temperatures were chosen after control experiments revealed that the actual temperature of the medium inside the Petri dish was 37°C (as measured by a thermocouple inside the medium) when the target temperatures were both set to 40°C.

4.5 METHOD BOX: AUTOMATED CELL TRACKING TOOL

In order to facilitate cell tracking that was performed manually at the Kumar lab (UC Berkeley), we developed an automated cell migration tracking tool that uses ImageJ and Matlab. We chose these software packages because they are very commonly used by the research community. At the date of redaction of this manuscript, this program is being used by about ten researchers in three laboratories, and it has been validated against manual tracking, which is the current gold standard.

The basic workflow of this algorithm is detailed in the image below (Figure 4.17).

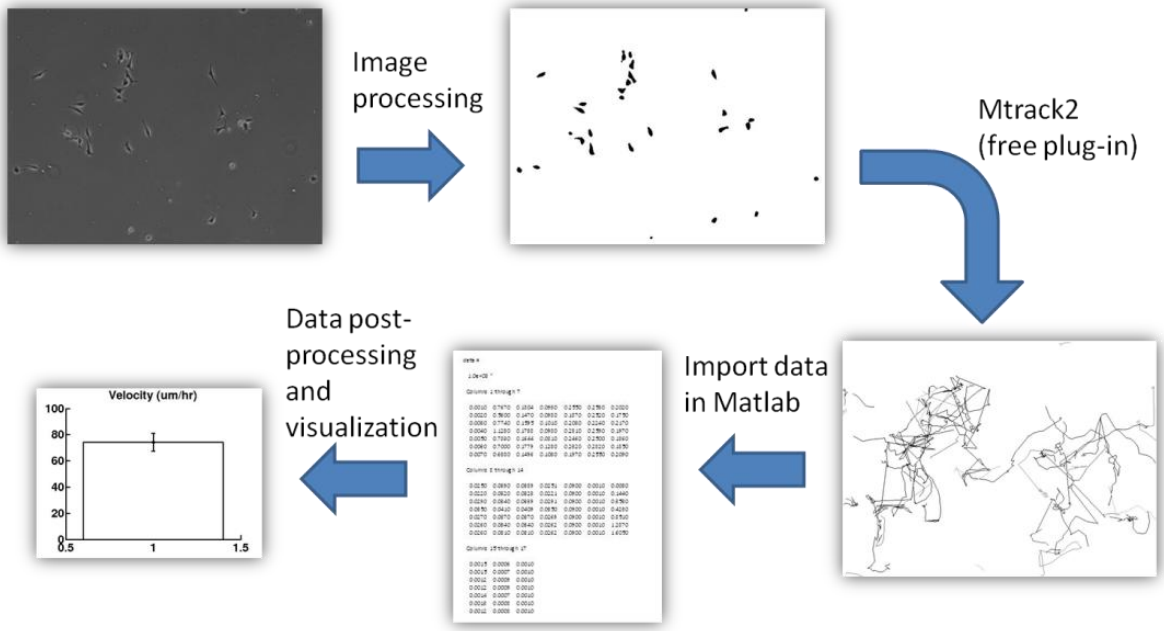

FIGURE 4.17: Key algorithm steps to track cells automatically.

To use the algorithm in practice, one must open Matlab, load the Matlab code, and follow the steps described in the "USER MANUAL" section of the Matlab code found below.

Matlab code

```
clear all;
close all;
clc;

% Author: Lionel Guillou, based on initial protocol by Elaine Su
% Date: 2015/03/18 (v5)
% (c) Kumar Lab, UC Berkeley

%%%%%%%%%%%%%%%%%%%%%%%%%%%%%%%%%%%%%%%%%%%%%%%%%%%%%%%%%%%%%%%
%                          USER MANUAL                        %
%%%%%%%%%%%%%%%%%%%%%%%%%%%%%%%%%%%%%%%%%%%%%%%%%%%%%%%%%%%%%%%

%{

    1. Do not use spaces while naming folders and files
    2. This .m file comes with a .ijm file (cellTrackIJ_v2.ijm)
    3. Convert images to 8-bit before starting program
    4. Fill "Parameters" section. Follow protocole to help with choice of
    parameter values for "ImageJ pre-treatment" and "mtrack2"
    5. If this is your first time using algo with a cell type
    (and therefore size) or a given magnification, verify manually
    that algo is of right order of magniture
    6. Test sensitivity of output to key parameters, mainly maxVel and
    minTL

%}

%%%%%%%%%%%%%%%%%%%%%%%%%%%%%%%%%%%%%%%%%%%%%%%%%%%%%%%%%%%%%%%
%                           PARAMETERS                        %
%%%%%%%%%%%%%%%%%%%%%%%%%%%%%%%%%%%%%%%%%%%%%%%%%%%%%%%%%%%%%%%

% Folder locations
datafolder                                                                    =
'/home/guillou/Desktop/KumarLab/CellTrackingAutomation/original/';
datafile        = 'img0001';
imageJfolder    = '/home/guillou/Documents/ImageJ/ImageJ/ImageJ';
macrofolder          =  '/home/guillou/Desktop/KumarLab/CellTrackingAutomation/';  %
location of associated imageJ macro

% Time
nbIm            = 62; % total number of images
tbf             = 15; % time between frames (min)

% Space
scale           = 3.42; % (um per px)

% Plot
plotResult      = 0; % 1 = plot, 0 = no plot

% ImageJ pre-treatment
rBR = 5; % rolling ball radius (in pixels) for substracting background (default =
5)
sigma = 3; % sigma coefficient for Gaussian blur (default = 3)
intTh = 190; % threshold for intensity (needs to be calibrated) (default = 190 for
an 8-bit image)

% mtrack2
minCS = 5; % minimum cell size (in pixels) (default = 5)
maxVel = 30; % maximum velocity (in pixels/frame) (default = 40)
minTL = 5; % minimum track length (in # of frames) (default = 10)

% Optional
showCellPath = 0; %  1: show cell paths (default: 0)
minCellDist = 50; % minimum distance between 2 cells (in pixels) -> cells closer to
each other than this value are ignored
idCellExcl = []; % ID # of cells to ignore, with a space between each number (use
the number shown in imageJ when setting showPath = 1 above)
```

```
%%%%%%%%%%%%%%%%%%%%%%%%%%%%%%%%%%%%%%%%%%%%%%%%%%%%%%%%%%%%%
%                        RUN IMAGE J                        %
%%%%%%%%%%%%%%%%%%%%%%%%%%%%%%%%%%%%%%%%%%%%%%%%%%%%%%%%%%%%%

% Close open ImageJ windows before starting (can comment if inconvenient)
system(['ps -A | grep ''ImageJ'' | cut -c1-5 > ',datafolder,'pid.txt']);
fid             = fopen([datafolder,'pid.txt']);
pidImJ          = fscanf(fid,'%f',[1,inf])';
for k=1:size(pidImJ,1)
    system(['kill -9 ',num2str(pidImJ(k,1))]);
end

parseKey        = 'zzz';

input           = [datafolder,parseKey,...
    datafile,parseKey,...
    num2str(nbIm),parseKey,...
    num2str(rBR),parseKey,...
    num2str(sigma),parseKey,...
    num2str(intTh),parseKey,...
    num2str(minCS),parseKey,...
    num2str(maxVel),parseKey,...
    num2str(minTL),parseKey,...
    num2str(showCellPath)];
system([imageJfolder,' -macro ',macrofolder,'cellTrackIJ_v3.ijm ',input,' &']);

% If ImageJ closes before run is complete, reduce value of computerSpeed
computerSpeed = 20; % default = 10
pause(floor(1/computerSpeed*nbIm)+3);
if (showCellPath == 0)
    system(['ps -A | grep ''ImageJ'' | cut -c1-5 > ',datafolder,'pid.txt']);
    fid             = fopen([datafolder,'pid.txt']);
    pidImJ          = fscanf(fid,'%f',[1,inf])';
    for k=1:size(pidImJ,1)
        system(['kill -9 ',num2str(pidImJ(k,1))]);
    end
end

%%%%%%%%%%%%%%%%%%%%%%%%%%%%%%%%%%%%%%%%%%%%%%%%%%%%%%%%%%%%%
%                       PULL DATA                           %
%%%%%%%%%%%%%%%%%%%%%%%%%%%%%%%%%%%%%%%%%%%%%%%%%%%%%%%%%%%%%

datafileRes     = 'trackresults';
filename        = [datafolder,datafileRes,'.txt'];
fid = fopen(filename, 'r');
C = textscan(fid, '%s', 'Delimiter', '\t');
D = C{1};

% get number of cell tracks
loopContinue = true;
i = 1;
while (loopContinue == true)
    word = D{i};
    if strcmp(word,'1')
       loopContinue = false;
    end
    i = i+1;
end
str = D{i-2};
strlist = strread(str,'%s','delimiter',' ');
strlist4 = strlist(4);
nbCell = str2num(strlist4{1});

X = zeros(nbIm,nbCell);
Y = zeros(nbIm,nbCell);
indexIm = 1;
countIm = 0; % to know whether to start a new frame (and skip frameCount)
indexCell = 1;
```

```
countCell = 0; % to know whether it is frameCount, X, Y or ignore
skip = false;

for j=i:length(D)
    if(skip)
        skip = false;
    else
        if((countIm)==3*nbCell-1)
            if(D{j} == '*')
                indexIm = indexIm + 1;
                countIm =0;
                indexCell = 1;
                countCell = 0;
                skip = true;
            else
                indexIm = indexIm + 1;
                countIm =0;
                indexCell = 1;
                countCell = 0;
            end
        else
            countIm = countIm + 1;
            switch countCell
                case 0
                    if(not(isempty(D{j})))
                        X(indexIm,indexCell)=str2num(D{j});
                    end
                case 1
                    if(not(isempty(D{j})))
                        Y(indexIm,indexCell)=str2num(D{j});
                    end
                case 2
                    indexCell = indexCell + 1;
            end
            countCell = mod(countCell+1,3);
        end
    end
end
fclose(fid);

%%%%%%%%%%%%%%%%%%%%%%%%%%%%%%%%%%%%%%%%%%%%%%%%%%%%%%%%%%%%%%%%
%                        ANALYZE DATA                          %
%%%%%%%%%%%%%%%%%%%%%%%%%%%%%%%%%%%%%%%%%%%%%%%%%%%%%%%%%%%%%%%%

distance    = zeros(1,nbCell);
velocity    = zeros(1,nbCell);
persistence = zeros(1,nbCell);
startPos    = zeros(2,nbCell);

for i=1:nbCell
    Xnz = nonzeros(X(:,i));
    Ynz = nonzeros(Y(:,i));
    distance(i) = sum(sqrt((Xnz(2:end)-Xnz(1:end-1)).^2+...
        (Ynz(2:end)-Ynz(1:end-1)).^2));
    velocity(i) = distance(i)./size(Xnz,1);
    persistence(i) = distance(i)./(sqrt((Xnz(end)-Xnz(1)).^2+...
        (Ynz(end)-Ynz(1)).^2));
end

% Exclude cells that are too close from another cell
for i=1:nbIm
    for j=1:nbCell
        for k=j+1:nbCell
            posj = [X(i,j) Y(i,j)];
            posk = [X(i,k) Y(i,k)];
            if(posj(1)*posj(2)*posk(1)*posk(2)~=0)
                distjk = sqrt(sum((posj-posk).^2));
                if(distjk <= minCellDist)
```

```
                    idCellExcl = [idCellExcl j k];
                end
            end
        end
    end
end
idCellExcl = unique(idCellExcl)
X(:,idCellExcl) = [];
Y(:,idCellExcl) = [];
distance(idCellExcl) = [];
velocity(idCellExcl) = [];
persistence(idCellExcl) = [];

% Conversion
distance    = distance.*scale; % px -> um
velocity    = velocity.*scale./tbf.*60; % px/frame -> um/hr

%%%%%%%%%%%%%%%%%%%%%%%%%%%%%%%%%%%%%%%%%%%%%%%%%%%%%%%%%%%%%
%                       PLOT                                %
%%%%%%%%%%%%%%%%%%%%%%%%%%%%%%%%%%%%%%%%%%%%%%%%%%%%%%%%%%%%%

if (plotResult)

figure;
hold on;
bar(mean(velocity),...
    'FaceColor',[1 1 1],'EdgeColor',[0 0 0],'LineWidth',3);
errorbar(mean(velocity),...
    std(velocity)./sqrt(size(velocity,2)),...
    'ko','LineWidth',3,'MarkerSize',5);
title(['Velocity (um/hr)']);
set(gca,'FontSize',24,'LineWidth',3,'FontWeight','bold','TickLength',[0.025
0.025]);
set(findall(gcf,'type','text'),'FontSize',24,'FontWeight','bold');
hold off;

figure;
hold on;
bar(mean(persistence),...
    'FaceColor',[1 1 1],'EdgeColor',[0 0 0],'LineWidth',3);
errorbar(mean(persistence),...
    std(persistence)./sqrt(size(persistence,2)),...
    'ko','LineWidth',3,'MarkerSize',5);
title(['Persistence']);
set(gca,'FontSize',24,'LineWidth',3,'FontWeight','bold','TickLength',[0.025
0.025]);
set(findall(gcf,'type','text'),'FontSize',24,'FontWeight','bold');
hold off;

end

cellMeanVelocity = mean(velocity)
cellMeanPersistence = mean(persistence)
```

To speed up the process of choosing the parameters required in the “Parameters” section of the Matlab code, we suggest using the table below as a starting point (Table 4.1).

	How to choose	Comment
rBR	cell diameter (in px) (fit circle around cell nucleus and divide width by 2)	Must be at least (cell diameter)*1/2, too high a value is ok, but not too low
sigma	3	Do not change
intTh	High enough so that center of cells are almost completely in black, but low enough that cells do not lump together	When value is too low, algo does not work and cells dissapear. So although sensitive parameter, getting it right is rather easy
minCS	same as rBR	Relatively low impact
maxVel	Look at fastest cell and estimate roughly speed (in px/frame) manually	Most sensitive parameter for cell velocity, should ideally be inferior to cell / cell distance (algorithm may have a hard time if cell density is too high and mix cells up)
minTL	Estimate # of consecutive frames where a cell can be seen. Rule of thumb is image size (in px) / maxVel (in px/frame). Then can try decreasing value until algo bugs.	Impacts persistence but not cell velocity. Too high keeps most cells out. Too low generates bugs, which could theoretically be fixed if really needed.

TABLE 4.1: Choosing algorithm parameters

Finally, for reference, below is the ImageJ code that is called by the Matlab code. Please note that file nomenclatures are different across operating systems and that the code given here is for Linux OS. For Windows or Mac OS, a few lines of code would need to be adjusted, specifically the ones that open files or other programs automatically.

ImageJ code

```
inputString = getArgument();
parts1=split(inputString,"zzz")
datafolder = parts1[0];
datafile = parts1[1];
n = parts1[2]; // number of images to analyze
rBR = parts1[3];
sigma = parts1[4];
intTh = parts1[5];
minCS = parts1[6];
maxVel = parts1[7];
minTL = parts1[8];
showCellPath = parts1[9];

run("Image Sequence...", "open="+datafolder+datafile+".tif number="+n+" starting=1
increment=1 scale=100 file=[] sort");
run("Enhance Contrast...", "saturated=0.4 normalize process_all");
run("Despeckle", "stack");
run("Despeckle", "stack");
run("Despeckle", "stack");
```

```
run("Subtract Background...", "rolling="+rBR+" light stack");
run("Gaussian Blur...", "sigma="+sigma+" stack");
setThreshold(0, intTh);
setOption("BlackBackground", false);
run("Convert to Mask", "method=Default background=Light");
if (showCellPath == "1") {
      run("MTrack2   ",   "minimum="+minCS+"   maximum=999999   maximum_="+maxVel+"
minimum_="+minTL+" save show save="+datafolder+"trackresults.txt");
   } else {
      run("MTrack2   ",   "minimum="+minCS+"   maximum=999999   maximum_="+maxVel+"
minimum_="+minTL+" save save="+datafolder+"trackresults.txt");
   }
```

4.6 UNPUBLISHED DATA: MODELING MICROPIPETTE ASPIRATION IN FEBIO

We wanted to understand where the maximum strains were located for cells being aspirated into a micropipette, as we initially thought membrane rupture might be a purely local phenomenon (experiments later revealed this hypothesis to be incorrect). To do so, we modeled micropipette aspiration using FEBio, a freely available finite element code, which we had already employed to model microindentation. We present here this work in the hopes that it might be useful in future studies involving micropipette aspiration of living cells (for instance, in projects that look for coupling between local or global cell strains and phenomena such as pore opening, exocytosis or membrane permeability to proteins or chemicals).

This code requires Matlab, FEBio (http://febio.org/febio/), Postview (http://febio.org/febio/) and Gmsh (http://geuz.org/gmsh/). The code is launched from the file "upipette_aspiration_exec_v2.m", and is made for Linux OS. This code was derived from a code originally written by Cecile Gouget, a former student in our group. It is provided in the Appendix section of this manuscript.

Below is a visualization of the output for the parameters in the code given in the Appendix (Figure 4.18):

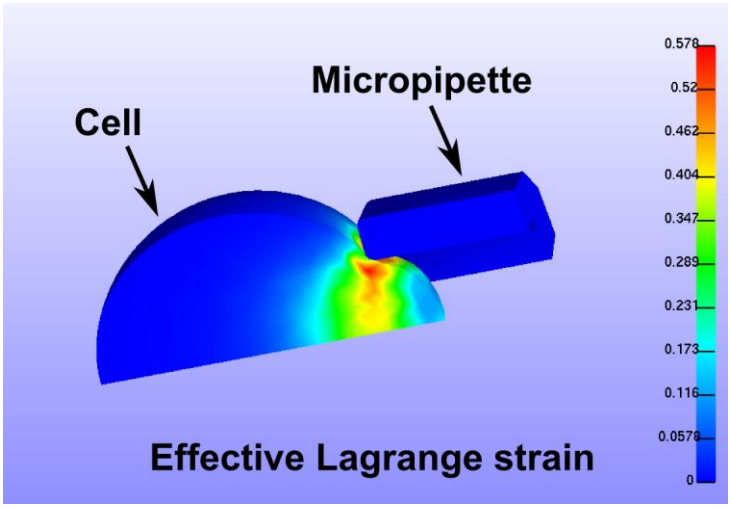

FIGURE 4.18: Visualization of simulation results using Postview

4.7 UNPUBLISHED DATA: CHEMO-MECHANICAL COUPLING BETWEEN THE STRETCHING OF A CELL MEMBRANE AND THE EFFICIENCY OF A PORE-FORMING MOLECULE

There are several known examples of cell-cell contact in which one cell significantly strains the membrane of the other cell. For instance, Ueda *et al.* reported that during the formation of the immune synapse, T-cells extend pseudopodia that penetrate deeply into the antigen-presenting cell (Ueda *et al.*, 2011). Another example is transmigration, in which T lymphocytes use so-called invadosome-like protrusions to probe endothelial cells and to select the location to undergo transcellular diapedesis (Carman *et al.*, 2007).

Moreover, it has recently been shown by Basu, Whitlock, Husson *et al.* that cytotoxic T cells use mechanical forces to enhance perforin pore formation in target cells, and that an increase in cell tension generated using a micropipette promotes perforin pore formation (Basu *et al.*, 2016). Therefore, we wondered if cell tension generated using a micropipette could enhance the efficiency of other pore-forming molecules. To this end, we employed micropipette aspiration to aspirate a Jurkat cell while "whiffing" saponin on it using a second micropipette (Figure 4.19).

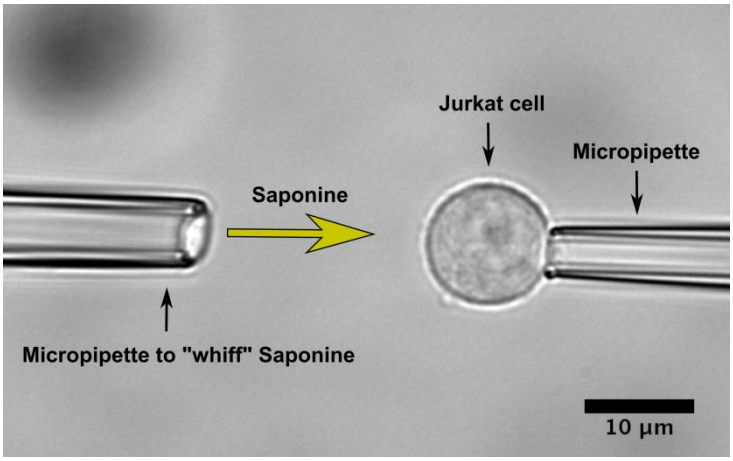

FIGURE 4.19: "Whiffing" saponin on a Jurkat cell whose membrane is strained

To estimate Jurkat cell tension, we computed the apparent membrane surface area increase. Indeed, as previously shown, apparent membrane surface area is a robust and instantaneous predictor of cell tension and effective stiffness for T lymphocytes (Figure 4.2). As a measure of the effectiveness of saponin, we timed how long the Jurkat cell was able to hold before rupture, using propidium iodide as a reporter of cell membrane rupture (Figure 4.20).

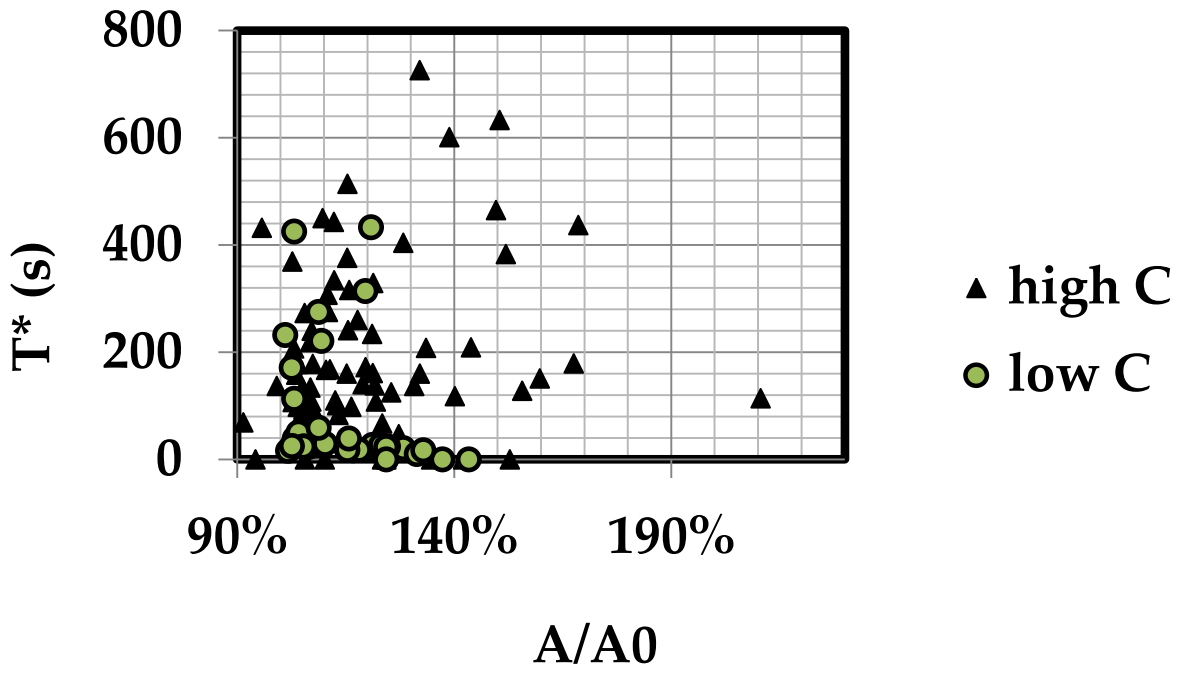

FIGURE 4.20: Jurkat cell survival time as a function of apparent membrane surface area increase, in the presence of a relatively low or high saponin concentration

In these experimental conditions, we conclude that there is no discernible effect of the Jurkat cell tension on the effectiveness of saponin, whether at low concentration ("low C", 0.0002% weight by volume) or high concentration ("high C", 0.0005% weight by volume). However, this hypothesis might still be valid for other chemicals, cell types, or different types of strain (for example, a purely local strain as occurs in invadosome-like protrusions).

CONCLUSIONS

In Chapter 1, we showed that we could measure the viscoelastic properties of both adherent and non-adherent cells using an optical microscope, a single-axis piezoelectric translation stage, and one or two micromanipulators. We further investigated whether this system would be able to detect the mechanical "footprint" of transendothelial migration but had limited success there. We concluded that profile microindentation was not the best method to investigate this important question.

In Chapter 2, we described the development of a microfluidic cross-slot device that is able to measure the viscoelastic properties of non-adherent cells without the need to hold the cells in place, rendering the measurement closer to *in vivo* conditions. In doing so, we derived a novel analytical model that we validated using dextran beads of known stiffness. Importantly, this device was able to detect the mechanical "signature" of changes in the cytoskeleton due to pharmacological agents, something that had only been partially achieved previously. This capability opens the door to applications in the clinical setting to help inform diagnosis of diseases as varied as cancer and diabetes.

In Chapter 3, we found a physical criterion predictive of membrane rupture of endothelial cells. We found that this criterion was best defined as a critical stress (as opposed to a force or a tension, for instance), and that it was greatly exceeded during stenting procedures. Because the difference was so large, it appeared that minor modifications to the procedure (such as reducing the balloon pressure) would be insufficient to avoid endothelial cell damage.

In Chapter 4, we found that passive deformations of T lymphocytes are both enabled and limited by their external membrane surface reservoirs. When the membrane surface area increase exceeded the membrane stored in microvilli and membrane folds, however, the T lymphocyte ruptured. During active deformations, such as transendothelial migration, T lymphocytes showed an ability to increase their membrane surface area far beyond this limit. This suggests that exocytosis is necessary to key processes such as transendothelial migration and therefore may be necessary for an effective immune response.

PERSPECTIVES

Studying the role of mechanics in the development of atherosclerosis

In our work, we were able to set up a protocol to obtain transendothelial migration *in vitro*, with very good reproducibility. In analyzing those experiments, we observed that the pore size half-way during transendothelial migration was directly related to the size of the T lymphocyte (Figure 4.7). This raises an interesting question about whether or not endothelial cells also play a role in this process. Indeed, it would be interesting to test whether the strength of endothelial cell-cell junctions plays a role in determining the pore size and, possibly concurrently, the transmigration rate. As a matter of fact, it is possible that looser junctions favor larger pores (as the energetic cost of opening space between endothelial cells decreases) and increase the permeability of the endothelial cell barrier. This hypothesis could be tested by performing transendothelial migration experiments on three types of endothelium: 1) a control case where endothelial cells are grown to confluence in a Petri dish as previously, 2) a patterned case where endothelial cells are aligned using micropatterns and 3) a flow case where endothelial cells are aligned using shear flow (we obtained alignment of human aortic endothelial cells in preliminary flow experiments). Presumably, the strength of endothelial cell-cell junctions would increase as one goes from cases 1) to 3), which could be verified for instance using impedance measurement, as previously done by Burns *et al.* (Burns *et al.*, 2000). The outcome of those experiments would have relevance to important features of atherosclerosis development *in vivo* because the alignment of endothelial cells is poor in zones that are prone to atherosclerosis (Davies, 1995). By decoupling cell alignment and flow, these experiments would help us understand the links between cell alignment and strength of cell-cell junctions and between the strength of the junctions and leukocyte transmigration rate. It would then follow that higher transmigration rates due to loose junctions would be expected to promote the development of atherosclerosis.

Transforming the cross-slot device for clinical use

We derived an analytical model to measure the viscoelastic properties of non-adherent cells in suspension using a cross-slot device (section 2.2). This design has some advantages over competing devices. In particular, if we compare it to the only available commercial solution offered by ZELL MECHANIK (Dresden, Germany), which was spun off the Guck group (Mietke *et al.*, 2015; Otto *et al.*, 2015), it can be used for bodies of a much wider size range. Consequently, this technology would not require devices of various sizes, unlike what is being done by ZELL MECHANIK, which sells devices of 4 different sizes (from 15 to 40 μm) depending on the cell type

of interest. However, to compete with the commercial device, the cross-slot device would need to be enhanced to increase throughput through automation. To do so would require focusing cells at the center to facilitate cell detection, possibly through inertial microfluidics (Di Carlo, 2009), and using an automated contour detection algorithm to "read" cell deformation in real time, much like was done by the Guck group (Otto *et al.*, 2015). To take the potential of this solution further, it would be interesting to combine it with flow cytometry. In the cross-slot device, all that is required to do so is that the microscope be able to do fluorescence microscopy. The difficulty here (which is the same challenge as in standard flow cytometry) is in obtaining a sufficiently strong fluorescence signal that it can be detected within the ~10 ms that the cell spends in the camera's field of view. Such a device could prove very useful in establishing the diagnosis (or at least providing a rapid and automated initial screening) of diseases which are known to affect cellular mechanical properties, such as cancer and diabetes. We could also imagine reducing the cost of such a device and making it more transportable by replacing expensive laboratory cameras with smartphones, as done for instance by CELLSCOPE (San Francisco, California, US), a company spun off from the Fletcher laboratory at UC Berkeley.

Developing live deformation tracking in adherent cells

We showed that tracking mitochondria using fluorescence microscopy allowed us to visualize the planar deformations of endothelial cells (Figure 3.12). This process is simple experimentally, as Mitotracker requires only a simple incubation of 30 min (which could probably be reduced further by increasing the concentration of Mitotracker) after which no further instrumentation is needed besides a microscope that can do fluorescence imaging. However, the analysis of subcellular displacements is currently done by post-treatment of the fluorescent images. We think this could be greatly improved upon, most notably in order to enable live deformation tracking. Indeed, detecting cell deformations essentially comes down to cross-correlation of images to determine the best transformation function between the frame of reference and the current frame. The optimal transformation function is then equated to the displacements. This cross-correlation computation could be done live using Matlab, which has an application programming interface (API) that allows it to import images live from MicroManager. The computing time should allow doing this cross-correlation at least once a second, if not significantly faster. Indeed, this cross-correlation is the same method as was used in our profile microindentation experiment for live detection of the position of the microindenter. Using Matlab interfaced with MicroManager, Julien Husson was able to increase the frequency of microindenter position detection to over 300 Hz (up from ~30 Hz using LabView), which suggests that even with larger images (the detection of microindenter position is done over an image of 4 pixels in width), the frequency could be on the order of 1-10 Hz at least. By building this tool in Matlab and interfacing it with MicroManager,

we would have a simple Matlab plug-in that could be downloaded and used on any microscope able to do fluorescence imaging (with the only requirements being that Matlab and MicroManager need to be installed on the computer), and that would enable it to perform live adherent cell deformation tracking. Because it does not require any instrument, this deformation tracking could be combined with other forms of fluorescence imaging (albeit at different wavelengths than the Mitotracker, for which several colors are available) and experiments (cell migration, membrane rupture through microindentation, traction force microscopy, etc.).

BIBLIOGRAPHY

Ailenberg, M., and Silverman, M. (2003). Cytochalasin D disruption of actin filaments in 3T3 cells produces an anti-apoptotic response by activating gelatinase A extracellularly and initiating intracellular survival signals. Biochim. Biophys. Acta - Mol. Cell Res. *1593*, 249–258.
Alcaraz, J., Buscemi, L., Grabulosa, M., Trepat, X., Fabry, B., Farré, R., and Navajas, D. (2003). Microrheology of human lung epithelial cells measured by atomic force microscopy. Biophys. J. *84*, 2071–2079.
Andrews, N. W., Almeida, P. E., and Corrotte, M. (2014). Damage control: Cellular mechanisms of plasma membrane repair. Trends Cell Biol. *24*, 734–742.
von Andrian, U. H., and Mempel, T. R. (2003). Homing and cellular traffic in lymph nodes. Nat. Rev. Immunol. *3*, 867–878.
Bajno, L., Peng, X. R., Schreiber, A. D., Moore, H. P., Trimble, W. S., and Grinstein, S. (2000). Focal exocytosis of VAMP3-containing vesicles at sites of phagosome formation. J. Cell Biol. *149*, 697–705.
Balland, M., Desprat, N., Icard, D., F??r??ol, S., Asnacios, A., Browaeys, J., H??non, S., and Gallet, F. (2006). Power laws in microrheology experiments on living cells: Comparative analysis and modeling. Phys. Rev. E - Stat. Nonlinear, Soft Matter Phys. *74*, 1–17.
Bao, S., Wu, Q., McLendon, R. E., Hao, Y., Shi, Q., Hjelmeland, A. B., Dewhirst, M. W., Bigner, D. D., and Rich, J. N. (2006). Glioma stem cells promote radioresistance by preferential activation of the DNA damage response. Nature *444*, 756–760.
Basu, R. *et al.* (2016). Cytotoxic T Cells Use Mechanical Force to Potentiate Target Cell Killing. Cell, 1–11.
Beckman, J. A., Creager, M. A., and Libby, P. (2002). Diabetes and atherosclerosis: epidemiology, pathophysiology, and management. JAMA *287*, 2570–2581.
Berliner, J. a., Navab, M., Fogelman, a. M., Frank, J. S., Demer, L. L., Edwards, P. a., Watson, a. D., and Lusis, a. J. (1995). Atherosclerosis: Basic Mechanisms◎: Oxidation, Inflammation, and Genetics. Circulation *91*, 2488–2496.
Bevington, P. R., and Robinson, D. K. (2003). Data reduction and error analysis. McGraw-Hill.
Bissell, M. J., Radisky, D. C., Rizki, A., Weaver, V. M., and Petersen, O. W. (2002). The organizing principle: Microenvironmental influences in the normal and malignant breast. Differentiation *70*, 537–546.
Blanchard, N., Lankar, D., Faure, F., Regnault, A., Dumont, C., Raposo, G., and Hivroz, C. (2002). TCR Activation of Human T Cells Induces the Production of Exosomes Bearing the TCR/CD3/ Complex. J. Immunol. *168*, 3235–3241.
Boesen, A. M., and Hokland, P. (1982). Stereological Analysis of the Ultrastructure in Isolated Human T and Non-T Lymphoid Cells. Cell Pathol *39*, 273–284.
Braun, V., Fraisier, V., Raposo, G., Hurbain, I., Sibarita, J.-B., Chavrier, P., Galli, T.,

and Niedergang, F. (2004). TI-VAMP/VAMP7 is required for optimal phagocytosis of opsonised particles in macrophages. EMBO J. *23*, 4166–4176.
Buffinton, C. M., Tong, K. J., Blaho, R. A., Buffinton, E. M., and Ebenstein, D. M. (2015). Comparison of mechanical testing methods for biomaterials: Pipette aspiration, nanoindentation, and macroscale testing. J. Mech. Behav. Biomed. Mater. *51*, 367–379.
Bufi, N., Saitakis, M., Dogniaux, S., Buschinger, O., Bohineust, A., Richert, A., Maurin, M., Hivroz, C., and Asnacios, A. (2015). Human primary immune cells exhibit distinct mechanical properties that are modified by inflammation. Biophys. J. *108*, 2181–2190.
Burns, a R., Bowden, R. a, MacDonell, S. D., Walker, D. C., Odebunmi, T. O., Donnachie, E. M., Simon, S. I., Entman, M. L., and Smith, C. W. (2000). Analysis of tight junctions during neutrophil transendothelial migration. J. Cell Sci. *113 (Pt 1*, 45–57.
Butcher, D. T., Alliston, T., and Weaver, V. M. (2009). A tense situation: forcing tumour progression. Nat. Rev. Cancer *9*, 108–122.
Butt, H. J., and Franz, V. (2002). Rupture of molecular thin films observed in atomic force microscopy. I. Theory. Phys. Rev. E - Stat. Nonlinear, Soft Matter Phys. *66*, 1–9.
Carl, P., and Schillers, H. (2008). Elasticity measurement of living cells with an atomic force microscope: Data acquisition and processing. Pflugers Arch. Eur. J. Physiol. *457*, 551–559.
Di Carlo, D. (2009). Inertial microfluidics. Lab Chip *9*, 3038–3046.
Carman, C. V (2009). Mechanisms for transcellular diapedesis: probing and pathfinding by "invadosome-like protrusions". J. Cell Sci. *122*, 3025–3035.
Carman, C. V., and Martinelli, R. (2015). T lymphocyte-endothelial interactions: Emerging understanding of trafficking and antigen-specific immunity. Front. Immunol. *6*.
Carman, C. V., Sage, P. T., Sciuto, T. E., de la Fuente, M. A., Geha, R. S., Ochs, H. D., Dvorak, H. F., Dvorak, A. M., and Springer, T. A. (2007). Transcellular Diapedesis Is Initiated by Invasive Podosomes. Immunity *26*, 784–797.
Carman, C. V., and Springer, T. A. (2004). A transmigratory cup in leukocyte diapedesis both through individual vascular endothelial cells and between them. J. Cell Biol. *167*, 377–388.
Cartagena, A., and Raman, A. (2014). Local viscoelastic properties of live cells investigated using dynamic and quasi-static atomic force microscopy methods. Biophys. J. *106*, 1033–1043.
Cartagena-Rivera, A. X., Logue, J. S., Waterman, C. M., and Chadwick, R. S. (2016). Actomyosin Cortical Mechanical Properties in Nonadherent Cells Determined by Atomic Force Microscopy. Biophys. J. *110*, 2528–2539.
Chan, C. J., Ekpenyong, A. E., Golfier, S., Li, W., Chalut, K. J., Otto, O., Elgeti, J., Guck, J., and Lautenschläger, F. (2015). Myosin II activity softens cells in suspension. Biophys. J. *108*, 1856–1869.
Chang, I. Y.-T. (2011). Study of T cell activation and migration at the single-cell and

single-molecule level.
Chaudhuri, O., Parekh, S. H., Lam, W. A., and Fletcher, D. A. (2009). Combined atomic force microscopy and side-view optical imaging for mechanical studies of cells. Nat. Methods *6*, 383–387.
Chemin, K., Bohineust, A., Dogniaux, S., Tourret, M., Guégan, S., Miro, F., and Hivroz, C. (2012). Cytokine secretion by CD4+ T cells at the immunological synapse requires Cdc42-dependent local actin remodeling but not microtubule organizing center polarity. J. Immunol. *189*, 2159–2168.
Cook, S., Walker, A., Hügli, O., Togni, M., and Meier, B. (2007). Percutaneous coronary interventions in Europe: Prevalence, numerical estimates, and projections based on data up to 2004. Clin. Res. Cardiol. *96*, 375–382.
Crotty, S. (2015). A brief history of T cell help to B cells. Nat. Rev. Immunol. *15*, 185–189.
Daily, B., Elson, E. L., and Zahalak, G. I. (1984). Cell poking. Determination of the elastic area compressibility modulus of the erythrocyte membrane. Biophys. J. *45*, 671–682.
Darling, E. M., Topel, M., Zauscher, S., Vail, T. P., and Guilak, F. (2008). Viscoelastic properties of human mesenchymally-derived stem cells and primary osteoblasts, chondrocytes, and adipocytes. J. Biomech. *41*, 454–464.
Davies, P. F. (1995). Flow-mediated endothelial mechanotransduction. Physiol. Rev. *75*, 519–560.
Deleyrolle, L. P. *et al.* (2011). Evidence for label-retaining tumour-initiating cells in human glioblastoma. Brain *134*, 1331–1343.
Deleyrolle, L. P., and Reynolds, B. A. (2009). Identifying and enumerating neural stem cells: application to aging and cancer. Prog Brain Res *175*, 43–51.
Desprat, N., Richert, A., Simeon, J., and Asnacios, A. (2005). Creep function of a single living cell. Biophys. J. *88*, 2224–2233.
Detournay, E., and Cheng, A. H.-D. (1993). Fundamentals of poroelasticity1. Chapter 5 Compr. Rock Eng. Princ. Pract. Proj. II, 113–171.
Diener, J., Barbacci, A., Hemon, P., de Langre, E., and Moulia, M. (2012). CR–KinePlant toolbox. Proc. 7th Int. Biomech. Conf. Clermont-Ferrand, 179.
Dimitriadis, E. K., Horkay, F., Maresca, J., Kachar, B., and Chadwick, R. S. (2002). Determination of elastic moduli of thin layers of soft material using the atomic force microscope. Biophys. J. *82*, 2798–2810.
Discher, D. E., Janmey, P., and Wang, Y. L. (2005). Tissue cells feel and respond to the stiffness of their substrate. Science *310*, 1139–1143.
Ducker, W. a., Senden, T. J., and Pashley, R. M. (1991). Direct measurement of colloidal forces using an atomic force microscope. Nature *353*, 239–241.
Dudani, J. S., Gossett, D. R., Tse, H. T., and Di Carlo, D. (2013). Pinched-flow hydrodynamic stretching of single-cells. Lab Chip *13*, 3728–3734.
DuPage, M., and Bluestone, J. A. (2016). Harnessing the plasticity of CD4(+) T cells to treat immune-mediated disease. Nat Rev Immunol *16*, 149–163.
Edelman, E. R., and Rogers, C. (1998). Pathobiologic responses to stenting. Am. J.

Cardiol. *81*, 98–100.
Edelstein, A., Amodaj, N., Hoover, K., Vale, R., and Stuurman, N. (2010). Computer control of microscopes using manager. Curr. Protoc. Mol. Biol., 1–17.
Edelstein, A. D., Tsuchida, M. a, Amodaj, N., Pinkard, H., Vale, R. D., and Stuurman, N. (2014). Advanced methods of microscope control using μManager software. J. Biol. Methods *1*, 10.
Edmond, E., Farquhar, S., Dunstone, J. R., and Ogston, A. G. (1968). The osmotic behaviour of Sephadex and its effects on chromatography. Biochem. J. *108*, 755–763.
Egeblad, M., Rasch, M. G., and Weaver, V. M. (2010). Dynamic interplay between the collagen scaffold and tumor evolution. Curr. Opin. Cell Biol. *22*, 697–706.
Einstein, A. (1905). Investigations on the theory of the brownian movement. Ann. Phys. *19*, 579.
Engler, A. J., Sen, S., Sweeney, H. L., and Discher, D. E. (2006). Matrix Elasticity Directs Stem Cell Lineage Specification. Cell *126*, 677–689.
Evans, E., Heinrich, V., Ludwig, F., and Rawicz, W. (2003). Dynamic Tension Spectroscopy and Strength of Biomembranes. Biophys. J. *85*, 2342–2350.
Evans, E., and Kukan, B. (1984). Passive material behavior of granulocytes based on large deformation and recovery after deformation tests. Blood *64*, 1028–1035.
Evans, I. D., and Lips, A. (1990). Concentration dependence of the linear elastic behaviour of model microgel dispersions. J. Chem. Soc. Faraday Trans. *86*, 3413.
Fabry, B., Maksym, G. N., Butler, J. P., Glogauer, M., Navajas, D., and Fredberg, J. J. (2001). Scaling the microrheology of living cells. Phys. Rev. Lett. *87*, 1–4.
Figard, L., Xu, H., Garcia, H., Golding, I., and Sokac, A. (2013). The plasma membrane flattens out to fuel cell-surface growth during drosophila cellularization. Dev. Cell *27*, 648–655.
Fung, Y. (2013). Biomechanics: circulation, Springer Science & Business Media.
Galli, R., Binda, E., Orfanelli, U., Cipelletti, B., Gritti, A., De Vitis, S., Fiocco, R., Foroni, C., Dimeco, F., and Vescovi, A. (2004). Isolation and characterization of tumorigenic, stem-like neural precursors from human glioblastoma. Cancer Res. *64*, 7011–7021.
Gauthier, N. C., Fardin, M. A., Roca-Cusachs, P., and Sheetz, M. P. (2011). Temporary increase in plasma membrane tension coordinates the activation of exocytosis and contraction during cell spreading. Proc. Natl. Acad. Sci. U. S. A. *108*, 14467–14472.
Geddes, D. M., Cargill, R. S., and LaPlaca, M. C. (2003). Mechanical stretch to neurons results in a strain rate and magnitude-dependent increase in plasma membrane permeability. J. Neurotrauma *20*, 1039–1049.
Gonzalez-Rodriguez, D., Sart, S., Babataheri, A., Tareste, D., Barakat, A. I., Clanet, C., and Husson, J. (2015). Elastocapillary Instability in Mitochondrial Fission. Phys. Rev. Lett. *115*.
Gossett, D. R., Tse, H. T. K., Lee, S. a., Ying, Y., Lindgren, a. G., Yang, O. O., Rao, J., Clark, a. T., and Di Carlo, D. (2012). Hydrodynamic stretching of single cells for large population mechanical phenotyping. Proc. Natl. Acad. Sci. *109*, 7630–7635.
Grivel, J.-C., Ivanova, O., Pinegina, N., Blank, P. S., Shpektor, A., Margolis, L. B., and

Vasilieva, E. (2011). Activation of T lymphocytes in atherosclerotic plaques. Arterioscler. Thromb. Vasc. Biol. *31*, 2929–2937.
Groulx, N., Boudreault, F., Orlov, S. N., and Grygorczyk, R. (2006). Membrane reserves and hypotonic cell swelling. J. Membr. Biol. *214*, 43–56.
Guck, J. *et al.* (2005). Optical deformability as an inherent cell marker for testing malignant transformation and metastatic competence. Biophys. J. *88*, 3689–3698.
Guillou, L., Babataheri, A., Puech, P.-H., Barakat, A. I., and Husson, J. (2016). Dynamic monitoring of cell mechanical properties using profile microindentation. Sci. Rep. *6*, 21529.
Guo, H., Nickel, J. C., Iwasaki, L. R., and Spilker, R. L. (2012). An augmented Lagrangian method for sliding contact of soft tissue. J. Biomech. Eng. *134*, 084503.
Hackam, D. J., Rotstein, O. D., Sjolin, C., Schreiber, a D., Trimble, W. S., and Grinstein, S. (1998). v-SNARE-dependent secretion is required for phagocytosis. Proc. Natl. Acad. Sci. U. S. A. *95*, 11691–11696.
Harris, A. R., and Charras, G. T. (2011). Experimental validation of atomic force microscopy-based cell elasticity measurements. Nanotechnology *22*, 345102.
Hategan, A., Law, R., Kahn, S., and Discher, D. E. (2003). Adhesively-tensed cell membranes: lysis kinetics and atomic force microscopy probing. Biophys. J. *85*, 2746–2759.
Haward, S. J., Ober, T. J., Oliveira, M. S. N., Alves, M. a., and McKinley, G. H. (2012). Extensional rheology and elastic instabilities of a wormlike micellar solution in a microfluidic cross-slot device. Soft Matter *8*, 536.
Herant, M., Heinrich, V., and Dembo, M. (2005). Mechanics of neutrophil phagocytosis: behavior of the cortical tension. J. Cell Sci. *118*, 1789–1797.
Hibbeler, R. C. Mechanics of Materials, New York: Macmillan.
Hochmuth, R. M. (2000). Micropipette aspiration of living cells. J. Biomech. *33*, 15–22.
Hogan, B., Babataheri, A., Hwang, Y., Barakat, A. I., and Husson, J. (2015). Characterizing Cell Adhesion by Using Micropipette Aspiration. Biophys. J. *109*, 209–219.
Holzapfel, G. A. (2005). Changes in the Mechanical Environment of Stenotic Arteries During Interaction With Stents: Computational Assessment of Parametric Stent Designs. J. Biomech. Eng. *127*, 166.
Hooke, R. (1665). Micrographia, or, Some physiological descriptions of minute bodies made by magnifying glasses◎:with observations and inquiries thereupon
Huang, H., Kamm, R. D., and Lee, R. T. (2004). Cell mechanics and mechanotransduction: pathways, probes, and physiology. Am. J. Physiol. Cell Physiol. *287*, C1–C11.
Hung, W. C., Chen, S. H., Paul, C. D., Stroka, K. M., Lo, Y. C., Yang, J. T., and Konstantopoulos, K. (2013). Distinct signaling mechanisms regulate migration in unconfined versus confined spaces. J. Cell Biol. *202*, 807–824.
Husson, J., Dogterom, M., and Pincet, F. (2009). Force spectroscopy of a single artificial biomolecule bond: The Kramers' high-barrier limit holds close to the critical force. J. Chem. Phys. *130*.

Jennings, S., Bennett, K., Shelley, E., Kearney, P., Daly, K., and Fennell, W. (2014). Trends in percutaneous coronary intervention and angiography in Ireland, 2004-2011: Implications for Ireland and Europe. IJC Hear. Vessel. *4*, 35–39.
Johnson, K. L. (1985). Contact Mechanics. J. Am. Chem. Soc. *37*, 1–17.
Johnson-Léger, C., Aurrand-Lions, M., and Imhof, B. a (2000). The parting of the endothelium: miracle, or simply a junctional affair? J. Cell Sci. *113 (Pt 6*, 921–933.
Kagiwada, H., Nakamura, C., Kihara, T., Kamiishi, H., Kawano, K., Nakamura, N., and Miyake, J. (2010). The mechanical properties of a cell, as determined by its actin cytoskeleton, are important for nanoneedle insertion into a living cell. Cytoskeleton *67*, 496–503.
Kang, I., Wang, Q., Eppell, S. J., Marchant, R. E., and Doerschuk, C. M. (2010). Effect of neutrophil adhesion on the mechanical properties of lung microvascular endothelial cells. Am. J. Respir. Cell Mol. Biol. *43*, 591–598.
Kantsler, V., Segre, E., and Steinberg, V. (2008). Critical dynamics of vesicle stretching transition in elongational flow. Phys. Rev. Lett. *101*.
Karalis, I., Ahmed, T. a H. N., and Jukema, J. W. (2012). Late acquired stent malapposition: why, when and how to handle? Heart *98*, 1529–1536.
Khan, Z. S., and Vanapalli, S. A. (2013). Probing the mechanical properties of brain cancer cells using a microfluidic cell squeezer device. Biomicrofluidics *7*.
Krause, M., te Riet, J., and Wolf, K. (2013). Probing the compressibility of tumor cell nuclei by combined atomic force–confocal microscopy. Phys. Biol. *10*, 065002.
Ku, D. N., Giddens, D. P., Zarins, C. K., and Glagov, S. (1985). Pulsatile flow and atherosclerosis in the human carotid bifurcation. Positive correlation between plaque location and low oscillating shear stress. Arterioscler. Thromb. Vasc. Biol. *5*, 293–302.
Kuzmin, A., Luisier, M., and Schenk, O. (2013). Fast methods for computing selected elements of the Green's function in massively parallel nanoelectronic device simulations. Lect. Notes Comput. Sci. (Including Subser. Lect. Notes Artif. Intell. Lect. Notes Bioinformatics) *8097 LNCS*, 533–544.
Laan, L., Husson, J., Munteanu, E. L., Kerssemakers, J. W. J., and Dogterom, M. (2008). Force-generation and dynamic instability of microtubule bundles. Proc. Natl. Acad. Sci. U. S. A. *105*, 8920–8925.
Lally, C., Dolan, F., and Prendergast, P. J. (2005). Cardiovascular stent design and vessel stresses: A finite element analysis. J. Biomech. *38*, 1574–1581.
Lam, J., Herant, M., Dembo, M., and Heinrich, V. (2009). Baseline Mechanical Characterization of J774 Macrophages. Biophys. J. *96*, 248–254.
Lange, J. R., Steinwachs, J., Kolb, T., Lautscham, L. A., Harder, I., Whyte, G., and Fabry, B. (2015). Microconstriction Arrays for High-Throughput Quantitative Measurements of Cell Mechanical Properties. Biophys. J. *109*, 26–34.
Larghi, P., Williamson, D. J., Carpier, J.-M., Dogniaux, S., Chemin, K., Bohineust, A., Danglot, L., Gaus, K., Galli, T., and Hivroz, C. (2013). VAMP7 controls T cell activation by regulating the recruitment and phosphorylation of vesicular Lat at TCR-activation sites. Nat. Immunol. *14*, 723–731.
Laurent, V. M., Hénon, S., Planus, E., Fodil, R., Balland, M., Isabey, D., and Gallet, F.

(2002). Assessment of mechanical properties of adherent living cells by bead micromanipulation: comparison of magnetic twisting cytometry vs optical tweezers. J. Biomech. Eng. *124*, 408–421.
Lee, G. Y. H., and Lim, C. T. (2007). Biomechanics approaches to studying human diseases. Trends Biotechnol. *25*, 111–118.
Lee, H., Ham, D., and Westervelt, R. M. (2007). CMOS biotechnology, Springer.
Lee, T., Leok, M., and McClamroch, N. H. (2011). Geometric numerical integration for complex dynamics of tethered spacecraft. Proc. 2011 Am. Control Conf., 1885–1891.
Levental, K. R. *et al.* (2009). Matrix Crosslinking Forces Tumor Progression by Enhancing Integrin Signaling. Cell *139*, 891–906.
Ley, K., Laudanna, C., Cybulsky, M. I., and Nourshargh, S. (2007). Getting to the site of inflammation: the leukocyte adhesion cascade updated. Nat. Rev. Immunol. *7*, 678–689.
Li, Q. S., Lee, G. Y. H., Ong, C. N., and Lim, C. T. (2008). AFM indentation study of breast cancer cells. Biochem. Biophys. Res. Commun. *374*, 609–613.
Loi, S., Sun, G., Franz, V., and Butt, H. J. (2002). Rupture of molecular thin films observed in atomic force microscopy. II. Experiment. Phys. Rev. E - Stat. Nonlinear, Soft Matter Phys. *66*, 1–7.
Lomakina, E. B., Spillmann, C. M., King, M. R., and Waugh, R. E. (2004). Rheological analysis and measurement of neutrophil indentation. Biophys. J. *87*, 4246–4258.
Ma, G., Petersen, E., Leong, K. W., and Liao, K. (2012). Mechanical behavior of human embryonic stem cell pellet under unconfined compression. Biomech. Model. Mechanobiol. *11*, 703–714.
Maas, S. A., Ellis, B. J., Ateshian, G. A., and Weiss, J. A. (2012). FEBio: Finite Elements for Biomechanics. J. Biomech. Eng. *134*, 011005.
Mahaffy, R. E., Park, S., Gerde, E., Käs, J., and Shih, C. K. (2004). Quantitative analysis of the viscoelastic properties of thin regions of fibroblasts using atomic force microscopy. Biophys. J. *86*, 1777–1793.
Mahaffy, R. E., Shih, C. K., MacKintosh, F. C., and Käs, J. (2000). Scanning probe-based frequency-dependent microrheology of polymer gels and biological cells. Phys. Rev. Lett. *85*, 880–883.
Majstoravich, S., Zhang, J., Nicholson-Dykstra, S., Linder, S., Friedrich, W., Siminovitch, K. A., and Higgs, H. N. (2004). Lymphocyte microvilli are dynamic, actin-dependent structures that do not require Wiskott-Aldrich syndrome protein (WASp) for their morphology. Blood *104*, 1396–1403.
Malek, a M., and Izumo, S. (1996). Mechanism of endothelial cell shape change and cytoskeletal remodeling in response to fluid shear stress. J. Cell Sci. *109 (Pt 4*, 713–726.
Maniotis, A. J., Chen, C. S., and Ingber, D. E. (1997). Demonstration of mechanical connections between integrins, cytoskeletal filaments, and nucleoplasm that stabilize nuclear structure. Proc. Natl. Acad. Sci. U. S. A. *94*, 849–854.
Mathur, A. B., Collinsworth, A. M., Reichert, W. M., Kraus, W. E., and Truskey, G. A.

(2001). Endothelial, cardiac muscle and skeletal muscle exhibit different viscous and elastic properties as determined by atomic force microscopy. J. Biomech. *34*, 1545–1553.
McConnaughey, W. B., and Petersen, N. O. (1980). Cell poker: An apparatus for stress-strain measurements on living cells. Rev. Sci. Instrum. *51*, 575–580.
McMillan, D. E., Utterback, N. G., and Puma, J. La (1978). Reduced Erythrocyte Deformability in Diabetes. Diabetes *27*, 895–901.
McNeil, P. L., and Steinhardt, R. a (1997). Loss, restoration, and maintenance of plasma membrane integrity. J. Cell Biol. *137*, 1–4.
Mietke, A., Otto, O., Girardo, S., Rosendahl, P., Taubenberger, A., Golfier, S., Ulbricht, E., Aland, S., Guck, J., and Fischer-Friedrich, E. (2015). Extracting Cell Stiffness from Real-Time Deformability Cytometry: Theory and Experiment. Biophys. J. *109*, 2023–2036.
Mitrossilis, D., Fouchard, J., Guiroy, A., Desprat, N., Rodriguez, N., Fabry, B., and Asnacios, A. (2009). Single-cell response to stiffness exhibits muscle-like behavior. Proc. Natl. Acad. Sci. U. S. A. *106*, 18243–18248.
Moeendarbary, E., Valon, L., Fritzsche, M., Harris, A. R., Moulding, D. a, Thrasher, A. J., Stride, E., Mahadevan, L., and Charras, G. T. (2013). The cytoplasm of living cells behaves as a poroelastic material. Nat. Mater. *12*, 253–261.
Muller, W. A. (2011). Mechanisms of leukocyte transendothelial migration. Annu. Rev. Pathol. *6*, 323–344.
Murata, T. (1981). Deformation of an elastic particle suspended in an arbitrary flow field. J. Phys. Soc. Japan *50*, 1009–1016.
Murphy, B. P., Savage, P., McHugh, P. E., and Quinn, D. F. (2003). The stress-strain behavior of coronary stent struts is size dependent. Ann. Biomed. Eng. *31*, 686–691.
Niedergang, F., Colucci-Guyon, E., Dubois, T., Raposo, G., and Chavrier, P. (2003). ADP ribosylation factor 6 is activated and controls membrane delivery during phagocytosis in macrophages. J. Cell Biol. *161*, 1143–1150.
Nijenhuis, N., Zhao, X., Carisey, A., Ballestrem, C., and Derby, B. (2014). Combining AFM and acoustic probes to reveal changes in the elastic stiffness tensor of living cells. Biophys. J. *107*, 1502–1512.
Or-Tzadikario, S., and Gefen, A. (2011). Confocal-based cell-specific finite element modeling extended to study variable cell shapes and intracellular structures: The example of the adipocyte. J. Biomech. *44*, 567–573.
Østerud, B., and Bjørklid, E. (2003). Role of Monocytes in Atherogenesis. Physiol. Rev. *83*, 1069–1112.
Otto, O. *et al.* (2015). Real-time deformability cytometry: on-the-fly cell mechanical phenotyping. Nat. Methods *12*, 199–202, 4 p following 202.
Paszek, M. J. *et al.* (2005). Tensional homeostasis and the malignant phenotype. Cancer Cell *8*, 241–254.
Peeters, E. A. G., Oomens, C. W. J., Bouten, C. V. C., Bader, D. L., and Baaijens, F. P. T. (2005). Mechanical and failure properties of single attached cells under compression. J. Biomech. *38*, 1685–1693.

Pesen, D., and Hoh, J. H. (2005). Micromechanical architecture of the endothelial cell cortex. Biophys. J. *88*, 670–679.
Petersen, N. O., McConnaughey, W. B., and Elson, E. L. (1982). Dependence of locally measured cellular deformability on position on the cell, temperature, and cytochalasin B. Proc. Natl. Acad. Sci. U. S. A. *79*, 5327–5331.
Pettus, E. H., Christman, C. W., Giebel, M. L., and Povlishock, J. T. (1994). Traumatically induced altered membrane permeability: its relationship to traumatically induced reactive axonal change. J. Neurotrauma *11*, 507–522.
Pettus, E. H., and Povlishock, J. T. (1996). Characterization of a distinct set of intra-axonal ultrastructural changes associated with traumatically induced alteration in axolemmal permeability. Brain Res. *722*, 1–11.
Poiseuille, J. L. (1844). Recherches expérimentales sur le mouvement des liquides dans les tubes de très-petits diamètres, Imprimerie Royale.
Raman, a., Trigueros, S., Cartagena, a., Stevenson, a. P. Z., Susilo, M., Nauman, E., and Contera, S. A. (2011). Mapping nanomechanical properties of live cells using multi-harmonic atomic force microscopy. Nat. Nanotechnol. *6*, 809–814.
Ribeiro, C. M. P., Reece, J., and Putney, J. W. (1997). Role of the Cytoskeleton in Calcium Signaling in NIH 3T3 Cells. J. Biol. Chem. *272*, 26555–26561.
Roca-Cusachs, P., Almendros, I., Sunyer, R., Gavara, N., Farré, R., and Navajas, D. (2006). Rheology of passive and adhesion-activated neutrophils probed by atomic force microscopy. Biophys. J. *91*, 3508–3518.
Rodriguez, M. L., McGarry, P. J., and Sniadecki, N. J. (2013). Review on Cell Mechanics: Experimental and Modeling Approaches. Appl. Mech. Rev. *65*, 60801.
Rogers, C., Tseng, D. Y., Squire, J. C., and Edelman, E. R. (1999). Design as Contributors to Vascular Injury. October, 378–383.
Ronald, J. A., Ionescu, C. V, Rogers, K. A., and Sandig, M. (2001). Differential regulation of transendothelial migration of THP-1 cells by ICAM-1/LFA-1 and VCAM-1/VLA-4. J. Leukoc. Biol. *70*, 601–609.
Rosenbluth, M. J., Lam, W. A., and Fletcher, D. A. (2006). Force microscopy of nonadherent cells: a comparison of leukemia cell deformability. Biophys. J. *90*, 2994–3003.
Ross, P. E., Garber, S. S., and Cahalan, M. D. (1994). Membrane chloride conductance and capacitance in Jurkat T lymphocytes during osmotic swelling. Biophys. J. *66*, 169–178.
Rotsch, C., Braet, F., Wisse, E., and Radmacher, M. (1997). AFM imaging and elasticity measurements on living rat liver macrophages. Cell Biol. Int. *21*, 685–696.
Rotsch, C., Jacobson, K., and Radmacher, M. (1999). Dimensional and mechanical dynamics of active and stable edges in motile fibroblasts investigated by using atomic force microscopy. Proc. Natl. Acad. Sci. U. S. A. *96*, 921–926.
Rubashkin, M. G., Ou, G., and Weaver, V. M. (2014). Deconstructing signaling in three dimensions. Biochemistry *53*, 2078–2090.
Rudijanto, A. (2007). The role of vascular smooth muscle cells on the pathogenesis of atherosclerosis. Acta Med. Indones. *39*, 86–93.

Saha, R., and Nix, W. D. (2002). Effects of the substrate on the determination of thin film mechanical properties by nanoindentation. Acta Mater. *50*, 23–38.
Satcher, R. L., and Dewey, C. F. (1996). Theoretical estimates of mechanical properties of the endothelial cell cytoskeleton. Biophys. J. *71*, 109–118.
Sato, M., Nagayama, K., Kataoka, N., Sasaki, M., and Hane, K. (2000). Local mechanical properties measured by atomic force microscopy for cultured bovine endothelial cells exposed to shear stress. J. Biomech. *33*, 127–135.
Sato, M., Suzuki, K., Ueki, Y., and Ohashi, T. (2007). Microelastic mapping of living endothelial cells exposed to shear stress in relation to three-dimensional distribution of actin filaments. Acta Biomater. *3*, 311–319.
Sato, M., Theret, D. P., Wheeler, L. T., Ohshima, N., and Nerem, R. M. (1990). Application of the micropipette technique to the measurement of cultured porcine aortic endothelial cell viscoelastic properties. J. Biomech. Eng. *112*, 263–268.
Schmid-Schönbein, G. W., Shih, Y. Y., and Chien, S. (1980). Morphometry of human leukocytes. Blood *56*, 866–875.
Schneider, C. a, Rasband, W. S., and Eliceiri, K. W. (2012). NIH Image to ImageJ: 25 years of image analysis. Nat. Methods *9*, 671–675.
Sen, S., Subramanian, S., and Discher, D. E. (2005). Indentation and adhesive probing of a cell membrane with AFM: theoretical model and experiments. Biophys. J. *89*, 3203–3213.
Shin, D., and Athanasiou, K. (1999). Cytoindentation for obtaining cell biomechanical properties. J. Orthop. Res. *17*, 880–890.
Shin, J. H., Gardel, M. L., Mahadevan, L., Matsudaira, P., and Weitz, D. a (2004). Relating microstructure to rheology of a bundled and cross-linked F-actin network in vitro. Proc. Natl. Acad. Sci. U. S. A. *101*, 9636–9641.
Shulman, Z. *et al.* (2011). Transendothelial migration of lymphocytes mediated by intraendothelial vesicle stores rather than by extracellular chemokine depots. Nat Immunol *13*, 67–76.
Solon, J., Levental, I., Sengupta, K., Georges, P. C., and Janmey, P. A. (2007). Fibroblast Adaptation and Stiffness Matching to Soft Elastic Substrates. Biophys. J. *93*, 4453–4461.
Springer, T. A. (1994). Traffic signals for lymphocyte recirculation and leukocyte emigration: The multistep paradigm. Cell *76*, 301–314.
Stroka, K. M., and Aranda-Espinoza, H. (2011). Endothelial cell substrate stiffness influences neutrophil transmigration via myosin light chain kinase-dependent cell contraction. Blood *118*, 1632–1640.
Sunyer, R., Trepat, X., Fredberg, J. J., Farré, R., and Navajas, D. (2009). The temperature dependence of cell mechanics measured by atomic force microscopy. Phys. Biol. *6*, 025009.
Tan, S. C. W., Yang, T., Gong, Y., and Liao, K. (2011). Rupture of plasma membrane under tension. J. Biomech. *44*, 1361–1366.
Tee, S. Y., Fu, J., Chen, C. S., and Janmey, P. A. (2011). Cell shape and substrate rigidity both regulate cell stiffness. Biophys. J. *100*.

Theret, D. P., Levesque, M. J., Sato, M., Nerem, R. M., and Wheeler, L. T. (1988). The application of a homogeneous half-space model in the analysis of endothelial cell micropipette measurements. J. Biomech. Eng. *110*, 190–199.
Thoumine, O., and Ott, a (1997). Time scale dependent viscoelastic and contractile regimes in fibroblasts probed by microplate manipulation. J. Cell Sci. *110 (Pt 1*, 2109–2116.
Trepat, X., Deng, L., An, S. S., Navajas, D., Tschumperlin, D. J., Gerthoffer, W. T., Butler, J. P., and Fredberg, J. J. (2007). Universal physical responses to stretch in the living cell. Nature *447*, 592–595.
Trickey, W. R., Baaijens, F. P. T., Laursen, T. A., Alexopoulos, L. G., and Guilak, F. (2006). Determination of the Poisson's ratio of the cell: Recovery properties of chondrocytes after release from complete micropipette aspiration. J. Biomech. *39*, 78–87.
Tse, H. T. K., Gossett, D. R., Moon, Y. S., Masaeli, M., Sohsman, M., Ying, Y., Mislick, K., Adams, R. P., Rao, J., and Di Carlo, D. (2013). Quantitative diagnosis of malignant pleural effusions by single-cell mechanophenotyping. Sci. Transl. Med. *5*, 212ra163.
Tseng, Y., Kole, T. P., and Wirtz, D. (2002). Micromechanical mapping of live cells by multiple-particle-tracking microrheology. Biophys. J. *83*, 3162–3176.
Ueda, H., Morphew, M. K., McIntosh, J. R., and Davis, M. M. (2011). CD4+ T-cell synapses involve multiple distinct stages. Proc. Natl. Acad. Sci. U. S. A. *108*, 17099–17104.
Ulrich, T. A., Jain, A., Tanner, K., MacKay, J. L., and Kumar, S. (2010). Probing cellular mechanobiology in three-dimensional culture with collagen-agarose matrices. Biomaterials *31*, 1875–1884.
Ulrich, T. A., De Juan Pardo, E. M., and Kumar, S. (2009). The mechanical rigidity of the extracellular matrix regulates the structure, motility, and proliferation of glioma cells. Cancer Res. *69*, 4167–4174.
Valignat, M. P., Theodoly, O., Gucciardi, A., Hogg, N., and Lellouch, A. C. (2013). T lymphocytes orient against the direction of fluid flow during LFA-1-mediated migration. Biophys. J. *104*, 322–331.
Vargas-Pinto, R., Gong, H., Vahabikashi, A., and Johnson, M. (2013). The effect of the endothelial cell cortex on atomic force microscopy measurements. Biophys. J. *105*, 300–309.
Verstraete, M. (1990). Coronary atherosclerosis and thrombosis. Recenti Prog. Med. *81*, 221–227.
Walke, W., Paszenda, Z., and Filipiak, J. (2005). Experimental and numerical biomechanical analysis of vascular stent. J. Mater. Process. Technol. *164-165*, 1263–1268.
Wang, Q., Chiang, E. T., Lim, M., Lai, J., Rogers, R., Janmey, P. A., Shepro, D., and Doerschuk, C. M. (2001). Changes in the biomechanical properties of neutrophils and endothelial cells during adhesion. Blood *97*, 660–668.
Wang, Q., and Doerschuk, C. M. (2000). Neutrophil-induced changes in the biomechanical properties of endothelial cells: roles of ICAM-1 and reactive oxygen

species. J. Immunol. *164*, 6487–6494.
Wei, C.-C., Huang, S.-W., and Bau, C.-T. (2012). Using the spring constant method to analyze arterial elasticity in type 2 diabetic patients. Cardiovasc. Diabetol. *11*, 39.
Weiss, A., and Elixhauser, A. (2014). Trends in Operating Room Procedures in U.S. Hospitals, 2001–2011: Statistical Brief #171. Healthc. Cost Util. Proj. Stat. Briefs.
Weiss, L., Harlos, J. P., and Elkin, G. (1991). Measurements of compression of Ehrlich ascites tumor cells and their relevance to hematogenous metastasis. Biorheology *28*, 185–193.
Wong, S. Y., Ulrich, T. A., Deleyrolle, L. P., MacKay, J. L., Lin, J. M. G., Martuscello, R. T., Jundi, M. A., Reynolds, B. A., and Kumar, S. (2015). Constitutive activation of myosin-dependent contractility sensitizes glioma tumor-initiating cells to mechanical inputs and reduces tissue invasion. Cancer Res. *75*, 1113–1122.
Woollard, K. J., and Geissmann, F. (2010). Monocytes in atherosclerosis: subsets and functions. Nat. Rev. Cardiol. *7*, 77–86.
Wottawah, F., Schinkinger, S., Lincoln, B., Ananthakrishnan, R., Romeyke, M., Guck, J., and K??s, J. (2005). Optical rheology of biological cells. Phys. Rev. Lett. *94*.
Wu, M.D, K. K., and Thiagarajan, M.D, P. (1996). Role of Endothelium in Thrombosis and Hemostasis. Annu. Rev. Med. *47*, 315–331.
Wu, H. W., Kuhn, T., and Moy, V. T. (1998). Mechanical properties of L929 cells measured by atomic force microscopy: effects of anticytoskeletal drugs and membrane crosslinking. Scanning *20*, 389–397.
Xia, Y., and Whitesides, G. M. (1998). Soft Lithography. Annu. Rev. Mater. Sci. *28*, 153–184.
Xie, X., Aalipour, A., Gupta, S. V., and Melosh, N. A. (2015). Determining the Time Window for Dynamic Nanowire Cell Penetration Processes. ACS Nano *9*, 11667–11677.
Xie, X., Xu, A. M., Angle, M. R., Tayebi, N., Verma, P., and Melosh, N. A. (2013). Mechanical model of vertical nanowire cell penetration. Nano Lett. *13*, 6002–6008.
Yamada, S., Wirtz, D., and Kuo, S. C. (2000). Mechanics of living cells measured by laser tracking microrheology. Biophys. J. *78*, 1736–1747.
Yanai, M., Butler, J. P., Suzuki, T., Sasaki, H., and Higuchi, H. (2004). Regional rheological differences in locomoting neutrophils. Am. J. Physiol. Cell Physiol. *287*, C603–C611.
Yu, H. Y., Sanday, S. C., and Rath, B. B. (1990). The effect of substrate on the elastic properties of films determined by the indentation test - axisymmetric boussinesq problem. J. Mech. Phys. Solids *38*, 745–764.
Yu, Q. C., and McNeil, P. L. (1992). Transient disruptions of aortic endothelial cell plasma membranes. Am. J. Pathol. *141*, 1349–1360.
Zhou, E. H., Quek, S. T., and Lim, C. T. (2010). Power-law rheology analysis of cells undergoing micropipette aspiration. Biomech. Model. Mechanobiol. *9*, 563–572.

APPENDIX

FEBio micropipette aspiration code

First, we provide the main Matlab script to be executed: upipette_aspiration_exec_v2.m. All the other scripts will be called by this one.

upipette_aspiration_exec_v2.m

```
close all;
clear all;
clc;

%% Input paramaters

% Geometry

param.dgrid             = 1; % mesh size parameter for upipette 1 // 5
param.layers_upipette   = 10; % mesh layers for micropipette quarter geometry 10 //
3
param.rint_upipette     = 5; % micropipette internal radius
param.margin                = 0.1; % margin to avoid imposing negative pressure on
contact area (may be able to reduce as mesh gets finer)
param.e_upipette        = 3; % micropipette thickness
param.redge_upipette    = 0.5; % radius to smooth micropipette edge
param.h_upipette        = 10; % micropipette height

param.dgrid_cell        = 1; % mesh size parameter for cell 1 // 3
param.r_cell            = 10; % cell radius 10
param.z_cell                  =  -sqrt(param.r_cell.^2-param.rint_upipette.^2)  ;  %
vertical position of cell -> make cell move until param.z_cell+param.redge_upipette

% Physics (cell modeled as neo-hookean material)

param.v                 = 0.4; % cell Poisson's ratio
param.E                 = 1000; % cell Young's modulus
param.suction_pressure  = 1000; % negative suction pressure (do not put minus sign
here)

% Computations

param.nsteps            = 100;
param.penalty           = 10^5;

%% Execute FEBio and save output

outFEBio = upipette_aspiration_v2 (param);

%% Save all outputs

% save(['output_FEBio.mat']);
```

upipette_aspiration_v2.m

```
function [out] = upipette_aspiration_v2 (param)

close all;
```

```
clc;

%% Some parameters of the problem

whereisgmsh    = '/home/guillou/Documents/FEBio/gmsh-2.8.3-Linux/bin/'; % not used
for Silkspectre (use alias instead)
currentfolder  =  '/home/comsol/lionel/FEBio/micropipette_aspiration/';  %  current
folder
pathWR          = 'upipette_aspiration.feb'; % name of the feb file that will be
written
title         = 'spherical cell aspiration by micropipette with quarter symmetry';

v             = param.v;
E             = param.E;
penalty       = param.penalty; % penalty factor
nsteps        = param.nsteps;
margin        = param.margin;

tsimu         = 1;
tol           = 1e-1*E ;

%% parametrize geometry in gmsh

paragmsh                = 'parameter.geo'; % input to other gmsh files

fid = fopen(paragmsh,'w');
    fprintf(fid,'%s\n',['dgrid  =  ',num2str(param.dgrid),';  //  mesh  size  parameter
for upipette']);
    fprintf(fid,'%s\n',['rint_upipette   =   ',num2str(param.rint_upipette),';   //
micropipette internal radius']);
    fprintf(fid,'%s\n',['e_upipette     =     ',num2str(param.e_upipette),';     //
micropipette thickness']);
    fprintf(fid,'%s\n',['redge_upipette   =   ',num2str(param.redge_upipette),';   //
radius to smooth micropipette edge']);
    fprintf(fid,'%s\n',['h_upipette     =     ',num2str(param.h_upipette),';     //
micropipette height']);
    fprintf(fid,'%s\n',['layers_upipette  =  ',num2str(param.layers_upipette),';  //
mesh layers for micropipette quarter geometry']);
    fprintf(fid,'%s\n',['dgrid_cell  =  ',num2str(param.dgrid_cell),';  //  mesh  size
parameter for cell']);
    fprintf(fid,'%s\n',['r_cell = ',num2str(param.r_cell),'; // cell radius']);
    fprintf(fid,'%s\n',['z_cell  =  ',num2str(param.z_cell),';  //  vertical  position
of cell']);
fclose(fid);

%% mesh cell and read mesh

pathcell = 'cell';
system(['gmsh -3 ',currentfolder,pathcell,'.geo']);

fid = fopen([pathcell,'.msh']);
    fscanf(fid,'%s',6);
    nb_nodes_cell = fscanf(fid,'%d',1);
    nodes_cell = fscanf(fid,'%d %f %f %f',[4,nb_nodes_cell]);
    fscanf(fid,'%s',2);
    nb_elts_cell_temp = fscanf(fid,'%d',1);
    elts_cell = fscanf(fid,'%f');
fclose(fid);

nodes_cell = [nodes_cell(2:4,:);zeros(1,nb_nodes_cell)];

reading_index           = 1;
flag                    = true;
nb_point_cell           = 0;
nb_line_cell            = 0;
nb_tri_cell             = 0;
nb_tetra_cell           = 0;
index                   = 0;
```

```
% count number of each type of elements
while (flag)

    if (index == nb_elts_cell_temp)
        flag                = false;
    else

        switch (elts_cell(reading_index+1)) % elm_type
            case 15
                reading_index        = reading_index + 6;
                nb_point_cell        = nb_point_cell + 1;
                index                = index + 1;
            case 1
                reading_index        = reading_index + 7;
                nb_line_cell         = nb_line_cell + 1;
                index                = index + 1;
            case 2
                reading_index        = reading_index + 8;
                nb_tri_cell          = nb_tri_cell + 1;
                index                = index + 1;
            case 4
                reading_index        = reading_index + 9;
                nb_tetra_cell        = nb_tetra_cell + 1;
                index                = index + 1;
        end

    end

end

% surface elements
tri_cell                = elts_cell(1+6*nb_point_cell+7*nb_line_cell:...
    6*nb_point_cell+7*nb_line_cell+8*nb_tri_cell);
tri_cell            = reshape(tri_cell,8,nb_tri_cell);
tri_cell(1:4,:)         = [];
tri_cell_temp           = [tri_cell(2,:) tri_cell(3,:) tri_cell(4,:);...
                            tri_cell(1,:) tri_cell(1,:) tri_cell(1,:)]; % 2 is the
entity number in Gmsh
[nb,I]                  = unique(tri_cell_temp(1,:));
lnb                     = tri_cell_temp(2,I);
nodes_cell(4,nb)        = lnb;
[tri_cell(1,:),Ib]      = sort(tri_cell(1,:),'descend');
tri_cell(2:4,:)           = tri_cell(2:4,Ib); % we add the number of nodes of the
upipette to get a global number of nodes

% volume elements
tetra_cell = elts_cell(1+6*nb_point_cell+7*nb_line_cell+8*nb_tri_cell:...
    6*nb_point_cell+7*nb_line_cell+8*nb_tri_cell+9*nb_tetra_cell);
tetra_cell = reshape(tetra_cell,9,nb_tetra_cell);
tetra_cell(1:4,:) = [];
tetra_cell = [tetra_cell(2:5,:);tetra_cell(1,:)]; % we add the number of nodes of
the upipette to get a global number of nodes


%% mesh upipette and read mesh

pathcell = 'upipette';
system(['gmsh -3 ',currentfolder,pathcell,'.geo']);

fid = fopen([pathcell,'.msh']);
    fscanf(fid,'%s',6);
    nb_nodes_upipette = fscanf(fid,'%d',1);
    nodes_upipette = fscanf(fid,'%d %f %f %f',[4,nb_nodes_upipette]);
    fscanf(fid,'%s',2);
    nb_elts_temp = fscanf(fid,'%d',1);
    elts_upipette = fscanf(fid,'%f');
fclose(fid);
```

```
nodes_upipette = [nodes_upipette(2:4,:);zeros(1,nb_nodes_upipette)];

reading_index           = 1;
flag                    = true;
nb_point_upipette       = 0;
nb_line_upipette        = 0;
nb_tri_upipette         = 0;
nb_quad_upipette        = 0;
nb_hexa_upipette        = 0;
nb_prism_upipette       = 0;
index                   = 0;

% count number of each type of elements
while (flag)

    if (index == nb_elts_temp)
        flag                = false;
    else

        switch (elts_upipette(reading_index+1)) % elm_type
            case 15
                reading_index        = reading_index + 6;
                nb_point_upipette    = nb_point_upipette + 1;
                index                = index + 1;
            case 1
                reading_index        = reading_index + 7;
                nb_line_upipette     = nb_line_upipette + 1;
                index                = index + 1;
            case 2
                reading_index        = reading_index + 8;
                nb_tri_upipette      = nb_tri_upipette + 1;
                index                = index + 1;
            case 3
                reading_index        = reading_index + 9;
                nb_quad_upipette     = nb_quad_upipette + 1;
                index                = index + 1;
            case 5
                reading_index        = reading_index + 13;
                nb_hexa_upipette     = nb_hexa_upipette + 1;
                index                = index + 1;
            case 6
                reading_index        = reading_index + 11;
                nb_prism_upipette    = nb_prism_upipette + 1;
                index                = index + 1;
        end

    end

end

% surface elements
tri_upipette                                                                    =
elts_upipette(1+6*nb_point_upipette+7*nb_line_upipette:...
    6*nb_point_upipette+7*nb_line_upipette+8*nb_tri_upipette);
tri_upipette            = reshape(tri_upipette,8,nb_tri_upipette);
tri_upipette(1:4,:)     = [];
tri_upipette_temp                        =    [tri_upipette(2,:)    tri_upipette(3,:)
tri_upipette(4,:);...
                            tri_upipette(1,:)  tri_upipette(1,:)  tri_upipette(1,:)];
% 2 is the entity number in Gmsh
[nb,I]                  = unique(tri_upipette_temp(1,:));
lnb                     = tri_upipette_temp(2,I);
nodes_upipette(4,nb)    = lnb;
[tri_upipette(1,:),Ib]  = sort(tri_upipette(1,:),'descend');
tri_upipette(2:4,:)     = tri_upipette(2:4,Ib) + nb_nodes_cell;
```

```
quad_upipette                                                                    =
elts_upipette(1+6*nb_point_upipette+7*nb_line_upipette+8*nb_tri_upipette:...
    6*nb_point_upipette+7*nb_line_upipette+8*nb_tri_upipette+9*nb_quad_upipette);
quad_upipette           = reshape(quad_upipette,9,nb_quad_upipette);
quad_upipette(1:4,:)    = [];
quad_upipette_temp       = [quad_upipette(2,:) quad_upipette(3,:) quad_upipette(4,:)
quad_upipette(5,:);...
                            quad_upipette(1,:)                    quad_upipette(1,:)
quad_upipette(1,:) quad_upipette(1,:)]; % 2 is the entity number in Gmsh
[nb,I]                  = unique(quad_upipette_temp(1,:));
lnb                     = quad_upipette_temp(2,I);
nodes_upipette(4,nb)    = lnb;
[quad_upipette(1,:),Ib] = sort(quad_upipette(1,:),'descend');
quad_upipette(2:5,:)    = quad_upipette(2:5,Ib) + nb_nodes_cell;

% volume elements

hexa_upipette                                                                    =
elts_upipette(1+6*nb_point_upipette+7*nb_line_upipette+8*nb_tri_upipette+9*nb_quad_
upipette:...

6*nb_point_upipette+7*nb_line_upipette+8*nb_tri_upipette+9*nb_quad_upipette+13*nb_h
exa_upipette);
hexa_upipette           = reshape(hexa_upipette,13,nb_hexa_upipette);
hexa_upipette(1:4,:)    = [];
hexa_upipette                            =   [hexa_upipette(2:9,:)   +   nb_nodes_cell
;hexa_upipette(1,:)];

prism_upipette                                                                   =
elts_upipette(1+6*nb_point_upipette+7*nb_line_upipette+8*nb_tri_upipette+9*nb_quad_
upipette+13*nb_hexa_upipette:...

6*nb_point_upipette+7*nb_line_upipette+8*nb_tri_upipette+9*nb_quad_upipette+13*nb_h
exa_upipette+11*nb_prism_upipette);
prism_upipette          = reshape(prism_upipette,11,nb_prism_upipette);
prism_upipette(1:4,:)   = [];
prism_upipette                           =   [prism_upipette(2:7,:)   +   nb_nodes_cell
;prism_upipette(1,:)];

%% write .feb file

fid = fopen(pathWR,'w');

fprintf(fid,'%s\n',['<?xml version="1.0" encoding="ISO-8859-1"?>']);
fprintf(fid,'%s\n',['<febio_spec version="1.0">']);
fprintf(fid,'%s\n',['<Module type="solid"/>']);

%% control section
fprintf(fid,'%s\n',['<Control>']);
  fprintf(fid,'%s\n',['<title>',title,'</title>']);
fprintf(fid,'%s\n',['</Control>']);

%% material section
fprintf(fid,'%s\n',['<Material>']);
  fprintf(fid,'%s\n',['<material id="1" name="elastic" type="neo-Hookean">']);
    fprintf(fid,'%s\n',['<E>',num2str(E),'</E>']);
    fprintf(fid,'%s\n',['<v>',num2str(v),'</v>']);

% think about how to prescribe nodal displacements for phase 1
%              fprintf(fid,'%s\n',['<trans_z   type="prescribed"   lc="1">',num2str(-
Z*ind),'</trans_z>']);


  fprintf(fid,'%s\n',['</material>']);
  fprintf(fid,'%s\n',['<material id="2" name="upipette" type="rigid body">']);
    fprintf(fid,'%s\n',['<density>1</density>']);
    fprintf(fid,'%s\n',['<trans_x type="fixed"></trans_x>']);
    fprintf(fid,'%s\n',['<trans_y type="fixed"></trans_y>']);
```

```
    fprintf(fid,'%s\n',['<trans_z type="fixed"></trans_z>']);
    fprintf(fid,'%s\n',['<rot_x type="fixed"></rot_x>']);
    fprintf(fid,'%s\n',['<rot_y type="fixed"></rot_y>']);
    fprintf(fid,'%s\n',['<rot_z type="fixed"></rot_z>']);
  fprintf(fid,'%s\n',['</material>']);
fprintf(fid,'%s\n',['</Material>']);

%% geometry section

fprintf(fid,'%s\n',['<Geometry>']);

  fprintf(fid,'%s\n',['<Nodes>']);
    for n = 1:nb_nodes_cell
      fprintf(fid,'%s\n',['<node
id="',num2str(n),'">',num2str(nodes_cell(1,n)),',',...
          num2str(nodes_cell(2,n)),',', num2str(nodes_cell(3,n)),'</node>']);
    end
    for n = 1:nb_nodes_upipette
      fprintf(fid,'%s\n',['<node
id="',num2str(n+nb_nodes_cell),'">',num2str(nodes_upipette(1,n)),',',...
          num2str(nodes_upipette(2,n)),',',
num2str(nodes_upipette(3,n)),'</node>']);
    end
  fprintf(fid,'%s\n',['</Nodes>']);

  fprintf(fid,'%s\n',['<Elements>']);
    for n = 1:nb_tetra_cell % cell elements (material 1)
      fprintf(fid,'%s\n',['<tet4                                id="',num2str(n),'"
mat="1">',num2str(tetra_cell(1,n)),',',...
          num2str(tetra_cell(2,n)),',',                num2str(tetra_cell(3,n)),',',
num2str(tetra_cell(4,n)),'</tet4>']);
    end
    for n = 1:nb_hexa_upipette % upipette elements (material 2)
        fprintf(fid,'%s\n',['<hex8                 id="',num2str(n+nb_tetra_cell),'"
mat="2">',num2str(hexa_upipette(1,n)),',',...
          num2str(hexa_upipette(2,n)),',',          num2str(hexa_upipette(3,n)),',',
num2str(hexa_upipette(4,n)),',',...
          num2str(hexa_upipette(5,n)),',',          num2str(hexa_upipette(6,n)),',',
num2str(hexa_upipette(7,n)),',',...
          num2str(hexa_upipette(8,n)),'</hex8>']);
    end
    for n = 1:nb_prism_upipette % upipette elements (material 2)
        fprintf(fid,'%s\n',['<penta6               id="',num2str(n+nb_tetra_cell),'"
mat="2">',num2str(prism_upipette(1,n)),',',...
          num2str(prism_upipette(2,n)),',',        num2str(prism_upipette(3,n)),',',
num2str(prism_upipette(4,n)),',',...
          num2str(prism_upipette(5,n)),',',
num2str(prism_upipette(6,n)),'</penta6>']);
    end
  fprintf(fid,'%s\n',['</Elements>']);

fprintf(fid,'%s\n',['</Geometry>']);

%% boundary section

nodes_cell = [[1:1:nb_nodes_cell];nodes_cell];
[temp,I] = sort(nodes_cell(5,:),'descend'); % sorts by Gmsh entity if there is one
nodes_cell = nodes_cell(:,I);

fprintf(fid,'%s\n',['<Boundary>']);

       % cell nodes that are on the (OY) axis of symmetry
        n=1;
        fprintf(fid,'%s\n',['<fix>']);
        while (n<=nb_nodes_cell)
            if (nodes_cell(2,n) == 0)
                fprintf(fid,'%s\n',['<node         id="',num2str(nodes_cell(1,n)),'"
bc="x">></node>']);
```

```
            end
            n=n+1;
        end
        fprintf(fid,'%s\n',['</fix>']);

        % cell nodes that are on the (OX) axis of symmetry
        n=1;
        fprintf(fid,'%s\n',['<fix>']);
        while (n<=nb_nodes_cell)
            if (nodes_cell(3,n) == 0)
                fprintf(fid,'%s\n',['<node         id="',num2str(nodes_cell(1,n)),'"
bc="y"></node>']);
            end
            n=n+1;
        end
        fprintf(fid,'%s\n',['</fix>']);

        %        fprintf(fid,'%s\n',['<trans_z  type="prescribed"  lc="1">',num2str(-
Z*ind),'</trans_z>']);

        fprintf(fid,'%s\n',['<contact type="facet-to-facet sliding">']);

            fprintf(fid,'%s\n',['<laugon>1</laugon>']);   %   original   value:   not
present (1 works as well)
            fprintf(fid,'%s\n',['<tolerance>0.01</tolerance>']); % 0.01
            fprintf(fid,'%s\n',['<penalty>',num2str(penalty),'</penalty>']);       %
original value: 500000 (1000 works as well if laugon is 1)
            %  fprintf(fid,'%s\n',['<auto_penalty>1</auto_penalty>']);  %  original
value: not present (0)
            fprintf(fid,'%s\n',['<two_pass>1</two_pass>']); % original value: 1
            %  fprintf(fid,'%s\n',['<gaptol>0.001</gaptol>']);  %  not  present  in
baseline case

            fprintf(fid,'%s\n',['<surface  type="master">']);  %  master  surface  =
surface of the indenter
                j = 1;
                for n=1:length(tri_upipette(1,:))
                    if    (tri_upipette(1,n)==85    ||    tri_upipette(1,n)==67    ||
tri_upipette(1,n)==29 || tri_upipette(1,n)==50)
                        fprintf(fid,'%s\n',['<tri3
id="',num2str(j),'">',num2str(tri_upipette(2,n)),',',...

num2str(tri_upipette(3,n)),',',num2str(tri_upipette(4,n)),'</tri3>']);
                        j = j+1;
                    end
                end
                for n=1:length(quad_upipette(1,:))
                    if    (quad_upipette(1,n)==85    ||    quad_upipette(1,n)==67    ||
quad_upipette(1,n)==29 || quad_upipette(1,n)==50)
                        fprintf(fid,'%s\n',['<quad4
id="',num2str(j),'">',num2str(quad_upipette(2,n)),',',...

num2str(quad_upipette(3,n)),',',num2str(quad_upipette(4,n)),',',...
                            num2str(quad_upipette(5,n)),'</quad4>']);
                        j = j+1;
                    end
                end
            fprintf(fid,'%s\n',['</surface>']);

            fprintf(fid,'%s\n',['<surface type="slave">']);
                for n=1:length(tri_cell(1,:))
                    if ~(tri_cell(1,n)==11 || tri_cell(1,n)==13) % slave surface =
surface 1 (upper face) of the cell
                        fprintf(fid,'%s\n',['<tri3
id="',num2str(j),'">',num2str(tri_cell(2,n)),',',...

num2str(tri_cell(3,n)),',',num2str(tri_cell(4,n)),'</tri3>']);
                        j = j+1;
```

```
                    end
                end
            fprintf(fid,'%s\n',['</surface>']);

        fprintf(fid,'%s\n',['</contact>']);

fprintf(fid,'%s\n',['</Boundary>']);

%% load data section

fprintf(fid,'%s\n',['<LoadData>']);

    fprintf(fid,'%s\n',['<loadcurve id="1">']);
    fprintf(fid,'%s\n',['<loadpoint>0,0</loadpoint>']);
    fprintf(fid,'%s\n',['<loadpoint>1,1</loadpoint>']);
    fprintf(fid,'%s\n',['</loadcurve>']);

    fprintf(fid,'%s\n',['<loadcurve id="2">']);
    fprintf(fid,'%s\n',['<loadpoint>1,0</loadpoint>']);
    fprintf(fid,'%s\n',['<loadpoint>2,1</loadpoint>']);
    fprintf(fid,'%s\n',['</loadcurve>']);

fprintf(fid,'%s\n',['</LoadData>']);

%% step section

% Step 1

fprintf(fid,'%s\n',['<Step>']);

    fprintf(fid,'%s\n',['<Control>']);
      fprintf(fid,'%s\n',['<time_steps>',num2str(nsteps),'</time_steps>']);
      fprintf(fid,'%s\n',['<step_size>',num2str(tsimu/nsteps),'</step_size>']);
      fprintf(fid,'%s\n',['<max_refs>5</max_refs>']); % base 10
      fprintf(fid,'%s\n',['<max_ups>5</max_ups>']); % base 10
      fprintf(fid,'%s\n',['<dtol>0.001</dtol>']); % 0.01
      fprintf(fid,'%s\n',['<etol>0.01</etol>']); % 0.01
      fprintf(fid,'%s\n',['<rtol>0</rtol>']);
      fprintf(fid,'%s\n',['<time_stepper>']);
          fprintf(fid,'%s\n',['<dtmin>',num2str(tsimu/nsteps),'</dtmin>']);        %
default is to divide by 3
          fprintf(fid,'%s\n',['<dtmax>',num2str(tsimu/nsteps*3),'</dtmax>']);
          fprintf(fid,'%s\n',['<max_retries>2</max_retries>']); % default 5
          fprintf(fid,'%s\n',['<opt_iter>2</opt_iter>']); % default 10
      fprintf(fid,'%s\n',['</time_stepper>']); % not enabled in base case
      fprintf(fid,'%s\n',['<lstol>0.9</lstol>']); % 0.1
      fprintf(fid,'%s\n',['<optimize_bw>1</optimize_bw>']);
    fprintf(fid,'%s\n',['</Control>']);

    fprintf(fid,'%s\n',['<Boundary>']);

        n=1;
        fprintf(fid,'%s\n',['<prescribe>']);
        while (n<=nb_nodes_cell)
            if (true)
                fprintf(fid,'%s\n',['<node  id="',num2str(nodes_cell(1,n)),'"  bc="z"
lc="1">',num2str(param.redge_upipette/2),'</node>']);
            end
            n=n+1;
        end
        fprintf(fid,'%s\n',['</prescribe>']);

    fprintf(fid,'%s\n',['</Boundary>']);

fprintf(fid,'%s\n',['</Step>']);

% Step 2: as a first proxy, I do not update as I go the list of nodes to
% which a negative pressure is applied
```

```
fprintf(fid,'%s\n',['<Step>']);

    fprintf(fid,'%s\n',['<Control>']);
      fprintf(fid,'%s\n',['<time_steps>',num2str(nsteps),'</time_steps>']);
      fprintf(fid,'%s\n',['<step_size>',num2str(tsimu/nsteps),'</step_size>']);
      fprintf(fid,'%s\n',['<max_refs>5</max_refs>']); % base 10
      fprintf(fid,'%s\n',['<max_ups>5</max_ups>']); % base 10
      fprintf(fid,'%s\n',['<dtol>0.001</dtol>']); % 0.01
      fprintf(fid,'%s\n',['<etol>0.01</etol>']); % 0.01
      fprintf(fid,'%s\n',['<rtol>0</rtol>']);
      fprintf(fid,'%s\n',['<time_stepper>']);
          fprintf(fid,'%s\n',['<dtmin>',num2str(tsimu/nsteps),'</dtmin>']);        %
default is to divide by 3
          fprintf(fid,'%s\n',['<dtmax>',num2str(tsimu/nsteps*3),'</dtmax>']);
          fprintf(fid,'%s\n',['<max_retries>2</max_retries>']); % default 5
          fprintf(fid,'%s\n',['<opt_iter>2</opt_iter>']); % default 10
      fprintf(fid,'%s\n',['</time_stepper>']); % not enabled in base case
      fprintf(fid,'%s\n',['<lstol>0.9</lstol>']); % 0.1
      fprintf(fid,'%s\n',['<optimize_bw>1</optimize_bw>']);
    fprintf(fid,'%s\n',['</Control>']);

    fprintf(fid,'%s\n',['<Boundary>']);

        [temp,I] = sort(nodes_cell(1,:),'ascend'); % sorts by node number
        nodes_cell = nodes_cell(:,I);

        n=1;
        fprintf(fid,'%s\n',['<pressure>']);
        while (n<=nb_tri_cell)

            if (tri_cell(1,n)==17 && ...
                    norm([nodes_cell(2,tri_cell(2,n))
nodes_cell(3,tri_cell(2,n))])<=param.rint_upipette-margin && ...
                    norm([nodes_cell(2,tri_cell(3,n))
nodes_cell(3,tri_cell(3,n))])<=param.rint_upipette-margin && ...
                    norm([nodes_cell(2,tri_cell(4,n))
nodes_cell(3,tri_cell(4,n))])<=param.rint_upipette-margin)  %  test  that  node  is  on
the top surface and within Rint
                fprintf(fid,'%s\n',['<tri3   id="',num2str(j),'"   lc="2"   scale="-
',num2str(param.suction_pressure),'">',...
                    num2str(tri_cell(2,n)),',',num2str(tri_cell(3,n)),',',...
                    num2str(tri_cell(4,n)),'</tri3>']);
            j = j+1;
            end
            n=n+1;
        end
        fprintf(fid,'%s\n',['</pressure>']);

    fprintf(fid,'%s\n',['</Boundary>']);

fprintf(fid,'%s\n',['</Step>']);

%% output section

fprintf(fid,'%s\n',['<Output>']);
    fprintf(fid,'%s\n',['<logfile file="res.txt">']);
    fprintf(fid,'%s\n',['<node_data data="x;y;z;ux;uy;uz"></node_data>']);
    fprintf(fid,'%s\n',['<element_data
data="x;y;z;sx;sy;sz;sxy;syz;sxz;s1;s2;s3;Ex;Ey;Ez;Exy;Eyz;Exz;E1;E2;E3;Fxx;Fyy;Fzz
;Fxy;Fyz;Fxz;J"></element_data>']);
    fprintf(fid,'%s\n',['<rigid_body_data
data="x;y;z;Fx;Fy;Fz"></rigid_body_data>']);
    fprintf(fid,'%s\n',['</logfile>']);
    fprintf(fid,'%s\n',['<plotfile                                        type="febio"
file="output_upipette_aspiration.xplt">']);
    fprintf(fid,'%s\n',['<var type="displacement"/>']);
    fprintf(fid,'%s\n',['<var type="stress"/>']);
```

```
    fprintf(fid,'%s\n',['<var type="contact pressure"/>']);
    fprintf(fid,'%s\n',['<var type="contact force"/>']);
    fprintf(fid,'%s\n',['<var type="contact gap"/>']);
    fprintf(fid,'%s\n',['</plotfile>']);
fprintf(fid,'%s\n',['</Output>']);

fprintf(fid,'%s\n',['</febio_spec>']);

fclose(fid);

%% launch FEBio and write .plt file

system(['febio              -i              ',currentfolder,pathWR]);              %
system(['/home/guillou/Documents/FEBio/FEBio/febio.lnx64                          -i
',currentfolder,'/',pathWR]);

out.test = 'testrun';

end
```

cell.geo

```
// Include geometrical parameter
Include "parameter.geo";

// rcell = 10; // cell radius
// zcell = -10; // vertical position of cell

// cell points
p1 = newp; Point(p1) = {0,0,z_cell,dgrid_cell};
p2 = newp; Point(p2) = {-r_cell,0,z_cell,dgrid_cell};
p3 = newp; Point(p3) = {0,r_cell,z_cell,dgrid_cell};
p4 = newp; Point(p4) = {0,0,z_cell+r_cell,dgrid_cell};
p5 = newp; Point(p5) = {0,0,z_cell-r_cell,dgrid_cell};

// cell circles
c1 = newreg; Circle(c1) = {p3,p1,p2};
c2 = newreg; Circle(c2) = {p2,p1,p4};
c3 = newreg; Circle(c3) = {p4,p1,p3};
c4 = newreg; Circle(c4) = {p3,p1,p5};
c5 = newreg; Circle(c5) = {p5,p1,p2};

// cell lines
l1 = newreg; Line(l1) = {p1,p2};
l2 = newreg; Line(l2) = {p1,p3};
l3 = newreg; Line(l3) = {p1,p4};
l4 = newreg; Line(l4) = {p1,p5};

// Indenter surfaces
s1 = newreg; Line Loop(s1) = {c5,c2,-l3,l4}; Plane Surface(s1+1) = {s1};
s2 = newreg; Line Loop(s2) = {c3,c4,-l4,l3}; Plane Surface(s2+1) = {s2};
s3 = newreg; Line Loop(s3) = {c5,-c1,c4}; Ruled Surface(s3+1) = {s3};
s4 = newreg; Line Loop(s4) = {c1,c2,c3}; Ruled Surface(s4+1) = {s4};

// Final Volume
vl = newreg; Surface Loop(vl) = {s1+1,s2+1,s3+1,s4+1};
Volume(1) = {vl};
```

parameter.geo

```
dgrid = 0.1; // mesh size parameter for upipette
rint_upipette = 5; // micropipette internal radius
e_upipette = 3; // micropipette thickness
redge_upipette = 0.5; // radius to smooth micropipette edge
h_upipette = 10; // micropipette height
layers_upipette = 10; // mesh layers for micropipette quarter geometry
```

```
dgrid_cell = 1; // mesh size parameter for cell
r_cell = 10; // cell radius
z_cell = -8.6603; // vertical position of cell
```

upipette.geo

```
// Include geometrical parameter
Include "parameter.geo";

// upipette slice points
p1 = newp; Point(p1) = {0,rint_upipette+e_upipette,redge_upipette,dgrid};
p2 = newp; Point(p2) = {0,rint_upipette+e_upipette-redge_upipette,0,dgrid};
p3 = newp; Point(p3) = {0,rint_upipette+e_upipette-
redge_upipette,redge_upipette,dgrid};
p4 = newp; Point(p4) = {0,rint_upipette+redge_upipette,0,dgrid};
p5 = newp; Point(p5) = {0,rint_upipette,redge_upipette,dgrid};
p6 = newp; Point(p6) = {0,rint_upipette+redge_upipette,redge_upipette,dgrid};
p7 = newp; Point(p7) = {0,rint_upipette+e_upipette,h_upipette,dgrid};
p8 = newp; Point(p8) = {0,rint_upipette,h_upipette,dgrid};

// upipette slice circles
c1 = newreg; Circle(c1) = {p1,p3,p2};
c2 = newreg; Circle(c2) = {p4,p6,p5};

// upipette slice lines
l1 = newreg; Line(l1) = {p2,p4};
l2 = newreg; Line(l2) = {p5,p8};
l3 = newreg; Line(l3) = {p8,p7};
l4 = newreg; Line(l4) = {p7,p1};
l5 = newreg; Line(l5) = {p1,p3};
l6 = newreg; Line(l6) = {p3,p6};
l7 = newreg; Line(l7) = {p6,p5};
l8 = newreg; Line(l8) = {p2,p3};
l9 = newreg; Line(l9) = {p4,p6};
l10 = newreg; Line(l10) = {p1,p5};

// upipette slice surface
s1 = newreg; Line Loop(s1) = {l1,l9,-l6,-l8};
Plane Surface(s1+1) = {s1};
s2 = newreg; Line Loop(s2) = {c1,l8,-l5};
Plane Surface(s2+1) = {s2};
s3 = newreg; Line Loop(s3) = {c2,-l7,-l9};
Plane Surface(s3+1) = {s3};
s4 = newreg; Line Loop(s4) = {l2,l3,l4,l10};
Plane Surface(s4+1) = {s4};

// impose structured mesh on upipette surface
Transfinite Surface{s1+1};
Recombine Surface(s1+1);
Transfinite Surface{s4+1};
Recombine Surface(s4+1);

// Extrude upipette
Extrude { {0,0,1}, {0,0,0}, Pi/2} { Surface{s1+1,s2+1,s3+1,s4+1};
Layers{layers_upipette}; Recombine;}
```

ÉCOLE DOCTORALE
INTERFACES
Approches Interdisciplinaires : Fondements, Applications et Innovation

Mécanique Cellulaire: Propriétés Mécaniques et Critères de Rupture de Membrane

Mots clés: Mécanique, Cellule, Rupture

Résumé: L'athérosclérose est une maladie artérielle chronique qui est une des causes majeures d'accidents vasculaires cérébraux et de crises cardiaques. Cette thèse a pour objectif de mieux comprendre certains facteurs spécifiques impliqués dans le dévelopement de cette maladie en abordant cette problématique sous l'angle de la mécanique.
Deux types de cellules qui jouent un rôle important dans le dévelopement et la progression de l'athérosclérose sont les cellules endothéliales adhérentes et les leucocytes non-adhérents (les globules blancs). Nous avons développé deux systèmes capables de mesurer les propriétés mécaniques de ces deux grands types cellulaires. Le premier, appelé "indentation de profil", utilise des micropipettes et des microindenteurs pour indenter la cellule, tandis que le second utilise la microfluidique pour soumettre les cellules à une contrainte d'élongation.
De plus, nous nous sommes demandé si la mécanique pouvait nous aider à comprendre quand les déformations des cellules, ou les contraintes exercées sur elles, pouvaient les endommager.
En effet, lorsque les plaques d'athérosclérose obstruent une partie trop grande du flux sanguin, le traitement le plus courant consiste à rouvrir le vaisseau avec un ballon et à le maintenir ouvert au moyen d'une endoprothèse artérielle, qui est un petit dispositif maillé et tubulaire. Cette procédure exerce des contraintes de compression considérables sur l'endothélium et l'endommage. Nous avons donc cherché à trouver un critère physique prédictif de la rupture de la membrane des cellules endothéliales en compression, puis avons comparé cela aux contraintes exercées sur l'endothélium durant la pose d'une endoprothèse artérielle, afin de voir si les dommages faits à l'endothélium pouvaient potentiellement être évités.
De façon similaire, nous avons cherché à obtenir un critère physique prédictif de la rupture de la membrane des leucocytes. Nous avons ensuite comparé les déformations maximales possibles des leucocytes selon que ces déformations soient passives (comme lors du passage dans la microvasculature) ou actives (comme lors de la traversée de l'endothélium par les leucocytes).

Cell Mechanics: Mechanical Properties and Criteria for Membrane Rupture

Keywords: Mechanics, Cell, Rupture

Abstract: Atherosclerosis is a chronic disease of the arteries that is a major cause of heart attacks and strokes. This thesis aims to provide novel insight into this disease by looking at specific factors involved in its development from a mechanical standpoint.
Two important cell types involved in the development and progression of atherosclerosis are adherent endothelial cells and non-adherent leukocytes (white blood cells). We developed two devices that are able to measure the mechanical properties of both of these cell types. The first one, termed "profile microindentation", uses micropipettes and microindenters to indent the cell, while the second one uses microfluidics to submit cells to an extensional stress.
Further, we wondered if mechanics could help us understand when deformations undergone by cells, or stresses exerted on them, could become harmful.
As a matter of fact, when atherosclerotic plaques occlude too much of the blood flow, the most common treatment consists of reopening the vessel with a balloon and keeping it open with a tubular wired mesh called a stent. This procedure exerts considerable compressive stress on the endothelium and is known to be associated with extensive endothelial damage. Hence, we seek to find a physical criterion that is predictive of endothelial cell membrane rupture under compression and to compare this to the stress exerted on the endothelium during the stenting procedure, to see if endothelial damage could potentially be avoided.
Similarly, we seek to obtain a physical criterion that is predictive of leukocyte membrane rupture. We then compare and contrast the maximum possible deformations of leukocytes depending on whether those deformations are passive (such as when going through the microvasculature) or active (such as when leukocytes traverse the endothelial barrier).